



ScuDo
Scuola di Dottorato ~ Doctoral School
WHAT YOU ARE, TAKES YOU FAR



Doctoral Dissertation
Doctoral Program in PhD program in
Electrical, Electronics and Communications Engineering (33rd Cycle)

Electronic design of innovative mini ultralight radioprobes aimed at tracking lagrangian turbulence fluctuations within warm clouds

Miryam Elizabeth Paredes Quintanilla

* * * * *

Supervisor

Prof. Flavio Canavero

Doctoral Examination Committee:

Dr. Ali Nadir Arslan, Referee, Finnish Meteorological Institute

Dr. Marco Gabella, Referee, MeteoSwiss

Prof. E.F. , Referee, University of....

Prof. G.H. , Referee, University of...

Prof. I.J. , Referee, University of....

Politecnico di Torino
September 01, 2021

This thesis is licensed under a Creative Commons License, Attribution - Noncommercial - NoDerivative Works 4.0 International: see www.creativecommons.org. The text may be reproduced for non-commercial purposes, provided that credit is given to the original author.

I hereby declare that, the contents and organisation of this dissertation constitute my own original work and does not compromise in any way the rights of third parties, including those relating to the security of personal data.
Republication licenses and permissions have been obtained for the copyright protected material here displayed.

Miryam Elizabeth Paredes
Quintanilla
Turin, September 01, 2021

.....

Summary

Clouds are a natural challenging element of Earth that play active role in climate change and climate sensitivity; and their evolution involves multi dynamical, radiative, and microphysical process on a vast range of temporal and spatial scales.

Turbulence plays an important role in the development and dynamics of clouds, spanning from the microphysics level (fraction of millimetres) to the weather and global climate scale (tens of kilometers) since, it leads entrainment, stirring and mixing processes. Specifically, at the smallest scales, turbulence affects the cloud's efficiency to produce rain since it enormously favours the motion and growth of rain droplets through collisions and coalescence, thus reducing significantly the time required for warm rain initiation. Nevertheless, turbulence mechanisms associated to particle dynamics are not yet fully understood partly due to the complexity in measuring clouds at such scales and the poor/lack of explicit representation of turbulence processes in general circulation models hence leaving open questions in atmospheric physics.

In an attempt to address these knowledge gaps, this work presents a novel in-situ experimental method for measuring the influence of small-scale turbulence in cloud formation and producing an in-field cloud Lagrangian dataset by means of an innovative ultra-light and expendable radioprobe. With a maximum target weight of 20 grams and a diameter of 30 cm, this radioprobe is designed to passively track small-scale turbulence fluctuations, such as air velocity, water vapor, pressure, and temperature inside warm clouds and neighboring ambient air according to the Lagrangian description.

This research work focuses on the electronic design of the complete radioprobe system (ultra-light radioprobes and ground stations) and presents the most significant results derived from laboratory and field experiments. The fully customized radioprobe board featuring small dimensions (5 cm x 5 cm), embeds a

set of compact size microprocessors, controllers, and sensors aimed to measure local inner cloud fluctuations in acceleration, trajectory, pressure, humidity, and temperature. For the duration of the flight, it acquires, partially processes, stores, organizes, and transmits in nearly real time the collected information to various ground stations spatially distributed on land. Due to the radioprobes' physical constraints and the environmental conditions that can be found inside warm clouds, the communication between the flying instrumented balloons and the ground stations is achieved thanks to the use of a dedicated long-range and power-saving wireless communication link. At the ground level, the ground stations are designed to capture, store, manage, process, and display the data coming from the floating devices.

The tests performed to validate the system design, both in the lab and in open air, confirm that the newly developed radioprobes together with the ground stations perform well, providing accurate information about small scale atmospheric turbulence variables, referenced in space. The combination of multiple mini radioprobes will consent systematic and accurate observations into small scale turbulence fluctuations inside warm clouds specifically over land and alpine environments. These unique in situ measurements are essential to enhance the current understanding of turbulence-related microphysical processes in warm clouds thus, improving actual studies of cloud formation.

Acknowledgment

This research work is part of the project COMPLETE (Cloud-MicroPhysics-Turbulence-Telemetry) that has received funding from the European Union's Horizon 2020 research and innovation programme under the Marie Skłodowska-Curie Actions (MSCA) grant agreement No. 675675.

I would like to express my sincere gratitude to my supervisor, Professor Flavio Canavero, for his guidance, patience, and continuous support throughout this research work.

I would like to express my deepest gratitude to Professor Daniela Tordella for making possible the realization of the entire Project COMPLETE. I also thank her for the support not only at the scientific level but also at the personal ambit, and for the profound belief in my work.

I would like to thank Professor Giovanny Perona, PhD. Marco Allegretti and PhD. Silvano Bertoldo who, through EnviSens Technologies S.r.l., gave me the opportunity to join the COMPLETE network. I thank them also for the valuable suggestions and resources during the conception and evolution of this research work.

I am extremely grateful to Professor Eros Pasero for his insightful suggestions and resources during the evolution of this work. I thank him also for letting me be part of his research group.

I would like to extend my sincere thanks to Professor Patrizia Savi for her precious guidance, support, and encouragement throughout the entire process.

Many thanks to the Istituto Nazionale di Ricerca Metrologica (INRiM), especially to PhD. Andrea Merlone and PhD. Chiara Musacchio, for supporting the experimental measurements held at the Applied Thermodynamics Laboratory and in field.

I would like to thank the Regional Agency for the Protection of the Environment (ARPA) of the Piedmont Region of Italy, especially to PhD. Luca Tomassone, for supporting the experimental measurements using their national atmospheric sounding system.

I would like to thank the Istituto Italiano di Tecnologia (IIT), especially to PhD. Athanassia Athanassiou and PhD. Giovanni Perotto, for supporting the development of the biodegradable balloons at the Smart Materials Department.

I also thank Shahbozbek Abdunabiev for his collaborative effort in this project.

Last but not least, I'm deeply indebted to my beloved family in this very intense academic period. Thanks for always believing in me, for the unconditional love and support. Without their tremendous understanding and encouragement, this research work and academic achievement would not have been possible.

*I would like to dedicate
this thesis to my
beloved family Alberto,
Danna, and Kristel.*

*Thanks for the
unconditional love
and for being always
there for me.*

Contents

1. Introduction.....	1
2. Atmospheric clouds as a source of uncertainty	6
2.1 Clouds and cloud turbulence basics	6
2.1.1 Clouds in the climate system.....	6
2.1.2 Clouds in the climate system.....	8
2.1.3 Cloud classification	9
2.1.4 Cloud challenges	12
2.1.5 Turbulence: its effects on cloud dynamics and available study framework.....	14
2.2 Lagrangian measurements	16
2.3 Radiosondes and weather balloons	18
2.3.1 Radiosondes	18
2.3.2 Weather balloons.....	19
2.3.3 Lagrangian balloons	20
3. New concept of ultra-light radioprobes for in-cloud turbulence measurement	22
3.1 Understanding the radioprobe environment and design requirements	22
3.1.1 Critical technical aspects	25
3.2 The proposed radioprobe system architecture and design methodology	25
3.2.1 Working principle	25
3.2.2 System architecture	27
3.2.3 Electronic system configuration.....	28
3.2.4 Flow diagram	29

3.3	Selection of system components.....	30
3.3.1	Radioprobe	30
3.3.2	Ground Station	47
3.4	Radioprobe system integration	53
3.4.1	Schematic Diagram Design.....	54
3.4.2	Board Layout Design	56
4.	Validation of the radioprobe system.....	61
4.1	Antenna Matching.....	61
4.1.1	Calibration of the equipment using the R&S ZVL Vector Network Analyzer.....	62
4.1.2	Impedance measurements and calculation of the matching network components.....	64
4.2	Data Transmission Ranges.....	72
4.2.1	Test 1	72
4.2.2	Test 2.....	76
4.2.3	Test 3.....	78
4.2.4	Test 4.....	80
4.3	Sensor Measurements	84
4.3.1	Test 1: Temperature, pressure, and humidity sensors unit.....	85
4.3.2	Test 2: Temperature, pressure, and humidity sensors unit.....	90
4.3.3	Test 3: Temperature, pressure, and humidity sensors unit.....	97
4.3.4	Test 4: Positioning and Tracking sensors unit	100
4.3.5	Test 5: Positioning and Tracking sensors unit	103
4.3.6	Test 6: Positioning and Tracking sensors unit	106
4.4	Power Consumption Analysis.....	110
4.4.1	Power saving strategies	110
4.4.2	Current Consumption Measurement	112
5.	Conclusions and future work	114
6.	References.....	117
7.	Appendix A: Initial tests	144
I.	Software environment and microcontroller	144
II.	Communication technology	145

III.	Temperature, Pressure and Relative Humidity sensor.....	161
IV.	Positioning and tracking sensors.....	169

List of Tables

Table 2.1 Cloud classification based on the height of their basis	10
Table 3.1 Determination of balloon size by balancing the atmosphere's density and the balloon's density (considering a fixed total weight of 20 g). Constant lapse rate = 6.5 K/km	22
Table 3.2 Summary of operational conditions for the radioprobes	24
Table 3.3 Range of possible spreading factors used in LoRa modulation.....	33
Table 3.4 Cyclic coding overhead LoRa	33
Table 3.5 Influence of BW on Time on Air and Sensitivity for CR = 4, SF = 10	34
Table 3.6 Electrical characteristics transceiver RFM95. Power consumption	36
Table 3.7 Main electrical characteristics of the BME280 sensor. Current consumption.....	40
Table 3.8 Humidity parameter specifications sensor BME280	40
Table 3.9 Pressure sensor specifications BME280	40
Table 3.10 Temperature sensor specifications BME280	40
Table 3.11 Main electrical characteristics of the LSM9DS1 module	42
Table 3.12 Sensor characteristics of the LSM9DS1 module	42
Table 3.13 Main electrical characteristics of the ZOE-M8B GNSS receiver.....	44
Table 3.14 ZOE-M8B GNSS performance for GPS and GLONASS	44
Table 4.1 Solutions for matching network configurations. Circuit 1	69
Table 4.2 Solutions for matching network configurations. Circuit 2	69
Table 4.3 Results of the matching and frequency-tuning procedures.....	71
Table 4.4 Results of the point-to-point communication setup in an outdoor urban environment.	77
Table 4.5 Results of the point-to-point dynamic communication setup in an outdoor environment	80
Table 4.6 Results of the point-to-point communication setup in an open area environment	83

Table 4.7 Statistical comparison between radioprobe sensors and reference sensors readings. Temperature.	89
Table 4.8 Statistical comparison between radioprobe sensors and reference sensors readings. Barometric pressure.....	89
Table 4.9 Statistical comparison between radioprobe sensors and reference sensors readings. Relative humidity.	89
Table 4.10 Statistical comparison between radioprobe sensors and reference sensors readings. Approximate altitude.....	90
Table 4.11 Statistical comparison between radioprobe sensors and reference sensors readings. Temperature. Radioprobe 1	95
Table 4.12 Statistical comparison between radioprobe sensors and reference sensors readings. Temperature. Radioprobe 2	95
Table 4.13 Statistical comparison between radioprobe sensors and reference sensors readings. Temperature. Radioprobe 3	95
Table 4.14 Statistical comparison between radioprobe sensors and reference sensors readings. Relative humidity. Radioprobe 1	95
Table 4.15 Statistical comparison between radioprobe sensors and reference sensors readings. Relative humidity. Radioprobe 2	96
Table 4.16 Statistical comparison between radioprobe sensors and reference sensors readings. Relative humidity. Radioprobe 3	96
Table 4.17 Statistical comparison between radioprobe sensors and ARPA reference sensors readings. Temperature, pressure, and relative humidity	100
Table 4.18 Statistical comparison between radioprobe sensors and ARPA reference sensors readings. GNSS receiver	102
Table 4.19 Statistical results of the radioprobe's positioning sensor accuracy during the test.....	105
Table A.1 Output power tests using a set output power of 5 dBm at different bandwidth.....	146
Table A.2 Output power tests using a set output power of 10 dBm at different bandwidth.....	146
Table A.3 Output power tests using a set output power of 14 dBm at different bandwidth.....	147
Table A.4 Results of indoor measurements. DET POLITO. Floor 4th	150
Table A.5 Results of outdoor measurements. DET POLITO. Rooftop	151
Table A.6 Results of outdoor measurements. DET POLITO. Rooftop	153
Table A.7 Results of outdoor measurements. DET POLITO. Rooftop	155
Table A.8 Results of star topology setup in an outdoor environment.	157
Table A.9 Signal attenuation introduced by some envelope materials	161

Table A.10 Accelerometer's systematic error (n = 10000 samples, sampling frequency = 100Hz)	171
Table A.11 Gyroscope's systematic error (n = 10000 samples, sampling frequency = 100Hz)	172
Table A.12 Magnetometer systematic error (n = 10000 samples, sampling frequency = 100Hz)	173

List of Figures

Figure 2.1 Tiny water droplets aggregating around a hygroscopic aerosol.....	6
Figure 2.2 Cloud development process.....	7
Figure 2.3 Climate system	8
Figure 2.4 Solar radiation intercepted by Earth. Effect of cloud reflection and scatter	9
Figure 2.5 Cloud classification	10
Figure 2.6 Cloud fraction on Earth	13
Figure 2.7 Presence of turbulence at all cloud scales	14
Figure 2.8 Global warm rain occurrence	15
Figure 2.9 Eulerian vs. Lagrangian description example	17
Figure 3.1 Kinetic energy spectrum of atmosphere turbulence	24
Figure 3.2 Working principle of the system	26
Figure 3.3 Block diagram of the mini radioprobe	28
Figure 3.4 Block diagram of the ground station	29
Figure 3.5 Main processing flow of the radioprobe system	30
Figure 3.6 Main parameters of LoRa modulation.....	34
Figure 3.7 Structure of a LoRa frame	34
Figure 3.8 L-section matching networks. a) Configuration for normalized load impedance inside the $1 + jx$ Smith Chart circle. b) Configuration for normalized load impedance outside the $1 + jx$ Smith Chart circle	39
Figure 3.9 Block diagram of the ground station	48
Figure 3.10 Node-RED environment. Example of a flow implemented to process and store data	50
Figure 3.11 Node-RED environment. Example of a function implemented to parse data.....	51
Figure 3.12 Command line interface to the start the InfluxDB database	52

Figure 3.13 Command line interface to the access and manage the database InfluxDB	52
Figure 3.14 Chronograf environment. Example of the graphical output provided by the post-processing system	53
Figure 3.15 Power system and filtering schematic diagram	54
Figure 3.16 Data processing and control unit schematic diagram	54
Figure 3.17 Radio communication system schematic diagram	55
Figure 3.18 Temperature, barometric pressure and relative humidity sensor unit schematic diagram	55
Figure 3.19 Positioning and tracking measurement unit schematic diagram	56
Figure 3.20 Top view of the radioprobe's board layout design	57
Figure 3.21 Bottom view of the radioprobe's board layout design	58
Figure 3.22 Manual soldering of the radioprobe components	59
Figure 3.23 Final PCB implementation of the tiny radioprobe. Left: top side, right: bottom side	59
Figure 3.24 Final PCB implementation of the tiny radioprobe. Main electronic components	60
Figure 4.1 RF front end. Left side: Transmitter section. Right side: Receiver section.	62
Figure 4.2 N7551A Electronic Calibration Module ECal	63
Figure 4.3 System setup for calibration of the Keysight P9371A VNA	63
Figure 4.4 One-port calibration screen. Keysight P9371A VNA	64
Figure 4.5 Initial matching network configuration RF circuit 1, transmission RF stage. Manufacturer's recommendation	65
Figure 4.6 Initial matching network configuration RF circuit 2, receiving RF stage. Manufacturer's recommendation	65
Figure 4.7 Initial measurements circuit 1, transmission RF stage. Return loss S_{11}	66
Figure 4.8 Initial measurements circuit 1, transmission RF stage. Complex impedance	66
Figure 4.9 Initial measurements circuit 2, receiving RF stage. Return loss S_{11}	66
Figure 4.10 Initial measurements circuit 2, receiving RF stage. Complex impedance	67
Figure 4.11 Antenna impedance measurements circuit 1, transmission RF stage. Return loss S_{11}	68
Figure 4.12 Antenna impedance measurements circuit 1, transmission RF stage.	68
Figure 4.13 Antenna impedance measurements circuit 2, receiving RF stage. Return loss S_{11}	68

Figure 4.14 Antenna impedance measurements circuit 2, receiving RF stage. Complex impedance	69
Figure 4.15 Final matching network configuration circuit 1, transmission RF stage.	70
Figure 4.16 Final antenna impedance measurements circuit 1, transmission RF stage. Complex impedance	71
Figure 4.17 Final matching network configuration circuit 2, receiving RF stage.	71
Figure 4.18 Final matching network configuration circuit 2, receiving RF stage.	71
Figure 4.19 Test to verify the power spectrum of the transmitted signal	73
Figure 4.20 System setup 1. Point-to-point configuration used to determine the transmission ranges reached by the communication system in an open urban environment, displayed on a map..	74
Figure 4.21 Some pictures of the outdoor communication test. Left: Location of the transmitter position at P2. Right: Location of receiving station and Spectrum Analyzer. DET POLITO. Rooftop.....	74
Figure 4.22 Data statistics System setup test 1. Transmitter position P1	74
Figure 4.23 Data statistics System setup test 1. Transmitter position P2	75
Figure 4.24 Data statistics System setup test 1. Transmitter position P3	75
Figure 4.25 Data statistics System setup test 1. Transmitter position P4	76
Figure 4.26 System setup 2. Point-to-point topology configuration used to determine the transmission ranges reached by the communication system in an urban environment, displayed on a map. Transmitter (P1 to P8) and receiver (Rx) positions.	77
Figure 4.27 Some pictures of the point-to-point communication test. Left: Location of the transmitter at P1. Right: Receiving station placed at the third floor of the DET POLITO.	77
Figure 4.28 System setup test 3. Point-to-point dynamic communication test using an UAV. Left: UAV holding the radioprobe. Right: Radioprobe ground stations and PC receiving the UAV data.	79
Figure 4.29 Some pictures of the point-to-point dynamic communication test using an UAV	79
Figure 4.30 Relative altitude reached by the UAV carrying the radioprobe. Left: First time interval. Right: Second time interval.....	80
Figure 4.31 Automatic atmospheric sounding system. Cuneo - Levaldigi meteorological station (LIMZ)	81
Figure 4.32 Mini radioprobe adhered to the reference atmospheric sounding system.	82
Figure 4.33 Radioprobe ground station.	82

Figure 4.34 Trajectory followed by the systems: mini radioprobe and sounding balloon, displayed on a map. The separation distance with respect to the ground station is indicated by the color bar.	83
Figure 4.35 Radioprobe sensors. Left side: TPH sensor stage. Right side: positioning and tracking sensor stage.	84
Figure 4.36 Test setup for the measurement of temperature, pressure, relative humidity and altitude estimation. Left side: Pair of measuring radioprobes. Right side: System setup.....	86
Figure 4.37 Ambient temperature comparison between radioprobe sensor readings and reference readings. Top left: pairs radioprobe 1 and radioprobe 2. Top right: pairs radioprobe 3 and radioprobe 4. Bottom left: pairs radioprobe 5 and radioprobe 6. Bottom right: pairs radioprobe 7 and radioprobe 8.....	87
Figure 4.38 Barometric pressure comparison between radioprobe sensor readings and reference readings. Top left: pairs radioprobe 1 and radioprobe 2. Top right: pairs radioprobe 3 and radioprobe 4. Bottom left: pairs radioprobe 5 and radioprobe 6. Bottom right: pairs radioprobe 7 and radioprobe 8.....	87
Figure 4.39 Relative humidity comparison between radioprobe sensor readings and reference readings. Top left: pairs radioprobe 1 and radioprobe 2. Top right: pairs radioprobe 3 and radioprobe 4. Bottom left: pairs radioprobe 5 and radioprobe 6. Bottom right: pairs radioprobe 7 and radioprobe 8.....	88
Figure 4.40 Approximate altitude comparison between radioprobe sensor readings and reference readings. Top left: pairs radioprobe 1 and radioprobe 2. Top right: pairs radioprobe 3 and radioprobe 4. Bottom left: pairs radioprobe 5 and radioprobe 6. Bottom right: pairs radioprobe 7 and radioprobe 8.....	88
Figure 4.41 General system setup test 2. Applied Thermodynamics Laboratory INRiM.....	91
Figure 4.42 System setup inside the climatic chamber. Applied Thermodynamics Laboratory INRiM.....	92
Figure 4.43 Comparison of temperature measurements. Radioprobes' sensors vs. reference temperature sensors measurements. Larger cycle test.	93
Figure 4.44 Radioprobes' humidity measurements during the larger cycle test. ..	93
Figure 4.45 Comparison of relative humidity measurements. Radioprobes' sensor measurements during humidity cycle test.....	94
Figure 4.46 Comparison of temperature measurements. Radioprobes' sensors vs. reference temperature sensors measurements. Humidity cycle test.	94
Figure 4.47 Mini radioprobe attached to the reference atmospheric sound.....	98
Figure 4.48 Comparison of temperature measurements between the ARPA reference sonde sensors and the radioprobe sensors.....	99

Figure 4.49 Comparison of pressure measurements between the ARPA reference sonde sensors and the radioprobe sensors.....	99
Figure 4.50 Comparison of relative humidity measurements between the ARPA reference sonde sensors and the radioprobe sensors.....	99
Figure 4.51 System setup. Mini radioprobe attached to the reference atmospheric sound through a thread.....	101
Figure 4.52 Trajectory followed by the systems: mini radioprobe and sounding balloon, displayed on a map.	102
Figure 4.53 Trajectory comparison between the systems, Google Maps view. Blue line: trajectory recorded by the radioprobe. Red line: trajectory recorded by the smartphone GPS logger	104
Figure 4.54 Latitude comparison between the systems in function of time. Blue line: latitude recorded by the radioprobe. Red line: latitude recorded by the smartphone GPS logger.....	104
Figure 4.55 Longitude comparison between the systems in function of time. Blue line: longitude recorded by the radioprobe. Red line: longitude recorded by the smartphone GPS logger	105
Figure 4.56 System setup test 5 for the detection of low-atmosphere fluctuations. Left: Radioprobe inserted inside a biodegradable balloon. Right: Radioprobe ground station.	107
Figure 4.57 Some pictures of the test 5 using a He-filled balloon as means of transportation.	107
Figure 4.58 Raw acceleration measured by the radioprobe sensors during the flight.	108
Figure 4.59 Raw angular rate measured by the radioprobe sensors during the flight.	108
Figure 4.60 Raw magnetic field measured by the radioprobe sensors during the flight.....	108
Figure 4.61 Trajectory followed by the radioprobe system (radioprobe board and biodegradable balloon) during the low-atmosphere flight, displayed on a map..	109
Figure 4.62 Temperature, atmospheric pressure and relative humidity fluctuations measured by the radioprobe sensors during the flight	109
Figure 4.63 Power system and filtering schematic diagram. Different voltage levels of the circuit.	111
Figure 4.64 Current consumption measurement of a fully operating radioprobe	112
Figure A.1 Development board Arduino Nano embedding the microcontroller ATmega328P	144

Figure A.2 LoRa-based transmitter node to initially test communication technology	145
Figure A.3 Short-range transmission test to initially test communication technology. Left side transmitter serial port output. Right side receiver serial port output	146
Figure A.4 System setup test 2. Point-to-point configuration used to determine the transmission ranges reached by the communication system in an indoor environment, displayed on a map..	149
Figure A.5 Some pictures of the indoor communication test. Left: Location of receiving station. Right: Location of the transmitter position at P7.	150
Figure A.6 System setup test 3. Point-to-point configuration used to determine the transmission ranges reached by the communication system in an open urban environment, displayed on a map..	151
Figure A.7 Some pictures of the outdoor communication test. Left: Location of the transmitter position at P4. Right: Location of receiving station. DET POLITO. Rooftop	151
Figure A.8 System setup test 4. Point-to-point configuration used to determine the transmission ranges reached by the communication system in an open urban environment, displayed on a map..	153
Figure A.9 Some pictures of the outdoor communication test. Left: Receiver view of the location of the transmitter placed at different positions. Rooftop of DET POLITO. Right: Receiving station. Building in the surroundings.	153
Figure A.10 System setup test 5. Point-to-point configuration used to determine the transmission ranges reached by the communication system in an open urban environment, displayed on a map. Transmitter (P1 to P3) and receiver (Rx) positions, with relative distance indications. Google earth view.....	154
Figure A.11 Some pictures of the outdoor communication test. Left: Receiver view of the location of the receiver placed at POLITO. Right: Power spectrum signal received by the SA when the transmitter was placed at P1	155
Figure A.12 System setup test 6. Star topology configuration used to determine the transmission ranges reached by the communication system in an open urban environment, displayed on a map..	156
Figure A.13 Some pictures of the star topology communication test. Left: Receiving station placed at ground level and position of three transmitter on rooftop. Right: Location of the transmitter T4.	156
Figure A.14 SNR of the received signals from transmitters T1, T2 and T5 for the star topology setup measurements.	157

Figure A.15 Some pictures of the dynamic point-to-point communication test. Left: Release of the end node held by some latex balloons. Right: Transmitter in movement and receiving station placed at ground level.	158
Figure A.16 SNR of the received packets during the field test 7.	158
Figure A.17 RSSI of the received packets during the field test 7.	159
Figure A.18 Acceleration measured during the field test 7. X-axis displayed in orange, y-axis displayed in green, z-axis displayed in purple.	159
Figure A.19 System setup used to determine the signal attenuation effect introduced by the envelope materials. Left: Transmitter side. Right: Receiver side.	160
Figure A.20 Some pictures of the experiment. Left: Test using a Mylar balloon envelope. Right: Power spectrum measured at the receiver side.	160
Figure A.21 Controlling board Arduino Nano and development board BME280	161
Figure A.22 Experiment setup for calibration and testing. Applied Thermodynamics Laboratory INRiM	163
Figure A.23 Experiment setup for calibration and testing inside climatic chamber. Applied Thermodynamics Laboratory INRiM	164
Figure A.24 Front panel of the Super-thermometer FLUKE 1594a used as reference	164
Figure A.25 Front panel of the humidity datalogger HD27.17TS Delta OHM used as reference	165
Figure A.26 Initial setting process measured by the radioprobe sensors until reaching the system stability. Temperature and humidity measurements. Calibration process.	165
Figure A.27 Initial setting process measured by the radioprobe sensors until reaching the system stability. Temperature and humidity measurements. Pressure and approximated altitude measurements. Calibration process.	166
Figure A.28 Comparison between temperature measurements during the thermal increase steps from +24°C to +30°C. Temperature calibration process.	167
Figure A.29 Relative humidity measurements during the thermal increase steps from +24°C to +30°C. Relative humidity constant. Temperature calibration process.	167
Figure A.30 Relative humidity measurements during the humidity decrease steps from 30 % RH to 15 % RH. Humidity calibration process.	168
Figure A.31 Comparison between temperature measurements during large cycles. Thermal variations steps: +30 °C, 0 °C and -10 °C.	169
Figure A.32 Relative humidity measurements during large cycles. Thermal variations steps: +30 °C, 0 °C and -10 °C. Relative humidity constant.	169

Figure A.33 Accelerometer measurements after bias removal	171
Figure A.34 Gyroscope measurements after bias removal	172
Figure A.35 Magnetometer measurements after bias removal	173
Figure A.36 System setup to test the GPS signals.....	174
Figure A.37 Left: Received GPS sentences. Right side: Translation of the GPS sentences on a map	174

List of acronyms

ABBREVIATION	MEANING
AHRS	Attitude and Heading Reference System
Al	Aluminum
API	Application programming interface
ARPA	Regional Agency for the Protection of the Environment
BoPet	biaxially-oriented polyethylene terephthalate
BW	Bandwidth
CCN	Cloud condensation nuclei
CMOS	Complementary metal-oxide semiconductor
CR	Correction rate
CRC	Cyclic redundancy check
CSS	Chirp spread spectrum
DDC	Display data channel
DET	Department of Electronics and Telecommunications
DUT	Device-under-test
ECAD	Electronic computer-aided design
EDA	Electronic design automation
EEPROM	Electrically erasable programmable read-only memory
ESD	Electrostatic Discharge
ETSI	European Telecommunications Standards Institute
FIFO	First In First Out
FSK	Frequency-shift keying
FTDI	Future Technology Devices International
GLONASS	GLOBAL NAVigation Satellite System
GNSS	Global Satellite Navigation System
GPIO	General-purpose input/output
GPS	Global Positioning System

He	Helium
I ² C	Inter-integrated circuit
IDE	Integrated Development Environment
IMU	Inertial measurement unit
INRiM	Italian National Metrology Institute
INS	Inertial Navigation Systems
ISM	Industrial, Scientific, and Medical
ISP	In-system programming
ITN COMPLETE	Innovative training network on Cloud-MicroPhysics-Turbulence-Telemetry
LDO	Low-dropout
LGA	Land grid array
LIMZ	Cuneo - Levaldigi meteorological station
LMO	Lithium Metal Oxide
LNA	Low noise amplifier
LoRa	Long range
LOS	Line-of-sight
LQE	Linear quadratic estimation
MARG	Magnetic, Angular Rate, and Gravity
MCU	Microcontroller
MEMS	Micro Electro-Mechanical Systems
NASA	National Aeronautics and Space Administration
NCAR-NOAA	National Center for Atmospheric Research - National Oceanic and Atmospheric Administration
n.d.	No date
NMEA	National Marine Electronics Association
PC	Personal computer
PCB	Printed circuit board
PCL	Polycaprolactone
Pet	Polyethylene terephthalate
POLITO	Politecnico di Torino
PWM	Pulse-width modulation

RF	Radio frequency
RH	Relative humidity
RSSI	Received Signal Strength Indicator
RTCM	Radio Technical Commission for Maritime Services
SA	Spectrum Analyzer
SF	Spreading factor
S-LGA	Soldered land grid array
SMA	SubMiniature version A
SMT	Surface mount technology
SNR	Signal-to-Noise ratio
SPI	Serial Peripheral Interface
SRAM	Static random-access memory
TELA	Tuning Element Loop Antenna
TPH	temperature, pressure, humidity
TQFP	Thin quad flat pack
TSSOP	Thin-shrink small-outline package
TTFF	Time-to-First-Fix
UAV	Unmanned aerial vehicles
UFS	Umweltforschungsstation Schneefernerhaus
UL	Underwriters Laboratories Inc
USART	Universal synchronous-asynchronous receiver/transmitter
USB	Universal Serial Bus
UTP	Unshielded Twisted Pair
VNA	Vector Network Analyzer
VSWR	Voltage Standing Wave Ratio
WSN	Wireless Sensor Network

Chapter 1

Introduction

Enhancing the knowledge of natural atmospheric events has been pursued by mankind for many years. Clouds and weather phenomena have attracted human attention for thousands of years. In fact, multiple studies and observations have been carried out along the years to understand and eventually predict their complex but fascinating behavior. Clouds are a natural challenging component of the Earth's climate system. They play a crucial role in climate change and climate sensitivity because they can largely affect the energy balance of the atmosphere and surface, thus directly affecting life on our planet. Cloud characteristics have a direct impact in the Earth radiation budget, the global hydrological cycle (through precipitation), and the atmospheric motion dynamics (Siebert, Franke, et al., 2006; Heintzenberg & Charlson, 2009)

Clouds are present from the planetary surface to the mesosphere layer and cover nearly two thirds of the Earth's atmosphere at any given time (Intergovernmental Panel on Climate Change, 2014). However, they continue to be the largest dominant source of uncertainty in weather and future climate estimation (Heintzenberg & Charlson, 2009; Bodenschatz et al., 2010; Stechmann & Stevens, 2010; Intergovernmental Panel on Climate Change, 2014). This is attributable to the multi dynamical, radiative, and microphysical processes that cloud evolution involves not only in temporal but also spatial scales. In fact, cloud behaviour and their development range from the sub-micrometre scale where the collision of particles and droplets occur, to the thousands of kilometers scale reachable by global circulation processes. This constitutes a major challenge for scientific comprehension and cloud modelling as a total representation of the cloud system and the connections across the multiple range of scales is not yet possible.

Turbulence plays a leading role in cloud evolution and precipitation, extending across the microphysics level to the weather and global climate scale since, it drives entrainment, stirring and mixing processes (Bodenschatz et al., 2010; Devenish et al., 2012). At the smallest scales, turbulence intensely facilitates the motion and

growth of rain droplets through collisions and coalescence. Turbulence supplies a random acceleration force, generating strong shear motions (Pumir & Wilkinson, 2016), which lead to spatially clustered particle distributions in vorticity regions of the cloud, thus reducing significantly the time required for warm rain initiation (Grabowski & Wang, 2012; Niedermeier et al., 2020).

Warm rain (rainfall) is formed from clouds (warm clouds) composed only of liquid water having temperatures above 0 °C (32 °F) and resulting primarily from coalescence of water droplets (Lau & Wu, 2003; Liu & Zipser, 2009). A relevant fraction of the total precipitation that falls on Earth is produced by warm clouds. Warm clouds typically form in the lower troposphere and are responsible for nearly 30 % of the total rainfall on the planet and nearly 70 % of the total rainfall in the Tropics, thus having significant influence on the Earth's radiative balance regulation (Lamb & Verlinde, 2011; Devenish et al., 2012).

Although turbulent flows associated to clouds and aerosols are critically important for prediction of weather and climate (Shaw et al., 2020), the complexity in measuring clouds at the smallest scales and the poor/lack of explicit representation of turbulence processes in general circulation models lead to fundamental questions about turbulence mechanisms still unanswered (Toschi & Bodenschatz, 2009; Siebert, Gerashchenko, et al., 2010; Devenish et al., 2012; Geerts et al., 2018; Hoffmann et al., 2019).

In an attempt to address these knowledge gaps, several laboratory experiments, numerical simulations, and field studies have been undertaken along the years to investigate and try to understand the complex cloud microphysical processes, particularly those inherent to turbulence interactions. At the beginning, the limited computational research tools and electronic instrumentation combined with the lack of understanding of these natural events made the achievement of the objectives even more challenging. However, over the years, thanks to the improved computational research tools and more sophisticated instrumentation availability, the study and better understanding of these natural phenomena observations have been highly improved. To name a few examples of these investigation methods (not limited to), remote sensing methods mainly involve the use of radars and lidars (K. B. Cooper & Chattopadhyay, 2014; Hubbert et al., 2018; Schmidt et al., 2019), laboratory experiments mostly include wind tunnels and aerosol–cloud chambers (Chang et al., 2016; Hoppel et al., 1994; H. Siebert et al., 2010; H Siebert et al., 2015), in-situ observations comprising manned and unmanned airborne platforms measurements (airplanes, helicopters, tethered lifted systems, hot-wire anemometry, etc.) (Lehmann et al., 2009; Malinowski et al., 2013; Holger Siebert et al., 2007; Holger Siebert, Lehmann, et al., 2006; H Siebert et al., 2015), and numerical computational simulation studies accomplished via Navier–Stokes direct numerical simulation of little sections of clouds (Kumar et al., 2014, 2018).

A method to describe the properties of turbulence is the use of the Lagrangian description, which consists of tracking the motion of individual fluid particles that have been sown to a moving flow. Here, the individual particles are “marked” or “tagged” and described in function of time (*Descriptions of Fluid Flows | The*

Pennsylvania State University, 2020; Toschi & Bodenschatz, 2009). Lagrangian experiments provide many benefits over studies made at fixed sites since the measurement resources can be centralized on the moving air volume in focus (Businger et al., 2006). The Lagrangian specification approach applied to turbulence particle pair diffusion was initially proposed by Richardson in 1926 (Richardson & Walker, 1926; Malik, 2018). From then on, the interest of turbulence Lagrangian statistics has risen significantly during the last decades (Lu et al., 2008).

Numerous analytical and experimental methods have been applied and improved for the investigation of Lagrangian turbulence from the viewpoint of fluid particles. Within the experimental part, some of the main techniques developed are optical tracking of tracer particles, acoustic Doppler, and instrumented particles (e.g., (Ayyalasomayajula et al., 2006; Brenguier & Bourriane, 1998; Uhlig et al., 1998; Gerashchenko et al., 2008; Lu et al., 2008; Salazar et al., 2008; Shew et al., 2007). Although nowadays it is possible to have high spatial and temporal resolution of turbulence through these methods, Lagrangian measurement techniques are mostly laboratory procedures that cannot mimic the high degree of turbulence fluctuations found in real-world atmospheric clouds (H. Siebert et al., 2010; Toschi & Bodenschatz, 2009).

In contrast to most of the traditional approaches, the present PhD. thesis is dedicated to the development of an in-situ experimental method for measuring the influence of small-scale turbulence in cloud formation by means of the design and implementation of an innovative ultra-light and expendable radiosonde (here referred to as radioprobe) capable of floating in warm clouds. This research work has been promoted and financed by the European Horizon 2020 Marie Skłodowska Curie project, which was approved in 2016 (H2020 MSCA ITN ETN COMPLETE, GA 675675: Innovative Training Network on Cloud-MicroPhysics-Turbulence-Telemetry (*CORDIS / European Commission*, 2015)), through one of the project's beneficiary partners EnviSens Technologies S.r.l.

COMPLETE is an inter-multidisciplinary research training network targeted to enhance the understanding and modeling of atmospheric clouds. This scientific network comprises an experimental program involving different research and development activities i.e., laboratory and numerical simulations, velocity Micro Electro-Mechanical Systems (MEMS), design and development of advanced fast temperature probes, field experiments, and innovative atmospheric mini radiosondes; all of them devoted to the production of Lagrangian datasets crucial to gain new understanding of in-cloud processes.

The mini radioprobes presented here are designed to passively track small-scale turbulence fluctuations, such as air velocity, water vapor, pressure, and temperature on the inside of warm clouds and neighboring ambient air (Paredes Quintanilla et al., 2021). According to the Lagrangian description of turbulent dispersion proposed by Richardson (Richardson & Walker, 1926; Malik, 2018), the tiny devices can be considered as markers in a Lagrangian strategy.

With a maximum target weight of 20 grams and a diameter of 30 cm, these innovative radioprobes are carefully designed to float at the target altitude of warm clouds, which ranges between 1 and 2 km above the surface level. They must be alive for few minutes, which is a sufficient time interval to measure fluctuations from the inner turbulence time scale (W. A. Cooper et al., 2013; Pumir & Wilkinson, 2016). In order to enable the radioprobes to float and drift with the air volume, the bio-balloons housing the electronics are filled with a suitable mixture of helium gas and ambient air to reach a buoyancy force equal to the total weight of the system. Bearing in mind that the mini radioprobes are not envisaged to be recovered after their mission, the design considers the utilization of environmental-friendly and less disruptive materials to reduce any possible negative impact on the environment. For this purpose, the balloon wrapping the electronics is made of biodegradable elements customized to provide hydrophobicity and flexibility properties (Basso et al., 2020).

Within the framework of research balloons, these newly developed devices can be categorized as instrumented weather balloons. Nevertheless, they are distinct from typical instrumented devices created for atmospheric observations because of their minimal size, weight, and floating capabilities. For instance, to name a few of them, the NCAR-NOAA (National Center for Atmospheric Research - National Oceanic and Atmospheric Administration) Global Hawk tethered dropsonde (sonde specifications: weight 167 g, length 30.5 cm, diameter 4.6 cm; parachute: square-cone design, size 20 cm on a side) conceived for vertical atmospheric profiling measurements (non-Lagrangian behavior) and launched by an unmanned aircraft from the National Aeronautics and Space Administration (NASA) (Wick et al., 2018), or the NOAA constant-volume, low-altitude smart balloon (balloon diameter about 335 cm) housing on-board instruments and used for atmospheric characterization through Lagrangian experiments or hurricane research (*Low Altitude Balloon Measurement Platforms*, 2011.).

Other examples are the ground-launched weather balloon from NOAA carrying a tethered radiosonde (initial balloon diameter about 152 cm and expanding until bursting) used for vertical profiling up to about 32 km in height (*Picture Climate: Balloons Aren't Just for Birthdays* / NOAA, n.d.), the ground-launched two-balloons tethered rawinsondes (sonde weight: 13 g, balloon: diameter for each balloon about 61 cm (weight information not available)) used for thermodynamic measurements in storms (Markowski et al., 2018), and the unmanned aircraft deployed balloons tethering a microsonde and used for supercell thunderstorm studies (total device weight 65.6 g) (Swenson et al., 2019).

The Lagrangian weather balloons described in this thesis act as instrumented particles featuring a relative constant volume, thus being neutrally buoyant at specific altitudes. Each tiny device embeds a set of compact size microprocessors, controllers, and sensors aimed to measure local inner cloud fluctuations in acceleration, trajectory, pressure, humidity, and temperature. Since the radioprobes are small and light enough to be easily transported, they are envisaged to be released into the atmosphere with the help of unmanned aerial vehicles (UAVs) or little

airplanes. For the duration of the flight, the ultra-light radioprobes acquire, partially process, store, organize, and transmit in nearly real time the collected information to various ground stations spatially arranged on land. Due to the radioprobes' physical constraints and the environmental conditions that can be found inside warm clouds, the communication between the flying instrumented balloons and the ground stations is achieved thanks to the use of a dedicated long-range and power-saving wireless communication link (Bertoldo et al., 2018). At the ground level, the ground stations are designed to capture, store, manage, process, and display the data coming from the floating devices.

The information resulting from the whole process reported above will provide an insight into small scale turbulence fluctuations inside warm clouds specifically over land and alpine environments. These unique in-situ observations are essential to enhance the current understanding of turbulence-related microphysical processes in warm clouds thus, improving actual weather forecasting and climate models.

This thesis focuses on the electronics design of the entire radioprobe system described above and is organized as follows:

- Chapter 2 presents an overview of basic concepts useful for the development of this work including clouds, cloud turbulence, Lagrangian measurements, radiosondes, and weather balloons.
- Chapter 3 describes the radioprobe environment, identifies the critical technical aspects of the system, addresses the design requirements, and introduces the proposed system architecture and design methodology. Also, it presents the final radioprobe system design.
- Chapter 4 reports on the performance evaluation of the radioprobe system under different conditions.
- Chapter 5 presents the presents the main conclusions and future work.

Chapter 2

Atmospheric clouds as a source of uncertainty

2.1 Clouds and cloud turbulence basics

2.1.1 Clouds in the climate system

A cloud is a visible aggregation of water drops, ice crystals, and other particles dispersed in the atmosphere (*Cloud / Glossary of Meteorology*, n.d.). Clouds are formed in the free atmosphere as a result of two processes: the condensation of water vapor into liquid water in ascending air flows, and the evaporation of the lowest layer of fog.

By condensation, two main elements are required: water vapor and hygroscopic aerosols. Hygroscopic aerosols can be defined as microscopic particles in free air that easily attract and retain water vapor molecules (*Hygroscopic Nucleus / Encyclopedia.Com*, n.d.). These aerosols serve as the nucleus of atmospheric cloud droplets and receive their name according to the type of cloud they belong to: cloud condensation nuclei (CCN) for water clouds or ice nuclei for ice-crystal clouds (*Cloud / Glossary of Meteorology*, n.d.). Figure 2.1 shows a hygroscopic aerosol catching tiny water droplets before becoming a cloud droplet.

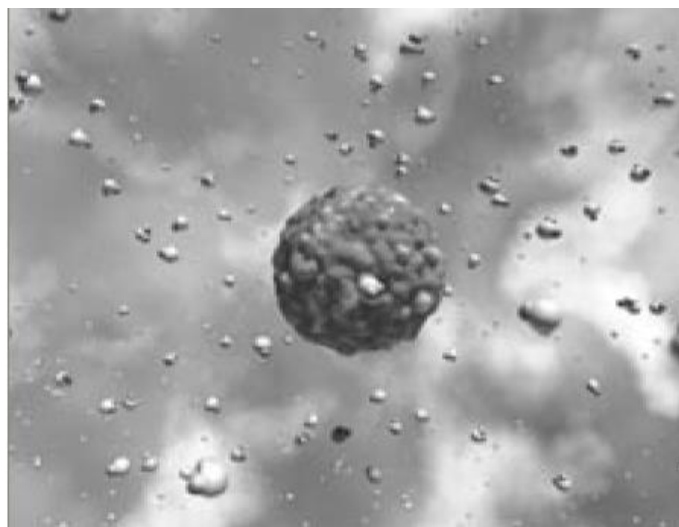


Figure 2.1 Tiny water droplets aggregating around a hygroscopic aerosol (The Importance of Understanding Clouds | NASA EOS, 2005)

Water vapor gets into the atmosphere through evaporation. It comes from different sources like soil, open water, or plants. Aerosols are generated either from natural sources like volcanoes (ash) or sea (salt), or from human activities like air pollutants. With a sufficient amount of water vapor and CCN, a cooling mechanism is required to reduce the air parcel temperature to the dewpoint temperature to form a cloud (*Cloud Development / Oklahoma Climatological Survey*, n.d.; Ward, 2005).

An air parcel is an imaginary bubble of air where the exchange of heat with the adjacent atmosphere is not present. In stable air conditions, an air parcel moving upwards or downwards in the atmosphere, will tend to come back to its original position. On the other hand, in unstable air conditions, an air parcel moving upwards or downwards in the atmosphere, will tend to continue rising or descending according to its initial motion direction. To find out if the atmosphere in which the air parcel is inserted, a comparison between the parcel's air temperature and the surrounding's atmosphere temperature must be made. At any given level in the atmosphere, environmental temperature highly varies with height. Generally, the atmospheric temperature decreases with increasing the height level. Based on this, as a parcel of air rises in the atmosphere, it tends to expand (because of the reduction of air pressure with the height grow) and cool. The rate at which this cooling is happening depends on the relative humidity of the air enclosed within the parcel. When the air parcel arrives at a relative humidity value of 100 %, it can be said that it is saturated. At this point, the air's parcel temperature reaches the so-called dew point temperature (Ward, 2005).

When a saturated volume of air cools, its ability to hold moisture is reduced and it cannot hold any more moisture. The extra amount of water vapor becomes a liquid (condensation) or solid (deposition). At the dew point, cloud droplets start developing through condensation onto the hygroscopic aerosol particles. Generally, cloud droplets range from 1–100 μm in diameter. To reach a raindrop size, cloud particles need to expand their mass a million of times or more (Wallace & Hobbs, 2006). With the continuing ascent of air parcels, cloud droplets keep growing in size. If they become large enough, they fall from the cloud in form of rainfall. This cloud development is depicted in Figure 2.2.

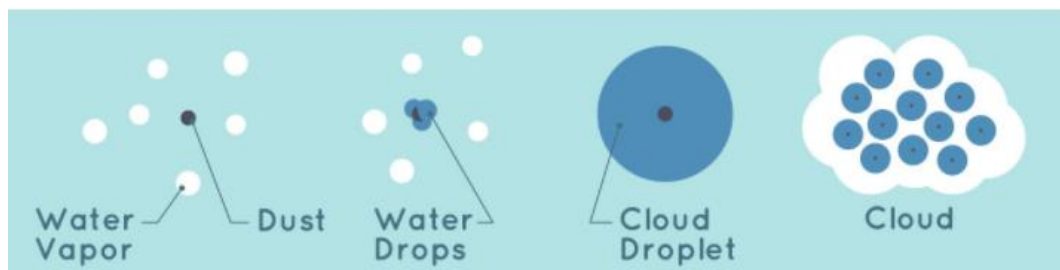


Figure 2.2 Cloud development process (*How Do Clouds Form?* / NASA, n.d.)

2.1.2 Clouds in the climate system

The climate system (Figure 2.3) is the result of the interaction between different components of the Earth's system such as atmosphere (air), hydrosphere (water), lithosphere (solid portion of the Earth), cryosphere (permafrost and ice), and biosphere (living organisms) (Taylor, 2005; *Climate System / Glossary of Meteorology*, n.d.; "Climate System," 2021). The result of these mutual interactions creates the conditions on and around the Earth's surface, hence determining the Earth's climate.

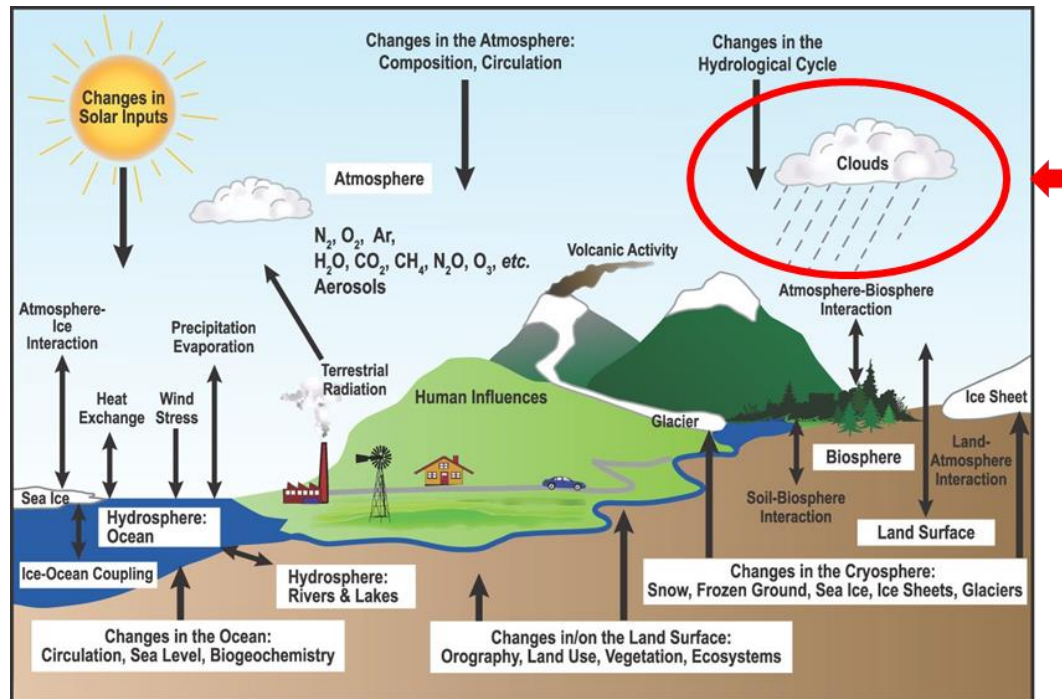


Figure 2.3 Climate system (Le Treut et al., 2007)

Clouds are a natural complex component of the Earth's climate system. They play a crucial role in climate change and climate sensitivity because they can largely affect the energy balance of the atmosphere and surface. For instance, cloud characteristics have a direct influence in the Earth radiation budget, the global hydrological cycle, and the atmospheric motion (Siebert, Franke, et al., 2006; Heintzenberg & Charlson, 2009).

The Earth's radiation budget is the balance between the incoming energy radiation from the Sun and the outgoing energy radiated by the Earth's system into outer space (*The Earth's Radiation Budget* | NASA, n.d.). Radiation from the Sun is essentially all the energy in the climate system (Taylor, 2005), and clouds can greatly influence the amount of solar radiation reaching the Earth's atmosphere in different manners; the net effect of them depend on the amount of Earth's surface they cover, their altitude, composition, thickness, and water or ice content (Hartmann, 2016; Ward, 2005). Clouds reflect and scatter the solar and terrestrial

radiation and absorb the planetary infrared energy. In fact, roughly the 30 % of the Sun's energy intercepted by the Earth is reflected by clouds (Figure 2.4).

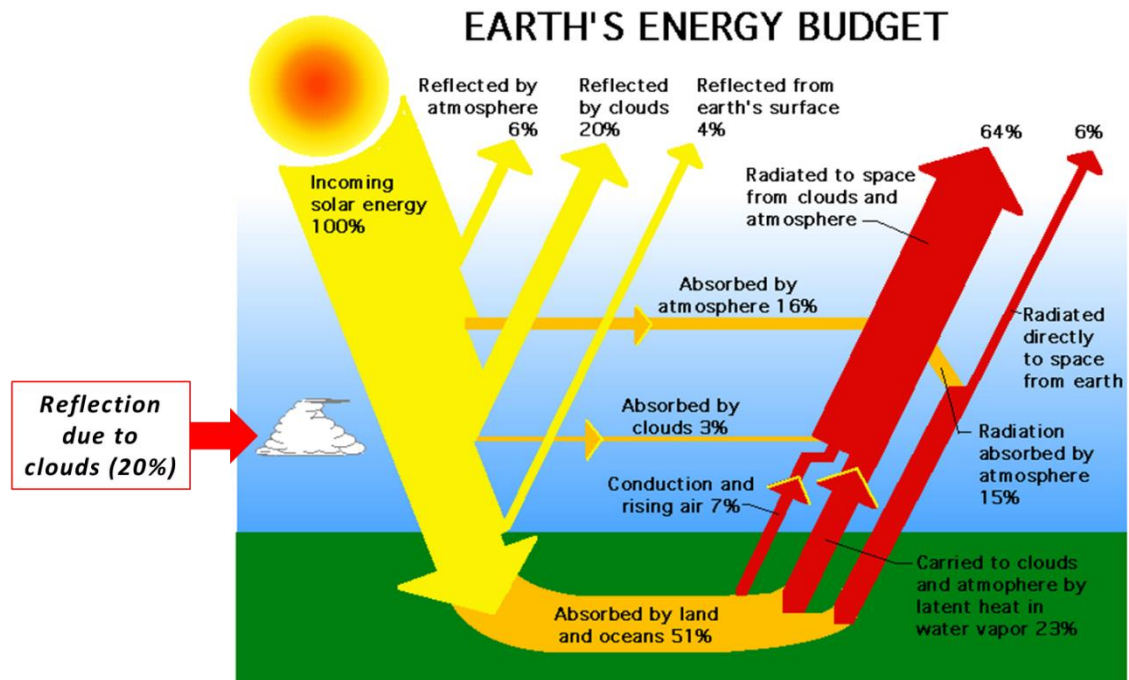


Figure 2.4 Solar radiation intercepted by Earth. Effect of cloud reflection and scatter (*Global Energy Budget / NASA GPM, n.d.*)

The global hydrological cycle, known also as the water cycle, describes the circulation of water from the ocean surface and land masses to the Earth's atmosphere, and back in the form of precipitation (National Research Council, 2007). Clouds play a vital role in the global hydrological cycle since they determine precipitation and the return of water all over the globe (oceans and land areas), hence leading to surface temperature changes.

The atmospheric motion, or atmospheric circulation, transports the surplus of heat from the tropics towards the poles (Hartmann, 2016). Clouds help the redistribution of extra heat, hence reducing extreme temperatures.

2.1.3 Cloud classification

Clouds are constantly changing and can present diverse structures, shapes, textures, colors, etc. They are mainly classified according to the altitude level at which they are found, and their physical appearance (*Cloud Classification / Glossary of Meteorology, n.d.*; *Cloud Names and Classifications / Met Office, n.d.*).

Based on their form, clouds can be grouped as:

- Cirrus: wispy, fibrous, hair-like appearance, curl of hair. High up level.
- Alto: medium level.

- Stratus (strato): layered, flat, widely extended, horizontal sheet.
- Cumulus: convex or conical heaps, puffy, covering small areas.
- Nimbus (Nimbo): rain, precipitation cloud.

Based on the height of their basis, clouds can be grouped as high-level clouds, medium-level clouds, and low-level clouds (*Cloud Classification / NOAA*, n.d.). Table 2.1 provides a summary of their main characteristics.

Figure 2.5 shows a summary of the classification of clouds according to their form and heigh basis.

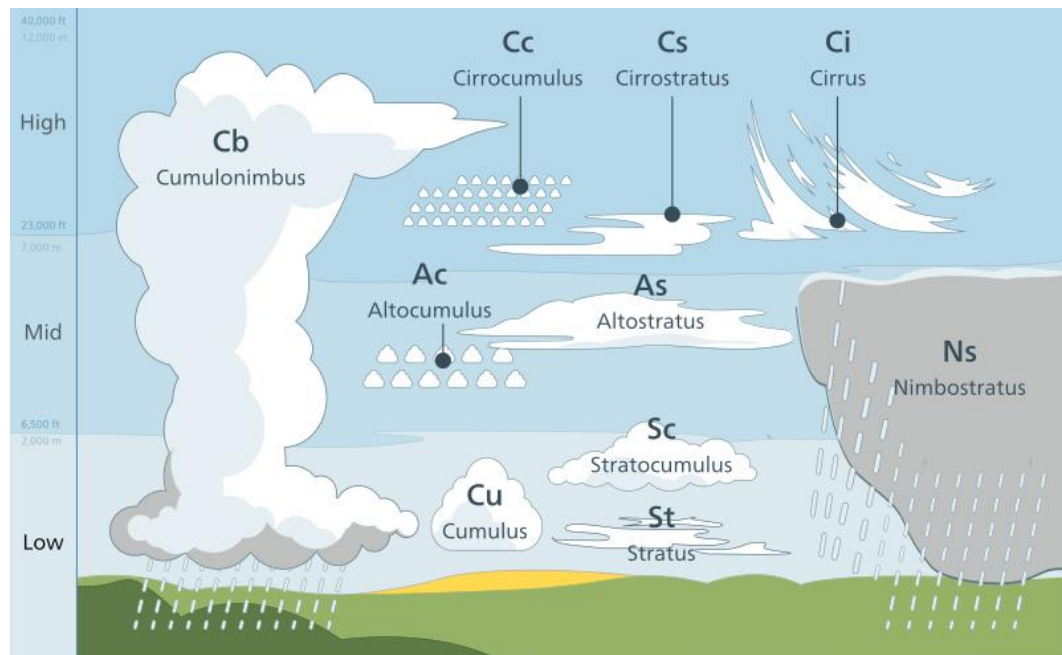





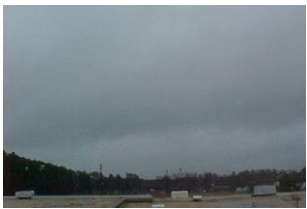






Figure 2.5 Cloud classification (Bruyn-Cotton, 2012)

Table 2.1 Cloud classification based on the height of their basis (*Cloud Classification | Glossary of Meteorology*, n.d.; *Cloud Classification Summary | WMO*, n.d.)

<p>High clouds occur above about 7 km. They are predominantly composed of ice crystals due to the cold temperatures present at these heigh levels (about -25 °C).</p>	<p>Cirrus clouds can be found at any time during the year. They appear in the form of silk strings or delicate filaments. Their composition is entirely of ice crystals, which give them their particular white color and form. The height of their base varies from about 6 km to 12 km. Technically this type of clouds produce rain, but it never reaches the surface.</p>	 <p>(Eugster, 2011)</p>
	<p>Cirrocumulus clouds rarely cover the sky. They are layered clouds made up of lots of small cumuliform bumps regularly spaced called cloudlets. Their composition is almost entirely of ice crystals and supercooled water. The height of their base varies from about 6 km to 12 km. Like the cirrus clouds, this type of</p>	 <p>(Hearts, 2010)</p>

	cloud also produces rain, but it never reaches the surface.	
	Cirrostratus are high, thin, and layered clouds usually covering totally or large areas of the sky. They are composed of ice crystals that disperse the light (moonlight or sunlight) passing through them producing a ring or halo effect. This kind of clouds does not produce precipitation.	 <p>(Whale, 2009)</p>
Medium clouds occur between 2 km and 7 km. They are found at middle levels in the troposphere, and are mainly composed of liquid water droplets, ice crystals, or both depending on the temperature profile present. Normally, the temperature at these levels varies from -25 °C to 0 °C.	Altostratus clouds are heap-like clouds with white or grey appearance and shaded sides. They are generally associated with settle weather. Altostratus are composed of cloud droplets and may contain ice crystals also. They generally form at altitudes between 2 km and 6 km. Rainfall from this kind of clouds is rare but it that happens, precipitation does not reach the ground.	 <p>(Rubinstein, 2007)</p>
	Altostratus clouds present a grey or blue-grey cloud sheet or thin layer covering the sky either totally or partially. They are generally composed of water droplets together with ice crystals. Normally, they form when a cirrostratus cloud layer drops down from a higher height; however, altostratus clouds do not show the halo phenomena typical of the cirrostratus type ones. They generally form at altitudes between 2 km and 7 km. Altostratus clouds usually point to a change in the weather because they tend to form before of a warm or occluded front. They may gradually thicken, becoming a nimbostratus clouds responsible for rain or snow.	 <p>(Cloudwatcher, 2011)</p>
	Nimbostratus clouds frequently present a grey, dark, and nearly uniform cloud layers. This type of cloud forms commonly in the middle level of the troposphere but then it broadens vertically towards the upper and lower levels. Nimbostratus clouds are composed of suspended water droplets, falling raindrops and/or snow crystals. They usually produces rain or snow, which reaches wide ground areas. Their base can be found from heights between 500 m to 3 km, and their thickness may vary between 2 and 4 km.	 <p>(“Nimbostratus Cloud,” 2021)</p>
Low clouds occur near the surface, below the 2 km of height. This type of clouds are generally composed of liquid	Stratocumulus clouds are hybrids of rounded masses and layered stratus. They are characterized by thick and thin areas with grey, white, or both colors forming waves, lines, and groups. Stratocumulus are often found in the atmosphere before or after a frontal system.	

<p>water droplets. The temperatures present at this level is usually greater than -5°C.</p>	<p>Precipitation from this kind of clouds is rare but if that happens, it is usually just light rain or snow. Stratocumulus can be found from heights between 500 m to 2 km.</p>	 <p>(Couch-scratching-cats, 2021)</p>
	<p>Stratus are very low clouds that extend uniformly over the sky. They are usually grey or nearly-white colored and can last for long time periods. Stratus may produce light precipitations or drizzle. They can be found from heights between 0 m to 2 km.</p>	 <p>(PiccoloNamek, 2005)</p>
	<p>Cumulus clouds present a detached fluffy appearance. They develop as result of convection processes. Usually they indicate fair weather; however, cumulus can grow becoming towering clouds, which might produce occasional rain showers. This type of clouds are generally found at altitudes lower than 2 km unless they grow vertically.</p>	 <p>(Ernst, 2017)</p>
	<p>Cumulonimbus clouds are characterized by an anvil multi-level appearance. They are formed by water droplets and ice particles and produce severe weather like lightning, hail, and thunder. Cumulonimbus can form in groups, alone or alongside a line of thunderstorms. They can extend from low to middle altitudes, taking shape between 200 m to 4 km with peaks reaching up to 12 km.</p>	 <p>(Nowacki, 2020)</p>

2.1.4 Cloud challenges

Clouds are a natural challenging element of Earth that play active role on the Earth's energy balance weather and climate. They represent the highest mass clustering of any atmospheric aerosol on the planet (Shaw, 2003). In fact, clouds blanket nearly two thirds of the Earth's atmosphere at any given time (Figure 2.6), being present from the planetary surface to the mesosphere layer (Heintzenberg & Charlson, 2009; Intergovernmental Panel on Climate Change, 2014). Moreover, clouds are very efficient in the interaction with radiation, both visible and infrared. Regarding the visible range, clouds redistribute light mainly by reflection and scattering of the solar and terrestrial radiation, while in the infrared range, clouds act as blackbodies altering the exchange of the planetary infrared energy through the atmosphere. In addition, clouds can alter the hydrological cycle through the formation of rain and transport of water and energy. It is important to mention also

that cloud features such as development, extent and duration, can be altered by anthropogenic and biological influences (Shaw, 2003).

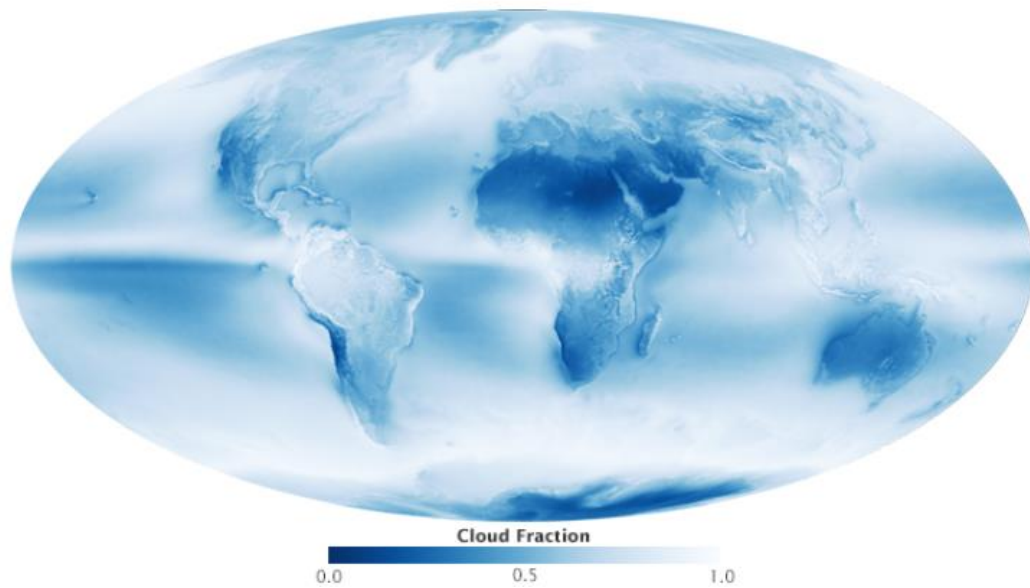


Figure 2.6 Cloud fraction on Earth (*Cloudy Earth* / NASA, 2015)

Despite their importance, clouds continue to be the largest dominant source of uncertainty in weather and future climate estimation (Heintzenberg & Charlson, 2009; Bodenschatz et al., 2010; Stechmann & Stevens, 2010; Intergovernmental Panel on Climate Change, 2014; Bony et al., 2015). This is rooted in the fact that cloud evolution involves multi dynamical, radiative, and microphysical process on a vast range of temporal and spatial scales (Siebert, Franke, et al., 2006; Stechmann & Stevens, 2010; Intergovernmental Panel on Climate Change, 2014).

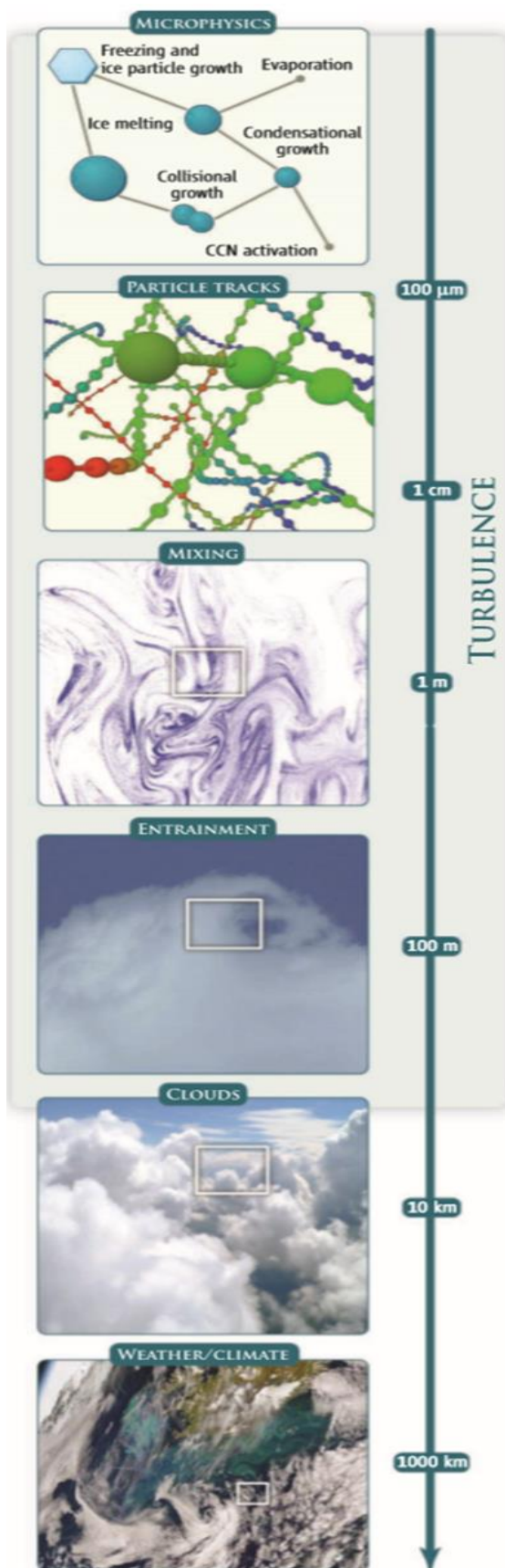
Cloud behaviour and development vary by as much as seven orders of magnitude (Warhaft, 2008). They range from the smallest scales (sub-micrometre) where the particles and droplets collide, to the largest scales (tens of kilometers) reachable by global circulation. This constitutes a major challenge for scientific comprehension and cloud modelling as a total representation of the cloud system and the interactions across scales is not yet possible. One example of this are current cloud-resolving models. They have limited computational resources for resolution, domain size, or simulation time, hence leading to capture issues of the micro-to-global cloud scale. Moreover, most climate models are not well resolved nor parameterized (Stechmann & Stevens, 2010; Intergovernmental Panel on Climate Change, 2014; Hoffmann et al., 2019). To fully improve our understanding in cloud dynamics and their function in the highly complex global system, not only every

single process on each scale but also the way in which they are linked together must be accounted for.

2.1.5 Turbulence: its effects on cloud dynamics and available study framework

Turbulence is usually associated to disorder and complexity. In fluid dynamics, it refers to the presence of spontaneous fluctuations along a wide range of lengths and time scales, resulting in an efficient mixing of fluid properties (Lévêque, 2006; *Turbulence / Glossary of Meteorology*, n.d.). It is the fluid motion characterized by the presence of excessive kinetic energy (“Turbulence,” 2021). Turbulence phenomena is characterized by the random nature of turbulent fluctuations and the fluid’s ability in a turbulence state to disperse properties (Gifford, 1955).

Figure 2.7 Presence of turbulence at all cloud scales (Bodenschatz et al., 2010)



Turbulence plays an important role in the development and dynamics of clouds, spanning from the microphysics level (fraction of millimetres) to the weather and global climate scale (thousands of kilometers) (Figure 2.7) since it leads entrainment, stirring and mixing processes (Bodenschatz et al., 2010). In fact, clouds can be defined as droplets in turbulent motion (Warhaft, 2008).

The properties of clouds at the microscales are delineated by thermodynamical and fluid-mechanical synergy within droplets and neighbouring air (Shaw, 2003). At the smallest scales, turbulence affects the cloud’s efficiency to produce rain since it enormously favours the motion and growth of rain droplets

through collisions and coalescence in a efficiency factor rate from 2 to 5 (Grabowski & Wang, 2012; Li et al., 2018). Turbulence supplies a random acceleration force, generating strong shear motions (Pumir & Wilkinson, 2016). It has been found that accelerations in atmospheric turbulence can be up to 10 g (Shaw, 2003). These motions lead to preferential spatially clustered particle distributions outside high vorticity regions of the cloud, thus reducing significantly the time required for **warm rain** initiation (Warhaft, 2008; Grabowski & Wang, 2012; Niedermeier et al., 2020). This enhancement in the precipitation formation process (rain initiation) represents the major challenge in the cloud physics community (S. Chen et al., 2018) because, combined with the radiative properties of clouds, have a direct influence in the global climate and weather (Pinsky et al., 2006).

Warm rain or rainfall is formed from clouds (warm clouds) composed only of liquid water having temperatures above 0 °C (32 °F) and resulting primarily from coalescence of water droplets (Lau & Wu, 2003; Liu & Zipser, 2009). In other words, warm rain does not involve processes related to ice-phase (ice-free) (R. Chen et al., 2011).

A relevant fraction of the precipitation that falls on Earth is produced by warm clouds (Figure 2.8). Warm clouds typically form in the lower troposphere and are responsible for approximately 30 % of the total planet rainfall and nearly 70 % of the total rainfall in the Tropics, thus having significant influence on the Earth's radiative balance regulation (Lamb & Verlinde, 2011; Devenish et al., 2012).

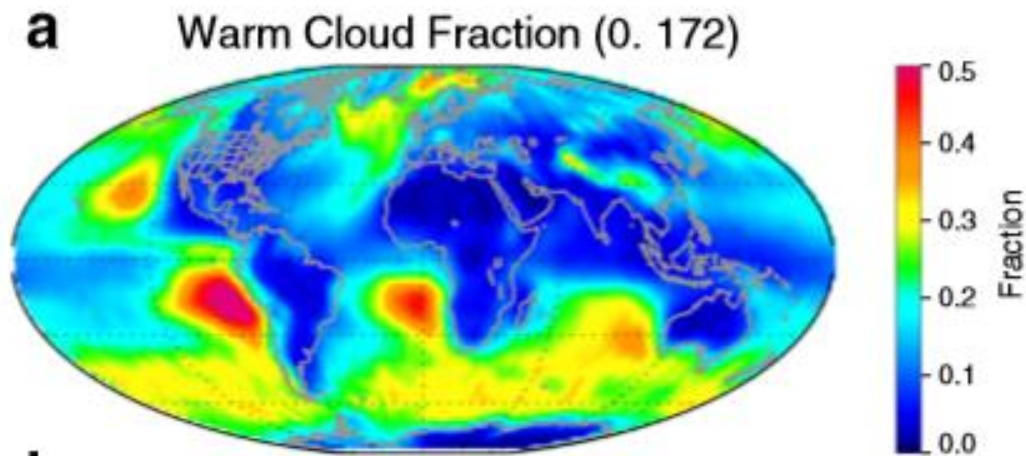


Figure 2.8 Global warm rain occurrence (Nuijens et al., 2017)

Although turbulent flows associated to clouds and aerosols are critically important for prediction of weather and climate (Bodenschatz, 2015; Shaw et al., 2020), the difficulty in measuring clouds at the smallest scales and the poor/lack of explicit representation of turbulence processes in general circulation models lead to fundamental questions about turbulence mechanisms still unanswered (Toschi & Bodenschatz, 2009; Siebert, Gerashchenko, et al., 2010; Devenish et al., 2012; Geerts et al., 2018; Hoffmann et al., 2019; *CORDIS / European Commission*, 2015).

To address these long-standing knowledge gaps, various laboratory experiments, numerical simulations, and field studies to understand the different microphysical processes and turbulence interactions involved in cloud formation and precipitation have been carried out along the last years (Bodenschatz et al., 2010; Devenish et al., 2012; Niedermeier et al., 2020; Shaw et al., 2020). All of these approaches have been possible thanks to the improved computational research tools, better instrumentation availability, and improved phenomena observations.

To name a few examples of these investigation methods (not limited to), remote sensing methods mainly involve the use of radars and lidars (K. B. Cooper & Chattopadhyay, 2014; Hubbert et al., 2018; Schmidt et al., 2019), laboratory experiments mostly include wind tunnels and aerosol–cloud chambers (Chang et al., 2016; Hoppel et al., 1994; Siebert, Gerashchenko, et al., 2010; Siebert et al., 2015), in-situ observations comprising manned and unmanned airborne platforms measurements (airplanes, helicopters, tethered lifted systems, hot-wire anemometry, etc.) (Lehmann et al., 2009, 2007; Malinowski et al., 2013; Siebert et al., 2007; Siebert, Lehmann, et al., 2006; Siebert et al., 2015; Beals et al., 2015), and numerical computational simulation studies accomplished via Navier–Stokes direct numerical simulation of little sections of clouds (Kumar et al., 2014, 2018).

2.2 Lagrangian measurements

Air motion has a broad spectrum not only in spatial but also temporal scales. For instance, it spans from random motions at microphysical levels to global circulation levels including the whole atmosphere layer (Iribarne & Cho, 1980). Air motion can be described in two ways, the first one is by using the Eulerian description and the second one is by using the Lagrangian description.

The Eulerian description consists in specifying the properties of fluid motion in a defined control volume as functions of position in space and in time. In other words, this method provides information about the flow in terms of what happens at different specific points in space through which the fluid passes (“Lagrangian and Eulerian Specification of the Flow Field,” 2021; Young et al., 2010). Here, individual fluid particles are not identified (*Descriptions of Fluid Flows | The Pennsylvania State University*, 2020).

The Lagrangian description consists in tracking the motion of individual fluid particles that have been sown to a moving flow. Here, the individual particles are “marked” or “tagged” and described in function of time (*Descriptions of Fluid Flows | The Pennsylvania State University*, 2020; Toschi & Bodenschatz, 2009). This approach has been successfully applied to address transport issues. For instance, it has been used for turbulent mixing treatment, processing of models spanning from air pollution transport to turbulent combustion modelling, turbulent entrainment processes, particle transport and aggregation (Toschi & Bodenschatz, 2009).

The difference between both descriptions can be observed in the smoke discharged from a chimney, example displayed in Figure 2.9. In the Eulerian

approach, if a sensor (i.e., thermometer) is located at position “0”, it can measure the temperature at that specific point as a function of time. Similarly, if various additional sensors are placed at other fixed points inside the same control volume, the temperature field can be obtained.

On the other hand, in the Lagrangian approach, the same sensor (temperature) can be attached to the fluid particle “A” and register the particle’s temperature measured as it moves as a function of time. If various sensors are attached to different fluid particles and record their temperature measurements, the result will be the temperature of these different fluid particles as a function of time (Young et al., 2010).

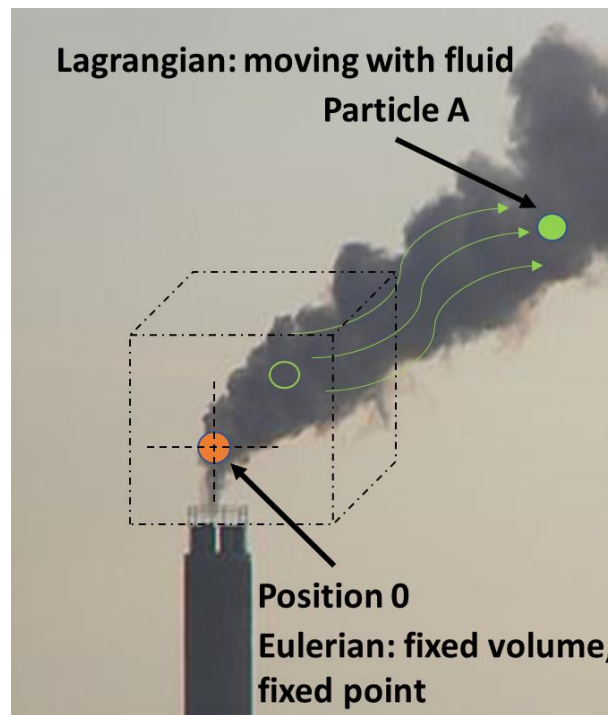


Figure 2.9 Eulerian vs. Lagrangian description example (Pöllö, 2010)

A way to describe the properties of turbulence is the use of the Lagrangian description, which captures the temporal development of a turbulent flow (Toschi & Bodenschatz, 2009). As mentioned in the previous section, at the smallest cloud scales, turbulence properties play a crucial role in the motion and collision of finite-inertia droplets in wet clouds. Moreover, it is important in determining the radiative emissivity of clouds.

Lagrangian experiments provide many benefits over studies made at fixed sites because the measurement resources can be concentrated on a fixed moving air volume under study (Businger et al., 2006). The Lagrangian specification approach applied to turbulence particle pair diffusion was initially proposed by Richardson in 1926 (Richardson & Walker, 1926; Malik, 2018). Since then, the attention to turbulence Lagrangian statistics has risen significantly during the last decades (Lu et al., 2008). Plenty of analytical and experimental methods have been employed and improved for the research of Lagrangian turbulence from the view point of fluid

particles. Inside the experimental part, some of the principal techniques developed are optical tracking of tracer particles where particle's position and acceleration are determined, acoustic and laser Doppler where particles are traced and acceleration is measured, and instrumented particles that include sensors for the measurement of temperature or acceleration with transmission capabilities (e.g., (Ayyalasomayajula et al., 2006; Brenguier & Bourrienne, 1998; Uhlig et al., 1998; Gerashchenko et al., 2008; Lu et al., 2008; Salazar et al., 2008; Shew et al., 2007)).

Although today it is possible to have high spatial and temporal resolution of turbulence through these methods, Lagrangian measurement techniques are mainly laboratory procedures that cannot mimic the high degree of turbulence fluctuations found in real-world atmospheric clouds (Siebert, Gerashchenko, et al., 2010; Toschi & Bodenschatz, 2009). Further explorative Lagrangian measurements performed in real clouds are still required to get additional information useful for the fully understanding of the turbulence-related microphysical processes at the smallest cloud scales. To this end, the improvement of instrument size and deployment cost, data rates and physical challenges inherent to measurements in clouds must be overcome to get valuable information related to the interaction between turbulence and cloud microphysics.

2.3 Radiosondes and weather balloons

2.3.1 Radiosondes

The term “sonde” is the French word for probe (“Sonde,” 2021). A sonde is generally used for collecting meteorological data. A radiosonde is a battery-powered instrument with radio transmitting capabilities that is carried into the atmosphere typically by a sounding (weather) balloon (Fletcher, 2017). A variant of radiosondes are called dropsondes. They are designed to be dropped down (rather than float up) from aircrafts at particular altitudes and then, they fall to the surface due to the gravity force (*What Is a Dropsonde?* / *Earth Observing Laboratory*, n.d.). Generally, dropsondes include a small parachute that helps to slow down their descent to ground. A radiosonde is an electronic unit composed of three parts: a meteorological sensors, a radio transmitter, and a signal processing section (Dabberdt et al., 2003). The meteorological estimation periodicity depends on the radiosonde's manufacturer, ranging from 1 to 6 s. Radiosondes are designed to capture different meteorological parameters along their ascending or descending pass through the atmosphere, i.e., temperature, relative humidity, pressure, position, wind, altitude, cosmic rays, etc (“Radiosonde,” 2020). They transmit the collected information via radio either to ground receivers or aircrafts. Usually, radiosondes are expendable instruments since the recovery after their release is not envisaged.

Radiosonde and dropsonde observations have been a vital part of weather forecasting and climate research for decades since they provide high-quality and high-vertical resolution for on-site measurements (Wick et al., 2018). They allow

to outline the atmosphere and get directly vertical profile information of the natural phenomena under study. Radiosonde data is used for different applications, for instance, as an input for weather prediction and air pollution models, for weather and climate change research, for local severe storms, hurricanes and marine forecasts, for aviation operations and defence applications, as calibration and validation source of satellite retrievals, among others (Sun et al., 2010; Dabberdt et al., 2003).

Air soundings started in the late 1800s. Recording devices called meteorographs were attached to kites or tied balloons and recorded the near-surface measurements retrieved by the devices. The next evolution step was the addition of a radio transmitter to the initially developed meteorographs. The aim of this addition was to transmit the retrieved data to ground in real time. The first recorded launch using this refined device was done in 1929 in France by Robert Bureau, who gave the name “radiosonde” to his instrument. It was carried by a balloon inflated with Hydrogen and measured atmospheric pressure and temperature parameters. Since then, radiosonde technology has been improved and refined along the years. They have become more accurate, more price affordable and smaller (*What Is a Radiosonde?*, n.d.).

Nowadays, hundreds of radiosondes are launched daily throughout the world to make measurements and provide a snapshot of the atmosphere. A global network of nearly 1300 radiosonde launch stations sends every day radiosondes to the atmosphere using free-rising balloons that can reach up to 35 km of height (*Radiosondes / NOAA*, n.d.).

2.3.2 Weather balloons

Generally, a radiosonde is carried aloft by a weather balloon, also called sounding balloons. Balloons are greatly used for in situ measurements from ground up to some tens of km above the surface. They provide valuable insights into a variety of complex processes throughout the atmosphere. Moreover, the incorporation of additional radionavigation systems (i.e., Global Positioning System (GPS)) and communication technologies (i.e., satellite communication) allow real time measurements. Although satellites are crucial tools for getting a global view of Earth, they still bear some sensitivity limitations in the presence of vertical variability of clouds and aerosols (Pommereau, 2003; Dubovik et al., 2021). Given that a single observation method does not provide extensive information about a targeted object in a challenging environment, complementary observations are needed. Balloon sounding is one complementary method for atmospheric research. Within the main advantages of using balloons for atmospheric observation are the simplicity of use, moderate cost, and the opportunity of reaching stratospheric levels (Sitnikov et al., 2014). Their relative low cost makes possible

the repetition of the observations throughout the year and the globe in a short time frame (Pommereau, 2003).

Balloons are made usually of highly flexible materials such as natural rubber (latex) or synthetic rubber (neoprene). The gas commonly used to provide them their lifting capacity is the Hydrogen; however, Helium and natural gas are also employed. Their physical size is determined by the total mass required to lift, the ascent rate, the maximum height of the sounding, and the type of gas used (Dabberdt et al., 2003).

Balloons are not new vehicles. In fact, they have been used for many decades not only as scientific observational platforms but also as spectacle events. The first series of unmanned weather balloons were launched for first time in France in 1896, to carry out atmosphere investigations of the tropopause and stratosphere (“Weather Balloon,” 2021). Since then, a variety of balloons have been developed becoming a popular standard tool for atmospheric structure observations.

2.3.3 Lagrangian balloons

As mentioned earlier, Lagrangian experiments focus in a limited volume of air that is moving. Lagrangian balloons differ from other kinds of weather balloons because they have a constant volume that allows them to float or drift in isopycnic (same density) surface levels. This characteristic is not applicable to the vertical atmospheric profiling where an atmospheric balloon is either ascending or descending because it has not reached its equilibrium buoyancy level (Doerenbecher et al., 2016). Buoyancy can be defined as an upward force exerted on an object at rest, which is entirely or partly immersed in a fluid (i.e. air, water, etc.) (Elert, n.d.). Buoyancy can be affected by the fluid density, the fluid volume, and the local acceleration due to the gravitational force. The equilibrium buoyancy, called also neutral buoyancy, is reached when the density of the immersed object is equal to the density of the fluid. The flight level of the balloon depends on its buoyancy, which in turn relies upon the gas mixture used to provide the lifting capacity.

Over the years, many experiments have been carried out using drifting or constant-level balloons as Lagrangian observers. Some of them (not limited to) have been developed for different applications such as the study of the evolution of vertical structure and cloud in the marine boundary layer (ASTEX-MAGE in 1992), collection of meteorological data (ACE-1 campaign in 1995), quantification of chemical and physical processes affecting aerosol evolution (ACE-2 in 1997), collection of ozone and meteorological data (ICARTT in 2004), hurricane intercepting (RAINEX in 2005), study the transit of pollutants and dust (ChArME_x in 2013, TRAQA campaigns in 2012), monitoring of ambient flow (INDOEX in 1999 and VASCO in 2007), space-time variability (AMMA in 2006), water vapour and dynamics (HyMeX SOP2 in 2013), (Businger et al., 1996; Doerenbecher et al., 2016).

For small-scale turbulence exploration using a Lagrangian approach, instrumented particles are highly promising tools (Toschi & Bodenschatz, 2009). Instrumented particles feature a relative constant volume to be neutrally buoyant and keep a fixed density at specific altitudes. Also, they contain sensors able to measure different local quantities (i.e., acceleration, temperature, pressure, etc.) and send the gathered information to receiving stations.

Balloons can be used as instrumented particles to follow in situ Lagrangian trajectories and report in real time the atmospheric structure. One of the main advantages of using instrumented balloons as Lagrangian markers is that they provide valuable fluid-based information in the reference frame of particles passively transported by fluid motion. Moreover, over the use of traditional models, the use of Lagrangian balloons allows the elimination of two major distortions that occur in common rising tethered balloons. Since the balloons are designed to float in a neutrally buoyant level, vertical resolution problems due to the high ascending velocity provided by traditional balloons are not present. Moreover, since the payload is placed inside the balloon, the pendulum motion of the bottom-attached payload moving the sensors and affecting their measurements is eliminated (Kräuchi et al., 2016).

Chapter 3

New concept of ultra-light radioprobes for in-cloud turbulence measurement

3.1 Understanding the radioprobe environment and design requirements

The tiny radioprobes must be designed to measure small-scale turbulence fluctuations and work at the submeter level where cloud microphysical processes such as phase transition, particle collisions and particle breakup take place. For this purpose, they must possess unique features that enable them to behave as instrumented floating particle devices and track 3-Dimensional Lagrangian trajectories after their deliverance into the atmosphere. To explore turbulence from the Lagrangian point of view, these particular kind of radioprobes must be as small in size as possible to feature a minimum inertia, and a minimum volume compared to the trajectory followed during the flight.

Moreover, the newly designed radioprobes must be capable of passively floating and follow small scale cloud fluctuations. The total target weight of each radioprobe is limited to approximately 20 g (*CORDIS / European Commission*, 2015), comprising the measurement instrumentation, the external housing, and the required additional supports.

In addition, to float on an isopycnic level where the surface keeps a constant density (*Isopycnic Surface / Glossary of Meteorology*, n.d.), the density of the radioprobes also must be kept as constant as possible to match the density of the atmosphere under study. This means that the combination of weight and volume of the instrumented balloon must persist moderately invariable during the flight at the target altitude of warm clouds (between 1 km – 2 km). Relying on this factor, the volume and size of the balloon was determined in (Basso et al., 2020) using the Archimedes' principle for buoyancy in stable floating conditions. Considering a constant atmospheric lapse rate of 6.5 K/km, both the volume and radius of the balloon were calculated as summarized in Table 3.1.

Table 3.1 Determination of balloon size by balancing the atmosphere's density and the balloon's density (considering a fixed total weight of 20 g). Constant lapse rate = 6.5 K/km (Basso et al., 2020)

Atmospheric parameters	Estimation of balloon dimensions
------------------------	----------------------------------

Altitude [m]	Temperature [K / °C]	Pressure [mbar]	Atmospheric density [kg/m³]	Volume [m³]	Radius [cm]
0	288 / 14.85	1000	1.22	0.019	16.5
500	285 / 11.85	950	1.17	0.020	16.8
1000	282 / 8.85	900	1.11	0.021	17.1
1500	278 / 4.85	850	1.06	0.022	17.7
2000	275 / 1.85	790	1.01	0.023	17.7
3000	269 / -4.15	700	0.90	0.026	18.3

Considering a fixed total mass of the system (20 g), the atmosphere density at the destination altitudes, and a constant environmental lapse rate, the sonde balloon dimension must be about 30 cm in diameter. Additionally, since the radioprobes will be working inside clouds containing water droplets, the enclosure balloon must be made of hydrophobic materials to avoid the absorption and adherence of water that can increase the system weight and damage the electronics.

It is expected that the radioprobes keep a stable trajectory when inserted into warm clouds. The foreseen observational domain in which the radioprobes will work ranges from a few meters in the vertical axis extent and a few kilometers in the horizontal axis extent, from their release point. This is an enough physical domain for the study of a cloud (or part of it) and some portion of surrounding air.

The radioprobes should be designed to be a low-cost solution compared with current similar systems since a large number of devices are required for the present research scope. Sondes dropped from aircrafts platforms are important for obtaining fine-resolution vertical profiling mainly over ocean and sometimes over mainland; however, they are expensive and usually drops over land from mother aircrafts are limited (Geerts et al., 2018). Balloon-borne radiosondes are similarly important to provide vertical profiles of atmosphere thermodynamics during the balloons' ascent and contrasted with launch procedures from aircraft platforms, the sounding system launch operation is not very costly. Although current radiosonde manufacturing and launch procedures (either from ground or aircraft) are affordable, the instrument downsizing, the non-necessity of a mother aircraft, expensive ground launch stations or complex logistics, will further downscale costs associated with their production and release. Moreover, being very small, overland use restrictions related to size and weight are not present.

The radioprobes must include a set of different microcontrollers (MCU), processors, and sensors for the measurement of turbulence-related fluctuations such as velocity, acceleration, vorticity, humidity, pressure, and temperature inside warm clouds. In accordance with the atmospheric spectra derived from in-field observations of the target atmosphere portion (Katul et al., 1998; Warhaft, 2008; Radkevich et al., 2008; Siebert, Shaw, et al., 2010; Golshan et al., 2021), a summary of the operational requirements for the radioprobe sensors is shown in Table 3.2.

The kinetic energy spectrum of atmosphere turbulence is displayed in Figure 3.1; however, the range of interest for the intended radioprobe observations is limited to the intervals marked in red:

- Kinetic energy of turbulence from about $-3 \text{ m}^2/\text{s}^2$ to $+1.5 \text{ m}^2/\text{s}^2$

- Wavenumber from about -3 m^{-1} to 3 m^{-1}

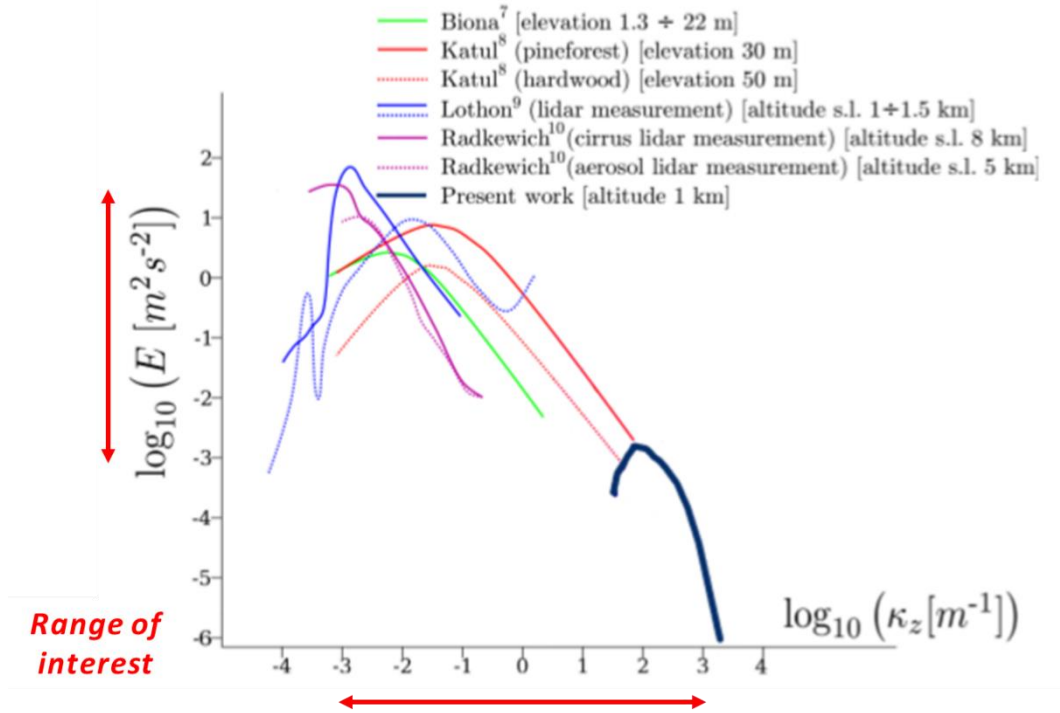


Figure 3.1 Kinetic energy spectrum of atmosphere turbulence (Golshan et al., n.d.).

Table 3.2 Summary of operational conditions for the radioprobes

Quantity	Values
Warm cloud height	1 km – 2 km
Temperature range (T)	0 °C - +30 °C
External relative humidity (RH)	0 % RH - 100 % RH
External pressure (P)	400 mbar - 1100 mbar
Trajectory	+/-100 mm
Air flow fluctuation inside cloud	Up to 5 m/s

Although their recovery and reuse would be favorable, the radioprobes must be designed to be expendable. They are not envisaged to be retrieved once their journey into atmospheric clouds is ended. In this context, it becomes evident that the data collected during the flight must be somehow retrieved. To do so, the data acquired while the device is alive should be sent wirelessly to a ground station(s) located on Earth. For that purpose, a communication technology that allows reaching the ground-based station and at the same time meets the size and weight physical constrains of the design is necessary. Moreover, due to the non-recoverable feature of the probes, they must be environmentally friendly to the best capabilities to narrow down any potential negative environmental impact. To this end, it is envisaged the use of radioprobe casings made of innovative biodegradable materials.

Lastly, but not least, the radioprobes must have power autonomy. They must last at least 30 minutes to be able to measure fluctuations from the inner turbulence time scale of few minutes (W. A. Cooper et al., 2013; Pumir & Wilkinson, 2016).

3.1.1 Critical technical aspects

The development of the radioprobes requires the deep analysis of different decisive aspects. Since this thesis is focused on the electronic design of the whole system, the main critical aspects are reported below.

- Due to the small form factor of these new kind of radioprobes, size and weight are the main constraints for their realization. As mentioned in the previous section, the total weight should be kept around 20 grams and the maximum diameter's balloon should be held around 30 centimeters hence, all the components must be carefully selected to match the requirements without compromising the proper operation of the radioprobe's system.
- Power consumption is another key factor during the design of the devices. Since the radio probes are battery-operated, the battery must provide enough power to the electronic circuit, which must incorporate a set of sensors, microcontrollers and at least one transceiver. Depending on the sampling frequency of the signals, energy usage of the sensors and the transmission rate of the data to the ground station, the battery lifetime can be affected. Also, due to the bottleneck in the size and weight of the radioprobe, the battery cannot exceed a few grams of weight and a few mm in size.

3.2 The proposed radioprobe system architecture and design methodology

The proposed radioprobe system aims to improve the understanding of the effect of turbulence in cloud processes by measuring turbulence velocity fluctuations and structure of thermodynamic fields in real clouds and generating new Lagrangian-based cloud fluctuation datasets. Part of the work described in this section has been published in *"Innovative mini ultralight radiosondes to track Lagrangian turbulence fluctuations within warm clouds: electronic design"* (Paredes Quintanilla et al., 2021).

3.2.1 Working principle

The working principle of the entire system is shown in Figure 3.2. The light-weighted (about 20 grams) radioprobe devices (1) are carefully designed to float and passively follow small-scale turbulence fluctuations inside and outside warm clouds on an isopycnic surface. In order to make their flight into clouds possible, the biodegradable balloon housing the electronic instrumentation is foreseen to be

filled up with a precise combination of air and Helium (He) in order to reach a buoyancy force that matches the total weight of the system. Every single radioprobe incorporates a collection of tiny microcontrollers, microprocessors, sensors, and other components that permit the local measurement of atmospheric parameters such as temperature, humidity, velocity, acceleration, vorticity, and pressure in clouds and surrounding air. Since the radiosondes are small and light enough to be easily carried, they will be liberated into the target atmosphere level with the aid of UAVs or small airplanes. During the air travel, each Lagrangian balloon acquires, partially processes, stores, organizes, and transmits in nearly real time the collected data to receiving and base stations situated on ground. It is to be noted that a long-range communication link technology with low power consumption features should be assured to connect and exchange data within the network. For this purpose, the devices are equipped with a communication system that allows the data delivery through a dedicated long-range power-saving wireless radio transmission link.

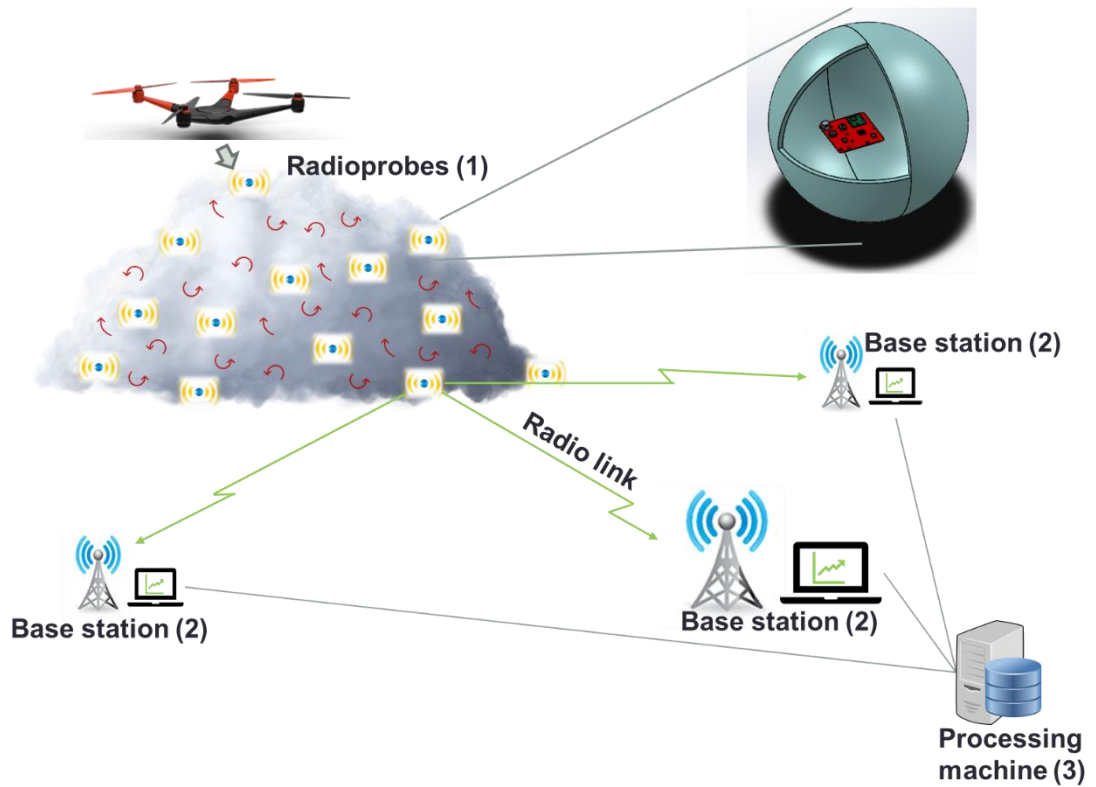


Figure 3.2 Working principle of the system (Paredes Quintanilla et al., 2021)

The base stations (2) are located at known fixed positions on ground. This provides a reference to the system and enables the execution of positioning and tracking algorithms to determine the trajectory followed by the radioprobes. Each base station is equipped with both, a receiving system and a data acquisition and control system. The former is used to capture the transmitted data from the floating devices, while the latter is used to receive, control, and manage the obtained information. In addition, each base station is connected to a personal computer (PC)

where the information is stored in a data base and partially processed and visualized. The post processing system (3) allows the management, filtering, storage, and final execution of trajectory tracking and position algorithms. It also provides the interface of the system to the user.

The information derived from the entire process will provide an insight into turbulence fluctuations in warm clouds, which are essential to enhance the current knowledge of turbulence-related microphysical processes thus, improving actual weather forecasting and climate models.

3.2.2 System architecture

Due to the characteristics of the network, the radioprobe system structure can be classified as a Wireless Sensor Network (WSN). A WSN is a network of spatially distributed, totally autonomous node devices inherently constrained in terms of battery life and processing functionalities (Lopez, 2008) that can convey the gathered data from a monitored environment through wireless communication links (*Wireless Sensor Networks : Types & Their Applications* | *ELPROCUS*, 2014). A WSN consists of a data acquisition network containing the sensor nodes and base stations, and a data dissemination network providing an interface of the data acquisition network to the user.

This WSN is structured in three main parts: the bio-balloon wrapped radioprobes, the base stations, and the processing system. The radioprobes are the sensor node devices of the network. They embed a radio transceiver, a data acquisition system, and a set of sensors for measuring the physical data of the target surroundings. At this point, the data are acquired, partially processed, encapsulated, and transmitted to ground. Each radioprobe is able to communicate directly with the receivers via a dedicated radio frequency (RF) transmission link.

Each base station comprises a receiver system to get the transmitted data from the sensor nodes. To form a reliable network, the base stations are spatially dispersed and configured to communicate with the same set of radioprobes thus, ensuring the reception of the diffused data. The base stations communicate in a wired way to a PC via an Universal Serial Bus (USB) port. Here, the data are directly collected through the COM port, then partly processed, stored, and previsualized. A graphical output of the initially processed data (e.g., radioprobe ID, Signal-to-Noise ratio (SNR), Received Signal Strength Indicator (RSSI) of the packets, temperature, pressure, relative humidity) is displayed through an application interface. At the end of the process, the data are passed to the next chain point.

The post processing system is the last step of the network structure. Here, the data are managed, filtered, completely processed, and stored. At this level, fusion algorithms are executed to complete the trajectory tracking and position processes. The obtained information is fully displayed through different application interfaces.

3.2.3 Electronic system configuration

This subsection presents the electronic system configuration of both, the radioprobes and the ground station. The radioprobe system is structured in different functional units as is illustrated in Figure 3.3. It consists of a data processing and control unit (1), a radiocommunication system (2), a temperature, pressure, and humidity sensor stage (3), a positioning and tracking sensor stage (4), and a power supply unit (5).

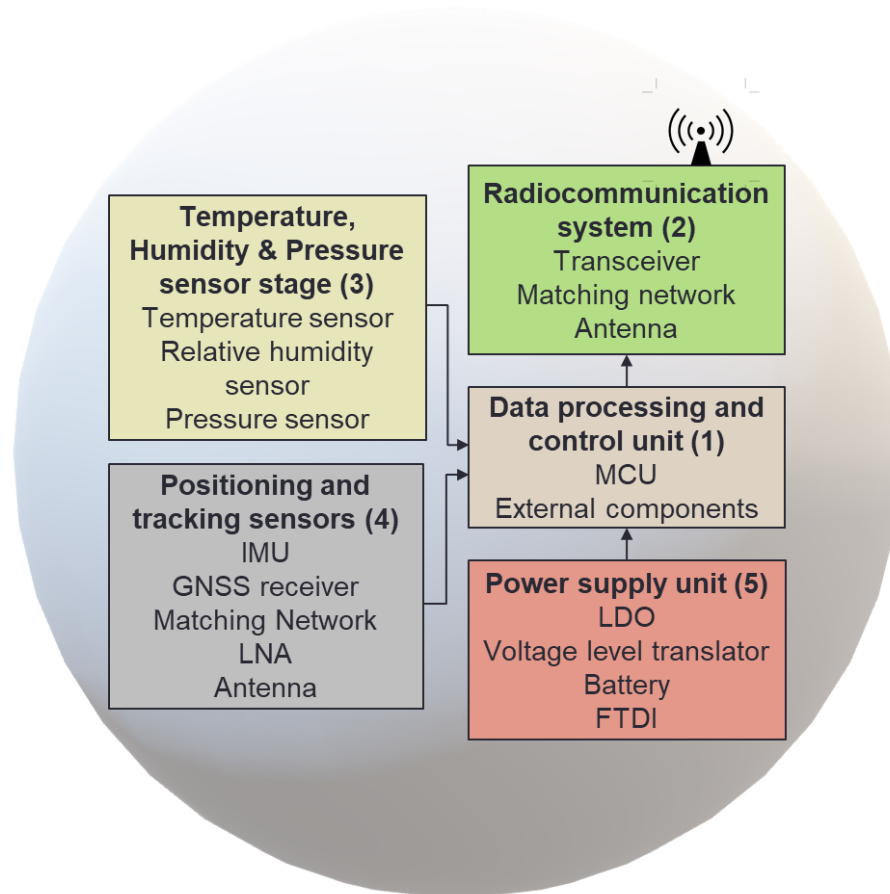


Figure 3.3 Block diagram of the mini radioprobe

The block diagram of the ground station is illustrated in Figure 3.4. It consists of a receiving system (1), a data acquisition and control unit (2), a power supply unit (3), and management, storage, visualization, and post-processing units (4).

A detailed description of each block diagram is given in the next sections.

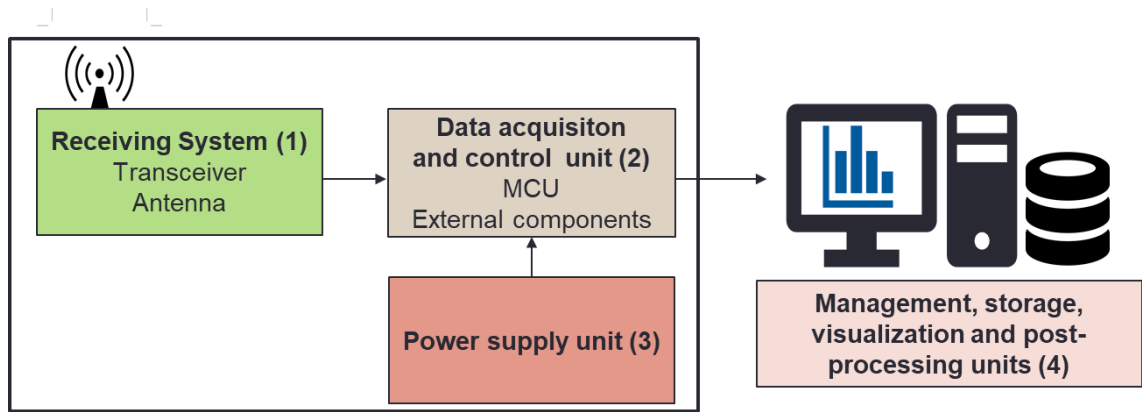


Figure 3.4 Block diagram of the ground station

3.2.4 Flow diagram

The main processing flow diagram of the radioprobe system is shown in Figure 3.5. Since the radioprobe device must have power autonomy, a single battery is used as source of energy for its functioning. While the radioprobe is powered-on, the microcontroller starts its operation and continuously executes the main code previously uploaded. It recurrently takes readings from the different sensors of the unit, that is temperature, pressure, humidity (TPH), acceleration, magnetic field, angular rate (Inertial measurement unit (IMU)), and Global Satellite Navigation System (GNSS). Then, the IMU data is used to update an Attitude and Heading Reference System (AHRS) orientation filter, which provides valuable information to identify the location of the radioprobe as a post-processing step executed at ground level. At the end, the partially processed information together with the remaining sensor data are encapsulated inside a data packet and sent to the ground stations via the LoRa transmission link. After the message is received at the ground station level, it is converted to a compatible data format, pre-processed, stored in a database, and finally visualized. This process is repeated while the radioprobe is alive and transmitting data. As a result, a unique Lagrangian dataset containing small-scale turbulence fluctuation information from warm clouds is generated for future use in weather prediction and cloud modelling analysis.

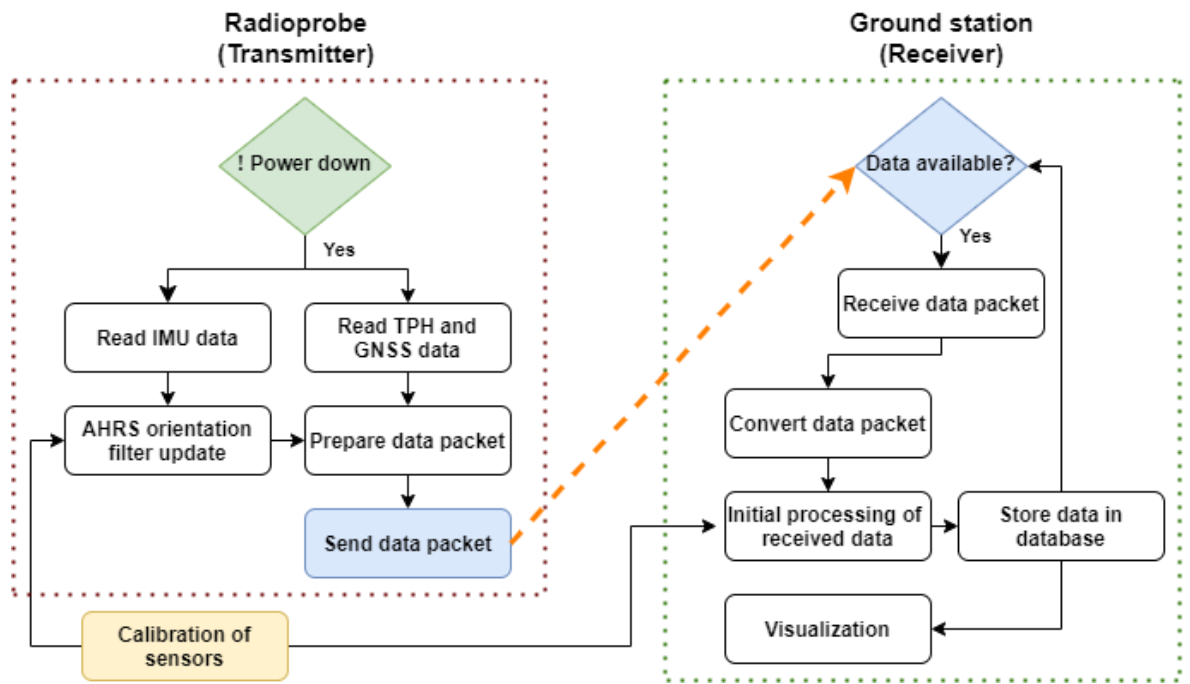


Figure 3.5 Main processing flow of the radioprobe system

3.3 Selection of system components

3.3.1 Radioprobe

3.3.1.1 Data processing and control unit

This electronic stage is the computational unit of the radioprobe. It allows the management and execution of the different subsystem operations inside the sensor node. In this unit, the data provided by the sensors are partially processed, arranged, and eventually encapsulated to be sent via the transmission module to the base stations.

The core of the data processing and control unit is an ATmega328P-AU microcontroller from Microchip (*ATmega328P* / *Microchip*, n.d.) based on a reduced instruction set computer RISC with a highly optimized set of instructions ("Reduced Instruction Set Computer," 2021). This type of microcontroller has been selected for the current development mainly due to its low-power operation, small size factor, and compatibility with a wide group of program and system development tools. It is a tiny, low power, complementary metal-oxide semiconductor (CMOS) 8-bit single-chip suitable for embedded systems. It comes in a highly compact thin quad flat pack (TQFP) package of 32 leads, dimension of 9 mm x 9 mm x 1 mm and weight of 70 mg. The Tmega328P requires an operating voltage in the range from 1.8 V to 5.5 V and operates within temperature ranges from -40 °C to +85 °C. In addition, this microcontroller incorporates a 32 Kbytes of in-system self-programmable flash program, a 2 KBytes of internal static random-access memory (SRAM), and a 1 KBytes of electrically erasable

programmable read-only memory (EEPROM). The current needed by the microcontroller to operate is very little: in active mode 0.2 mA, in power-down mode 0.1 μ A, and in power-save mode 0.75 μ A @ 1 MHz, 1.8 V, 25 °C. It supports different interfaces i.e., a master/slave Serial Peripheral Interface (SPI), a serial programmable universal synchronous-asynchronous receiver/transmitter (USART), and a Philips inter-integrated circuit (I²C) compatible interface. The microcontroller also incorporates an on-chip in-system programming (ISP) flash for reprogramming in-system the program memory via the SPI interface.

To generate the clock signal and control the timing of the microcontroller, the ceramic resonator CSTNE8M00GH5L000R0 (*CSTNE8M00GH5L000R0* / Murata, n.d.) from Murata has been selected. This kind of resonators provide high reliability at low cost (*Ceramic Resonators. Application Notes*, n.d.). This resonator is a surface mount technology (SMT) 3-leads component with a nominal oscillating frequency of 8.000 MHz, frequency tolerance of ± 0.07 % max., frequency tolerance on heat temperature changes of ± 0.11 %, a built-in load capacitance of 33 pF ± 20 % max., and operating temperature range from -40 °C to +85 °C.

The design includes also a built-in-led coupled to one of the microcontroller's digital I/O for system check purposes, and an external push bottom switch used to physically trigger a reset to the microcontroller. This switch is small-footprint, SMT, lead free compatible component with ultra-low current capabilities.

3.3.1.2 Radiocommunication system

Choosing the right wireless connectivity technology for a low power application can be quite challenging. Not only technical issues have to be considered but also frequency regulations according to the region. The radiocommunication system of the radioprobes allows them to “speak” wirelessly with the base stations using radiofrequency signals. Nowadays several wireless communication solutions for WSN exist, the choice relies on the amount of data exchange required, amount of energy resources available, and propagation conditions. As previously mentioned, a WSN is a network of embedded systems able to interact with the monitored environment by the use of sensors, locally process the gathered information, and finally convey this information via wireless communication links (Akyildiz & Vuran, 2010). The wireless communication is the key component of these kind of networks because it provides the communication capabilities to the system. Due to the expected characteristics of the artificial floating radioprobes, a long-range communication link (up to some km) as well as low power consumption technology will allow achieving the desired results.

Communication technology and transceiver

Based on the required criteria of the instrumented particles, a long-range saving-power modulation technique named LoRa (Long-Range) has been adopted as one-way wireless communication. LoRa is a proprietary chirp spread spectrum (CSS) modulation technique (*What Is LoRa?*, n.d.), which encodes the information in

linearly increasing and decreasing chirps (Raza et al., 2017; Croce et al., 2018). This modulation scheme allows improving the receiver sensitivity by the type of modulation itself and accomplishing high tolerance to misalignments in frequency between the transmitter and the receiver (*SX1272/3/6/7/8: LoRa Modem / SEMTECH*, n.d.). The chirp pulses used in LoRa modulation allow frequency offsets, equivalent to have timing offsets, between the receiver and the transmitter, increasing in this way its robustness against channel degradation mechanisms such as Doppler Effect, fading and multipath (Adelantado et al., 2017; Paredes et al., 2019). LoRa communication platform was originally developed by a French company called Cycleo, later acquired by Semtech. Since its release, it has exhibited enormous growth especially for Internet of things (IoT) solutions being adapted to a wide range of applications for example smart agriculture, smart metering, smart cities, smart environment monitoring, smart industrial control, smart electrical metering, smart healthcare, smart water metering, etc. (Rizzi et al., 2017; *LoRa Applications / Semtech*, n.d.). The distance ranges that can be achieved greatly depend on the environment and present obstacles; however, LoRa provides better link budget than other similar communication standards (“What Is LoRaWAN® | LoRa Alliance®,” n.d.).

LoRa is primarily used as physical layer of the open specification long-range wide area networking (LoRaWAN); nevertheless, it can be used by public, private and hybrid networks. The portion of the radio spectrum allocated to LoRa networks varies depending on the region. Usually, it operates in the 433 MHz, 868 MHz or 915 MHz Industrial, Scientific and Medical (ISM) frequency bands. In Europe, the license-free ISM band assigned is within the range from 863 MHz to 870 MHz (Lavric & Popa, 2017). LORA modulation offers significant flexibility to the user since its optimization is possible through the access to three critical design parameters. These parameters are spreading factor (SF), error correction rate (CR), and modulation bandwidth (BW), which can be customized depending on the user’s preferences in order to improve the trade-off between link budget, nominal data rate and spectral use (*SX1276 / Semtech*, n.d.). They are further explained hereunder.

The SF is the number of symbols sent per each bit of information and is defined as:

$$SF = \log_2 \left(\frac{R_c}{R_s} \right)$$

Where,

SF is the spreading factor

R_c is the chip rate

R_s is the symbol rate

The **spreading factor** (SF) is important because depending on its value, the sensitivity of the receiver is affected thus influencing the communication range. In addition, the SF value has a direct impact on the data rate and the duration of a packet. The higher the SF, the longer the communication range but the higher the time-on-air of a packet and the slower the transmission. The SF can take different

values ranging from 6 to 12 for a communication link; however, SF = 6 is a special use case for the maximum data transmission rate where the range link is very short. The range of spreading factors and are reported in Table 3.3.

Table 3.3 Range of possible spreading factors used in LoRa modulation (SX1276 / Semtech, n.d.)

SF range	Chips / symbol	Demodulator SNR [dB]
6	64	-5.0
7	128	-7.5
8	256	-10.0
9	512	-12.5
10	1024	-15.0
11	2048	-17.5
12	4096	-20.0

The **coding rate** (CR) is a cyclic error detecting code for forward error detection and correction of changes in the original data transmitted performed during LoRa modulation. The main goal of adding forward error correction to the communication is to strengthen the link reliability against interference; however, its employment incurs in additional data each transmission hence influencing the time-on-air of the LoRa packet as is shown in Table 3.4. The coding rate configuration options can range from 4/5 to 4/8, which means that every 4 useful bits of information will be encoded using from 5 to 8 transmission bits depending on the selected CR value (*Waspnote Lora*, 207).

Table 3.4 Cyclic coding overhead LoRa

CR	Overhead radio	Time-on-air [ms] (for SF = 10, BW = 250 KHz)
5	1.25	123.9
6	1.50	132.1
7	1.75	140.3
8	2.00	148.5

The **bandwidth** (BW) can be defined as the width of spectrum that is occupied by the transmission signal (Bertoldo et al., 2019). Typical bandwidths used to transmit the data are 125, 250 and 500 kHz. In LoRa standard, the BW is equal to the chirp rate (Augustin et al., 2016). This implies several consequences on the modulation itself since the BW value will directly affect the sensitivity of the receiver due to the integration of additional noise power in the channel for the higher ranges (Adelantado et al., 2017). An increase in the bandwidth allows an increase of the data rate and a reduction of the signal's time-on-air; however, the receiver's sensitivity is reduced thus affecting the link budget. This is summarized in Table 3.5.

Table 3.5 Influence of BW on Time on Air and Sensitivity for CR = 4, SF = 10

Bandwidth (kHz)	Sensitivity [dBm]	Time-on-air [ms]
125	-132	247.8
250	-129	123.9
500	-126	61.9

Figure 3.6 summarizes the main parameters to be considered when using LoRa modulation. As mentioned in this section, the main configurable parameters when using LoRa are SF, BW and CR. A LoRa transmission mode is the result of the combination of these three settings. The user needs to set them considering that there is a compromise between the transmission rate and the distance that can be reached when using one or another mode.

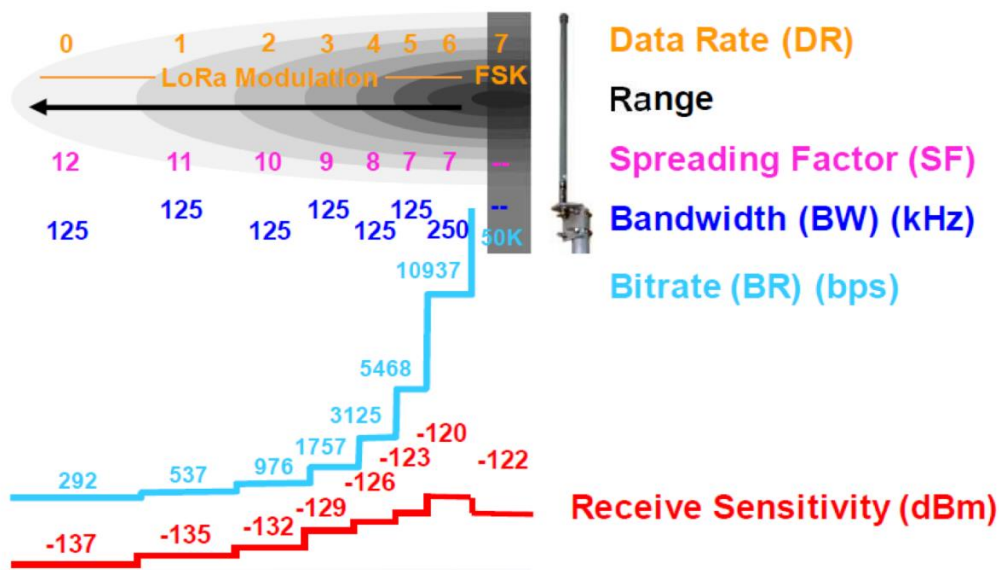


Figure 3.6 Main parameters of LoRa modulation (*LoRaWAN Modulation Settings (EU Band) / IoTNET, n.d.*)

A LoRa packet comprises different elements: a preamble, an optional header, and the payload (*RFM95W / HOPERF, n.d.*). It can be visualized in Figure 3.7.

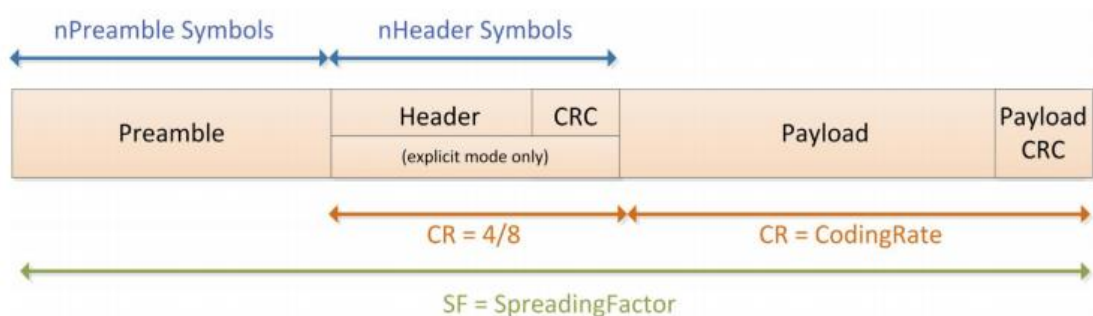


Figure 3.7 Structure of a LoRa frame (*RFM95W / HOPERF, n.d.*)

The preamble is the first element of the packet structure and is used to perform synchronization between the receiver and the incoming payload. Its value typically is set to 8 symbols; however, it can take values from 6 to 65535 symbols.

After the preamble, the header delivers information about the incoming payload: length, code rate, and presence of an optional cyclic redundancy check (CRC) for the payload. It is added to the packet only in the explicit mode where payload packet parameters are known in advance or fixed. When the header is present, it is transmitted with the maximum error correction code equals to 4/8 allowing the receiver the rejection of packets with invalid headers (Augustin et al., 2016; *RFM95W / HOPERF*, n.d.).

The last portion of the packet frame is the payload. It comprises the data itself, including a CRC field. Depending on the SF configured, the maximum size of the data portion can vary from 51 to 222 bytes.

A LoRa symbol is formed of 2^{SF} chirps spread in the entire frequency band. In a LORA symbol, the packet starts with the preamble through repeated up-chirps (1); then the start of the frame delimiter with 2.25 continuous down-chirps used for timing synchronization (2), and lastly the data with choppy up-chirps of different lengths (3).

Although LoRa is being used mostly as physical layer of the open-source LORAWAN specification, in this work it is used to build an ad-hoc private LoRa-based network and adapt the technology to the working conditions. For this purpose, the LoRa-based RFM95 transceiver module (*RFM95W / HOPERF*, n.d.) was employed. It is a device featuring long range spread spectrum communication linkage plus high immunity to interference while mitigating the power consumption. It uses the patented LoRa modulation technique that allows it accomplishing a high sensitivity in the order of -148 dBm.

Some of the main features of the RFM95 transceiver are listed below:

- Link budget maximum 168 dB
- Sensitivity greater than -148 dBm
- Programmable bit rate up to 300 kbps
- Equipped with standard frequency-shift keying (FSK) based and long-range spread spectrum LORA modems
- Low absorption current (see Electrical characteristics)
- Built-in temperature sensor
- LoRa frequency bands: 868 / 915 MHz
- Constant RF output up to +20 dBm
- Small dimension: 16 x 16 mm

This module needs a power supply voltage in the range from 1.8 V to 3.7 V and operates within temperature ranges from -20 °C to +70 °C. It allows power transmission ranges up to 20 dBm (100 mW), although based on the European regulations given by the European Telecommunications Standards Institute (ETSI),

the maximum power allowed in the European area is 14 dBm (25.12 mW) (*ETSI EN 300 220-2*, 2018). The electrical specifications of the RFM95 transceiver operating at 3.3V, temperature= 25 °C, Crystal Oscillator Frequency FXOSC= 32MHz, matching impedance= 50 Ω , are given in Table 3.6.

Table 3.6 Electrical characteristics transceiver RFM95. Power consumption

Description	Typical value	Conditions
Sleep mode	0.2 μ A	
Idle mode	1.5 μ A	
Standby mode	1.6 mA	
Synthesizer mode	5.8 mA	
Receive mode	10.8 mA	LNA BOOST On
	11.5 mA	LNA BOOST Off
Transmit mode (with	20.0 mA	Output power +7 dBm
impedance matching)	29.0 mA	Output power +13 dBm
	87.0 mA	Output power +17 dBm
	120.0 mA	Output power +20 dBm

The RFM95 module presents different bandwidth options spanning from 7.8 kHz to 500 kHz and spreading factor values from 6 to 12. The communication with the device and the access to its configuration registers are achieved via the SPI interface. This modem includes three main interfaces: the configuration registers, the status registers, and a First In First Out (FIFO) data buffer.

- As the name suggests, the configuration registers allow the user to set the modem parameters. These registers are readable in all device modes; however, they can be written only in sleep and standby modes.
- The status register allows getting status information when the modem is working in receiving operations.
- The FIFO data buffer allows accessing either the transmitted or received data. The LoRa chip includes a 256-bytes RAM dual data buffer that can be reached in all operating modes except sleep mode. The data can be stored simultaneously thanks to the duality feature of the data buffer.

Antennas

Nowadays, many applications are driven into compact size designs, which means smaller ground planes and limited power source, as it is the case of the radioprobes in development. Therefore, the selection process of every single component must be carefully analyzed to create a physical design that addresses these limitations and still performs well. Antennas are a key component in any wireless design because the RF link depends on their performance; however, they are the most overlooked party of a RF design (*Application Note AN-00501* / *Linx*, 2012).

“An antenna is an electrical device that converts electric currents into radio EM waves, and vice versa” (Le Nguyen Binh, 2017). Antennas allow the transmission and reception of electromagnetic radiation and are used with a radio transmitter or

radio receiver (Balanis, 2005). They are the key component for achieving the maximum distance in a wireless communication system and are considered one of the most complicated aspects of a RF design (*Application Note AN-00501* / Linx, 2012.). Today, there is a wide range of available antennas and their selection rely on the type of application they are intended for. Based on the requirements of this project, the criteria used for selecting the radioprobes' antennas was size, weight, operating frequency, RF performance, cost, design, and placement. Since physical space limitation and weight are the main factors influencing not only the antenna selection but also the rest of components of the radioprobe system, chip antennas provide the best solution.

Chip antennas are a good option for wireless applications with space limitations because they are small and compact. They typically need just few millimeters of space with additional ground clearance (*How to Properly Implement Chip Antennas* / Laird Connectivity, 2019). Chip antennas are passive elements usually made of ceramics with favorable electrical properties (*Antenna Selection Guide For ISM Bands* / Radiocrafts, 2017). To create a half-wave dipole, it is essential not only the chip antenna itself but also an appropriate ground plane. This is because the performance of the antenna is directly related to the dimension and shape of the ground plane, and its place on the printed circuit board (PCB). This kind of antennas offers reasonable performance; however, they can be easily detuned due to its very high Q. Furthermore, they often require additional matching networks for optimal RF performance and their implementation requires some level of RF expertise.

Each radioprobe incorporates two RF units, one used for the transmission of the collected data to ground and, the other used for receiving positioning and timing data from satellite signals in space. The antennas used for the version 1.0 of the radioprobes are quarter wave chip antennas embedded in the system. The main characteristics of the transmitter antenna are described below, while those of the receiving antenna are described in the subsection 3.3.1.4.4 Positioning and Tracking sensors – GNSS Receiver antenna.

Transmitter antenna

The transmitter antenna allows the radiation of energy from the radioprobe RF output into the space. For the transmission of the data, the sub-1GHz AA071 antenna (*ISM 868 MHz Ceramic Chip Antenna (AA701)*, 2020) from Unictron has been selected mainly because of its compact size and smaller clearance area required.

The AA071 is a SMT ceramic chip antenna using a patented design called TELA (Tuning Element Loop Antenna). The main feature of the TELA design is that, apart from the matching circuit, it incorporates additional components for adjusting the resonance frequency of the antenna (*TELA Chip Antenna* / Unictron, n.d.). The benefits of the additional passive components are the improvement of the efficiency and a smaller clearance area. The main features of the AA071 are listed below:

- Dimensions : 5 mm x 3 mm x 0.5 mm
- Clearance area: 10 mm x 10 mm

- Frequency of operation: 863 MHz to 870 MHz
- Linear polarization
- Voltage Standing Wave Ratio (VSWR): 2 max. using evaluation board with ground plane dimensions of 80 mm x 40 mm
- Peak gain: - 0.9 dBi typical @ 868 MHz
- Efficiency: 52 % typical @ 868 MHz

Matching network

The performance of an antenna system over a determined frequency range is not completely dependent on the antenna by itself. The operation of the system is influenced by the frequency characteristics of the combination antenna plus transmission line (Balanis, 2005). Impedance matching is a fundamental part during the design process of a system. The main reasons of performing impedance matching are (Pozar, 2012):

- To ensure that most of the power is delivered when the load is matched to the transmission line.
- To improve the SNR ratio of the system.

Antenna matching is a “technically challenging design process” typically carried out during the phases of the design (*AT16802: Antenna Tune Up*, 2016). Matching the antenna consist of changing the antenna impedance to match it to the corresponding RF circuitry’s output impedance. In this way, the antenna will operate in the desired frequency range and most of the power from the RF source will be transferred to the antenna for the transmission.

There are many choices for coupling-matching networks that can be used between the antenna element and the transmission line that provide an input impedance equivalent to the complex conjugate of the RF source’s output impedance. Considering factors such as complexity, adjustability and implementation, the matching network selected for the first prototype of the radioprobes is the L-section type. This configuration uses reactive elements, which store energy instead of dissipating it, to match the load impedance to the transmission line (Pozar, 2012). The reactive elements can be either inductors or capacitors, depending on the load impedance value. This value can be obtained using the normalize load impedance (in this case the antenna impedance), and its location on the Smith Chart. The Smith Chart is a graphical representation of the reflection coefficient, which is the complex ratio of the reflected wave to the incident wave, and is generally scaled in normalized impedance (White, 2004; “Smith Chart,” 2021).

When the normalized load impedance falls inside the $1 + jx$ Smith Chart circle, the first element from the load is a shunt susceptance $j\beta$, followed by a series reactance jX as is shown in Figure 3.8a. On the other hand, when the normalized load impedance falls outside the $1 + jx$ Smith Chart circle, the first element from the load is a series reactance jX , followed by a shunt susceptance $j\beta$ as is shown in

Figure 3.8b. Since both configurations include two lumped components, there are eight possible matching circuit configurations.

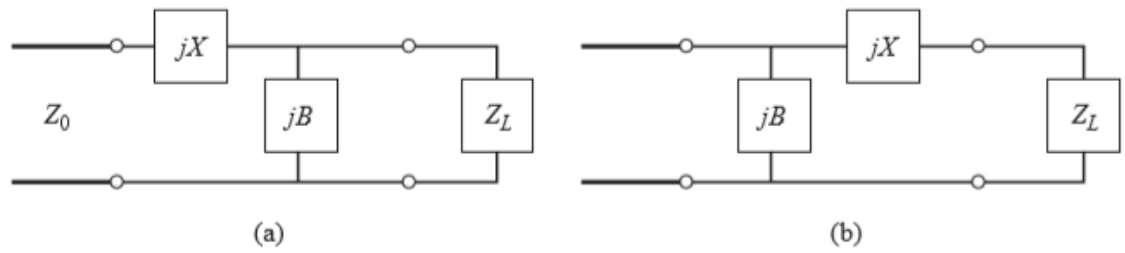


Figure 3.8 L-section matching networks. a) Configuration for normalized load impedance inside the $1 + jx$ Smith Chart circle. b) Configuration for normalized load impedance outside the $1 + jx$ Smith Chart circle (Pozar, 2012)

The determination of the matching network components was done during the antenna matching procedure, which is explained later in the section 4: “Validation of the radioprobe system”. This selection was carefully done following some important rules for the design. For instance, the capacitors selected are NP0 type, which provide the highest level of stability (*COG (NP0) Dielectric / AVX*, n.d.). Also, considering the effects of the element’s case size, small size components were chosen to avoid unwanted parasitic effects.

3.3.1.3 Temperature, Barometric Pressure and Relative Humidity Measurement

Due to the physical constraints of the mini radioprobes, the indispensable parameters required to design the temperature, humidity, and pressure sensor stage were low power consumption, light weight, and small form factor mainly. In addition, considering that in the final radioprobe version, these sensors will be placed outside the bio-balloon, the minimum number of connections between the internal and the external circuitry was evaluated to avoid possible contact errors. Moreover, since the SPI interface of the microcontroller was already used for the communication between it and the radiofrequency RF module, I²C was preferred due to the immunity features of digital signals to noise. In agreement with the operational requirements mentioned in Section 3.1, the TPH sensor specifications can be summarized as follows:

- Range for external temperature: -10 °C to +40 °C
- Range for external humidity: 0 to 100 % RH
- Range for external pressure: 400 to 1100 mbar

On this basis, a careful assessment between different sensors available in the market has been made to find the best solution. After a wide-ranging analysis of possible solutions, the module BME280 from Bosch (*BME280 / BOSCH*, n.d.) was selected as the most suitable choice for the disposable radioprobes. This all-in-one option is a miniature humidity sensor measuring ambient temperature, relative humidity, and barometric pressure, all integrated in a compact tiny package. These attributes allow reducing the physical connections between the inside-and-outside

of the balloon and also minimizing the use of the microcontroller peripherals. Furthermore, the BME280 consumes very little power (on the order of the uA), which makes it ideal for battery powered devices (See Table 3.7 Main electrical characteristics of the BME280 sensor. Current consumption).

This electronic device comes in a land grid array (LGA) package of 8 leads and dimensions of 2.5 mm x 2.5 mm x 0.93 mm. It requires a supply voltage in the range from 1.2 V to 3.6 V and supports I²C and SPI communication interfaces. In terms of overall accuracy and resolution, it achieves high performance in the three physical quantities in study as is reported hereinafter. Table 3.7, Table 3.8, Table 3.9, and Table 3.10 report the main electrical characteristics and TPH specifications of the BME280 module.

Table 3.7 Main electrical characteristics of the BME280 sensor. Current consumption (BME280 / BOSCH, n.d.)

Parameter BME280	Typical value	Unit
Supply voltage	1.8	V
Sleep mode	0.1	uA
Standby mode	0.2	uA
Total current consumption measuring humidity, pressure, and temperature @ 1 Hz	3.6	uA
Current consumption measuring humidity and temperature @ 1 Hz	1.8	uA
Current consumption measuring pressure and temperature @ 1 Hz	2.8	uA

Table 3.8 Humidity parameter specifications sensor BME280

Parameters for humidity sensor	Typical value	Unit
Operating range for temperatures from 0 °C to 60 °C	0 - 100	% RH
Resolution	0.008	% RH
Absolute accuracy	±3	% RH
Hysteresis	±1	% RH
Response time	1	s
Long term drift	±0.5	% RH / year

Table 3.9 Pressure sensor specifications BME280

Parameters for pressure sensor	Typical value	Unit
Operating range for pressure	300 - 1100	hPa
Resolution	0.18	Pa
Absolute accuracy	±1	hPa
Long term stability	±1	% hPa / year

Table 3.10 Temperature sensor specifications BME280

Parameters for temperature sensor	Typical value	Unit
Operating range for temperature	-40 - +85	°C
Resolution	0.01	°C
Absolute accuracy	±1	°C

The BME280 module presents three different modes that can be set according to the user need: sleep mode, normal mode and forced mode.

- When set to sleep mode, the device does not operate, and its power consumption is minimal. This mode allows the access to the registers.
- The normal mode allows continued cycles of measurement periods combined with idle periods. During the measurement periods, temperature, pressure and/or humidity measurements are performed in accordance to the set options.
- The forced mode allows to perform a single measurement and then send the device to sleep mode. The results of the measurements can be accessed through the data registers.

3.3.1.4 Positioning and Tracking Measurement

The Lagrangian reference system involves the motion tracking of individual “tagged” particles as they move along a fluid as a function of time (Young, 2007). In this context, every single radioprobe can be considered as a tagged particle seeded into a flow to measure temperature, pressure, humidity, velocity, vorticity, and acceleration along its trajectory as time passes. In such a way, if multiple fluid particles are followed simultaneously, the properties of the flow inside the domain under study can be extracted. The positioning and tracking electronic block, as its name suggests, enables the determination of the path followed by the radioprobe during its drift.

Based on the limitations of the radioprobe scenario, the trajectory tracking and position estimation process can be reduced to two different approaches. The first approach is the use of Inertial Navigation Systems (INS) to provide orientation, position, and localization of a moving object. The second approach is the use of radio signals combined with position estimation techniques to localize the target objects. During the development of the present work, both scenarios were carefully studied and tested. As result, the first approach using INS, which is further detailed hereinafter, provided the most suitable solution for this electronic block design.

The trajectory tracking and motion sensing process of each radioprobe is achieved by performing sensor fusion algorithms based on Kalman and Madgwick filters. Kalman filtering, known also as linear quadratic estimation (LQE), is an algorithm that generates estimates of unknown variables based on sets of measurements observed over time (“Kalman Filter,” 2021; Kim & Bang, 2019). Due to its good accuracy in the presence of large sources of noise, Kalman filtering has been used for a wide range of applications, being the most common guidance, navigation

object tracking, economics, and control of vehicles (Madgwick, 2010; Zarchan & Musoff, 2015; “Kalman Filter,” 2021). It consists of two steps: the propagation or prediction step where estimates of the current state variables together with their uncertainties are produced, and the correction or update step where these estimates are updated to be more accurate using a weighted average.

Madgwick filtering is an orientation algorithm applicable to inertial measurement units and Magnetic, Angular Rate, and Gravity (MARG) systems (also known as Attitude and Heading Reference System (AHRS)) to describe orientation in three-dimensions (Madgwick et al., 2011). It uses a four-dimensional complex number called quaternion to represent an object’s orientation (Ludwig et al., 2018).

The input data for these algorithm processes come from an IMU and a GNSS receiver, both embedded in the radiosonde system. Their characteristics are detailed in the next subsections.

Inertial Measurement Unit IMU

An IMU is a self-contained electronic system that incorporates a set of sensors such as accelerometers, gyroscopes, and magnetometers to measure and provide force, angular rate, and orientation of a body (“Inertial Measurement Unit,” 2021; *What Is IMU?*, n.d.). Accelerometers sense linear acceleration, gyroscopes detect angular or rotational rate, and magnetometers provide a heading reference (Jekeli, 2000). The IMU selected for the radioprobe’s electronic block is the nine-axis inertial module LSM9DS1 (*LSM9DS1 / STMicroelectronics*, n.d.). It is an electronic device that embeds in a single package a three-axis digital linear acceleration sensor, a three-axis digital angular rate sensor, and a three-axis digital magnetic sensor.

The device presents a compact 24-lead LGA package with dimensions of 2.5 mm x 2.5 mm x 0.93 mm. Its temperature operating ranges are from -40 °C to +85 °C. It requires a supply voltage in the range from 1.9 V to 3.6 V, and supports both, SPI, and I²C communication interfaces. The module specifications and main characteristics are reported in Table 3.11 and Table 3.12.

Table 3.11 Main electrical characteristics of the LSM9DS1 module (*LSM9DS1 / STMicroelectronics*, n.d.)

Parameter LSM9DS1	Typical value	Unit
Supply voltage	2.2	V
Current consumption of the accelerometer and magnetometer in normal mode @ V _{dd} = 2.2 V, T = 25 °C	600	uA
Current consumption of the gyroscope in normal mode @ V _{dd} = 2.2 V, T = 25 °C	4	mA

Table 3.12 Sensor characteristics of the LSM9DS1 module

Parameters for humidity sensor	Typical value	Unit
Linear acceleration measurement range	±2, ±4, ±8, ±16	g

Sensitivity for linear acceleration:		
Linear acceleration ± 2 g	0.061	mg / LSB
Linear acceleration ± 4 g	0.122	mg / LSB
Linear acceleration ± 8 g	0.244	mg / LSB
Linear acceleration ± 16 g	0.732	mg / LSB
Magnetic field full scale	$\pm 4, \pm 8, \pm 12, \pm 16$	gauss
Magnetic sensitivity		
Magnetic scale ± 4 gauss	0.14	mgauss / LSB
Magnetic scale ± 8 gauss	0.29	mgauss / LSB
Magnetic scale ± 12 gauss	0.43	mgauss / LSB
Magnetic scale ± 16 gauss	0.58	mgauss / LSB
Angular rate full scale	$\pm 245, \pm 500, \pm 2000$	dps
Sensitivity for angular rate		
Angular rate ± 245 dps	8.75	mdps / LSB
Angular rate ± 500 dps	17.50	mdps / LSB
Angular rate ± 2000 dps	70	mdps / LSB

The LSM9DS1 module presents different modes that can be set according to the user needs:

- The set accelerometer and gyroscope can be configured in two possible modes: only accelerometer active and gyroscope in power-down mode, and accelerometer and gyroscope in active mode.
- The gyroscope can be set to three operating modes available: normal mode, power saving and power-down.
- The magnetic sensor can be configured in three different modes: continuous conversion mode, single conversion mode and power down mode.

The configuration can be done through the different configuration registers by the correct setting of values.

Global Satellite Navigation System Receiver GNSS

GNSS is a standard term for satellite navigation systems that provide signals from space containing geolocation and time information (*What Is GNSS? / EGNOS User Support*, n.d.; *What Is the Difference Between GNSS and GPS? / Symmetry Electronics*, n.d.). A GNSS system includes different satellite constellations from navigation systems such as Global Positioning System, Galileo, GLObal NAVigation Satellite System (GLONASS) or Beidou (“GNSS Applications,” 2021). The key benefit of having access to various satellite constellations with global coverage at the same time is accuracy and availability of information. The GNSS receiver used for the Positioning and Tracking Measurement Unit is the ZOE-M8B module (*ZOE-M8B / U-Blox*, 2020). It is a 72-channel professional, ultra-small, energy efficient System-in-Package (SiP) device that offers good performance whilst consuming low power.

It comes in a compact soldered land grid array (S-LGA) package of dimensions 4.5 mm x 4.5 mm x 1.0 mm, and requires a single voltage supply of 1.8 V. Its operating temperature range goes from -40 °C to +85 °C. The ZOE-M8B receiver supports multiple GNSS systems: GPS @ 1575.42 MHz, GLONASS @ 1602 MHz, BeiDou @ 1561.098 MHz, and Galileo satellite constellations. The module provides interference suppression, integrity protection of messages, anti-jamming, and anti-spoofing, all of them with aim of supplying reliable positioning and security. This module supports three different protocols: National Marine Electronics Association (NMEA), the u-blox proprietary UBX, and Radio Technical Commission for Maritime Services (RTCM). All of them available through UART, SPI, and display data channel (DDC) interfaces.

For power management purposes, the ZOE-M8B receiver can be programmed to operate in two different modes: Super-E mode and continuous mode.

- The Super-E mode allows the best compromise between energy consumption and performance. Compared with previous u-blox versions, this mode provides triple saving of power while keeping high degrees of accuracy both, in speed and positioning. The default navigation update rate is 1 Hz, being possible the selection of 2 Hz and 4 Hz.
- The continuous mode offers the best reception performance of the receiver module at the expense of higher power consumption. In this mode, the full operation of the module results in the highest sensitivity and the fastest Time-to-First-Fix (TTFF). The navigation update rate can be set up to 10 Hz.

The ZOE-M8B module specifications and main characteristics are reported in Table 3.13 and Table 3.14.

Table 3.13 Main electrical characteristics of the ZOE-M8B GNSS receiver (ZOE-M8B / U-Blox, 2020)

Parameter ZOE-M8B	Typical value	Unit
Supply voltage	1.8	V
Average supply current @ Vdd = 1.8 V		
Acquisition	34.5	mA
Tracking (Continuous mode)	32.5	mA
Tracking (default Super E-mode)	7.3	mA
Tracking (save setting Super E-mode)	6.3	mA

Table 3.14 ZOE-M8B GNSS performance for GPS and GLONASS

Parameter GNSS ZOE-M8B	GPS & GLONASS	GPS	Unit
Horizontal position accuracy:			
Continuous mode	2.5	2.5	m
Super E-mode default	3.5	3.0	m

Super E-mode power-save	4.0	3.5	m
Time-to-First-Fix:			
Cold start	26	29	s
Hot start	1	1	s
Sensitivity in Super E-mode:			
Navigation and tracking	-160	-160	dBm
Reacquisition	-160	-160	dBm
Cold start	-148	-148	dBm
Hot start	-157	-157	dBm

The main operational limits of the ZOE-M8B GNSS receiver are ≤ 4 g for dynamics, 50 km for altitude and 500 m/s for velocity. The velocity accuracy provided by the receiver is 0.05 m/s for continuous mode and 0.2 m/s for Super E-mode in default setting.

Low noise amplifier

In order to improve the GNSS system performance in terms of sensitivity, robustness again RF power, jamming and Electrostatic Discharge (ESD), the design incorporates a low noise amplifier (LNA) connected to receiver's signal input. The GNSS LNA used is the NJG1143UA2, which features low noise figure (0.70 dB), low current consumption (4 mA), and high gain (20dB) (*NJG1143UA2*, n.d.). It comes in a tiny 6-leads package of dimensions 1 mm x 1 mm x 0.37 mm. This LNA embeds an on-chip ESD protection and requires just three external electronic components for its operation.

The NJG1143UA2 requires a supply voltage in the range from 1.5 V to 3.6 V and operates within temperature ranges from -40 °C to +105 °C.

GNSS Receiver antenna

As previously described in the subsection Radiocommunication System, each radioprobe incorporates two RF units: the first one used for the transmission of the in-flight collected data to ground, and the second one used for receiving positioning and timing data from satellite signals in space. In a similar way, the antenna used for the receiver side is a quarter wave chip antenna designed for GNSS band applications embedded in the system. This antenna intercepts the electromagnetic waves radiated from the GNSS satellite constellations for the successive radioprobe's positioning and tracking processes. To this end, the GNSS ceramic chip antenna AA088 (*GNSS Ceramic Chip Antenna AA088 / Unictron*, n.d.) from Unictron has been selected mainly because of its compact size and smaller clearance area required.

This SMT AA088 antenna also uses the patented design TELA, which incorporates additional components for adjusting the resonance frequency of the antenna (*TELA Chip Antenna / Unictron*, n.d.). The main features of the AA088 are listed below:

- Dimensions : 3.2 mm x 1.6 mm x 0.5 mm

- Clearance area: min. 5.5 mm x 5.5 mm
- Frequency of operation: 1560 MHz to 1606 MHz
- Linear polarization
- Voltage Standing Wave Ratio: 2 max. using evaluation board with ground plane dimensions of 80 mm x 40 mm
- Peak gain: 3.3 dBi typical @ 1575.42 MHz
- Efficiency: 83 % typical @ 1575.42 MHz

Matching network

As previously mentioned, the behavior of an antenna system across a frequency range is determined not only by the antenna itself but also its transmission line. In order to maximize the power transfer between the antenna and the RF circuitry, a L-section coupling-matching network (Figure 3.8) has been incorporated in the design. This configuration uses reactive elements, which store energy instead of dissipating it, to match the load impedance to the transmission line (Pozar, 2012). Depending on the load impedance value, the L-section elements can be either capacitors or inductors, and their values can be determined based on the normalized load impedance and its location on the Smith Chart. The determination of the matching network components was done during the antenna matching procedure, which is explained later in the section 4 “Validation of the radioprobe system”. This selection was carefully done following some important rules for the design. For instance, the capacitors selected are NP0 type, which provide the highest level of stability (*COG (NP0) Dielectric / AVX*, n.d.). Also, considering the effects of the element’s case size, small size components were chosen to avoid unwanted parasitic effects.

3.3.1.5 Power Supply Unit

As stated in section “Critical technical aspects”, power consumption is one of the key factors to consider during the radioprobe development since it is narrowly related to the total weight of the floating device. For instance, if the energy usage of the whole electronic circuit rises, a larger capacity battery will be demanded, hence increasing the total weight ratio.

The power supply unit supplies the electric power to the radioprobe system. This block was designed considering the main electrical requirements of the radioprobe system: total current consumption, pulse drain features, minimum and maximum voltage values, expected lifetime, environmental conditions, and mechanical specifications. As a result, the electronic components of this block were carefully selected. They are explained in the following subsections.

Low-dropout (LDO) voltage

Since the radioprobe circuit requires two different supply voltage values (1.8 V and 3.3 V), the dual LDO voltage regulator LP3996SD (*LP3996 / Texas Instruments*, n.d.) has been embedded into the power system. It has two voltage outputs with independent enable options, being able to source both 300 mA and 150 mA at an

ultra-low quiescent current of 35 μ A. The LP3996SD comes in a 10-lead tiny package of dimensions of 3 mm x 3 mm. It accepts input voltage ranges between 2 V and 6 V.

Voltage level translator

The GNSS receiver interacts with the microcontroller through the bidirectional non-inverting voltage level translator TXS0108EPW from Texas Instruments (*TXS0108E* / *Texas Instruments*, n.d.). This electronic device serves as interface for the different voltage requirements of the radioprobe system. It is an 8-bit non-inverting translator that offers two different power-supply ports, which can be configured by the user. The first port admits a power supply voltage within the range from 1.2 V to 3.6 V, while the second port admits a power supply voltage within the range from 1.65 V and 5.5 V.

The TXS0108EPW comes in a 20-leads thin-shrink small-outline package (TSSOP) of dimensions of 6.5 mm x 6.4 mm and operates within temperature ranges from -40 °C to +85 °C.

Power supply

The radioprobe design includes two alternatives to supply the power to the device: the first one through an external battery used during the radioprobe flight, and the second option through a Future Technology Devices International (FTDI) USB to serial connection used mostly for management purposes.

Since the radioprobes must be self-powered and considering that their recovery after the flight is not envisaged, a single non-rechargeable battery was the best option to energize the device while maintaining a system weight below 20 g. To this end, the high-power military grade TLM-1520HP battery has been selected (*TLM-1520HPM* / *TADIRAN*, n.d.). It is a Lithium Metal Oxide (LMO) battery featuring a nominal voltage of 4.0 V and a nominal capacity of 125 mAh. With a maximum discharge continuous current of 1.75 A and a maximum current capability of 3.75 A, this battery meets the pulse power requirements of the radioprobe circuit. This powering device weighs 9 g and has a volume of 3.2 cm³. Its operating temperature range goes from -55 °C to +85 °C.

This kind of TLM-series battery is fabricated using non-toxic and non-pressurized solvents and with anode materials that present lower explosive characteristic than the common lithium batteries. These batteries comply with the global Underwriters Laboratories Inc. (UL) safety standards (*TLM SERIES* / *TADIRAN*, n.d.).

3.3.2 Ground Station

The ground station is responsible for the reception of the information sent by the radioprobes as well as its processing, management, filtering, storage, and display. It comprises a base station and a post processing system. Its block diagram

is shown in Figure 3.9 and the explanation of each functional unit is detailed in the next subsections.

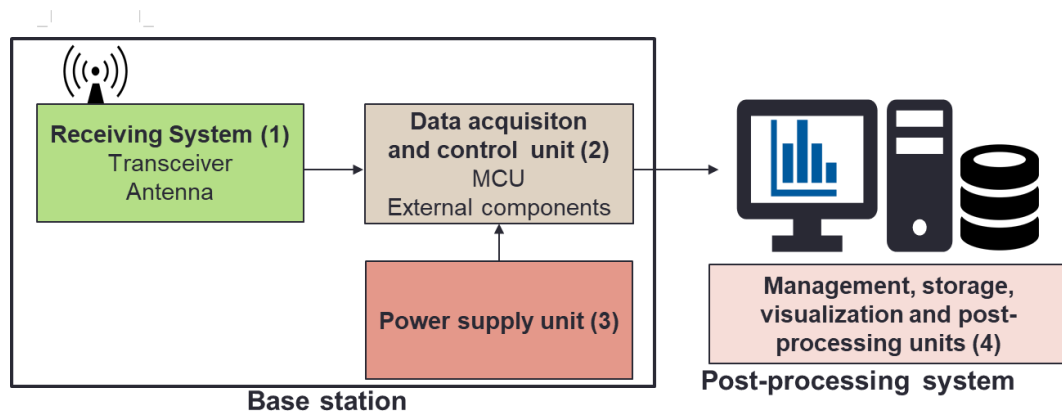


Figure 3.9 Block diagram of the ground station

3.3.2.1 Base station

The base station consists of a receiving system, a data acquisition and control unit, and a power supply unit. It is based on the module Adafruit Feather 32u4 LoRa Radio (RFM9x), which is an embedded module containing a LoRa-based transceiver and an ATmega32u4 microcontroller (*Adafruit Feather 32u4 RFM95 / Adafruit, n.d.*). The Adafruit Feather 32u4 LoRa Radio board provides 20 general-purpose input/output (GPIO) pins, 10 analog outputs, 7 pulse-width modulation PWM pins, and supports hardware serial, hardware I²C, and SPI interfaces. It also includes a voltage regulator of 3.3V and provides a peak current output of 500 mA.

The reception of the packets is done by using the RFM95 868/915 MHz radio module embedded in the system. This transceiver exhibits the same characteristics of the transceiver used for the radioprobe. It is a LoRa based module that offers long range communication ranges and low power consumption due to its modulation technology. It provides a power output capability from +5 to +20 dBm and works in the ISM license-free frequency bands. It offers a maximum link budget of 168 dB and sensitivity greater than -148 dBm (*RFM95W / HOPERF, n.d.*).

The control and management of the obtained information is done using the ATmega32u4 microcontroller equally integrated in the Adafruit module. It is a low power 8-bit microcontroller (*ATmega32U4 / Microchip, n.d.*) with 32 KB of flash program memory, 2.5 KB of RAM memory, and 1 KB of EEPROM memory. This microcontroller is fully compatible with the USB specification then debugging and programming processes can be done easily in this way.

Since at the ground station side the weight and size restrictions governing the radioprobe design are not present, an external quarter wave monopole antenna operating in the band from 850 MHz to 888 MHz is used. It has an omnidirectional pattern, a gain of 3.16 dBi and is connected to the receiver board through an uFL to SubMiniature version A (SMA) adapter. Its operating temperature range goes from -20 °C to +85 °C (*ANT-868-CW-RCS-Xxx / Linx, n.d.*).

The base station system captures the data coming from the radiosonde, pre-processes it and provides also signal quality information such as Signal-to-Noise ratio (SNR) and Received Signal Strength Indicator (RSSI) of the packets. The base station is connected to a personal computer (PC), which provides the required energy to the system through the USB port. This PC is part of the post-processing system.

As mentioned previously, the base stations are configured to capture the transmitted data from the floating devices. To reduce the chance of losing a transmitted packet from any of the radioprobes, the system is designed in such a way that the base stations are spatially dispersed around the cloud under study to ensure the reception of the data. In a similar way, to provide a reliable reference for the positioning and trajectory tracking calculations to determine the location of the radioprobes, the base stations are located at known fixed positions on the ground.

3.3.2.2 Post-processing system

The post-processing system consists of a set of computers where the information passed by the base stations is managed, filtered, processed, stored, and displayed. Each base station is connected to a portable computer where the information received in real time from the instrumented balloons is stored, partially processed, and initially displayed to the user.

As initial step, this information is passed, parsed, and organized through the browser-based flow editor called Node-RED. It is a visual programming tool that allows wiring together application programming interfaces (APIs), hardware, and online services using a wide selection of nodes (*Node-RED*, n.d.). This programming environment permits the creation of personalized functions using the programming language JavaScript. The created flows can be easily saved using the open standard file format JSON.

The information delivered by the base station to the PC is retrieved via serial communication. At this point, Node-RED is used to process and organize the incoming data using different functions and nodes. Here, the data is managed to be stored in a database and in a file. An example of an implemented flow used to parse and send the data to an InfluxDB database is shown in Figure 3.10 and Figure 3.11.

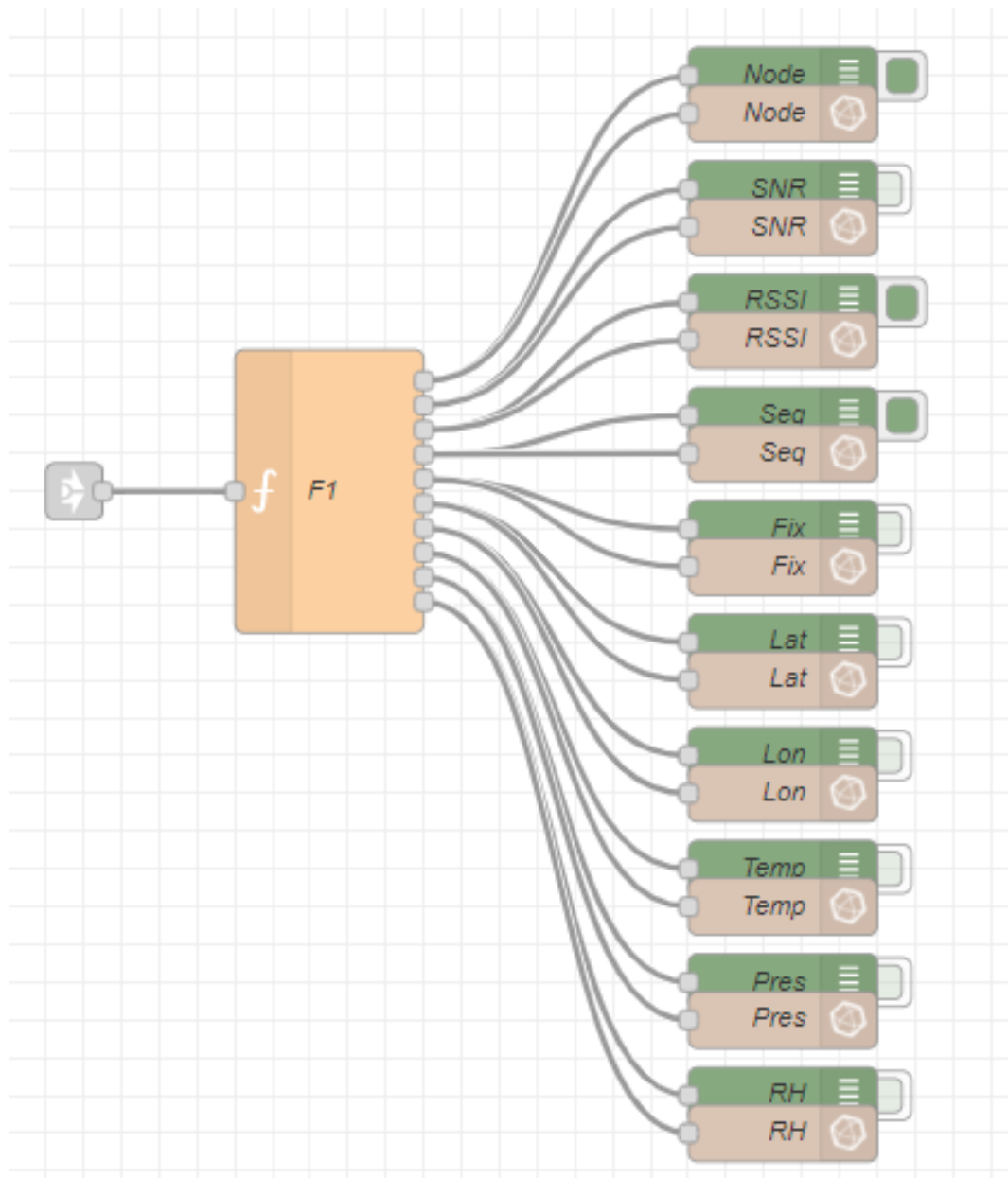


Figure 3.10 Node-RED environment. Example of a flow implemented to process and store data

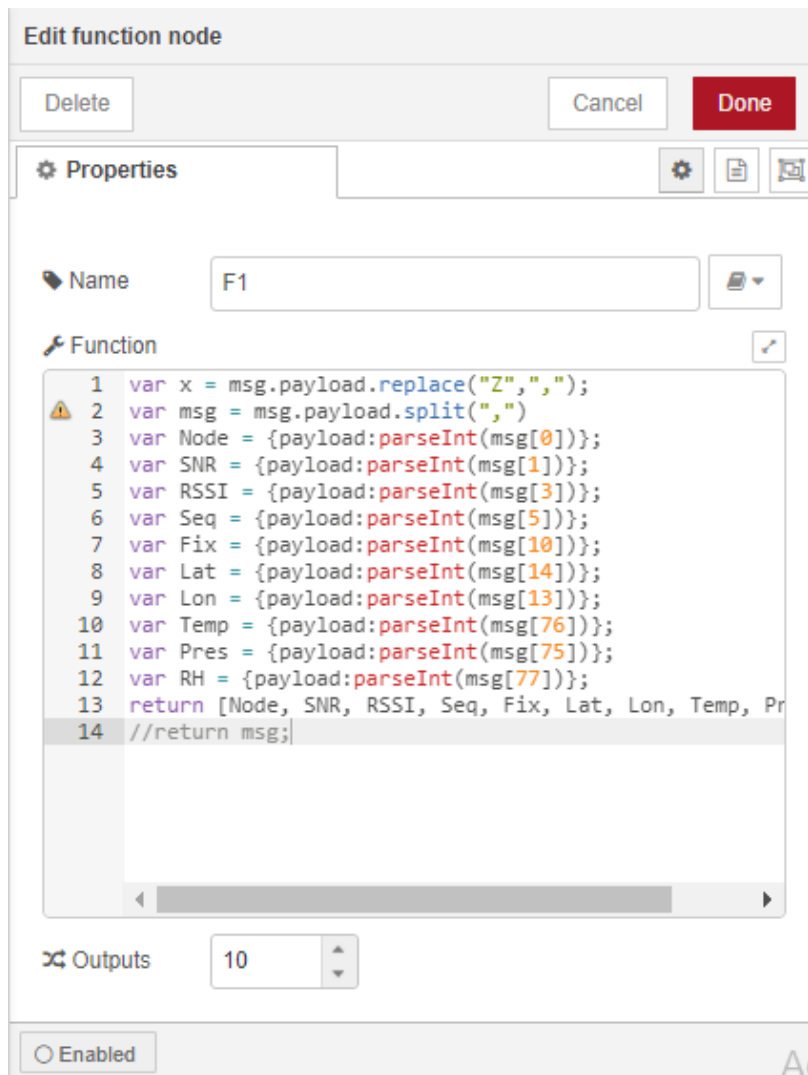


Figure 3.11 Node-RED environment. Example of a function implemented to parse data

The storage has been implemented through InfluxDB, which is a time-based read and write database developed by InfluxData (“InfluxDB,” 2021; “InfluxDB Open Source Time Series Database | InfluxDB,” n.d.). Here, the data is stored in collections aggregated over time and queried using a SQL-like language. Figure 3.12 and Figure 3.13 show the command line interface to start, access, and manage the data using InfluxDB.


```

Command Prompt - influxd.exe

88888888      .d888 888      88888888b. 8888888b.
888      d88P" 888      888      "Y88b 888      "88b
888      888      888      888      888 888      .88P
888 888888b. 888888 888 888 888 888 888 888 88888888K.
888 888 "88b 888      888 888 888 Y8bd8P' 888      888 888 "Y88b
888 888 888 888      888 888 888 X88K 888      888 888      888
888 888 888 888      888 Y88b 888 .d8""8b. 888 .d88P 888 d88P
88888888 888 888 888      888 "Y88888 888 888 88888888P" 88888888P"

2021-03-04T11:18:11.901981Z info InfluxDB starting {"log_id": "0SgFC4k0000", "version": "1.5
.2", "branch": "1.5", "commit": "02d7d4f043b34ecb4e9b2dbec298c6f9450c2a32"}
2021-03-04T11:18:11.902991Z info Go runtime {"log_id": "0SgFC4k0000", "version": "go1.9.2", "
maxprocs": 4}
2021-03-04T11:18:12.014277Z info Using data dir {"log_id": "0SgFC4k0000", "service": "store", "pa
th": "C:\\Users\\miryam\\.influxdb\\data"}
2021-03-04T11:18:12.014277Z info Open store (start) {"log_id": "0SgFC4k0000", "service": "sto
re", "trace_id": "0SgFC5BW000", "op_name": "tsdb open", "op_event": "start"}
2021-03-04T11:18:12.089207Z info Opened file {"log_id": "0SgFC4k0000", "engine": "tsm1", "serv
ice": "filestore", "path": "C:\\Users\\miryam\\.influxdb\\data\\DB1\\autogen\\2\\000000001-000000001.tsm"
, "id": 0, "duration": "0.999ms"}
2021-03-04T11:18:12.159079Z info Opened file {"log_id": "0SgFC4k0000", "engine": "tsm1", "serv

```

Figure 3.12 Command line interface to the start the InfluxDB database

```

Command Prompt - influx.exe

Connected to http://localhost:8086 version 1.5.2
InfluxDB shell version: 1.5.2
> show databases
name: databases
name
----
internal
DB1
DB2
DB3
>
>

```

Figure 3.13 Command line interface to the access and manage the database InfluxDB

As end point of the network, the time series data application interface Chronograf has been added to provide a preliminary graphical output of the information collected. Chronograf is a web application interface that allows the query and visualization of data stored in InfluxDB databases or other InfluxData's products ("Chronograf," n.d.). It is written in the open-source programming language Go and uses the JavaScript library React.js. Chronograf comes with a wide range of dashboard templates that can be edited and customized by the user. It also provides an additional way to manage the database and its retention policies. Figure 3.14 shows an example of the graphical interface implemented to visualize some radioprobe's information using Chronograf.

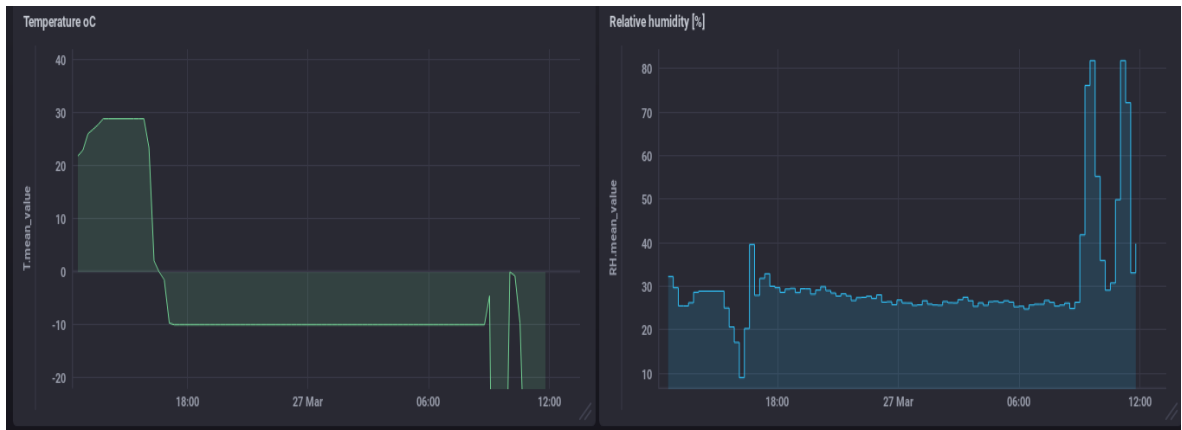


Figure 3.14 Chronograf environment. Example of the graphical output provided by the post-processing system

Once the field measurements have finished, the next step consists of putting all the data collected by the portable computers together for final processing and analysis. Here, these data are managed, filtered, fully processed, stored, and visualized. At this level, fusion algorithms are executed to complete the trajectory tracking and position processes aimed at determining the path followed by the radioprobes during their flight. Similarly, time series data application interfaces have been implemented to provide the visual output of the fully processed information. The post-processing analysis is based on the use of the programming platforms MATLAB and Python.

As a result, the information obtained from the whole process explained above will be shared with the atmospheric scientific community through the open access database of the Project COMPLETE. This with the aim of transferring the knowledge acquired during the field measurements for the reduction of the gap present in the cloud microphysics understanding correlated to turbulence.

3.4 Radioprobe system integration

Once the operational units of the radioprobes were carefully tested separately (see results in Appendix A), the next step comprised the integration of the radioprobe system into a unique electronic board. To this end, a specialized electronic design automation (EDA) or electronic computer-aided design (ECAD) tool for the PCB design called Eagle was used. Eagle stands for Easily Applicable Graphical Layout Editor and is an electronic design application that offers a schematic capture, PCB layout, PCB routing and CAM attributes (*EAGLE / Autodesk*, n.d.; “EAGLE (Program),” 2021). In the following subsections, these processes are further explained.

Moreover, and as mentioned earlier, the electronic design of the radioprobe board considers the use of SMD components to significantly reduce its size and increase the reliability of the system. In fact, apart from the main electronic components already described in detail in the previous sections, the additional passive components required by the system and populating the PCB design, have a very compact package style 0603 with dimensions of just 1.5 mm x 0.8 mm.

Next subsections describe the PCB electronic design of the radioprobe system including the schematic circuit design and the board layout design.

3.4.1 Schematic Diagram Design

The schematic diagram documents the logic and functionality of the electronic design (*Schematic Design* / Autodesk, n.d.). It describes the electronic components and their electrical connections in the most readable way. It uses abstract symbols to represent the elements of the electronic system.

The various electronic units of the radioprobe system are presented in a schematic way in Figure 3.15, Figure 3.16, Figure 3.17, Figure 3.18, and Figure 3.19.

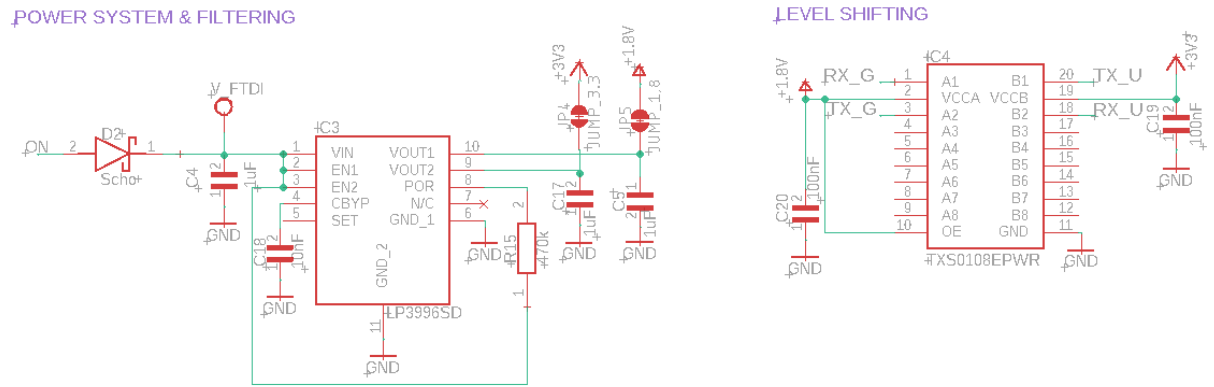


Figure 3.15 Power system and filtering schematic diagram

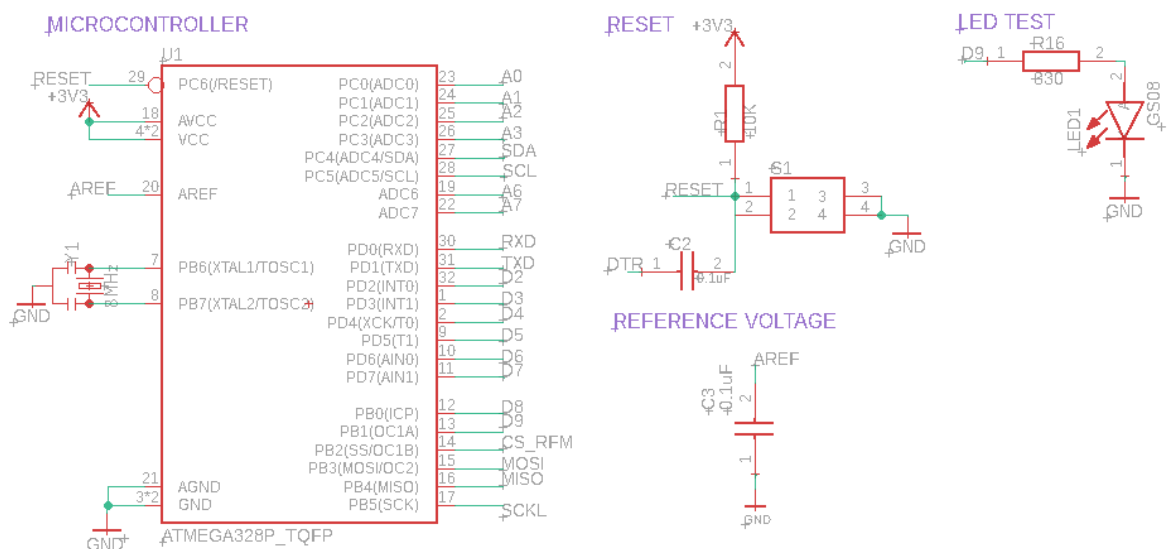
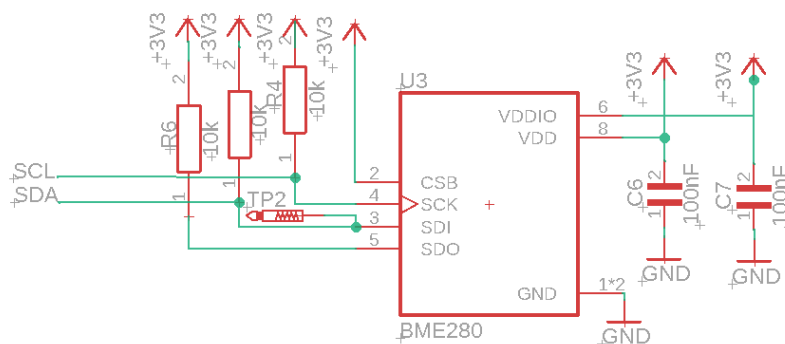


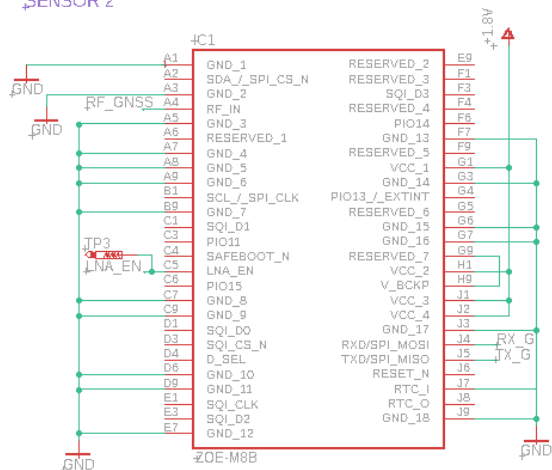
Figure 3.16 Data processing and control unit schematic diagram

[illegible]

SENSOR 1



SENSOR 2

[illegible]

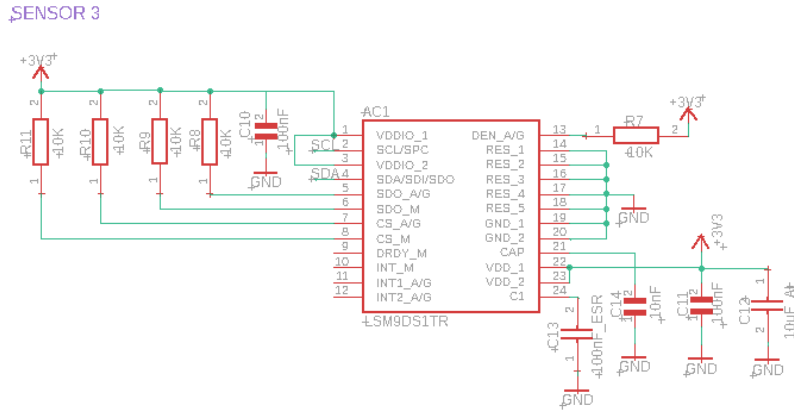


Figure 3.19 Positioning and tracking measurement unit schematic diagram

3.4.2 Board Layout Design

The board layout diagram derives from the schematic diagram and defines the final physical form and shape of the electronic circuit. It is used to design the final PCB through the creation of digital descriptive files used for its manufacturability (Mitzner, 2007).

The PCB implementation of the radioprobe was made using a two-layer board presenting wiring patterns on both sides with a common type substrate FR4, which is a glass-reinforced epoxy laminate material of thickness of 0.8 mm. The placement of the components and routing process were carefully done to improve functionality, manufacturability, and accessibility:

- Most of the components were grouped according to each functional unit.
- The connectors and exposed pins were placed at the edge of the board to ease the external access.
- The components were placed leaving enough gaps for the copper traces according to the manufacturer capabilities.
- The connection paths were reduced as much as possible.
- The clearance antenna regions were kept free to not affect the antenna performance.
- Via shielding along the RF signal paths and ground clearance areas was integrated into the design to minimize possible electric fields at the edge of the board and reduce the undesired crosstalk effect (*Altium Designer 20.2 User Manual* / Altium, n.d.).
- Addition of thermal reliefs to pin-populated components.

The final board layout design of the radioprobe, both top and bottom views, is shown in Figure 3.20 and Figure 3.21.

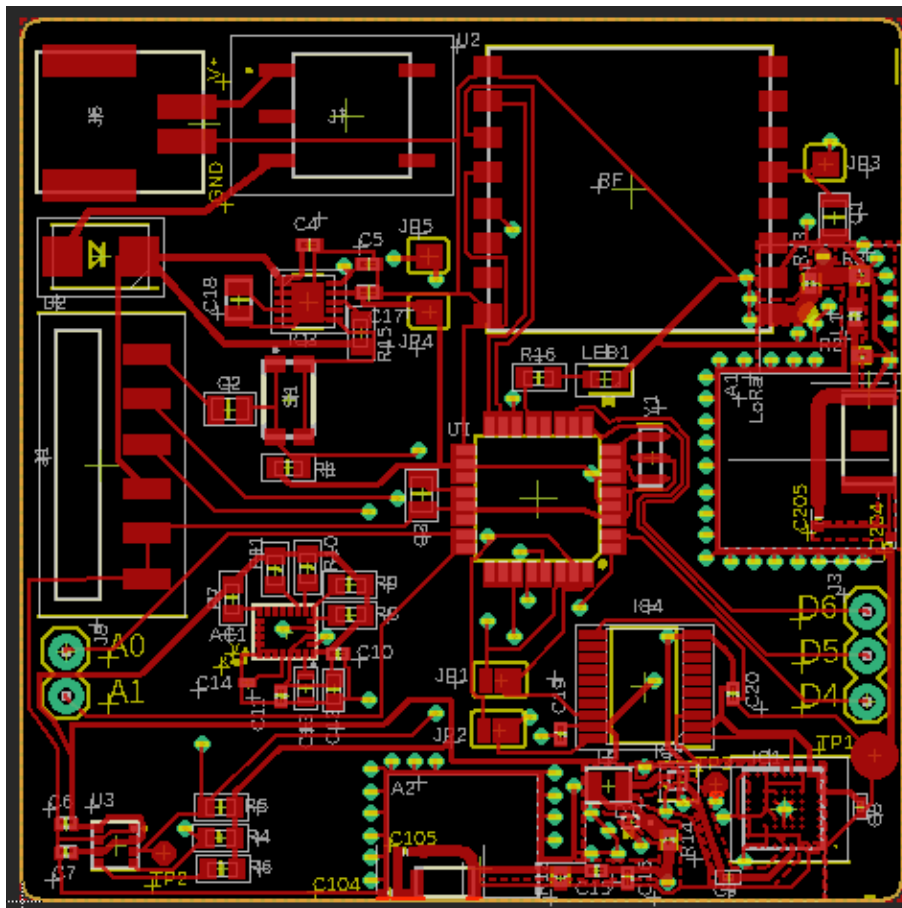


Figure 3.20 Top view of the radioprobe's board layout design

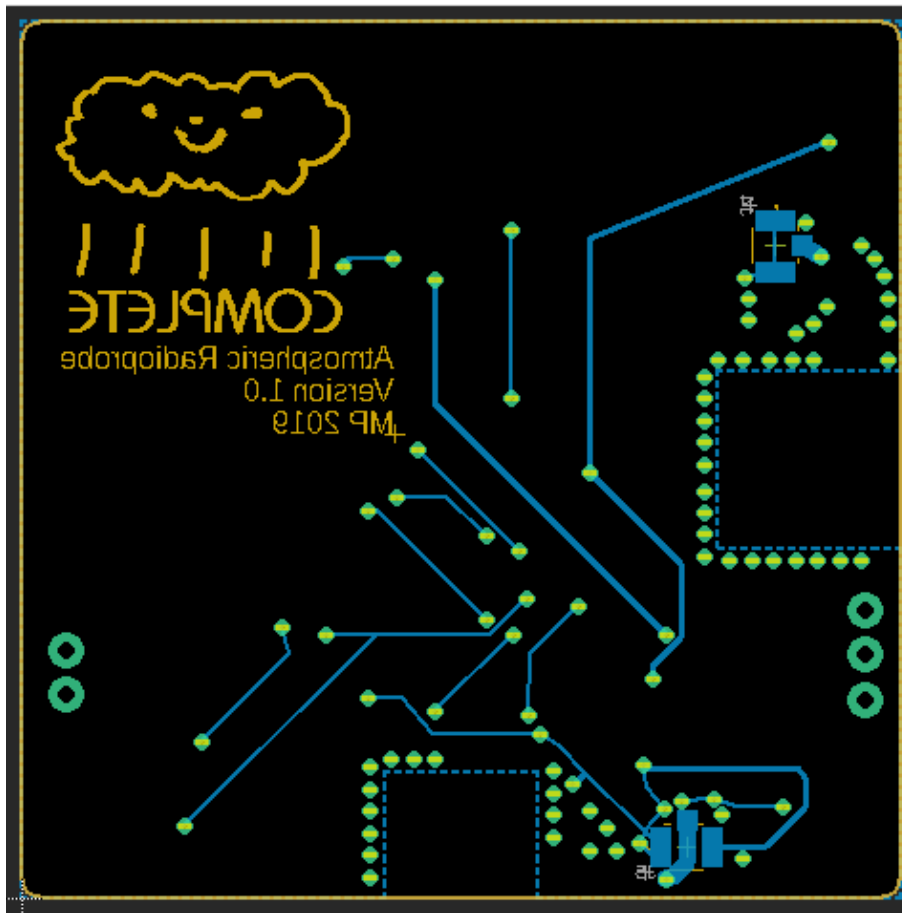


Figure 3.21 Bottom view of the radioprobe's board layout design

Once the electronic board design was finished and carefully analysed, the manufacturing machine files (known also as Gerber files) containing the complete description of the PCB image such as copper layers, drills, routes, solder mask, etc., were generated and sent to the PCB manufacturer for production. Since a few components featured underneath and tight leads requiring specialized soldering tools, some of the electronic parts were assembled by the PCB manufacturer. The remaining components were soldered manually at the Neuronica Lab of the Department of Electronics and Telecommunications of the Politecnico di Torino (Figure 3.22).

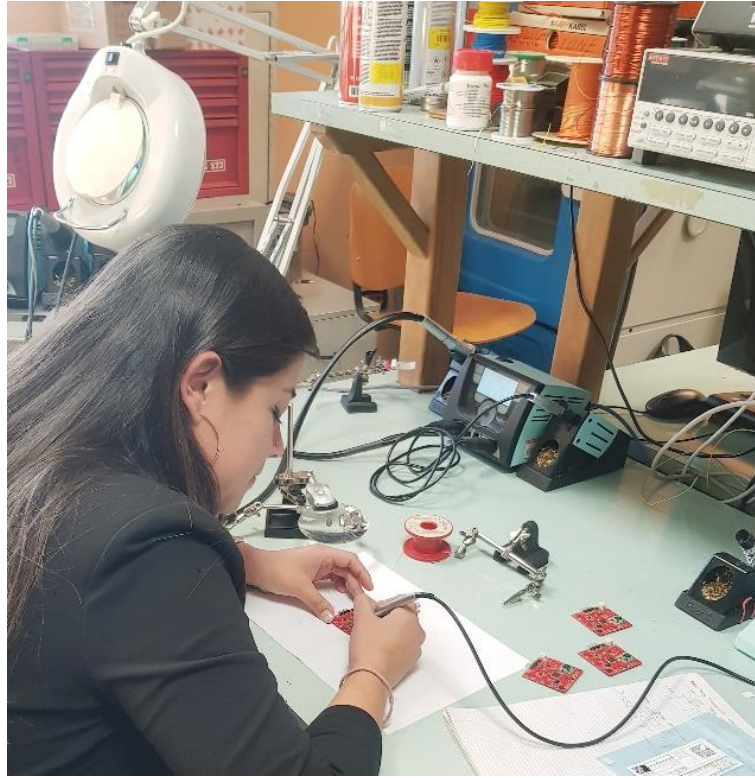


Figure 3.22 Manual soldering of the radioprobe components

As a result of this process, the final radioprobe PCB has a 5 cm x 5 cm rectangular structure with thickness of 0.8 mm and weight of 7 g (without considering the battery). The design incorporates a compact long-lead SMD header connector to access the microcontroller via FTDI for control and firmware uploading purposes. Moreover, the PCB features some exposed plated through-hole pins directly connected to analogue and digital ports of the microcontroller for possible sensor or peripheral expansion if necessary. The top and bottom views of the final implemented board are displayed in Figure 3.23. The main representative electronic components of each operational stage are labelled in Figure 3.24.



Figure 3.23 Final PCB implementation of the tiny radioprobe. Left: top side, right: bottom side.

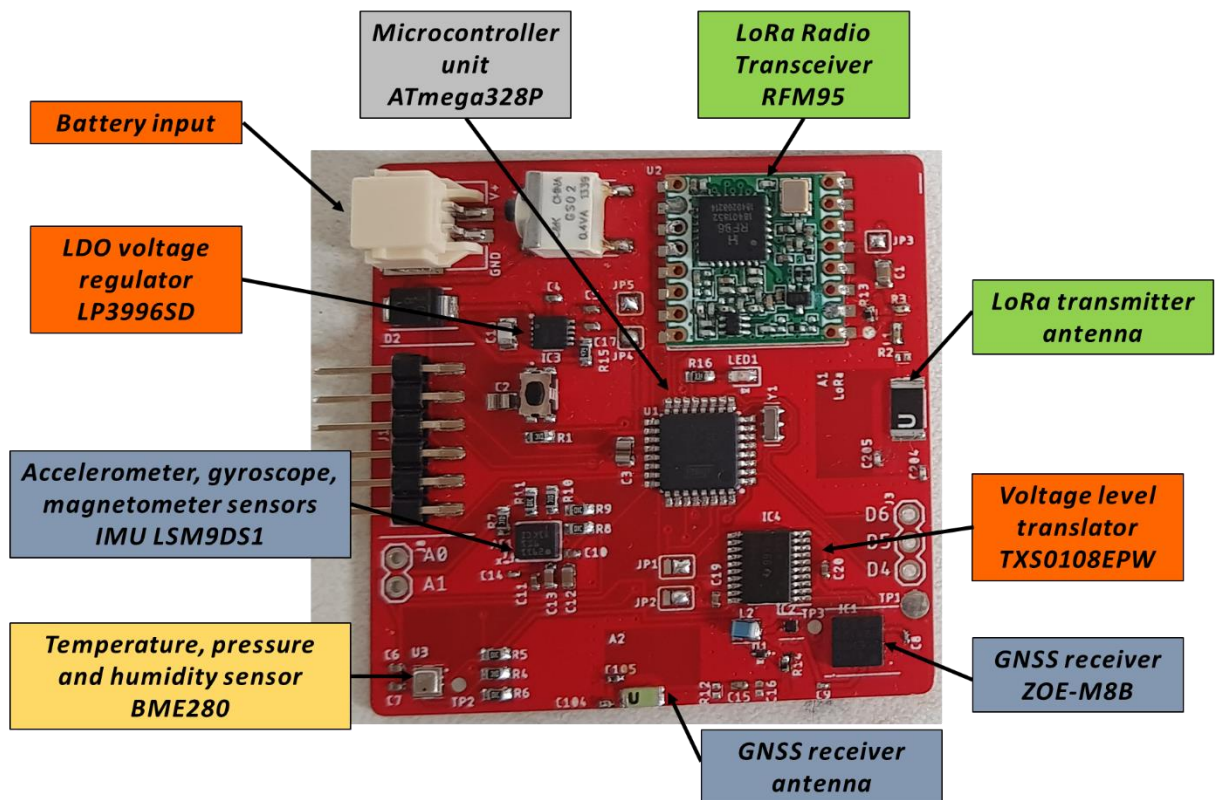


Figure 3.24 Final PCB implementation of the tiny radioprobe. Main electronic components

Chapter 4

Validation of the radioprobe system

This chapter reports on the outcomes of the different experiments and test carried out to validate the entire radioprobe system: tiny radioprobe and ground station. The performance of the system was evaluated based on communication reliability, sensor accuracy, and energy usage mainly.

4.1 Antenna Matching

As mentioned earlier, the performance of an antenna system over a determined frequency range depends not only on the antenna by itself but also on its transmission line characteristics. Since the antenna response is a function of its surrounding environment, the impedance matching must be done when the antenna is placed in its final scenario, in this case the final PCB.

With the size reduction of antennas and their placement in small modules together with other objects in proximity, antenna matching becomes a critical but necessary process. In order to characterize an antenna, a Vector Network Analyzer (VNA) can be used to measure important parameters such as return loss, impedance, and bandwidth. A VNA is a precision measuring tool that allows testing the electrical behavior of high frequency components at different frequency bands (Agilent Technologies, Inc, 2006). The VNA is used to produce a known stimulus signal into a device-under-test (DUT) and, to measure changes to this stimulus signal caused by the DUT. The method used to match the radioprobes' antennas was the theoretical engineering approach. It consists of measuring the antenna impedance with a VNA and, based on its value, adjusting the matching network components to obtain an acceptable S_{11} . For this purpose, the antenna section must be isolated from the rest of the circuit. This option was also considered during the design stage. Each front end of the RF parts can be disconnected from the rest of the circuitry by removing the electronic components R13 and R14 as can be seen in Figure 4.1.

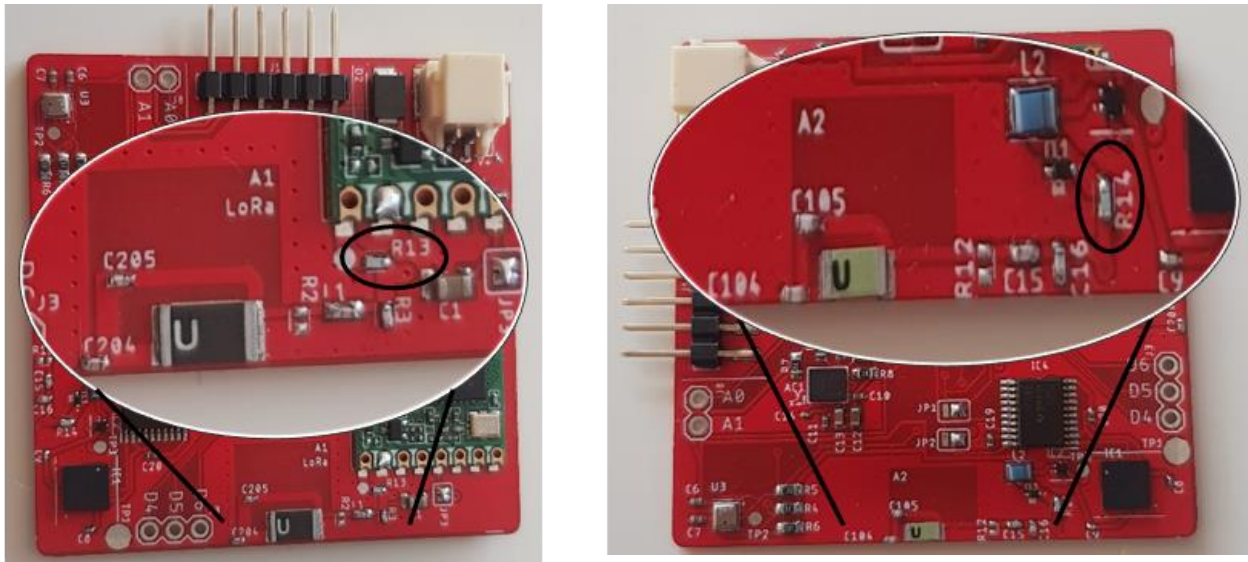


Figure 4.1 RF front end. Left side: Transmitter section. Right side: Receiver section.

4.1.1 Calibration of the equipment using the R&S ZVL Vector

Network Analyzer

The first step of antenna matching is the appropriate calibration of the test equipment to guarantee that the uncertainties are removed, and the readings are within the suitable limits (*Vector Network Analyzer VNA Calibration / Electronics Notes*, n.d.). With the calibration, the effect of cables, connectors, etc. are taken out before starting the measurements of the DUT. The instrument used for the measurements was the Keysight P9371A, which is a portable streamline USB VNA supporting Electronic Calibration modules (*P9371A VNA / Keysight*, n.d.). It has a wide coverage range that operates from 300 kHz up to 6.5 GHz.

This instrument incorporates ports with SMA connectors and an external electronic calibration module N7551A Electronic Calibration Module ECal (Figure 4.2). In addition, a specialized software installed in an external PC is required to control the system.



Figure 4.2 N7551A Electronic Calibration Module ECal

Before starting the measurements, the appropriate calibration of the Keysight P9371A VNA was conducted. The uncertainties were removed, and the reference plane of calibration was moved to the connection point of the SMA cable. Since the frequencies of interest are distant from each other, two frequencies ranges were defined: one containing the 868 MHz and close frequencies and, one containing the 1.575 GHz and close frequencies. The system setup for calibration includes the Keysight P9371A VNA, a SMA cable, the ECal and PC software (Figure 4.3).

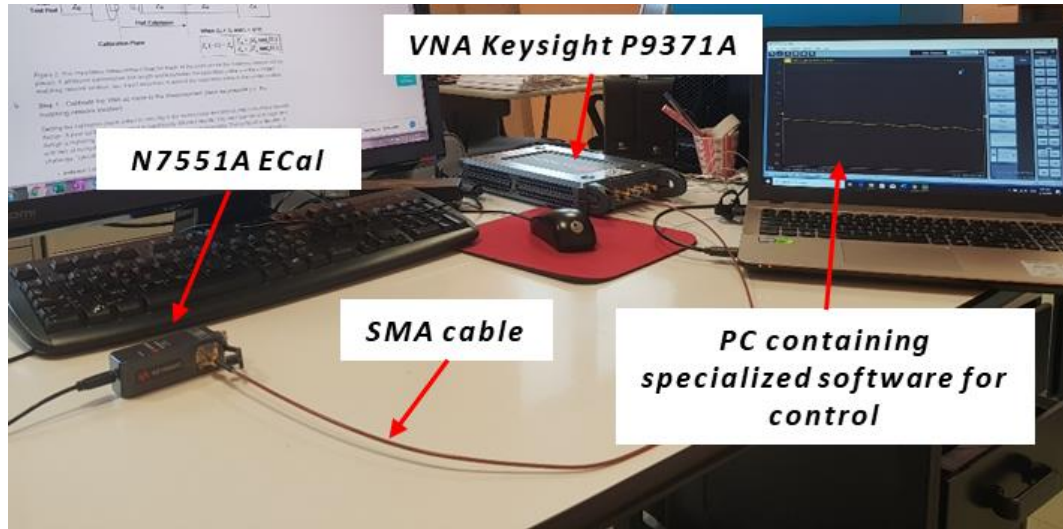


Figure 4.3 System setup for calibration of the Keysight P9371A VNA

The calibration type applied to the instrument was the full One-Port Calibration, which requires a short, open and match standard connected to one port done automatically by the ECal. This calibration is an accurate method applicable for reflection measurements. The three standard measurements are used to derive three error terms: directivity, source match and reflection tracking (Keysight Technologies, n.d.). The match standard is used to obtain the directivity error, which causes a leakage in the generated signal when being transmitted towards the DUT. The short and open standards are used to derive the source match and reflection tracking error terms. The source match error causes an additional reflection of the signal reflected off the DUT, while the reflection tracking error is a frequency-dependent variation of the ratio between the reflected wave to the wave used as reference. The screen showing the electronic calibration is shown in Figure 4.4.

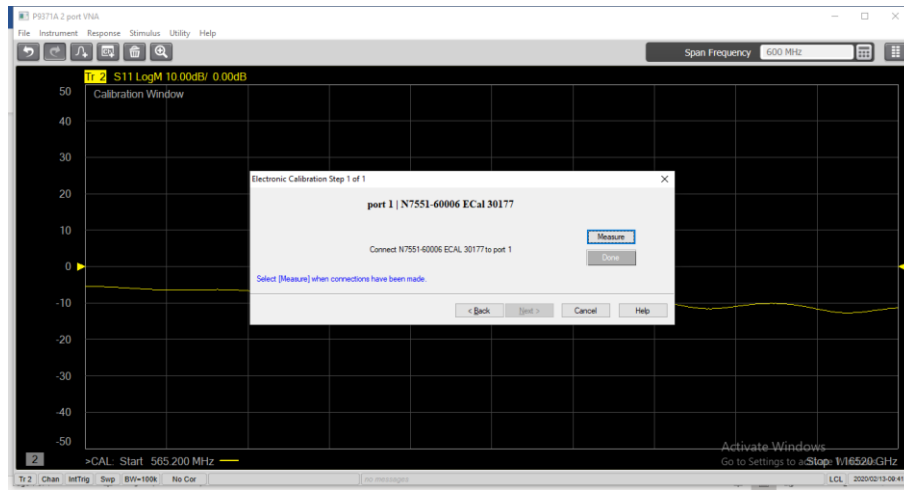


Figure 4.4 One-port calibration screen. Keysight P9371A VNA

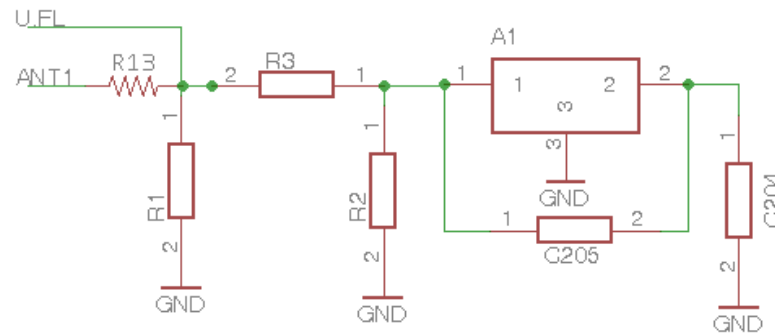
4.1.2 Impedance measurements and calculation of the matching network components

The Keysight P9371A VNA was used to measure the complex impedance and the reflection coefficient S_{11} of the mini radioprobes. The DUT, in this case the radioprobe PCB, was designed to incorporate two U. FL connectors, one for the transmission stage and one for the receiving stage, to overcome one of the most common measurement challenges when using surface-mount-based devices. With this modification during the design, just one additional U. FL to SMA cable was required to be introduced to the system and proceed with the measurements. As mentioned previously, the calibration step was divided into two frequency ranges; hence, the measurements also were divided into two frequency ranges with center frequencies of 865.2 MHz and 1.575 GHz respectively. Various measurements were performed to understand the behavior of the electronic circuits and their correlation with the theory. This thesis reports only the most significant findings.

4.1.2.1 Matching network measurements using the manufacturer's recommendations

The first measurement was performed using the antenna manufacturer's recommendations (*GNSS Ceramic Chip Antenna AA088*, 2020.; *ISM 868 MHz Ceramic Chip Antenna (AA701)*, 2020.) where the matching circuits are configured as displayed in Figure 4.5 and Figure 4.6.

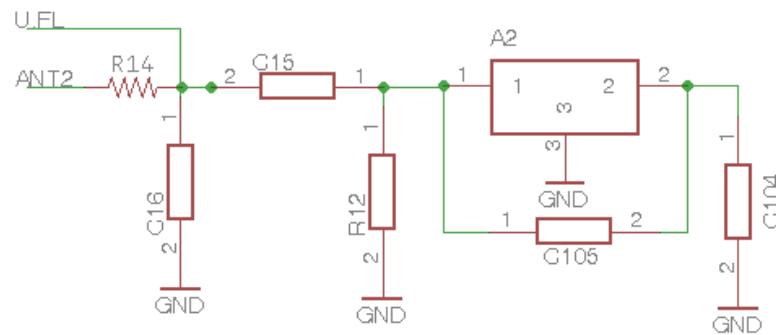
ANTENNA & TUNING 1



Component values.	
Matching circuit 1	
R1	Na
R3	2.7 nH
R2	NA
C204	3.9 pF
C205	3.0 pF
R13	Open

Figure 4.5 Initial matching network configuration RF circuit 1, transmission RF stage.
Manufacturer's recommendation

ANTENNA & TUNING 2



Component values.	
Matching circuit 2	
C16	1.5 pF
C15	2.7 pF
R12	NA
C104	3.9 pF
C105	1.0 pF
R14	Open

Figure 4.6 Initial matching network configuration RF circuit 2, receiving RF stage.
Manufacturer's recommendation

The measurements obtained from both circuits, using the manufacturer's recommended configuration, are displayed graphically in Figure 4.7, Figure 4.8, Figure 4.9, and Figure 4.10. Three fixed frequencies were considered as reference for each circuit: 863.2, 865.2 and 868 MHz for the circuit 1 (Tx) and, 1.561, 1.575 and 1.602 GHz for the circuit 2 (Rx). Additionally, the frequency at which the circuit response is better, is also displayed for both cases.

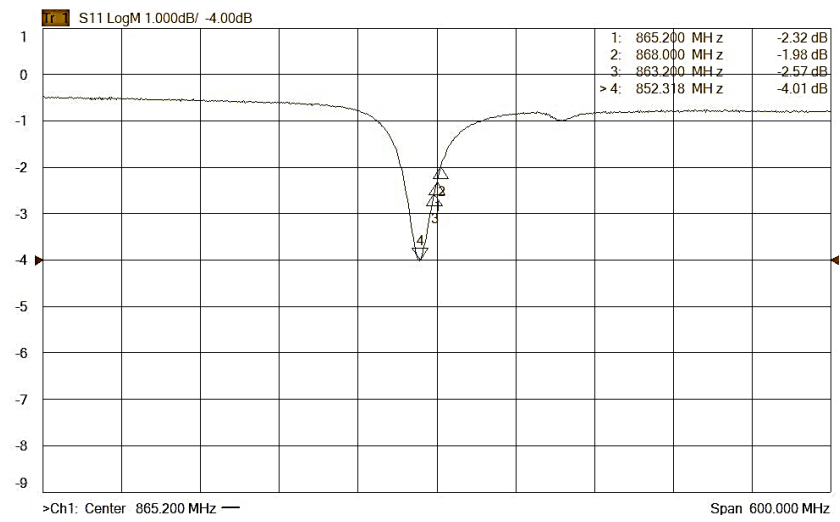


Figure 4.7 Initial measurements circuit 1, transmission RF stage. Return loss S_{11} .

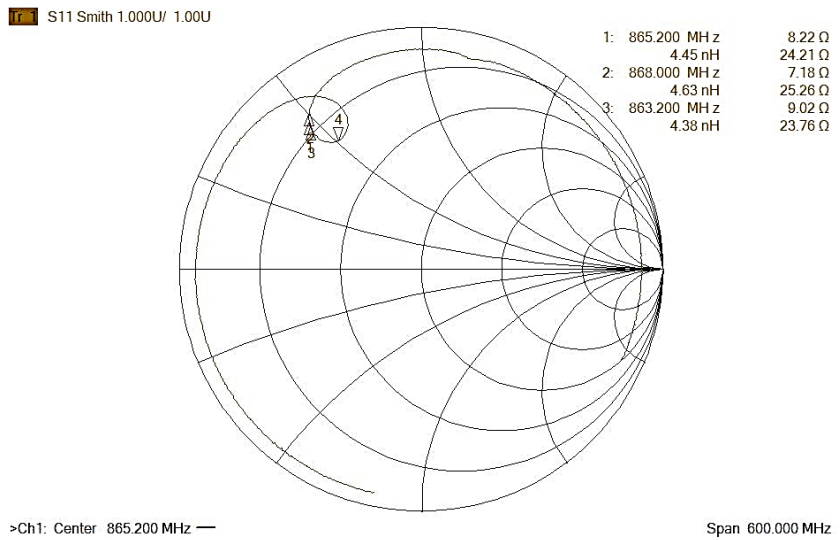


Figure 4.8 Initial measurements circuit 1, transmission RF stage. Complex impedance

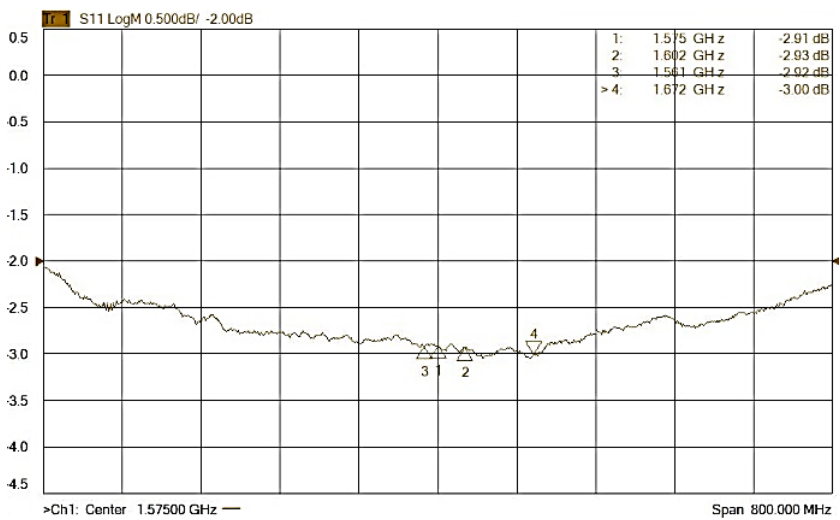


Figure 4.9 Initial measurements circuit 2, receiving RF stage. Return loss S_{11}

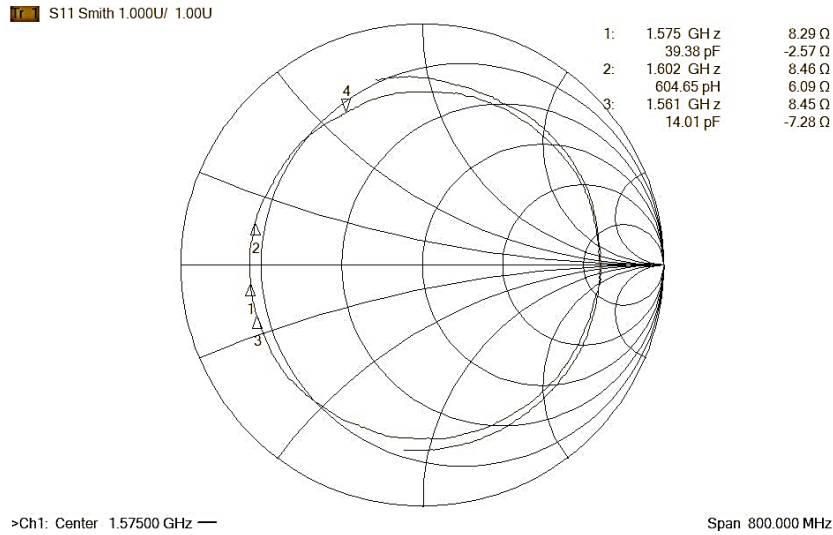


Figure 4.10 Initial measurements circuit 2, receiving RF stage. Complex impedance

From the figures above, it is possible to see that for the circuit 1 (Tx) at the three reference frequencies points, the best value in terms of S_{11} was -2.57 dB @ 863.2 MHz. While the minimum S_{11} value obtained was -4.01 dB at a resonance frequency of 852.3 MHz. In the same way, for the circuit 2 (Rx) at the three reference frequencies, the best value of S_{11} was -2.93 dB @ 1.602 GHz. While the minimum S_{11} value obtained was -3 dB at a resonance frequency of 1.672 GHz. The initial results obtained differed from the values provided as reference in the antenna datasheets mainly because the same test conditions cannot be reproduced for the radioprobe circuit. For instance, the ground plane dimension used for the specification is 80 x 40 mm, while the radioprobe ground plane dimension is 50 x 50 mm shared between the two antennas.

4.1.2.2 Antenna impedance measurements and calculation of the matching network components

Since the matching network circuit configurations recommended by the manufacturer were not suitable for the customized radioprobe circuits, the next step included the measurement of the complex antenna impedance, which is the real resistance and the imaginary reactance measured at the antenna terminals (*Application Note AN-00501.Pdf*, n.d.). For this purpose, all the shunt elements from the matching networks were removed and the series elements were replaced by 0-ohms resistances. In addition, the elements C204 and C104 were removed and replaced by 0-ohms resistances. The complex antenna impedance of both circuits, together with their respective reflection coefficients, were measured using the VNA. The obtained plots are shown in Figure 4.11, Figure 4.12, Figure 4.13 and Figure 4.14.

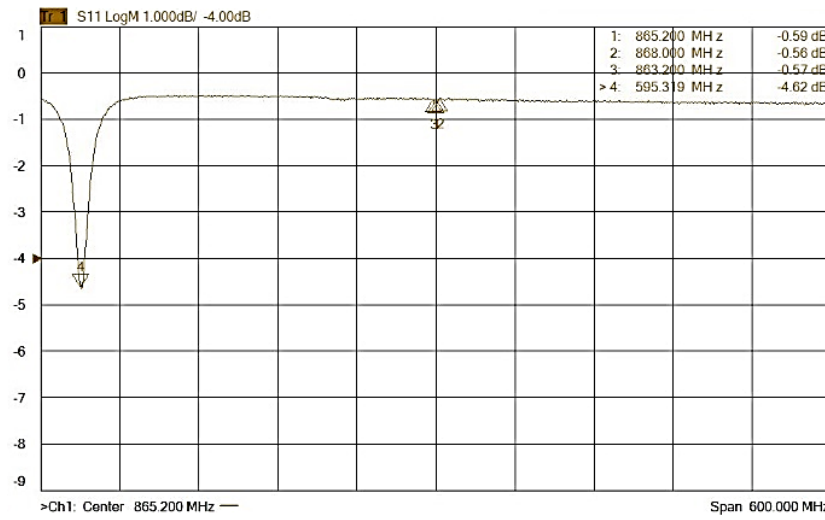


Figure 4.11 Antenna impedance measurements circuit 1, transmission RF stage. Return loss S₁₁.

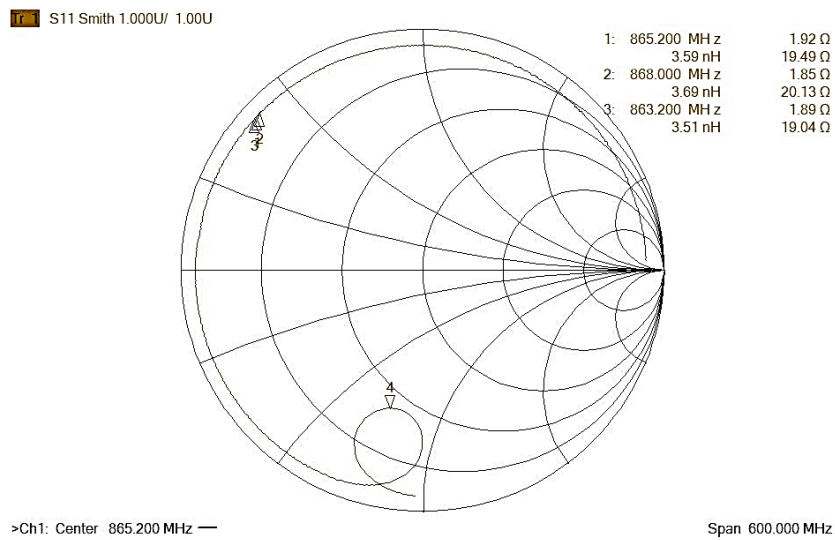


Figure 4.12 Antenna impedance measurements circuit 1, transmission RF stage. Complex impedance

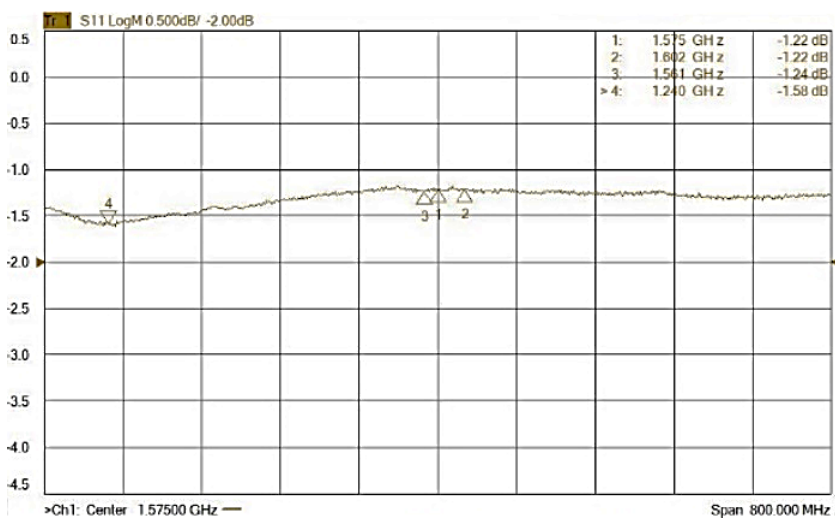


Figure 4.13 Antenna impedance measurements circuit 2, receiving RF stage. Return loss S₁₁

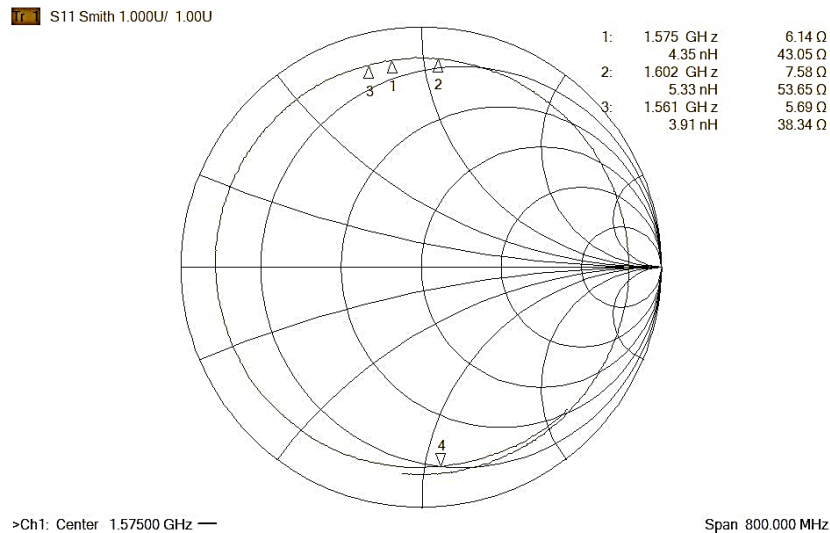


Figure 4.14 Antenna impedance measurements circuit 2, receiving RF stage. Complex impedance

Based on the above plots, it was possible to see a further change of the antenna resonance frequency towards a lower frequency for both cases when measuring only the complex antenna impedance. Also, the Smith Chart plots showed that the antenna impedances were not matched to 50 ohms, hence, improvements could be done to the circuits.

In order to improve the quality of the match between the antennas and the portion of transmission lines attached to them, the values of every component of the L-type matching networks were calculated based on the normalized load impedances obtained. Some possible solutions for the matching network component values are reported in Table 4.1 and Table 4.2.

Table 4.1 Solutions for matching network configurations. Circuit 1

Component	Value Option 1	Value Option 2	Value Option 3
R1	18.41 pF	1.84 nH	NA
R2	18.62 pF	6.32 pF	15.92 nF
R3	NA	NA	10.94 pF

Table 4.2 Solutions for matching network configurations. Circuit 2

Component	Value Option 1	Value Option 2	Value Option 3
C16	5.40 pF	1.89 nH	NA
C15	3.79 pF	1.70 pF	11.48 nH
R12	NA	NA	3.05 pF

The tables above show some possible matching network components suitable for matching the circuits' impedances; however, in real situations, there are practical restrictions to be considered. For instance, standard component values available in the market might not match the calculated ones. To continue with the experiments, the most similar components available from a RF sample kit were selected. This RF sample kit was acquired in advance for the matching and tuning

processes. It included a set of capacitors and inductors with similar electrical characteristics and different values.

Different experiments were performed in order to find the network configurations that offered the best results in terms of matching and tuning of the radioprobe RF circuits. The most suitable matching network components according to the different possible configurations were soldered on the PCBs and tested. In addition, since the design includes the supplementary TELA components (C204, C205, C104 and C105) for adjusting and improving the antenna resonance frequencies, those components were modified until reaching (or getting as close as possible) the frequency values of interest: 865.2 – 868.0 MHz and 1.575 – 1.602 GHz for both RF circuits.

As result, the most appropriate network configurations for both radioprobe front ends were found. The final complex antenna impedance and the reflection coefficients measured for both RF stages are shown in Figure 4.15, Figure 4.16, Figure 4.17 and, Figure 4.18. Table 4.3 highlights the improvements obtained from the matching and frequency tuning procedures.

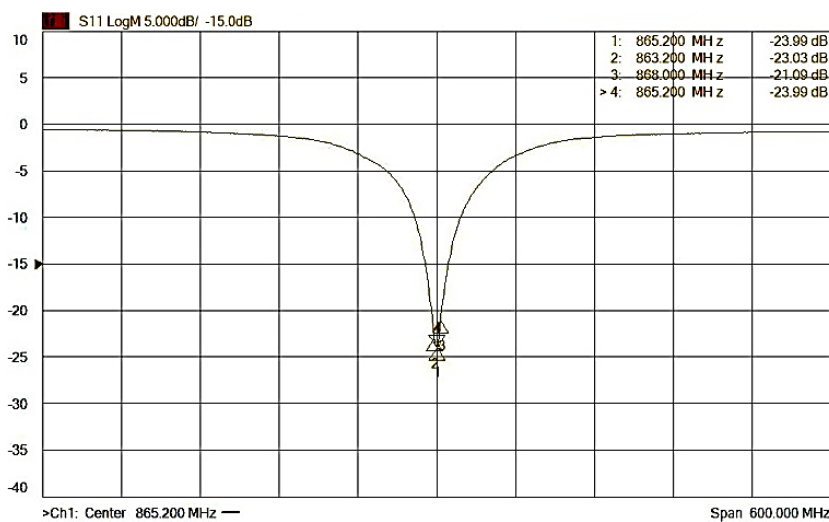


Figure 4.15 Final matching network configuration circuit 1, transmission RF stage. Return loss S_{11} .

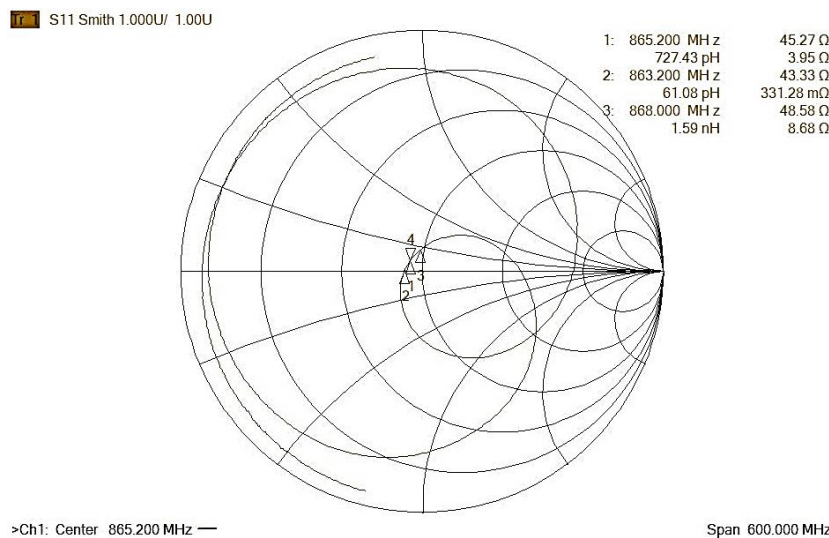


Figure 4.16 Final antenna impedance measurements circuit 1, transmission RF stage. Complex impedance

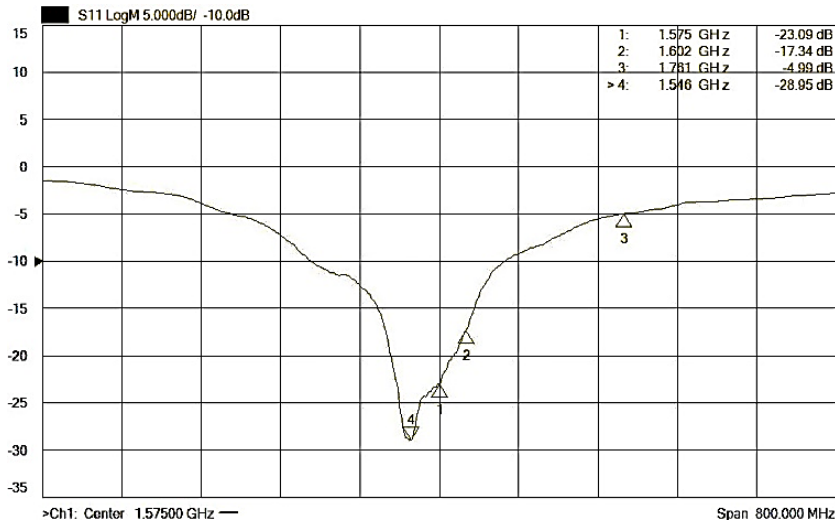


Figure 4.17 Final matching network configuration circuit 2, receiving RF stage. Return loss S11.

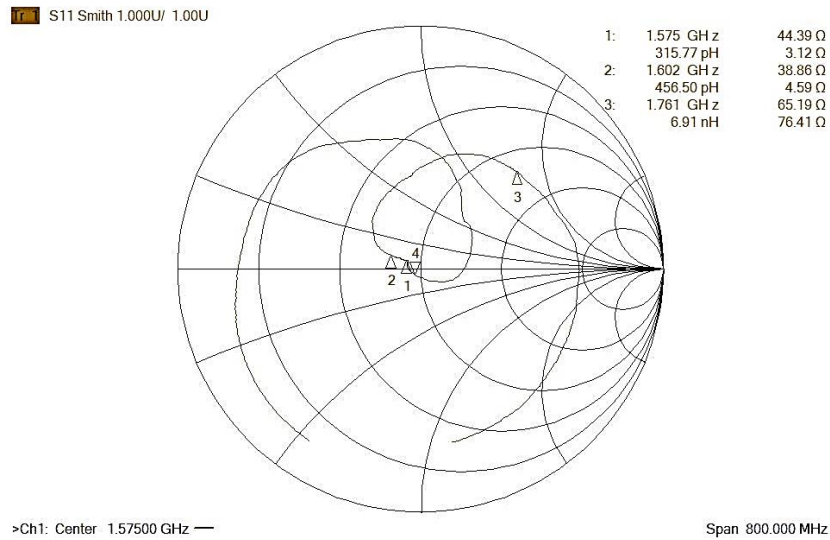


Figure 4.18 Final matching network configuration circuit 2, receiving RF stage. Complex impedance.

Table 4.3 Results of the matching and frequency-tuning procedures (Paredes Quintanilla et al., 2021)

Frequency [MHz]	Initial S ₁₁ [dB]	Final S ₁₁ [dB]
865.2	-0.59	-23.99
868.0	-0.56	-21.09
1575.0	-1.22	-23.09
1602.0	-1.22	-17.34

According to the obtained results, it is possible to see the RF performance improvements made for both RF stages. From the initial matching network

configurations to the final ones, an improvement of approximately 40 times for the transmission RF stage and an improvement of approximately 19 times for the receiving RF stage were observed. This means that the maximum power transfer in the RF units was considerably increased with the changes made. Part of this work has been published in the *Journal MDPI Sensors* (Paredes Quintanilla et al., 2021).

4.2 Data Transmission Ranges

Once the matching and frequency tuning procedures were tested and validated, the next step consisted of performing a variety of measurements to test the radiocommunication system of the radioprobes. As previously mentioned, the radiocommunication system enables the exchange of the meteorological and motion collected data at the radioprobe side towards the ground stations using radiofrequency signals. Due to the constraints of the present design, LoRa, which features power-saving and long-range characteristics, has been selected and incorporated into the system. For validation purposes, different network configurations were established to determine the transmission ranges that can be reached by the system. The following subsections report the most relevant tests made, together with the most significant findings.

4.2.1 Test 1

This test comprised propagation measurements in an urban environment using a point-to-point network configuration at close distances (setup 1). It was performed at the rooftop of the DET of POLITO in order to determine the correct operation of the fully integrated radioprobe's transmission system. The network included a radioprobe sending periodically a counter packet and, a ground station receiving the messages. The aim of the counter was to identify possible losses of packets having a known progressive number in the data frame. Before starting the measurements, a rapid test to verify the transmitter operation was performed using the R&S ZVL SA close to the transmitting radioprobe. The presence of the signal's power spectrum was verified as shown in Figure 4.19.

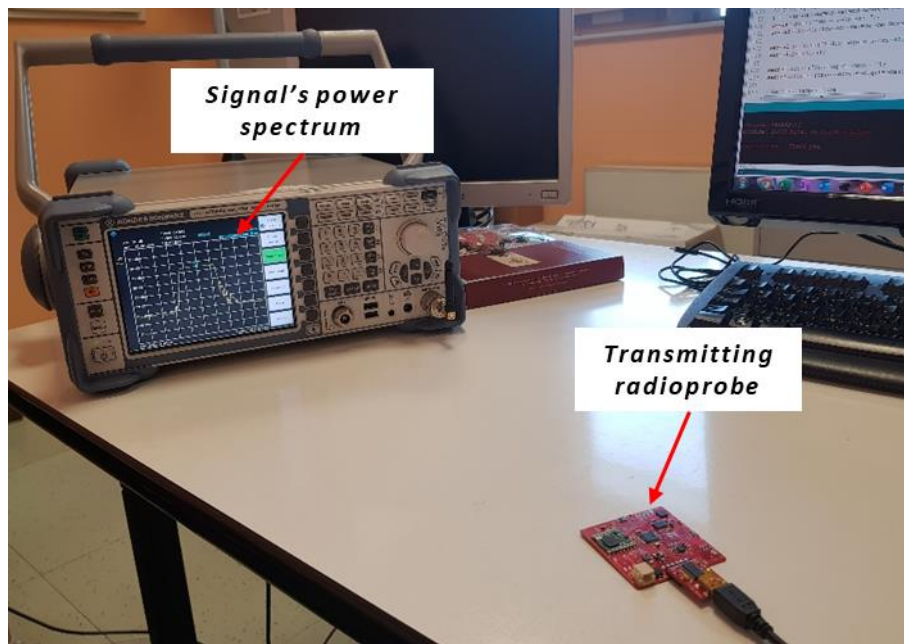


Figure 4.19 Test to verify the power spectrum of the transmitted signal

The transmitter was located at four different positions P1, P2, P3, P4 and the receiver was located at a fixed position Rx. The packets were received with both, the receiving station, and the R&S ZVL SA. The receiver module was programmed in order to provide useful information about the signal quality, for instance, Signal-to-Noise ratio SNR, Received Signal Strength Indicator RSSI of the packets, and Received Signal Strength Indicator mean. For this test, the radioprobe electronics was powered-on through its FTDI programmer, which was connected directly to a laptop. The tests were made using a programmed output power of 5 dBm, a central frequency of 865.2 MHz, a spreading factor of 10, and a bandwidth of 125 kHz. The fixed location of the receiving station plus the SA and, the different positions of the transmitter are shown in Figure 4.20. Some pictures of the test are displayed in Figure 4.21.

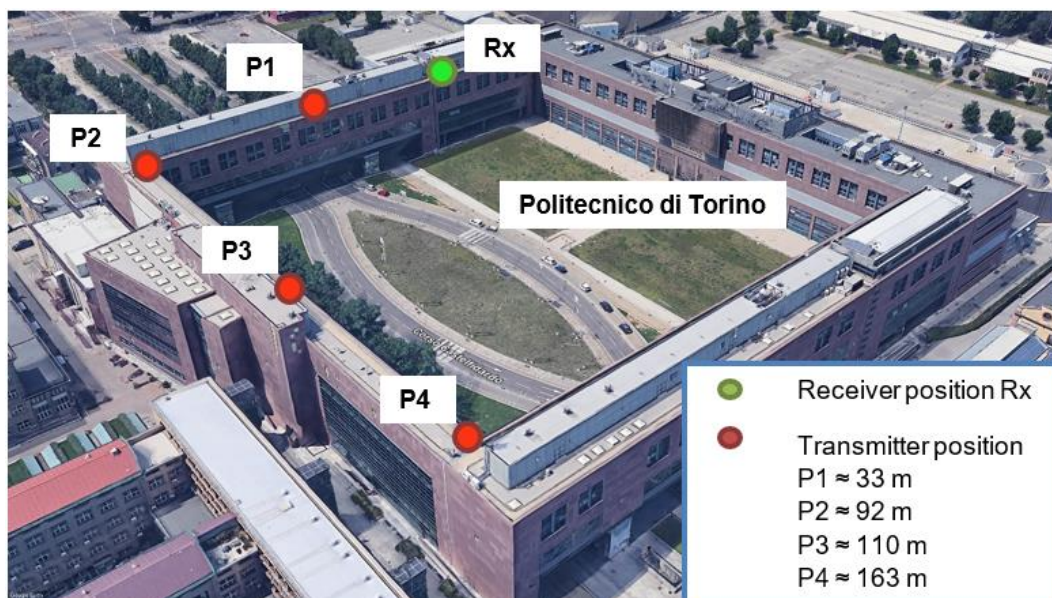


Figure 4.20 System setup 1. Point-to-point configuration used to determine the transmission ranges reached by the communication system in an open urban environment, displayed on a map. Transmitter (P1 to P4) and receiver (Rx) positions, with relative distance indications. Google earth view.

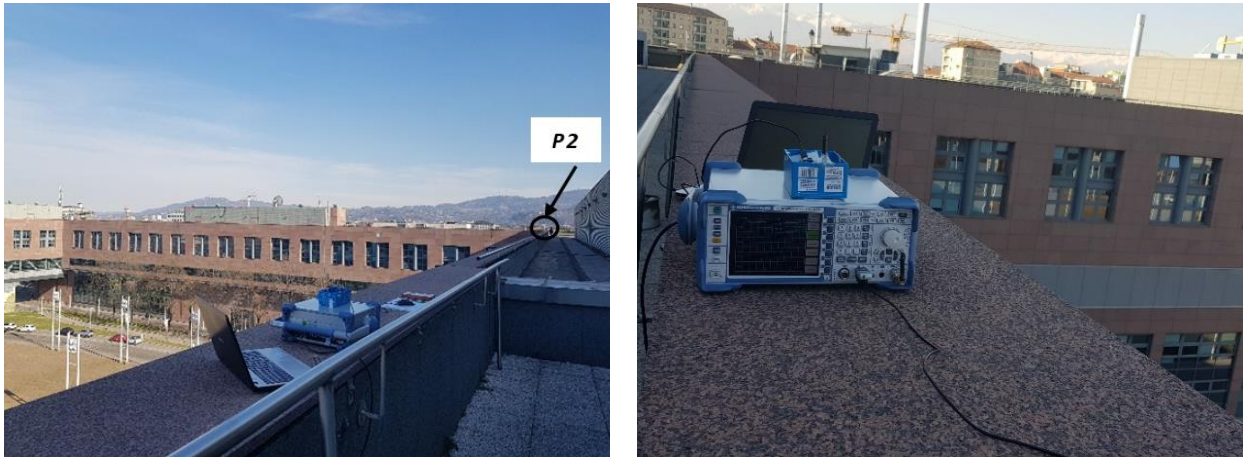


Figure 4.21 Some pictures of the outdoor communication test. Left: Location of the transmitter position at P2. Right: Location of receiving station and Spectrum Analyzer. DET POLITO. Rooftop

After processing the data obtained from the set of measurements at different short distances, the propagation results and statistics for the positions P1, P2, P3 and P4 are shown in Figure 4.22, Figure 4.23, Figure 4.24, and Figure 4.25 respectively. The data frame sent through the radio link included a counter from 0 to 50. The set of data analyzed considers 51 packets per each position. The counter packets were sent every second.

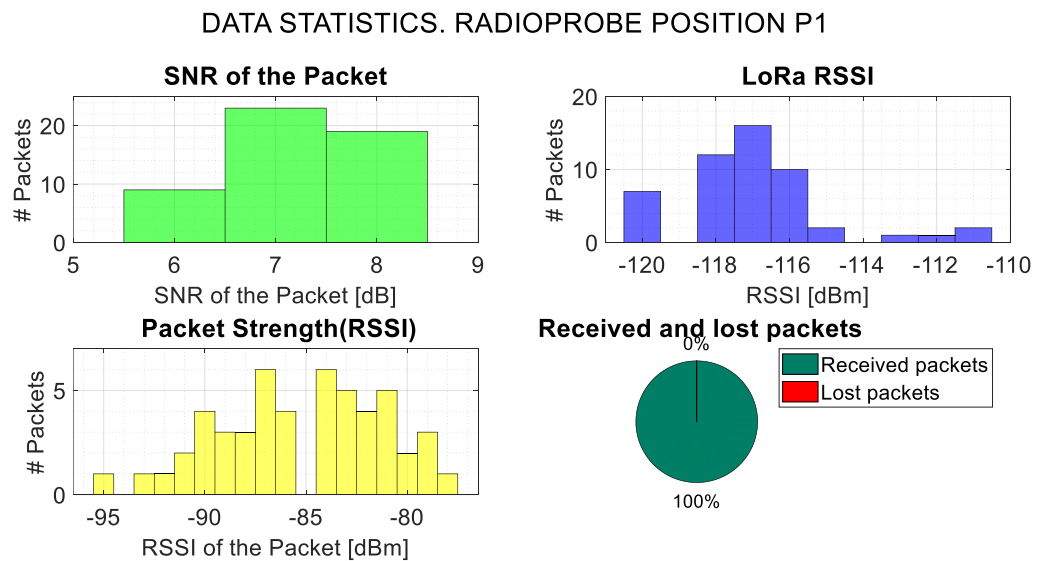


Figure 4.22 Data statistics System setup test 1. Transmitter position P1

DATA STATISTICS. RADIOPROBE POSITION P2

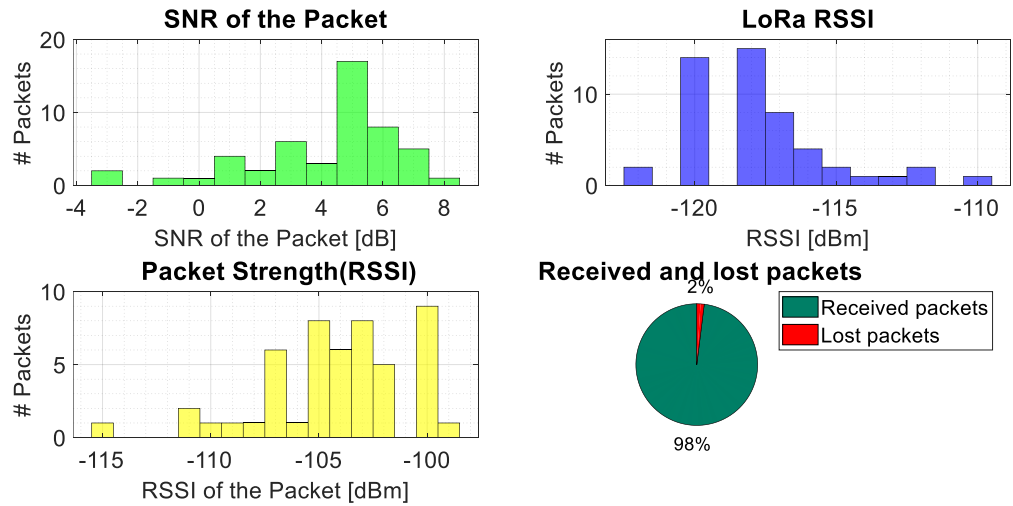


Figure 4.23 Data statistics System setup test 1. Transmitter position P2

DATA STATISTICS. RADIOPROBE POSITION P3

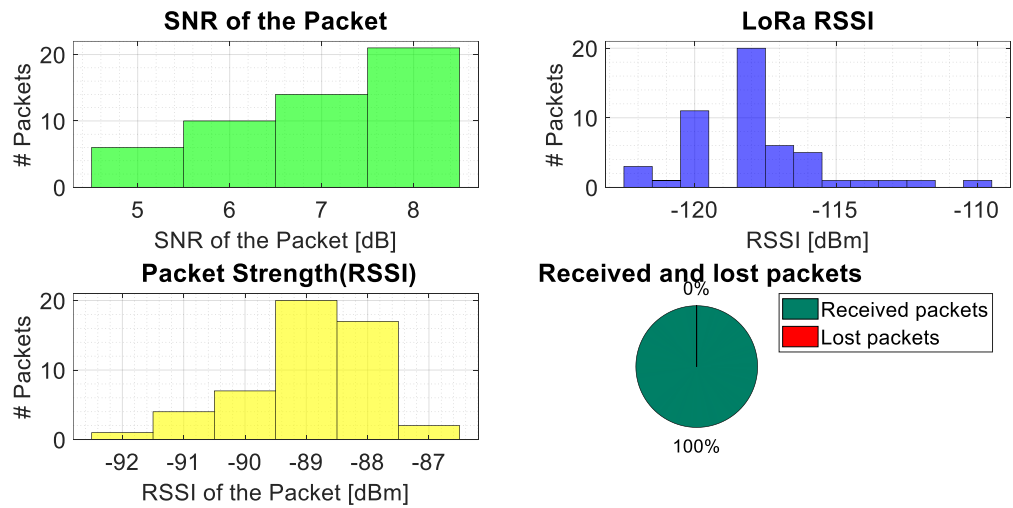


Figure 4.24 Data statistics System setup test 1. Transmitter position P3

DATA STATISTICS. RADIOPROBE POSITION P4

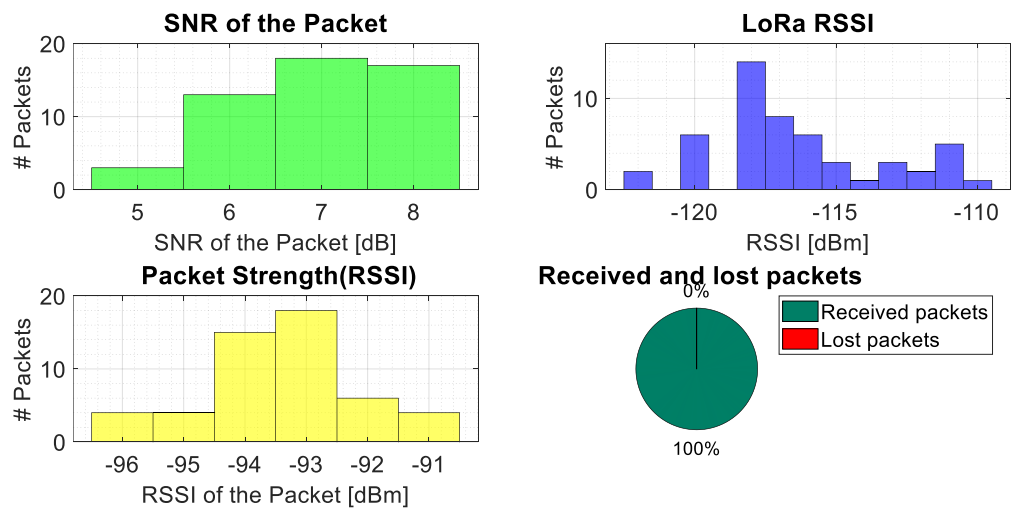


Figure 4.25 Data statistics System setup test 1. Transmitter position P4

As result of this set of propagation measurements, some short transmission links were tested at four different positions ranging in distance between the receiver and the transmitter from 33 to 163 meters. As expected, the RF transmission links worked well at close distances even if the transmitted power was low. From the analyzed data, it is possible to see that, for most of the positions, the SNR of the transmitted signals was positive, and the totality of packets was received. Only for the position P2, one transmitted packet was lost. This can be observed also in the negative SNR values and lower RSSI of the packets for some transmissions at this position. The signal could have been affected by a metallic structure placed below the path between the transmitter at P2 and the receiver. These first measurements provided an idea of the operation of the fully integrated radioprobe in an urban environment.

4.2.2 Test 2

This test also included propagation measurements in an urban environment using a point-to-point static network configuration (setup 2) but, in contrast with the previous test, this second test included longer distances between the transmitter and the receiver. It was performed at POLITO and its surroundings. The network setup consisted of a radioprobe generating and sending periodically a counter message including a unique sensor identification and a ground station acquired the packets. Again, the counter was created specifically to determine possible losses of the packets sent by the transmitter. The transmitter was placed at eight different locations from P1 to P8 along Corso Castelfidardo and Corso Inghilterra, while the receiver was located at a fixed position Rx on the third floor of the DET of POLITO. In addition, a SA model R&S ZVL was part of the measuring setup at the receiver point; however, for nearly all the tested locations, the instrument's noise floor was significantly higher than the inward signal, thus the measurement of the power spectrum was not possible. This behavior highlights the robustness of the communication technology and the window opportunity to build communication channels in demanding environments such as urban areas. Same as before, the receiver device was configured to deliver signal quality information such as SNR and RSSI of the packets. The distance between the transmitter and the receiver varied from 138 m for P1 to 1232 m for P8. The receiver was located at a height of approximately 17 m above the street level. In most of the positions, there was an obstructed line-of-sight between the receiver and the radioprobe's transmitter. The configuration set to the transmitter is as follow: output power 10 dBm, central frequency 865.2 MHz, spreading factor 10, and bandwidth 125 kHz. The data taken for the analysis consisted of data blocks, each one of 200 packets. The various positions of the transmitter, and the stationary position of the ground station together with the SA, are shown in the map in Figure 4.26. Some pictures of the test

are displayed in Figure 4.27. The results of the measurements are reported in Table 4.4.

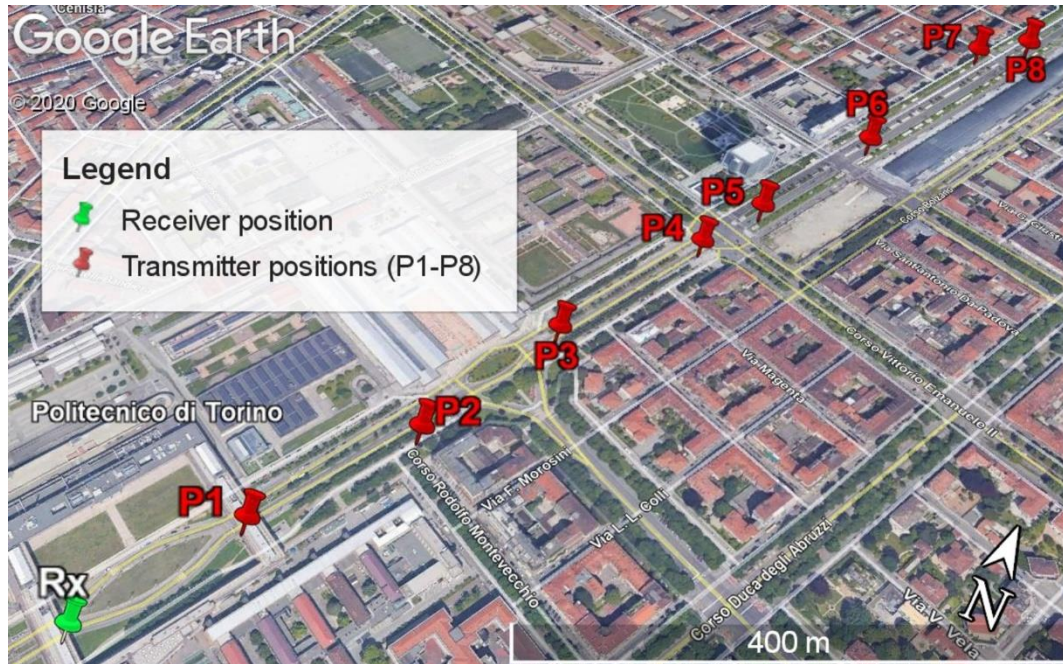


Figure 4.26 System setup 2. Point-to-point topology configuration used to determine the transmission ranges reached by the communication system in an urban environment, displayed on a map. Transmitter (P1 to P8) and receiver (Rx) positions. Google earth view (Paredes Quintanilla et al., 2021)



Figure 4.27 Some pictures of the point-to-point communication test. Left: Location of the transmitter at P1. Right: Receiving station placed at the third floor of the DET POLITO.

Table 4.4 Results of the point-to-point communication setup in an outdoor urban environment.

Position	Distance [m]	SNR mean [dB]	RSSI mean [dBm]	Received packets [%]
P1	138	7	-94.9	100.0
P2	280	1.8	-113.1	99.5
P3	455	-7.1	-123.4	99.5
P4	648	-9.1	-123.9	77.8
P5	737	-2.0	-120.2	99.5
P6	905	-8.9	-124.9	96.0
P7	1173	-13.0	-121.8	95.5

P8	1232	-12.4	-124.2	52.0
----	------	-------	--------	------

The information obtained from this test provided valuable information of the transmission ranges that the radioprobe's communication link can reach in a built-up area where partial or total block of the Fresnel zone exists. Several positions with different distances between the transmitter and the receiver were tested; however, the closest eight ones (P1 to P8) were picked for the present analysis because their received packet percentage was greater than 50 %. In most cases, the communication channel was affected by direct or total shielding and reflections from the surrounding environment, which is a typical propagation problem for urban areas. From Table 4.4 it is possible to see that for many points, the signal's SNR presented negative values, meaning that the signal power level was below the noise level (*SX1272/3/6/7/8: LoRa Modem* / *SEMTECH*, n.d.) . This behavior confirms the robustness of LoRa technology to work adequately in challenging environments. Although, the RSSI value was influenced by the LOS obstruction and the distance growth between the sender and the receiver, for most of the positions, the received packet percentage was greater than 95 %. Even though the final goal of the radioprobe system design is the operation under different environment conditions (open, free-of-obstacle environments), this test revealed significant insights about the possible transmission ranges that the flying radioprobe can reach when floating in the free atmosphere.

4.2.3 Test 3

A third field measurement included propagation measurements using a point-to-point dynamic network configuration in an open area environment (Setup 3). Unlike the previous experiments, the radiosonde transmitting the information was attached to a land remotely controlled UAV (drone) to simulate similar conditions in which the radioprobes will be released. This test was carried out in a small town called Isola d'Asti, which is in the Piedmont Region at the north of Italy. The network setup included a fully operational radioprobe gathering, processing, packing, and transmitting the information from the different sensors and, a ground station receiving, storing and post-processing the received messages. Furthermore, and additional PC was placed at the ground side to receive and collect the flight logs transmitted by the UAV during its flight, which were useful for the comparison of the radioprobe's data collected.

The radioprobe was attached to the bottom support of an eight propeller UAV called OCTOCOPTER from Envisens Technologies. It is a large payload capacity aircraft able to carry up to 2.5 kg and has a flight time up to 40 minutes (without payload weight). It can be piloted both manually and in autopilot mode. In manual mode, the UAV is controlled in real time by a remote operator via a secure wireless connection. This operating mode allows also to keep the unmanned aircraft flying at a constant altitude or remaining in the same position. In autopilot mode, the UAV

can follow a predefined track and execute preset commands. It can reach heights over 2000 m above the ground level and is equipped with different sensors for navigation such as accelerometer, magnetometer, barometer and GPS receiver; the latest used as reference source of the trajectory tracking and positioning sensors. The UAV was controlled to flight in an open space carrying the radioprobe board.

The radiosonde microcontroller was programmed to start reading, managing, and packing the data from the TPH sensors after some minutes after the system start. Then, the information collected, together with the counter messages, was transmitted wirelessly to the ground station through the dedicated radio link. At the other side of the communication system, two ground stations were configured to receive, store, partially process and display the received information. Since this set of measurements were carried out in a non-obstructed rural environment, the transmitter was in LOS with the receivers at all positions. The transceiver was programmed to provide 14 dBm as output power, with central frequency 865.2MHz, spreading factor of 10, and a bandwidth of 125kHz.

The UAV flew few times; however, for the present analysis, the two intervals of time at which the UAV reached the highest altitudes are considered: the first-time interval of approximately 6 minutes, and the second time interval of approximately 16 minutes. The system setup is displayed in Figure 4.28. Some pictures of the experiment are shown in Figure 4.29.

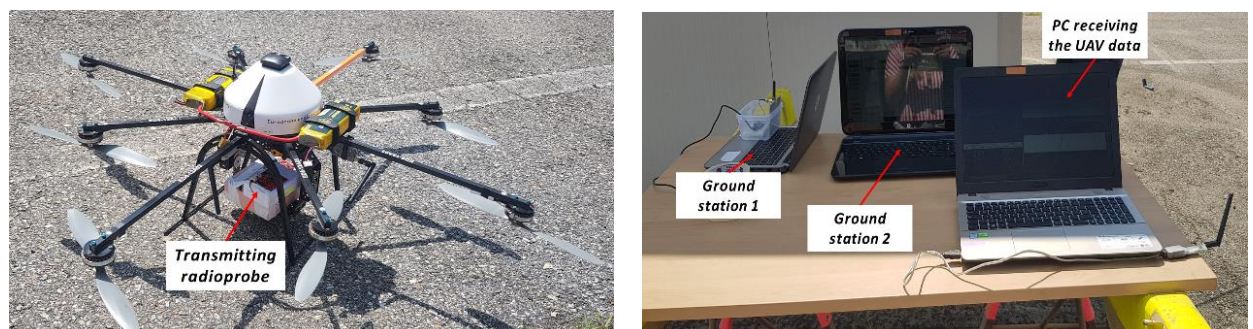


Figure 4.28 System setup test 3. Point-to-point dynamic communication test using an UAV. Left: UAV holding the radioprobe. Right: Radioprobe ground stations and PC receiving the UAV data.



Figure 4.29 Some pictures of the point-to-point dynamic communication test using an UAV

The relative altitude with respect to the ground level reached by the system (UAV + radioprobe) during both time intervals are presented in Figure 4.30.

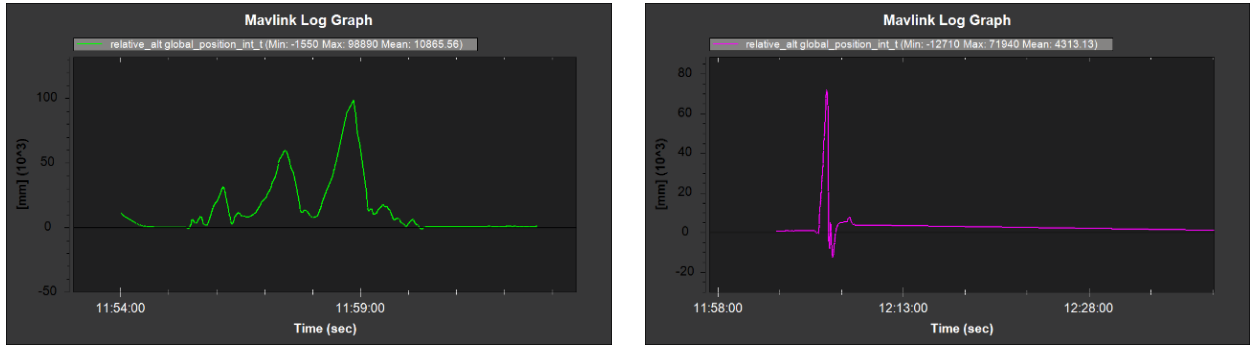


Figure 4.30 Relative altitude reached by the UAV carrying the radioprobe. Left: First time interval. Right: Second time interval. Mission planner plots.

The results of the radioprobe communication measurements are shown in Table 4.5.

Table 4.5 Results of the point-to-point dynamic communication setup in an outdoor environment

Flight interval [#]	Max. altitude [m]	SNR mean [dB]	RSSI mean [dBm]	Transmitted packets [#]	Received packets [#]	Received packets [%]
1	102	7.1	-71.3	69	67	98.0
2	72	7.2	-80.6	425	425	100.0

During this test, the drone covered an area of approximately 50 m by 30 m and reached maximum altitudes of 102 m and 72 m during the first and second flights respectively. In total, 492 packets were sent from the radiosonde during these intervals. Since the distances between the receiver and the transmitter were relatively close, the SNR values were higher than 7 dB and the RSSI values were greater than -80 dBm. In addition, most of the transmitted packets were received at the ground side. This test provided useful information about the radioprobe communication technology when working in a dynamic open area environment similar to the escenary in which the final instrumented balloons will work.

4.2.4 Test 4

In a similar way, another open area field test using a point-to-point dynamic network configuration (Setup 4) was done to establish the maximum transmission coverage that the radioprobe system can reach. In contrast to the previous test using a UAV to carry the radioprobe electronic system, this time an automatic atmospheric sounding system was used as means of transportation into the atmosphere. This test was carried out at the Cuneo Airport facilities, where the Cuneo - Levaldigi meteorological station (LIMZ) of the Regional Agency for the Protection of the Environment (ARPA) of the Piedmont Region – Italy, is located (Figure 4.31). Twice a day, this automatic atmospheric radio sounding system launches an atmospheric balloon to vertically profile the troposphere and the lower

stratosphere, up to about 30 km of altitude (*Sistema automatico di radiosondaggio dell'atmosfera* | Arpa Piemonte, n.d.).

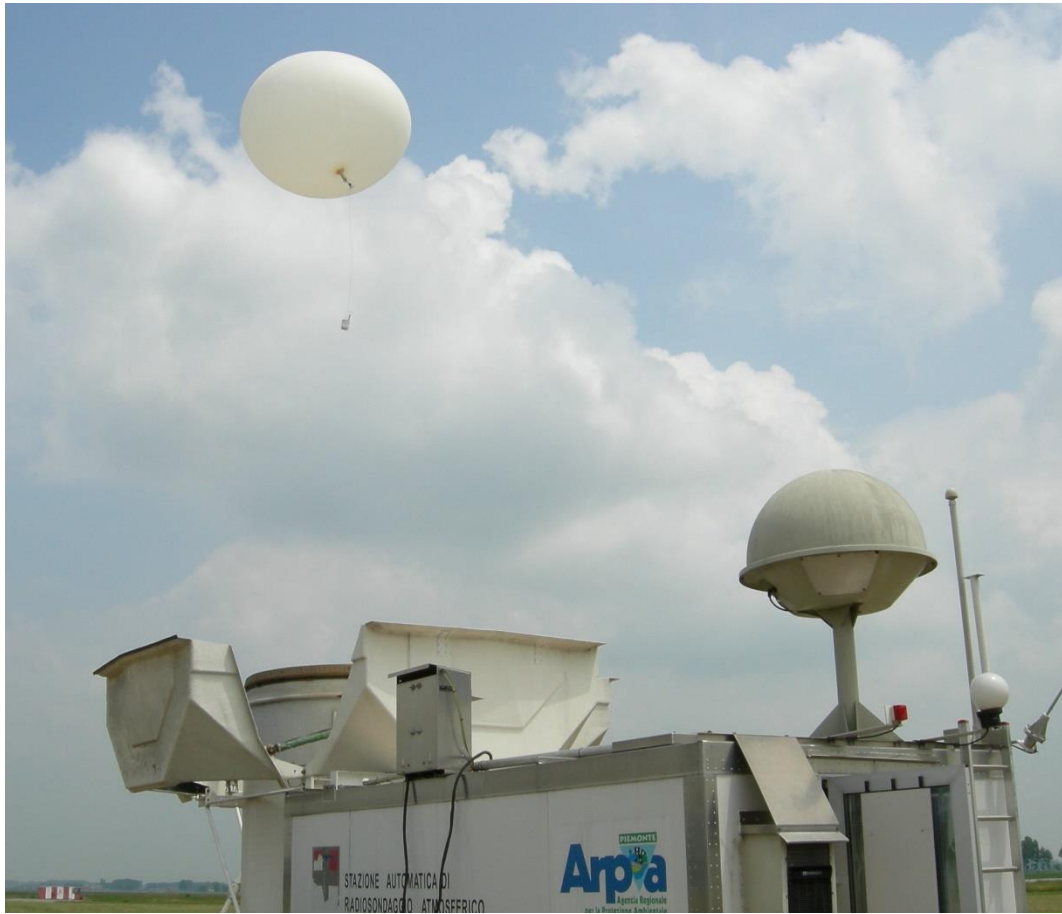


Figure 4.31 Automatic atmospheric sounding system. Cuneo - Levaldigi meteorological station (LIMZ) (*Sistema automatico di radiosondaggio dell'atmosfera* | Arpa Piemonte, n.d.)

The system setup for this test included an automatic sounding station, which is a weather observation system that allows up to 24 automatic soundings (*Automatic Sounding Station*, n.d.). It includes a sounding station and the balloon filling unit. The Helium-inflated observation balloon used had approximately 1.5 m of diameter. It tethered a Vaisala RS41 radiosonde through a polypropylene transparent string. This radiosonde, which was used as reference instrument, was equipped with different sensors to measure humidity, temperature, and atmospheric pressure along its pass across the atmosphere. It also incorporated a GPS receiver that allowed the estimation of wind velocity and direction. The gathered data was sent to ground via a long-range telemetry link up to 350 km using the frequency band in the range from 400.15 MHz to 406 MHz (*Vaisala Radiosonde RS41-SG / VAISALA*, n.d.). The atmospheric system had an ascending rate of about 300 m/min and achieved its maximum height in approximately 1.5 hours. The output of this atmospheric sounding system is used for meteorological forecasting and analysis purposes.

The radioprobe's network setup consisted of a fully operational radioprobe measuring, pre-processing, managing, and sending the information generated during the air travel, and a ground station gathering, storing, and partially

processing the received data packets. The mini radioprobe was adhered to the VAISALA's front cover with the help of a non-conductive adhesive tape. To reserve energy for the flight, the radioprobe was initialized just before the launch. The ground station was placed next to the sounding workstation. The system setup is displayed in Figure 4.32 and Figure 4.33.

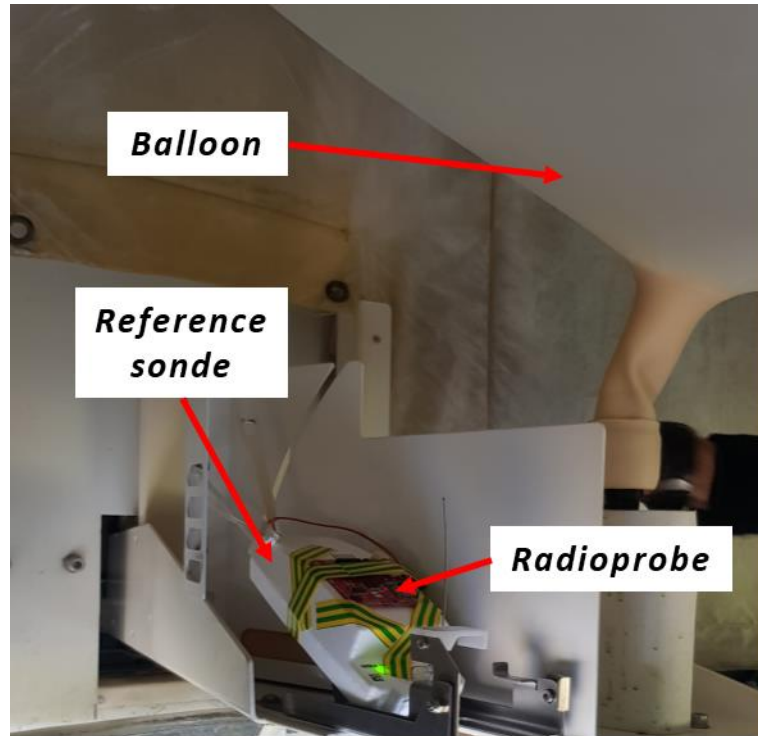


Figure 4.32 Mini radioprobe adhered to the reference atmospheric sounding system.

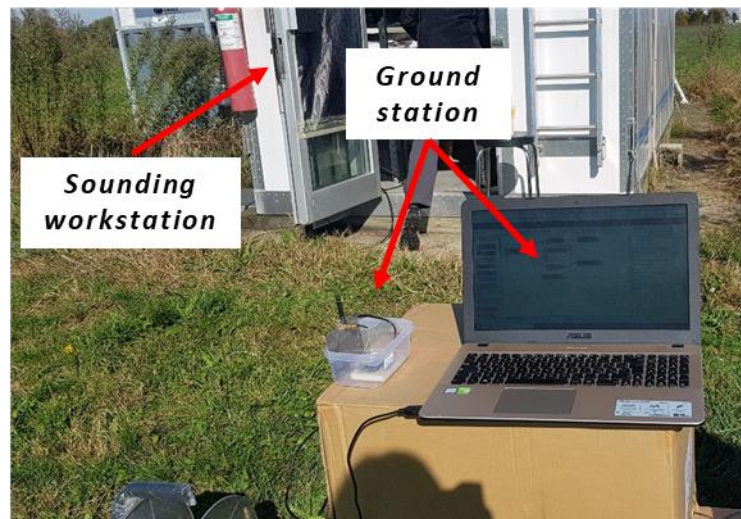


Figure 4.33 Radioprobe ground station.

The radioprobe transmitter was set to deliver a 14 dBm of output power, working at a frequency of 865.2 MHz, using a bandwidth of 125 KHz and a spreading factor of 10. Given that the test was performed in a totally open area, there was LOS between the receiver and the transmitter at almost all positions. The trajectory followed by the systems until receiving the last message coming from the

radioprobe, and the separation distance reached are displayed in Figure 4.34. The obtained results regarding the communication system are reported in Table 4.6.

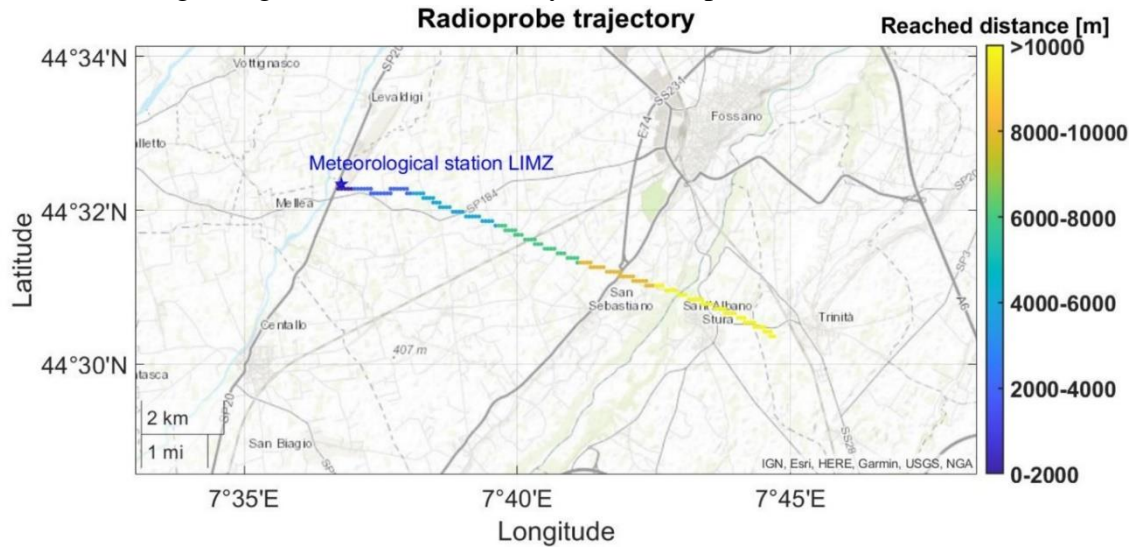


Figure 4.34 Trajectory followed by the systems: mini radioprobe and sounding balloon, displayed on a map. The separation distance with respect to the ground station is indicated by the color bar.

Table 4.6 Results of the point-to-point communication setup in an open area environment (Paredes Quintanilla et al., 2021)

Distance [m]	SNR mean [dB]	RSSI mean [dBm]	Total transmitted packets [#]	Received packets [#]	Received packets [%]
Up to 1000	5	-95	40	37	92.5
Up to 2000	4	-99	103	98	95.2
Up to 3000	2	-102	156	146	93.6
Up to 4000	2	-103	210	196	93.3
Up to 5000	1	-104	243	226	93.0
Up to 6000	1	-104	276	240	87.0
Up to 7000	0	-105	297	259	87.2
Up to 8000	0	-105	322	283	87.9
Up to 9000	-1	-106	348	294	84.5
Up to 10000	-1	-106	376	296	78.7
Up to 11000	-1	-106	449	297	66.2
Up to 14000	-1	-106	462	298	64.5

The outcomes of these propagation tests allowed determining the maximum transmission ranges that can be achieved by the radioprobe communication system when working in a dynamic real-atmosphere environment. During this test, the reference atmospheric sounding system outreached a peak height of about 32 km, a horizontal extent of about 108 km, and a straight distance of about 113 km with respect to the ground system previous the explosion of the balloon. While the mini radioprobe achieved a peak height of about 11 km, a horizontal extent of about 7 km, and a straight distance of about 14 km with respect to the ground system before losing communication with ground. After the system launch and before the loss of communication, the tiny radioprobe was able to send 462 data packets for a time

frame of about 22 minutes. From Table 4.6, it is possible to see that the variability of the SNR values fluctuated from +5 dB at the closest separations to -1 dB at the farthest ones. In the same way, the RSSI values underwent a decrease while the separation distance with ground increased, ranging from -95 dBm to -106 dBm for the minimum and maximum, respectively. Due to the high rising velocity of the sounding system, there were occasional packet losses; however, the percentage of correctly received packets for the initial 5 km was greater than 90 %, which is a good indicator for the observation heights required for warm clouds (within 1 and 2 km) having less intense fluctuation velocities. In addition, even though the reference atmospheric sounding system was meant to vertically profile the troposphere and the low stratosphere, and not for warm cloud conditions, it provided a significant reference to assess the radioprobe system when subject to a dynamic obstacle-free atmosphere environment.

During this test, meteorological data along the system trajectory (atmospheric balloon and tiny radioprobe board) was also collected. See more details in section 4.3.3.

Part of this work has been published in the *Journal MDPI Sensors* (Paredes Quintanilla et al., 2021).

4.3 Sensor Measurements

After validating the radio communication system of the mini radioprobes, the next step consisted of conducting some tests to verify the correct operation of the sensors nested within the tiny device. As previously mentioned, each radioprobe embeds a “temperature, pressure and humidity sensor stage”, and a “positioning and tracking sensor stage” (See subsection 3.2.3: Electronic system configuration). These both electronic units include a set of sensors (temperature, pressure, humidity, IMU, and GNSS receiver) to measure different parameters during the radioprobe flight across the atmosphere of warm clouds. The circuitry of both units integrated in this first design are shown in Figure 4.35.

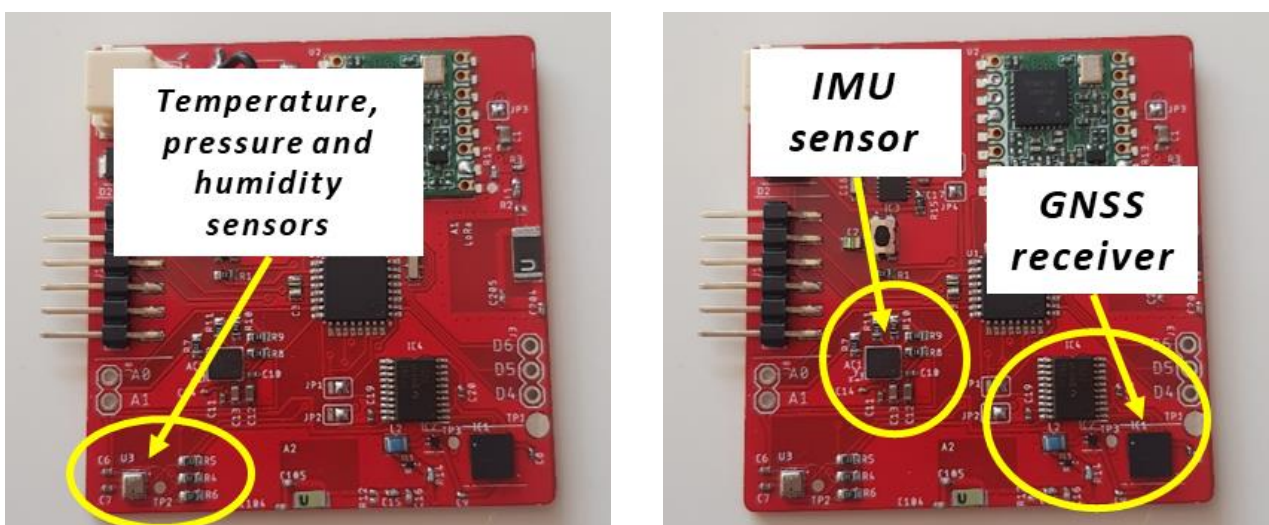


Figure 4.35 Radioprobe sensors. Left side: TPH sensor stage. Right side: positioning and tracking sensor stage.

Several test were made to test, optimize, and validate these operational units, either together or separately. Due to the global COVID-19 Coronavirus Pandemic, the first part of the tests was made in a non-controlled environment using the resources available at the time. Later, additional resources were used based on their availability. The following subsections report the most relevant experiments, together the most significant findings.

4.3.1 Test 1: Temperature, pressure, and humidity sensors unit

Once the visual inspection and electrical tests were performed following the manufacturing process of the first radioprobe prototype, the very first step consisted of testing the programming code used to control the temperature, humidity, and pressure sensors integrated in the BME280 unit. To this end, the previously developed algorithm to command the sensors was uploaded to the radioprobe's microcontroller using the I²C communication protocol. For these testing purposes, the microcontroller was programmed to enable the BME280 device to perform measurements of temperature, pressure, and humidity at an established period of 1 second. In addition, an estimation of the relative altitude was calculated from the measurements. The sensor mode used was the normal one, which comprises perpetual cycles of measurements and inactive periods (*BME280 / BOSCH*, n.d.).

As mentioned previously, due to the global COVID-19 Coronavirus Pandemic, the first sets of measurements reported in this subsection were carried out in a non-controlled urban real environment, both indoors and outdoors. Since the resources available at the time were limited, the experiments were performed to compare the sensor readings between pairs of radioprobes, in total 8, hereinafter called Radioprobe 1, 2, 3, 4, 5, 6, 7 and 8. Subsequently, these measurements were compared to the available reference data coming from the data base on local climatic parameters provided by the Istituto Nazionale di Ricerca Metrologica (INRiM) (*Parametri Ambientali / INRiM*, n.d.). The separation distance between the meteorological station acquiring the reference data and the test position was about 11 km.

The experiment setup (Figure 4.36) consisted in a pair of radioprobe boards, each one containing a TPH sensor unit, connected to a PC through a FTDI breakout board. The PC included the software tools for updating the programming code to the microcontroller and visualizing the readings. The data was collected through the serial monitor of Arduino platform at a data rate of 115200 Hz, and then stored for further analysis.

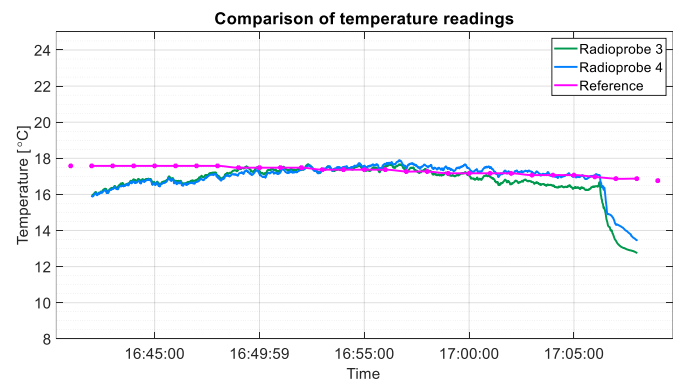
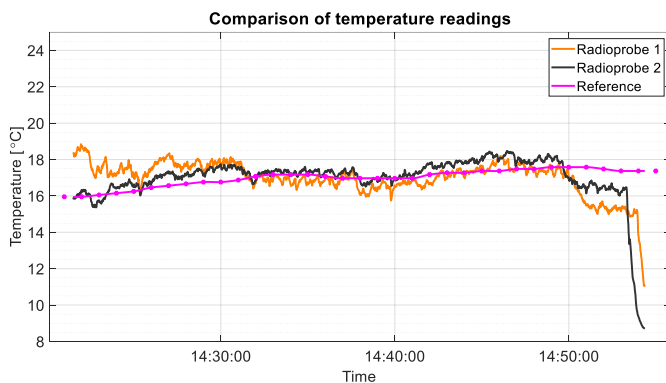


Figure 4.36 Test setup for the measurement of temperature, pressure, relative humidity and altitude estimation. Left side: Pair of measuring radioprobes. Right side: System setup.

Since the sampling frequency of the reference data was different from the sampling frequency used for the experiment, interpolation techniques for matching all the query points and statistically comparing the obtained data were tested using the numerical computing environment Matlab. After comparing some interpolation techniques such as linear, pchip, spline, nearest, next and makima, the last one provided the best results when following the trend of the data. Makima is a Matlab interpolation technique based on the Akima interpolation (*Interp1* / MathWorks, n.d.). The Makima method gives fits to curves where the second derivative is rapidly varying. The interpolated values at the query points are given based on polynomials functions.

The local temperature used as reference during this experiment varied from 13.8 °C to 17.9 °C with a margin error of ± 0.14 °C. The barometric pressure varied from 999.7 hPa to 1000.3 hPa with a margin error of ± 0.17 hPa. The relative humidity range was from 32.0 % to 49.7 % with a margin error of ± 2.5 %.

The graphical comparison between roughly calibrated data readings from the radioprobe pairs against the reference data values obtained from INRiM, are shown in Figure 4.37, Figure 4.38, Figure 4.39, and Figure 4.40, for temperature, pressure, humidity and approximated altitude respectively. The statistical results of the whole set of measurements are summarized in Table 4.7, Table 4.8, Table 4.9, and Table 4.10.



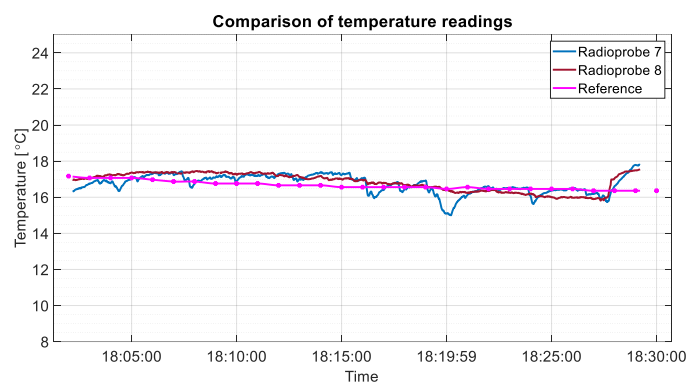
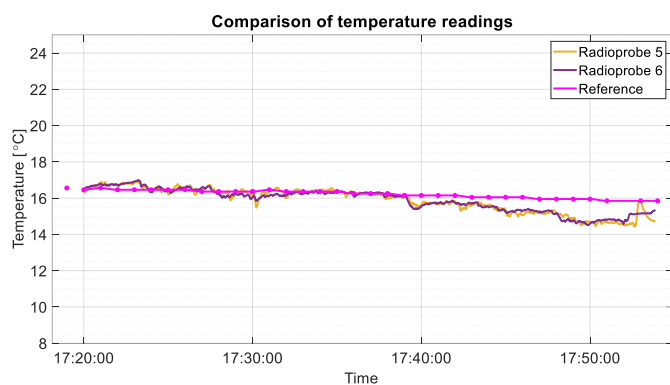


Figure 4.37 Ambient temperature comparison between radioprobe sensor readings and reference readings. Top left: pairs radioprobe 1 and radioprobe 2. Top right: pairs radioprobe 3 and radioprobe 4. Bottom left: pairs radioprobe 5 and radioprobe 6. Bottom right: pairs radioprobe 7 and radioprobe 8.

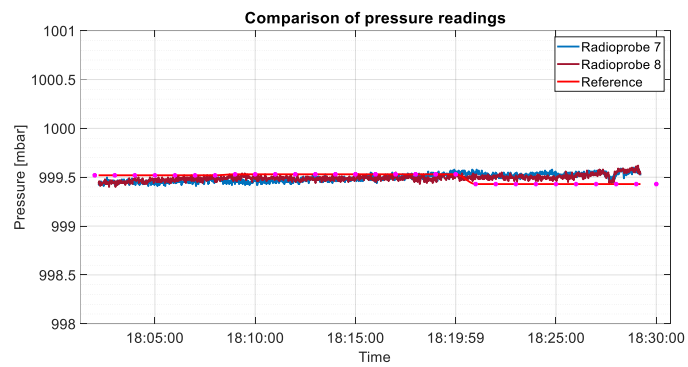
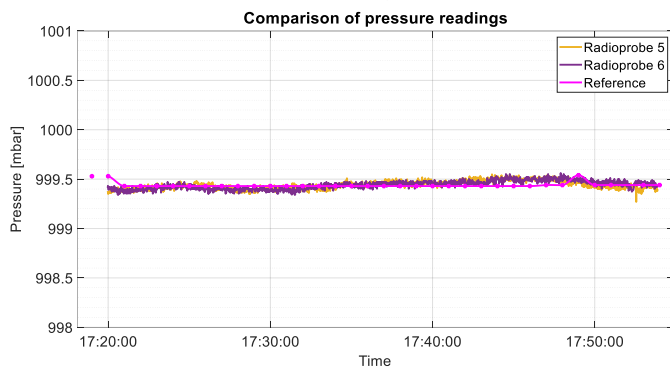
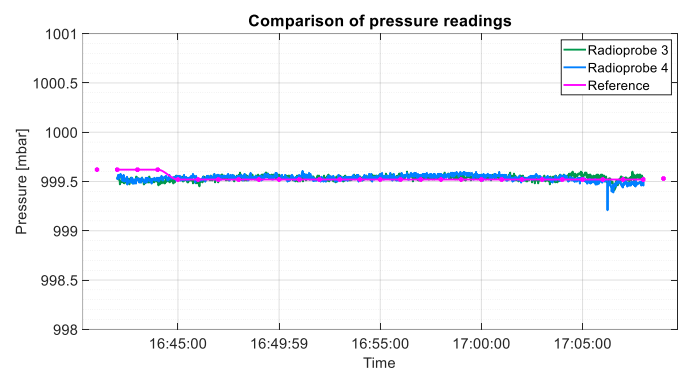
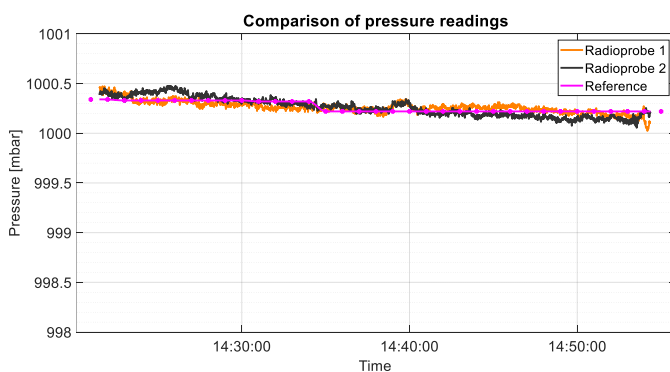


Figure 4.38 Barometric pressure comparison between radioprobe sensor readings and reference readings. Top left: pairs radioprobe 1 and radioprobe 2. Top right: pairs radioprobe 3 and radioprobe 4. Bottom left: pairs radioprobe 5 and radioprobe 6. Bottom right: pairs radioprobe 7 and radioprobe 8.

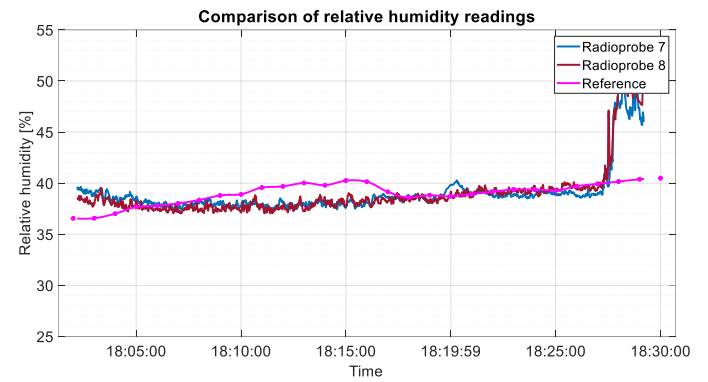
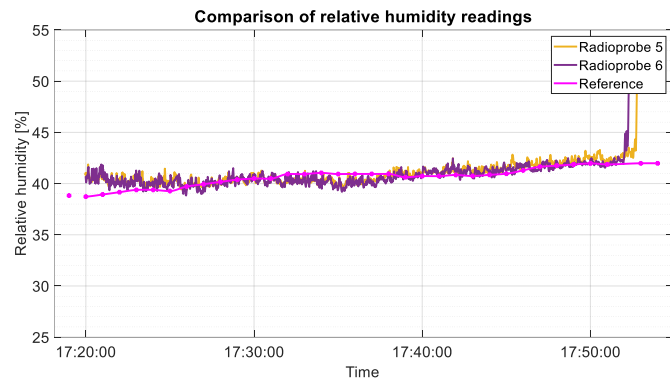
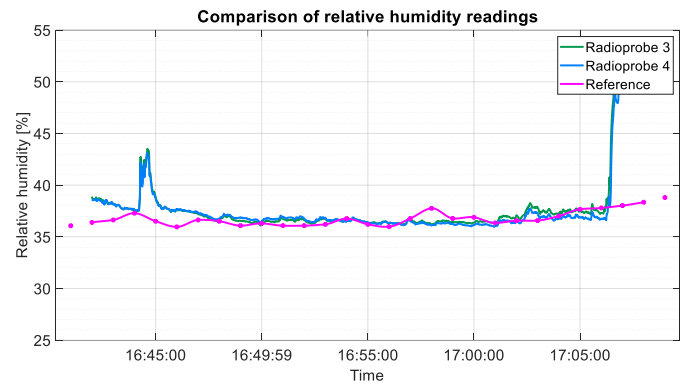
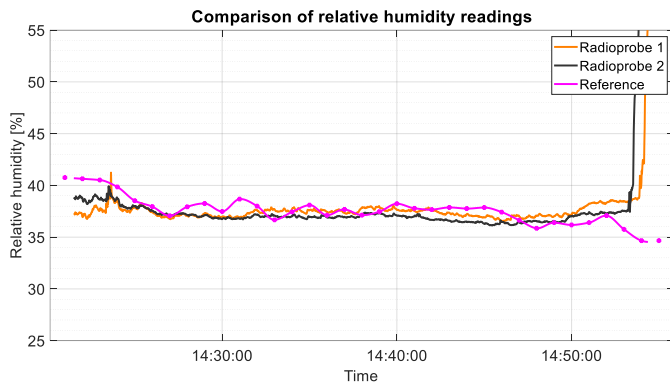


Figure 4.39 Relative humidity comparison between radioprobe sensor readings and reference readings. Top left: pairs radioprobe 1 and radioprobe 2. Top right: pairs radioprobe 3 and radioprobe 4. Bottom left: pairs radioprobe 5 and radioprobe 6. Bottom right: pairs radioprobe 7 and radioprobe 8.

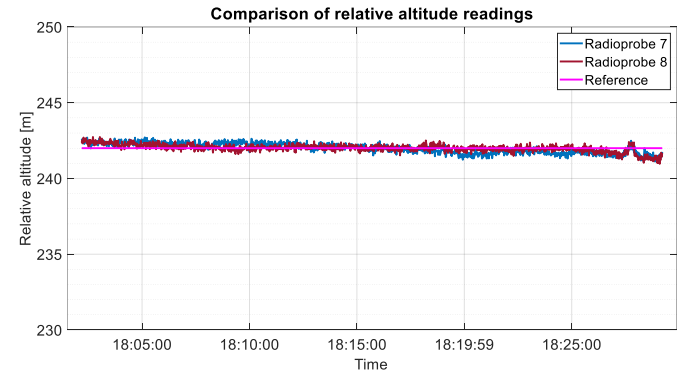
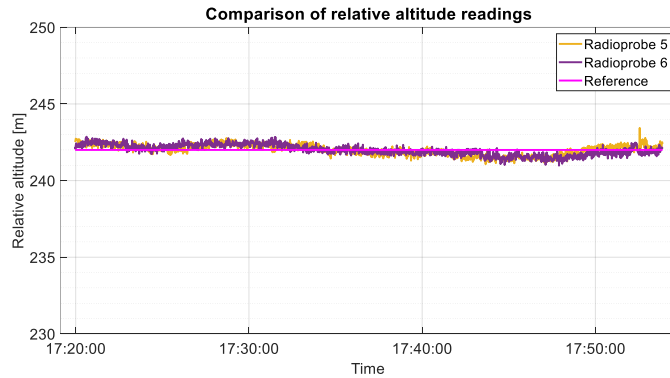
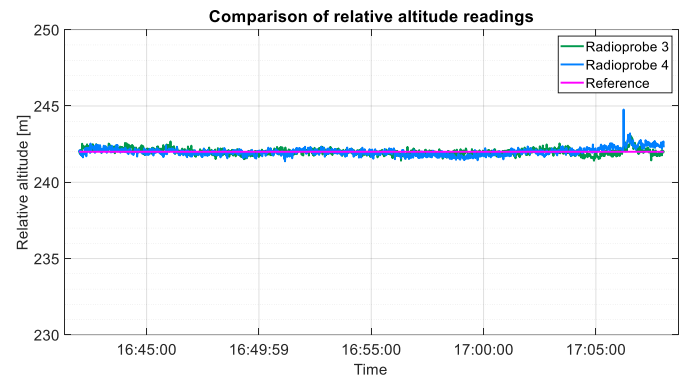
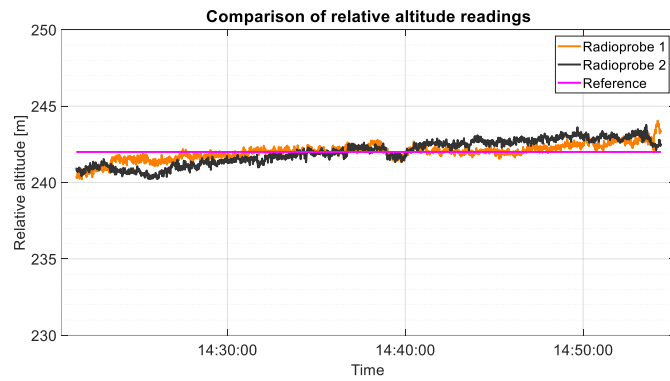


Figure 4.40 Approximate altitude comparison between radioprobe sensor readings and reference readings. Top left: pairs radioprobe 1 and radioprobe 2. Top right: pairs radioprobe 3 and radioprobe 4. Bottom left: pairs radioprobe 5 and radioprobe 6. Bottom right: pairs radioprobe 7 and radioprobe 8.

**Table 4.7 Statistical comparison between radioprobe sensors and reference sensors readings.
Temperature.**

Mean reference sensor [°C]	Radioprobes					
	Radioprobe [#]	Mean [°C]	Max. value [°C]	Min. value [°C]	Mean error ¹ [°C]	Standard deviation ² [°C]
17.0	1	17.0	18.8	11.0	0.8	0.8
17.0	2	17.0	18.5	8.7	0.7	1.1
17.3	3	16.8	17.7	12.8	0.6	0.8
17.3	4	16.9	17.9	13.4	0.5	0.7
16.2	5	15.9	16.9	14.4	0.4	0.4
16.2	6	15.9	17.0	14.5	0.4	0.4
16.7	7	16.7	17.8	15.0	0.4	0.3
16.7	8	16.7	17.6	15.8	0.7	0.4

¹ Temperature difference between reference sensor reading and the radioprobe sensor reading

² Standard deviation of radioprobe temperature reading

**Table 4.8 Statistical comparison between radioprobe sensors and reference sensors readings.
Barometric pressure.**

Mean reference sensor [mbar]	Radioprobes					
	Radioprobe [#]	Mean [mbar]	Max. value [mbar]	Min. value [mbar]	Mean error ¹ [mbar]	Standard deviation ² [mbar]
1000.3	1	1000.3	1000.5	1000.0	0.04	0.03
1000.3	2	1000.3	1000.5	1000.1	0.05	0.03
999.5	3	999.5	999.6	999.4	0.03	0.03
999.5	4	999.5	999.6	999.2	0.03	0.03
999.4	5	999.4	999.5	999.3	0.04	0.03
999.4	6	999.4	999.6	999.3	0.03	0.02
999.5	7	999.5	999.6	999.4	0.07	0.03
999.5	8	999.5	999.6	999.4	0.06	0.03

¹ Pressure difference between reference sensor reading and the radioprobe sensor reading

² Standard deviation of radioprobe pressure reading

**Table 4.9 Statistical comparison between radioprobe sensors and reference sensors readings.
Relative humidity.**

Mean reference sensor [%RH]	Radioprobes					
	Radioprobe [#]	Mean [%RH]	Max. value [%RH]	Min. value [%RH]	Mean error ¹ [%RH]	Standard deviation ² [%RH]
37.6	1	37.6	55.3	36.5	1.1	1.6
37.6	2	37.6	58.7	36.1	1.4	3.2
36.8	3	38.0	53.8	36.1	1.5	3.3
36.8	4	37.7	53.7	36.0	1.4	2.7
40.6	5	41.3	52.0	39.4	0.9	1.6
40.6	6	41.3	52.1	38.8	1.0	1.9
39.0	7	39.0	50.5	37.4	1.4	1.7
39.0	8	39.0	53.9	37.0	1.4	2.0

¹ Relative humidity difference between reference sensor reading and the radioprobe sensor reading

² Standard deviation of radioprobe relative humidity reading

Table 4.10 Statistical comparison between radioprobe sensors and reference sensors readings. Approximate altitude.

Mean reference sensor [m]	Radioprobes					
	Radioprobe [#]	Mean [m]	Max. value [m]	Min. value [m]	Mean error ¹ [m]	Standard deviation ² [m]
242.0	1	242.0	244.1	240.2	0.4	0.3
242.0	2	242.0	243.8	240.2	0.7	0.4
242.0	3	242.0	243.0	241.4	0.1	0.1
242.0	4	242.0	244.8	241.4	0.2	0.2
242.0	5	242.0	243.4	241.1	0.2	0.2
242.0	6	242.0	242.9	241.0	0.3	0.2
242.0	7	242.0	242.7	241.1	0.3	0.2
242.0	8	242.0	242.7	241.0	0.2	0.2

¹ Approximate altitude difference between reference sensor reading and the radioprobe sensor reading

² Standard deviation of radioprobe approximate altitude reading

As a result of this test performed in a non-controlled urban environment, eight different radioprobe boards measuring TPH data were tested in pairs and against a detached reference database. From the above plots, it is possible to see that the measurements collected by the radioprobe pairs placed closely follow the same trend for the four quantities of interest: temperature, pressure, humidity, and estimated altitude. With regards to the comparison with the available source of reference, it is possible to see that there are some intervals at which the radioprobe measurements have some differences. This is mainly because the reference sensors and the radioprobe sensors were deployed at different places (distant about 11 km) with different specific conditions, and in an uncontrolled environment. Nevertheless, from the results, it is possible to conclude that, even if the conditions of testing were different, the radioprobe sensors provided a reasonable response while keeping the mean error and standard deviation of the measurements within acceptable ranges.

4.3.2 Test 2: Temperature, pressure, and humidity sensors unit

A second test was carried out to full validate the response of the TPH sensor unit embedded in the radioprobe system. This test was conducted in the Applied Thermodynamics Laboratory of INRiM. To examine not only the accuracy but also the possible spread of different sensors' behaviour, the system setup consisted of three radioprobe electronic boards measuring temperature and humidity. Each radioprobe was placed inside a climatic chamber and connected to an external PC through a FTDI breakout board. The PCs comprised some database and visualization tools properly programmed and tested beforehand. The mentioned tools allowed acquiring, storing, manipulating, and visualizing in real time the information coming from the sensors. The sensor measurements were retrieved through reading instructions given by the microcontroller via the I²C communication interface.

The climatic chamber used for this test was a Kambic KK190 CHLT model specifically built for meteorology and climate metrology purposes (Merlone et al., 2015). Here, the temperature and humidity parameters could be precisely regulated according to the user settings. For instance, the relative humidity regulation allowed variations within the range from 10 % to 98 %, while the temperature regulation could be set from 40 °C up to 180 °C. Next to the radioprobes, four platinum resistance thermometers model Pt100 were placed to provide the reference temperature values. They were connected externally to a high-precision Super-Thermometer FLUKE 1594a. In addition, a humidity probe model Delta Ohm was settled inside the chamber to provide the relative humidity reference values. It was connected to an external datalogger model HD27.17TS. It is worth mentioning that all the reference probes (temperature and relative humidity) were properly calibrated in INRIM laboratory before starting the measurements. The total uncertainty of the instruments used as reference is listed below:

- Pt100 reference temperature probes:
 - 0.011 °C for positive temperature values
 - 0.020 °C for negative temperature values
- Delta Ohm reference humidity probe:
 - ±3 % RH

The general system setup is shown in Figure 4.42s. The system setup inside the climatic chamber is displayed in Figure 4.42.

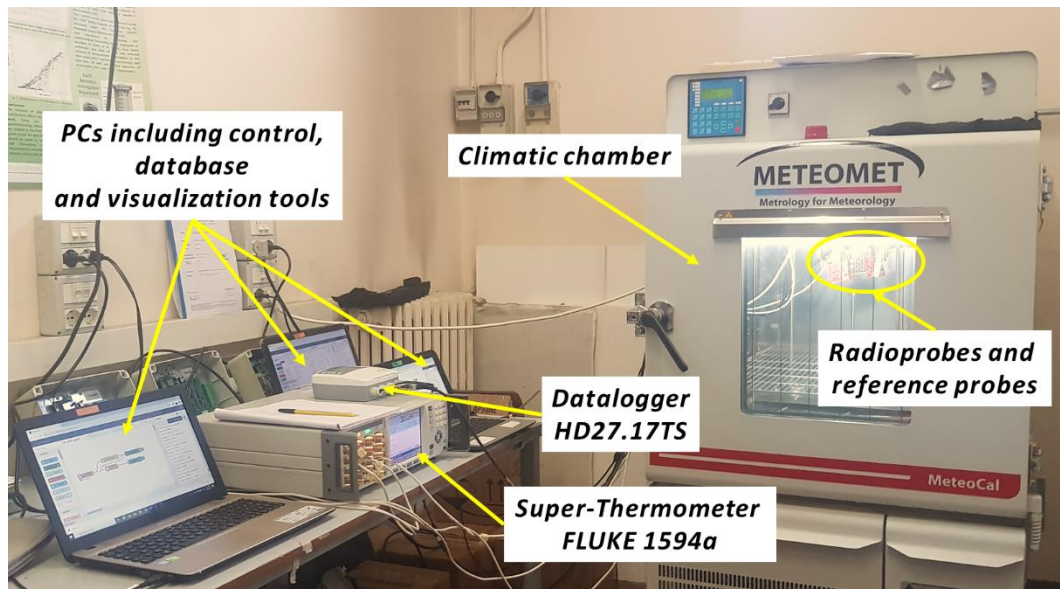


Figure 4.41 General system setup test 2. Applied Thermodynamics Laboratory INRiM

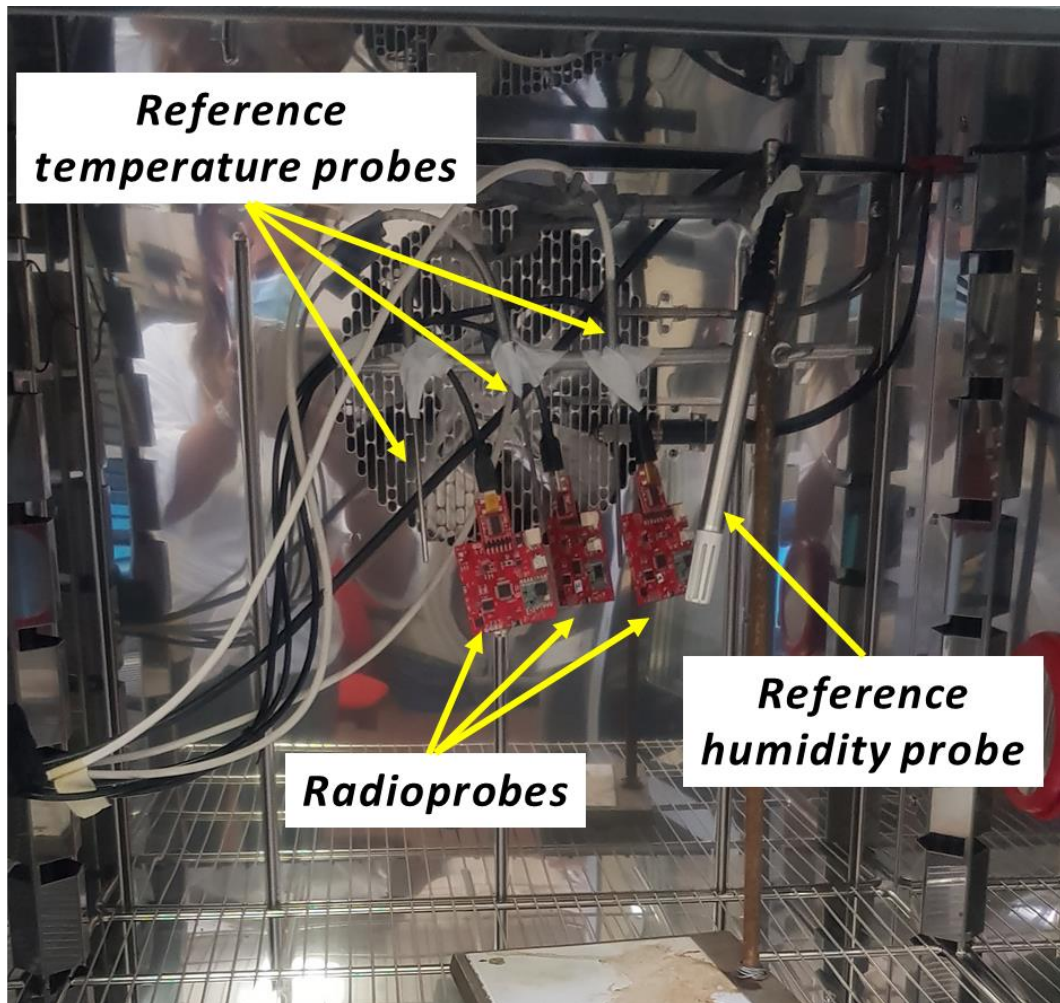


Figure 4.42 System setup inside the climatic chamber. Applied Thermodynamics Laboratory INRiM

The initial configuration set to the climatic chamber was $+20\text{ }^{\circ}\text{C}$ for temperature and 30 % RH for relative humidity. Once the system reached a stable condition, additional controlled variations of the chamber conditions, both in temperature and humidity, were programmed to verify the radioprobe sensors' response. The first test consisted of applying small incremental steps in temperature (until reaching $+24\text{ }^{\circ}\text{C}$), while keeping the relative humidity at a fixed value of 30 %. Each step lasted approximately 30 minutes. Afterwards, additional controlled variations of the chamber conditions, this time applying larger incremental steps in temperature, were configured in the climatic chamber. Starting from the current configuration $T = +24\text{ }^{\circ}\text{C}$, $\text{RH} = 30\text{ \%}$, the system was set to increase its temperature until reaching $-5\text{ }^{\circ}\text{C}$, $0\text{ }^{\circ}\text{C}$ and $10\text{ }^{\circ}\text{C}$. For this part, the relative humidity was not set to a fixed value inside the climatic chamber. Each step lasted approximately 1 hour to ensure that the whole system reached the temperature stability. These larger temperature cycles were programmed with the aim of simulating cloud conditions like those where the radioprobes will be released. Even if warm clouds have temperatures above $0\text{ }^{\circ}\text{C}$ ($32\text{ }^{\circ}\text{F}$), the tests comprised also negative temperature settings to test the sensors' performance under forced conditions. The measurement results coming from the larger cycle test are shown in Figure 4.43, where the mean of the temperature probe

measurements is used as comparison. In addition, the response of the radioprobe humidity sensors during this cycle is shown in Figure 4.44.

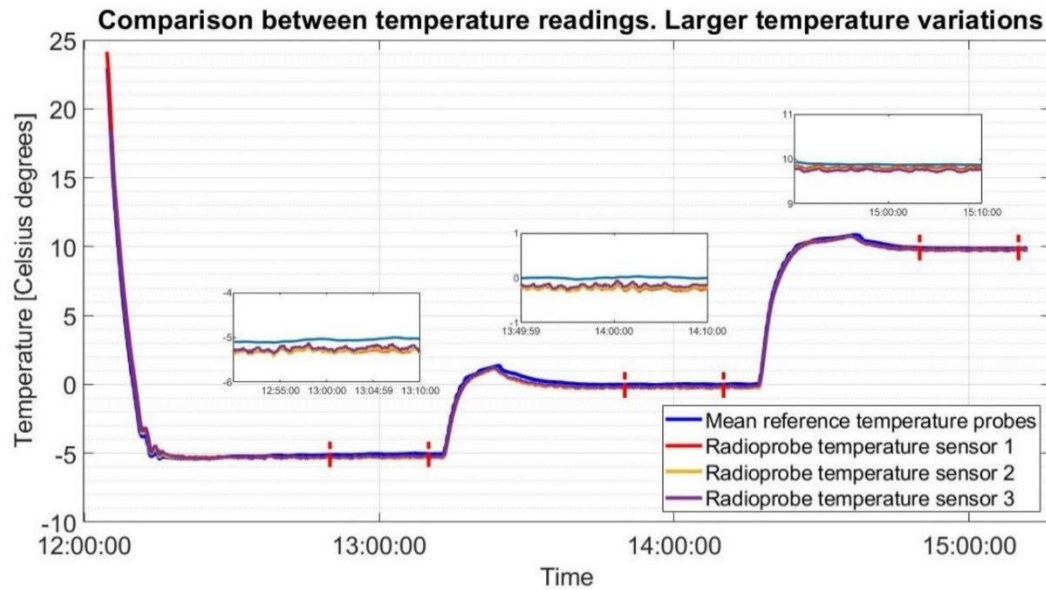


Figure 4.43 Comparison of temperature measurements. Radioprobes' sensors vs. reference temperature sensors measurements. Larger cycle test. Initial configuration $T = +24^{\circ}\text{C}$, $\text{RH} = 30\%$ until reaching the set points of $T = -5^{\circ}\text{C}$, $T = 0^{\circ}\text{C}$ and $T = 10^{\circ}\text{C}$ (Paredes Quintanilla et al., 2021)

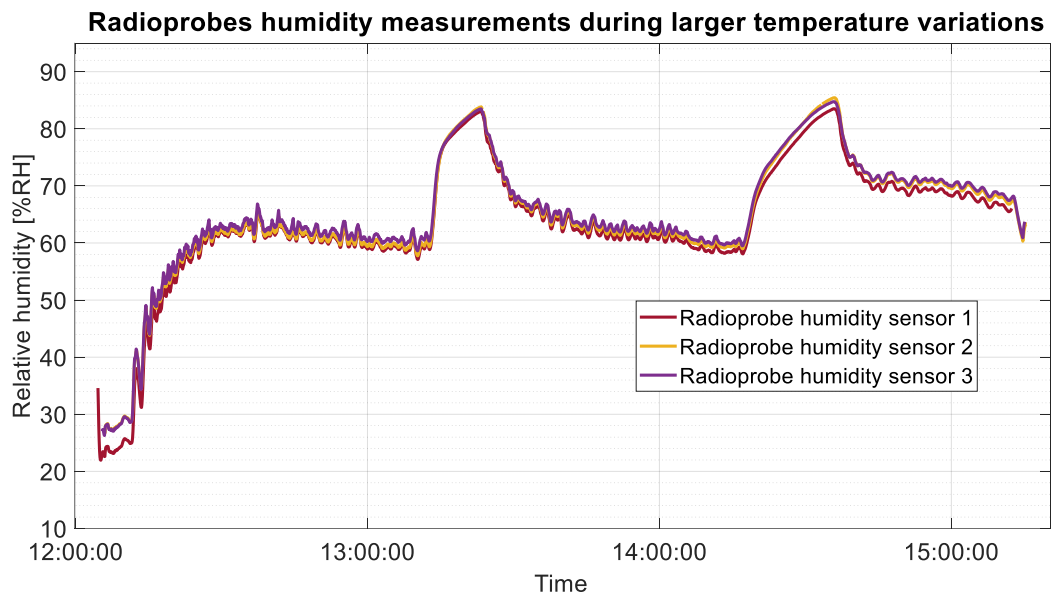


Figure 4.44 Radioprobes' humidity measurements during the larger cycle test. Initial configuration $T = +24^{\circ}\text{C}$, $\text{RH} = 30\%$ until reaching the set points of $T = -5^{\circ}\text{C}$, $T = 0^{\circ}\text{C}$ and $T = 10^{\circ}\text{C}$

The last test consisted of keeping a constant temperature of $+30^{\circ}\text{C}$ and changing the relative humidity values from 10% RH to 20% , 40% and 60% . Each step lasted approximately 30 minutes to ensure that the whole system reached the humidity stability. Since the information generated by the reference humidity sensor could not be extracted from the datalogger, the comparison was done based on the time at which the values were set at the climate chamber. Figure 4.45 shows the radioprobe sensor measurements during these humidity incremental steps. In

addition, the response of the radioprobe temperature sensors compared with the reference probe readings during this cycle is shown in Figure 4.46.

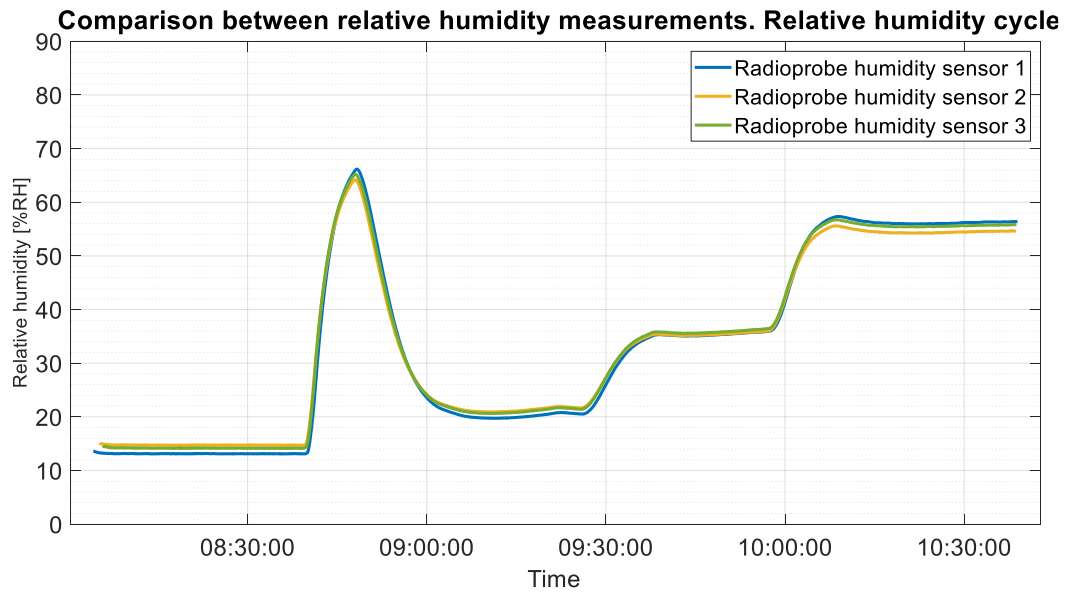


Figure 4.45 Comparison of relative humidity measurements. Radioprobes' sensor measurements during humidity cycle test. Initial configuration T = +30 °C, RH = 10 % until reaching the set points of RH = 20 %, RH = 40 %, and RH = 60 %

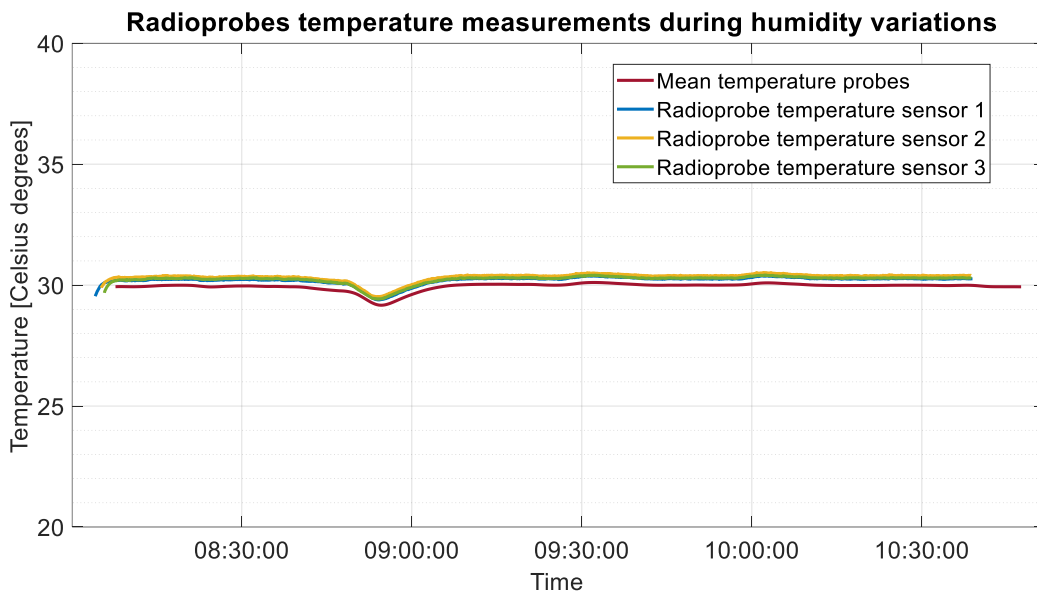


Figure 4.46 Comparison of temperature measurements. Radioprobes' sensors vs. reference temperature sensors measurements. Humidity cycle test. Initial configuration T = +30 °C, RH = 10 % until reaching the set points of RH = 20 %, RH = 40 %, and RH = 60 %

To statistically contrast the measurements coming from the radioprobes and those coming from the reference sensors, the numerical computing environment Matlab was used. Here, the interpolation technique makima was applied to match all the query points and then to statistically compare the obtained data. This analysis was done to selected time intervals (about 5 minutes each) where the system inside the climatic chamber reached stable states for both, temperature, and humidity. The

statistical results of the last two tests are summarized in Table 4.11, Table 4.12, and Table 4.13 for temperature, and in Table 4.14, Table 4.15, and Table 4.16 for relative humidity.

Table 4.11 Statistical comparison between radioprobe sensors and reference sensors readings.
Temperature. Radioprobe 1

Temperature set point for test [°C]	Temperature measured by reference sensors (mean) [°C]	Temperature measured by radioprobe sensor (mean) [°C]	Mean error¹ [°C]	Standard deviation² [°C]
-5	-5.063	-5.31	0.25	0.04
0	0.002	-0.25	0.25	0.03
10	9.878	9.82	0.065	0.02

¹ Temperature difference between reference sensor reading and the radioprobe sensor reading

² Standard deviation of radioprobe temperature reading

Table 4.12 Statistical comparison between radioprobe sensors and reference sensors readings.
Temperature. Radioprobe 2

Temperature set point for test [°C]	Temperature measured by reference sensors (mean) [°C]	Temperature measured by radioprobe sensor (mean) [°C]	Mean error¹ [°C]	Standard deviation² [°C]
-5	-5.063	-5.30	0.24	0.04
0	0.002	-0.23	0.23	0.03
10	9.878	9.75	0.13	0.03

¹ Temperature difference between reference sensor reading and the radioprobe sensor reading

² Standard deviation of radioprobe temperature reading

Table 4.13 Statistical comparison between radioprobe sensors and reference sensors readings.
Temperature. Radioprobe 3

Temperature set point for test [°C]	Temperature measured by reference sensors (mean) [°C]	Temperature measured by radioprobe sensor (mean) [°C]	Mean error¹ [°C]	Standard deviation² [°C]
-5	-5.063	-5.25	0.18	0.04
0	0.002	-0.17	0.18	0.03
10	9.878	9.74	0.13	0.02

¹ Temperature difference between reference sensor reading and the radioprobe sensor reading

² Standard deviation of radioprobe temperature reading

Table 4.14 Statistical comparison between radioprobe sensors and reference sensors readings.
Relative humidity. Radioprobe 1

RH set point for test [%RH]	RH measured by reference sensors (mean) [%RH]	RH measured by radioprobe sensor (mean) [%RH]	Mean error¹ [%RH]	Standard deviation² [%RH]
10	10.50	13.12	2.62	0.01
20	19.75	19.85	0.09	0.08

40	37.68	35.31	2.37	0.10
60	59.70	56.13	3.57	0.07

¹ Relative humidity difference between reference sensor reading and the radioprobe sensor reading

² Standard deviation of radioprobe relative humidity reading

Table 4.15 Statistical comparison between radioprobe sensors and reference sensors readings.
Relative humidity. Radioprobe 2

RH set point for test [%RH]	RH measured by reference sensors (mean) [%RH]	RH measured by radioprobe sensor (mean) [%RH]	Mean error¹ [%RH]	Standard deviation² [%RH]
10	10.50	14.74	4.24	0.02
20	19.75	21.35	1.60	0.17
40	37.68	35.64	2.04	0.12
60	59.70	54.53	5.17	0.05

¹ Relative humidity difference between reference sensor reading and the radioprobe sensor reading

² Standard deviation of radioprobe relative humidity reading

Table 4.16 Statistical comparison between radioprobe sensors and reference sensors readings.
Relative humidity. Radioprobe 3

RH set point for test [%RH]	RH measured by reference sensors (mean) [%RH]	RH measured by radioprobe sensor (mean) [%RH]	Mean error¹ [%RH]	Standard deviation² [%RH]
10	10.50	14.16	3.66	0.02
20	19.75	21.09	1.34	0.18
40	37.68	36.06	1.62	0.12
60	59.70	55.69	4.01	0.04

¹ Relative humidity difference between reference sensor reading and the radioprobe sensor reading

² Standard deviation of radioprobe relative humidity reading

From the obtained results, using a high-accuracy climatic chamber together with well calibrated reference sensors, the operation of the radioprobe sensors was assessed. The radioprobe sensor measurements followed the same trend as the reference ones, specially at the periods where the system was stable. For most of the measurements, their performance agreed within the technical specifications provided by the producer, that is a maximum uncertainty of ± 3 % RH for relative humidity, and a maximum uncertainty of ± 1 °C for temperature measurements. There were a few exceptions in the relative humidity estimations that might be generated due to the reference humidity sensor, which declares uncertainties up to ± 3 % RH. However, considering the design constraints, it can be said that the radioprobe sensors provided good accuracy in temperature and relative humidity measurements thus making them suitable for the observation of warm cloud environments, which is the final goal of the mini radioprobe.

Part of this work has been published in the *Journal MDPI Sensors* (Paredes Quintanilla et al., 2021).

4.3.3 Test 3: Temperature, pressure, and humidity sensors unit

A third test was carried out to fully validate the temperature, pressure, and humidity sensors unit of the radioprobe. The aim of this test was to have a comparison of readings between a commonly used atmospheric system and the newly developed radioprobes. This system setup was already described in subsection “4.2.4: Data transmission ranges: Test 4”, where the maximum data transmission ranges reached by the radioprobe system were evaluated. As previously mentioned, this test was carried out at the Cuneo - Levaldigi meteorological station of ARPA Piedmont Region – Italy. An automatic atmospheric sounding system was used as means of transportation into the atmosphere. It consisted of a large Helium-inflated observation balloon hooking a Vaisala RS41-SG radiosonde, which was used as reference instrument for this experiment. The reference radiosonde embedded various sensors to measure humidity, temperature, and atmospheric pressure along its pass across the atmosphere. It also incorporated a GPS receiver that allowed the estimation of wind velocity and direction. The collected data is sent to sounding workstation through a telemetry radio link. According to the reference’s sonde technical specifications (*Vaisala Radiosonde RS41-SG / VAISALA*, n.d.), its maximum uncertainties for sounding are:

- Temperature (sounding ≤ 16 km): 0.3 °C
- Humidity: 4 % RH
- Pressure (pressure ≥ 100 hPa): 1.0 hPa / 0.5 hPa

The tiny radioprobe used for this assessment was attached to the front case of the Vaisala radiosonde with the help of a non-conductive adhesive tape (Figure 4.47). It was enabled to continuously measure, process, and send the information collected during its travel along the atmosphere. To reserve energy for the flight, the radioprobe was initialized just before the launch. Since the atmospheric sounding system is freely released into the air, the recovery of the whole instrumentation was not foreseen. At the ground side, a base station was deployed next to the sounding workstation to receive the transmitted packets.



Figure 4.47 Mini radioprobe attached to the reference atmospheric sound.

The data collected by the tiny radioprobe was statistically compared with the data gathered by the reference sonde. The data considered for the statistical analysis corresponded to the intervals where the percentage of the ground received packets was higher than 90 % (See Table 4.6). Based on this fact, the analyzed data corresponded to the first 5 km of straight distance between the ground station and the flying instrumentation.

The graphical comparison between the data readings from the radioprobe instrumentation against those from the reference VAISALA sonde, are shown in Figure 4.48, Figure 4.49, and Figure 4.50 for temperature, pressure, and humidity respectively. The statistical results of the whole set of measurements are summarized Table 4.17.

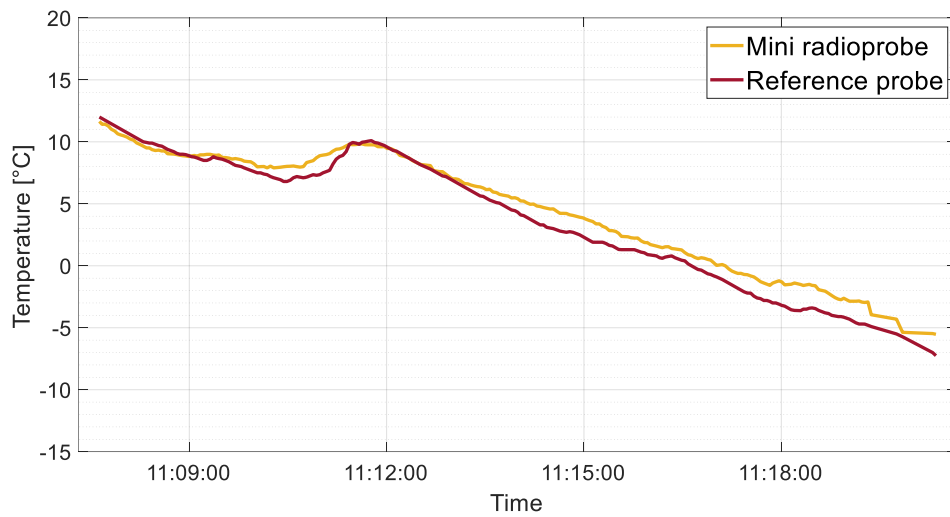


Figure 4.48 Comparison of temperature measurements between the ARPA reference sonde sensors and the radioprobe sensors.

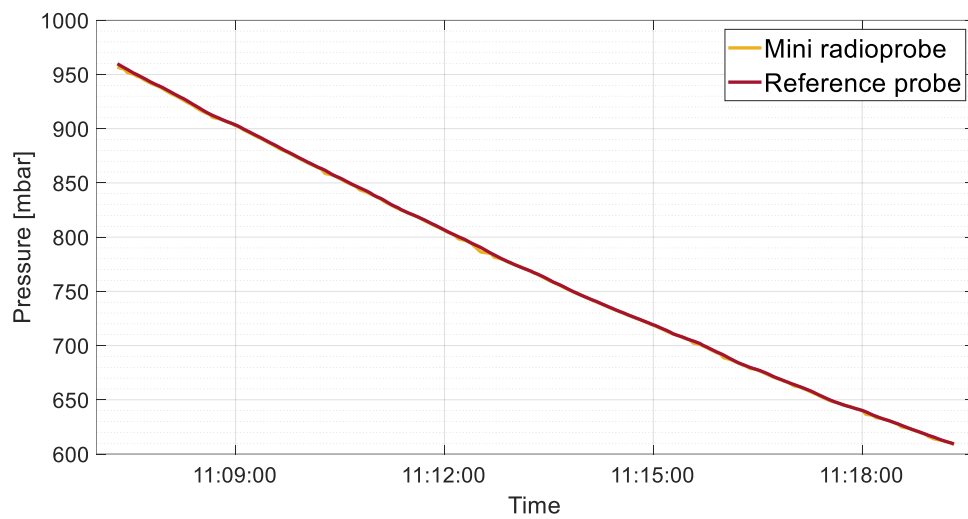


Figure 4.49 Comparison of pressure measurements between the ARPA reference sonde sensors and the radioprobe sensors.

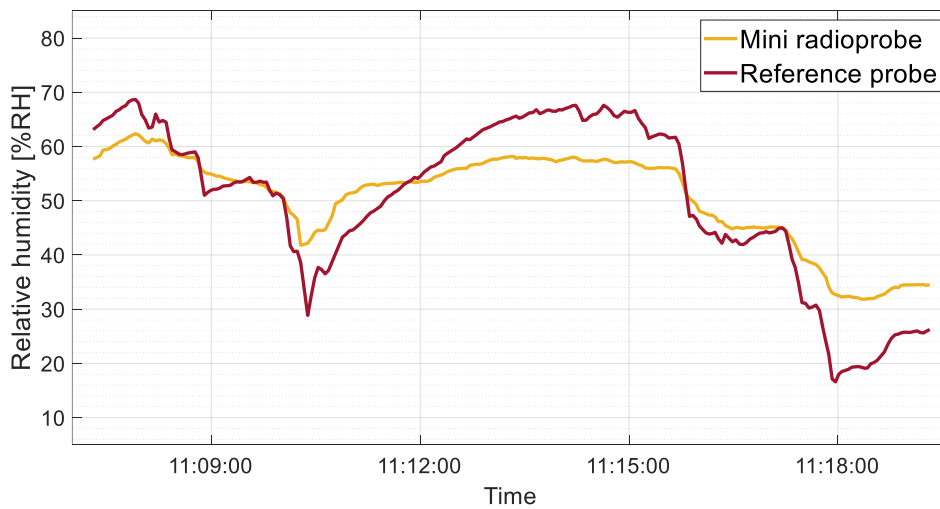


Figure 4.50 Comparison of relative humidity measurements between the ARPA reference sonde sensors and the radioprobe sensors.

Table 4.17 Statistical comparison between radioprobe sensors and ARPA reference sensors readings. Temperature, pressure, and relative humidity (Paredes Quintanilla et al., 2021)

	Mean reference sensors	Radioprobe measurements		
		Mean	Mean Error ¹	Standard deviation ²
Temperature [°C]	4.16	4.93	0.87	0.56
Pressure [mbar]	774.14	773.53	0.63	0.58
Relative humidity [%RH]	50.74	50.86	5.53	3.71

¹ Difference between reference sensor readings and the radioprobe sensor readings

² Standard deviation of radioprobe sensor readings

This test provided useful insights regarding the operation of the TPH radioprobe sensors when compared with a standard sonde used for atmospheric profiling. From the above plots, it is possible to notice some relatively small differences between the measurements from both systems. This could be due to the physical location of the mini radioprobe onto the reference probe that resulted in a potential impact on the output values. In the absence of enough space, and to prevent its drop during the flight, the radioprobe was tightly secured to the main body of the reference sonde. Being in narrow contact, some thermal variation due to the dissipated energy from the reference sonde could have been measured by the mini radiosonde. Also, since the air circulation towards the BME280 ventilation hole was partially blocked, an adequate air exchange was not feasible hence leading to errors' contribution during the readings. However, from the statistical analysis, reasonable values for mean error and standard deviation, especially for temperature and pressure measurements, were obtained. Despite the mentioned issues, and considering the design limitations, it can be said that the TPH sensor unit of the radioprobe works well enough in accordance with the specifications given by the manufacturer and the needs of the target cloud observation system.

Upcoming tests should envisage a new way to attach the tiny radioprobe to the sounding system in such a way that the TPH sensors are in direct contact with the atmosphere without the total or partial path obstruction.

Part of this work has been published in the *Journal MDPI Sensors* (Paredes Quintanilla et al., 2021).

4.3.4 Test 4: Positioning and Tracking sensors unit

By using the same system setup already described in subsections 4.2.4 and 4.3.3, using an automatic atmospheric sounding system from ARPA as reference system, this test was performed to validate the positioning and tracking sensor unit of the radioprobe. This test was carried out at the Cuneo - Levaldigi meteorological station (LIMZ). The automatic sounding system consisted in a large Helium-inflated observation balloon carrying a tethered Vaisala RS41-SG radiosonde. This

reference radiosonde included different sensors to provide different measurements along the system ascending path, among them wind velocity and position.

The radioprobe's network setup consisted of a fully operational radioprobe measuring, pre-processing, managing, and sending the information generated during the air travel, and a ground station gathering, storing, and partially processing the received data packets. In contrast to the first field test already described, where the mini radioprobe was tightly adhered to the main body of the reference sonde, in this second test the mini radioprobe was attached to the system through a hanging thread as can be seen in Figure 4.51. This configuration allowed the direct contact of the sensors with the atmosphere and the non-obstruction of the GNSS receiver. The radioprobe was initialized just before the launch in order to save energy for the flight. The ground station was placed next to the sounding workstation to receive the data coming from the radioprobe. The radioprobe system setup is shown in Figure 4.51.

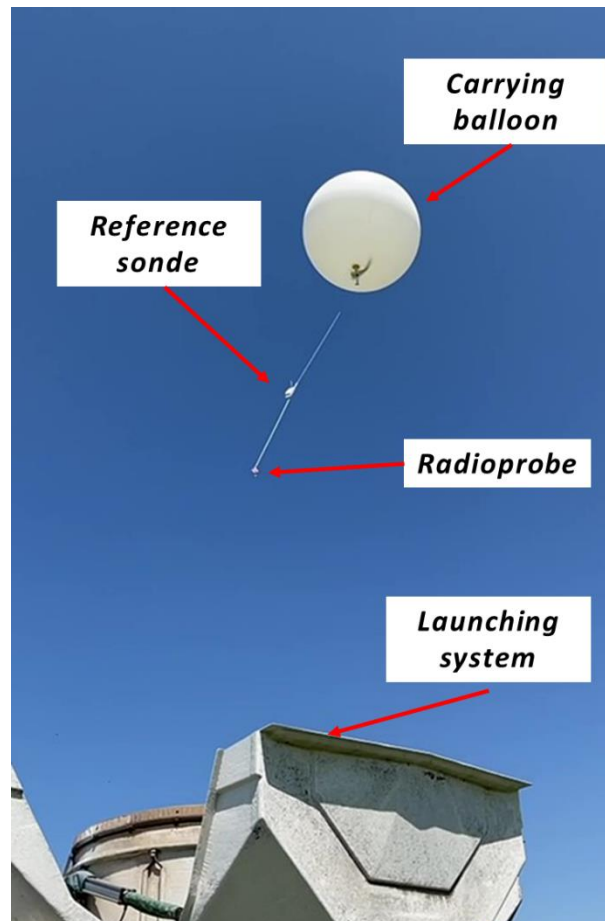


Figure 4.51 System setup. Mini radioprobe attached to the reference atmospheric sound through a thread.

The radioprobe transmitter was set to deliver an output power of 14 dBm, working at a frequency of 865.2 MHz, using a bandwidth of 125 KHz and a spreading factor of 10. Given that the test was performed in a totally open area, there was LOS between the receiver and the transmitter at almost all positions. The

graphical comparison of the trajectory measurements from both systems until receiving the last message coming from the radioprobe is displayed in Figure 4.52.

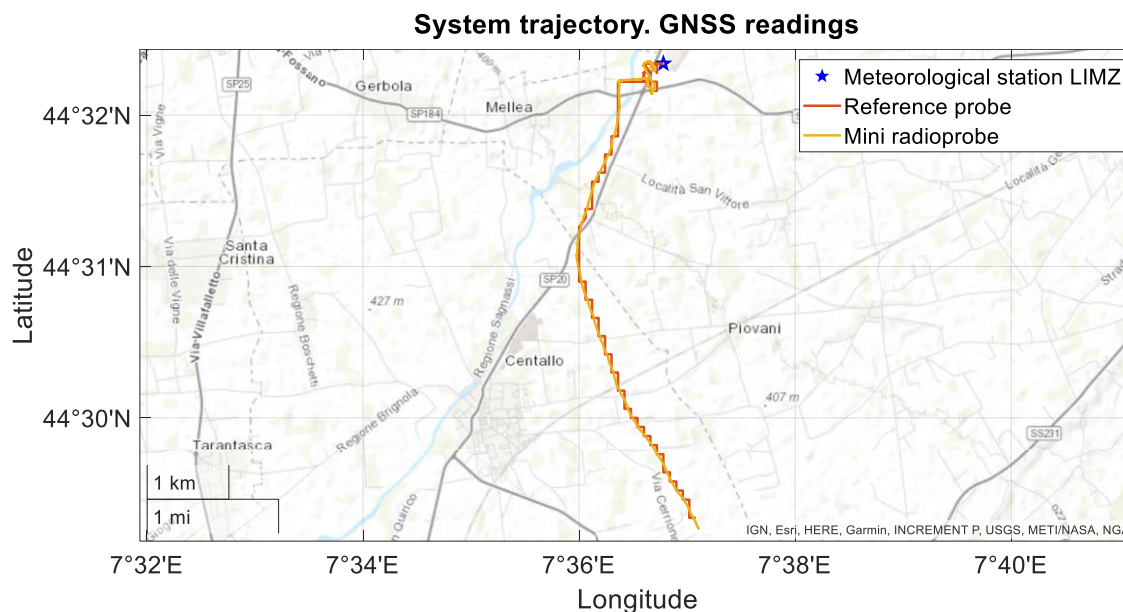


Figure 4.52 Trajectory followed by the systems: mini radioprobe and sounding balloon, displayed on a map.

The GNSS data collected by the tiny radioprobe was statistically compared with the data gathered by the GPS of the reference sonde. The statistical results of this set of measurements are summarized in Table 4.18.

Table 4.18 Statistical comparison between radioprobe sensors and ARPA reference sensors readings. GNSS receiver

	Mean reference sensors	Radioprobe measurements		
		Mean	Mean Error ¹	Standard deviation ²
Latitude [degrees]	44.53	44.53	3.33e-04	2.47e-04
Longitude [degrees]	7.61	7.61	3.26e-04	2.29e-04

¹ Difference between reference sensor readings and the radioprobe sensor readings

² Standard deviation of radioprobe sensor readings

From the obtained outcomes, using the GPS data provided by the reference system as reference for positioning information, the operation of the tracking and positioning sensor unit of the radioprobe was tested. From the above results, it is possible to notice that the position data provided by the GNSS receiver embedded in the radioprobe follow well the data provided by the GPS of the reference sonde. It should be noticed that the radioprobe operated with limited resources (i.e., most power saving mode, updates every 3 s) compared with those from the VAISALA reference sonde. Nevertheless, the performance of the positioning sensor was satisfactory for the initial reconstruction of the radioprobe's path during the in-cloud travel. It should be noted also that the GNSS output composes the input for the following ground step where postprocessing techniques are applied to reconstruct the radioprobes' trajectories inside clouds.

4.3.5 Test 5: Positioning and Tracking sensors unit

Another test was performed to validate the operation of the positioning and tracking system. It consisted of collecting positioning data from a smartphone device and then use them to compare with the data measured by the radioprobe. This test was carried out at Piazza D'Armi, which is an open-area park located in the center side of Turin. The system setup comprised a radioprobe continuously collecting the data coming from the IMU and the GNSS receiver. The IMU was set to provide acceleration, angular velocity, and magnetic field while the GNSS to provide time and geolocation updates. The data gathered from the IMU was partially processed by the control unit to reduce the amount of information collected during the test. The microcontroller was programmed to control the sensor unit and get four IMU sensor updates and one GNSS update each 2 seconds. The radioprobe was connected to a PC through a FTDI breakout board for storage purposes. In parallel, a smartphone based on Android operation system was used as reference source for the test. It included a GNSS logger application, which recorded the different positions followed during the walk around the park. Prior to starting the experiment, the calibration of the IMU device was conducted to guaranty the accuracy and quality of the measurements. The systematic error (bias) and the presence of noise due to the sensors themselves (accelerometer, magnetometer, and gyroscope) were recognized while the system was in an idle state.

Throughout the experiment, all the equipment setup was carried by hand. Both, the radioprobe and the smartphone were placed close together and recorded simultaneously the positioning data required for the test. Because the GNSS updates from both systems were different (radioprobe GNSS update = 2 s, GPS logger application update = 1 s), the readings coming from the IMU device were also gathered to make the position predictions in-between the radioprobe GNSS updates. This last process will be useful for the post-processing analysis step where the absolute position (in clouds) of the radioprobes will be obtained.

During this test, the walking distance travelled around the park was about 1.6 km for a half an hour time frame. The graphical comparison between the trajectories recorded by the radioprobe and the smartphone GPS logger is displayed in Figure 4.53. The coordinates comparison (latitude and longitude) recorded by both systems is shown in Figure 4.54 and Figure 4.55.



Figure 4.53 Trajectory comparison between the systems, Google Maps view. Blue line: trajectory recorded by the radioprobe. Red line: trajectory recorded by the smartphone GPS logger

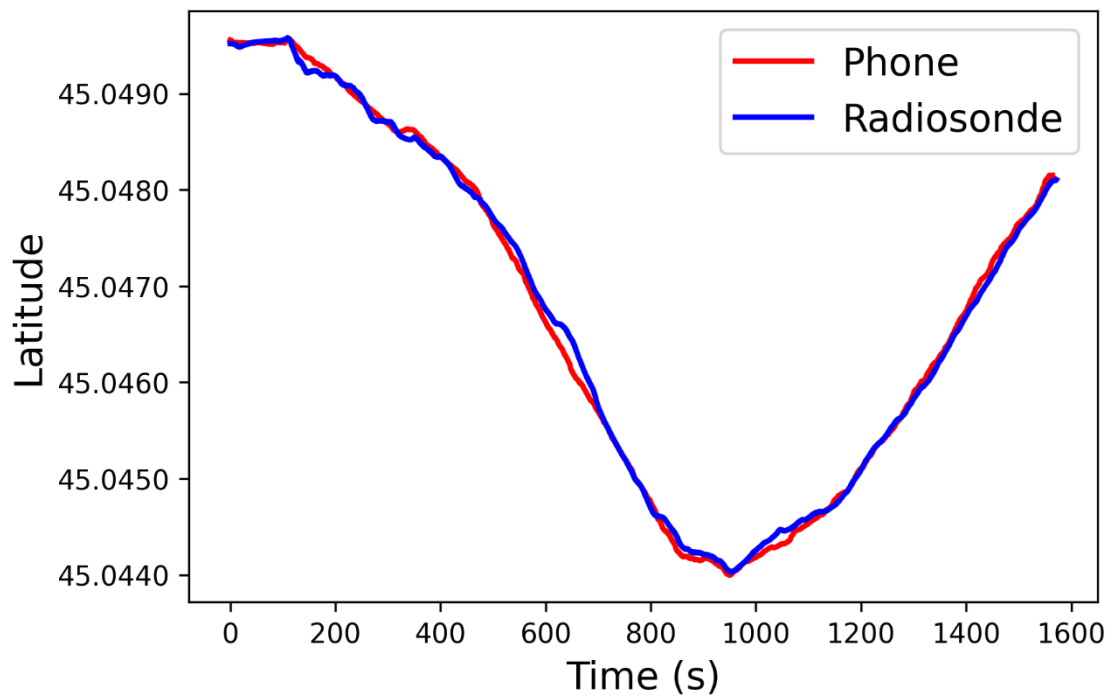


Figure 4.54 Latitude comparison between the systems in function of time. Blue line: latitude recorded by the radioprobe. Red line: latitude recorded by the smartphone GPS logger

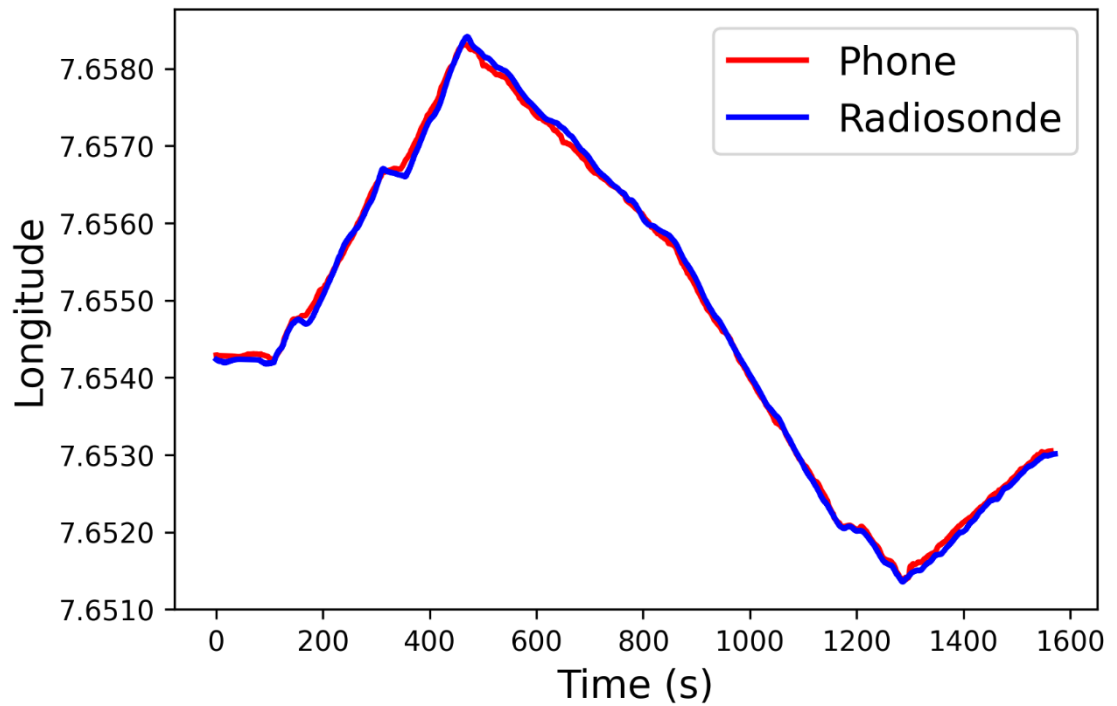


Figure 4.55 Longitude comparison between the systems in function of time. Blue line: longitude recorded by the radioprobe. Red line: longitude recorded by the smartphone GPS logger

The statistical results of the accuracy provided by the radioprobe's positioning and tracking sensors are summarized in Table 4.19.

Table 4.19 Statistical results of the radioprobe's positioning sensor accuracy during the test (Paredes Quintanilla et al., 2021)

Positioning and tracking sensor	Unit	Axis / coordinate	Sensor bias	Standard deviation
Accelerometer	[m/s ²]	x	0.26	0.03
		y	0.21	
		z	-0.45	
Magnetometer	[mGauss]	x	84.56	4.20
		y	-211.68	
		z	-271.32	
Gyroscope	[degree/s]	x	1.03	0.10
		y	1.22	
		z	8.80	
GNSS receiver	[degree]	latitude	-8.80 x 10 ⁻⁶	5.73 x 10 ⁻⁵
		longitude	-7.78 x 10 ⁻⁶	7.40 x 10 ⁻⁵

From the obtained results, using a GPS logger application as reference for positioning information, the operation of the tracking and positioning sensor unit of the radioprobe was tested. From the above plots, it is possible to see that both systems presented very similar measurements during the progress of the test. Although the radioprobe design envisages an operation with limited resources compared with those from a smartphone, the performance of the sensors was reasonably good for the partial reconstruction of the path followed during the walk. It should be noted that the output of this radioprobe stage composes the input for

the following step where postprocessing techniques are applied to reconstruct the radioprobes' trajectories inside clouds.

Part of this work has been published in the *Journal MDPI Sensors* (Paredes Quintanilla et al., 2021).

4.3.6 Test 6: Positioning and Tracking sensors unit

An additional test to further validate the positioning and tracking radioprobe sensor unit was carried out, this time in a more realistic cloud environment. It was performed at Parco Piemonte, which is an open area park located at the southern part of the Turin city. The test consisted in releasing the radioprobe in a true atmospheric condition and see its capability to detect fluctuations. The radioprobe was inserted in the middle of a bio helium-filled balloon, which was used as mean of transportation into the low Earth's atmosphere. The balloon was tethered through a fine thread and held by one of the experiment participants. It was kept at a low altitude range of about 30 m to 50 m above the surface level.

The configuration used for this test was a point-to-point network connection. The system setup consisted of a fully functional radioprobe measuring, packing, and sending the collected information, and a ground station receiving and storing the received packets. The transceiver was set to work at a central frequency of 865.2 MHz, using a spreading factor of 10, a bandwidth of 125 kHz and providing a power output of 14 dBm. The receiver was based on the ground side, at an elevation of about 1 m above the surface level. The estimated distance between the ground station position and the balloon release point was about 25 m. Since this set of measurements were carried out in a non-obstructed open area environment, the transmitter was in LOS with the receiver at all positions during the flight. The experiment setup is shown in Figure 4.56. Some pictures of the experiment are shown in Figure 4.57.

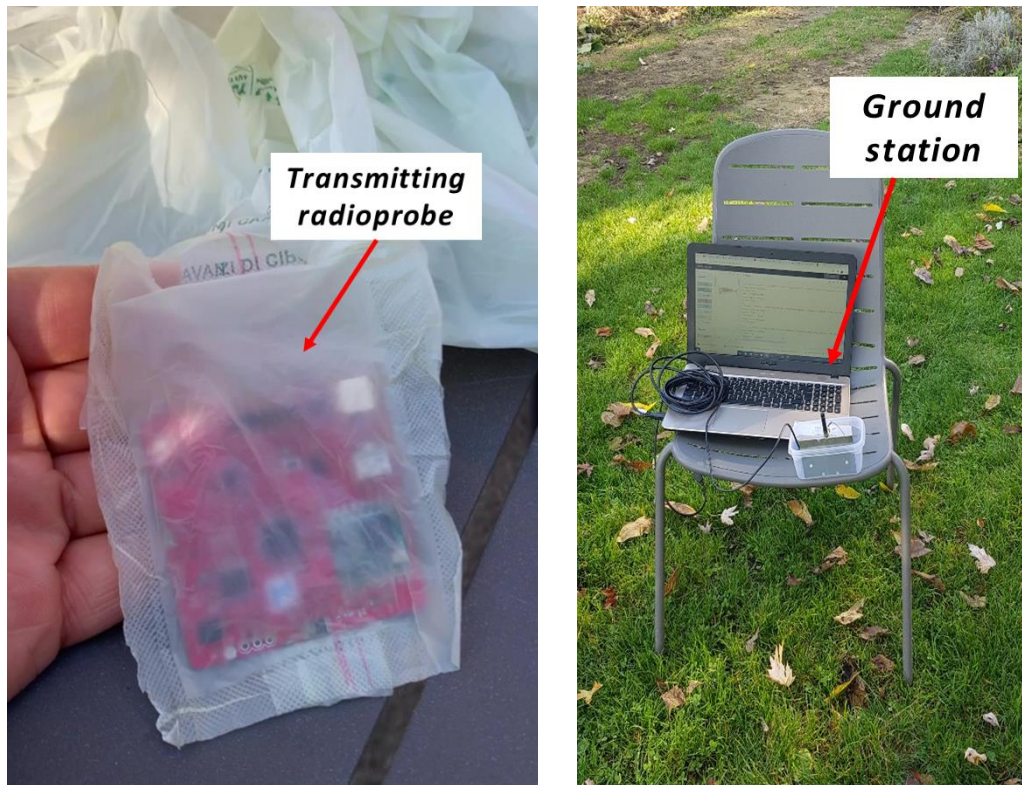


Figure 4.56 System setup test 5 for the detection of low-atmosphere fluctuations. Left: Radioprobe inserted inside a biodegradable balloon. Right: Radioprobe ground station.



Figure 4.57 Some pictures of the test 5 using a He-filled balloon as means of transportation.

The measurements taken by the accelerometer, gyroscope and magnetometer sensors are displayed in Figure 4.61, Figure 4.59, and Figure 4.60, respectively. The radioprobe system trajectory during the air travel is displayed in Figure 4.61.

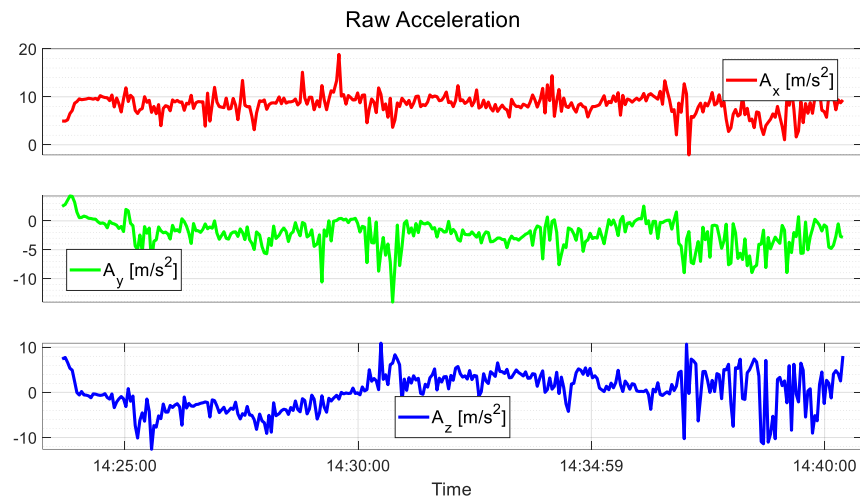


Figure 4.58 Raw acceleration measured by the radioprobe sensors during the flight.

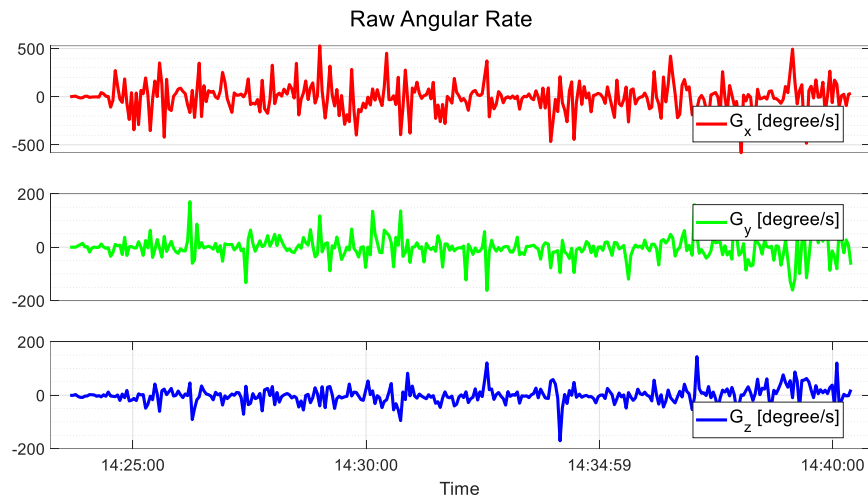


Figure 4.59 Raw angular rate measured by the radioprobe sensors during the flight.

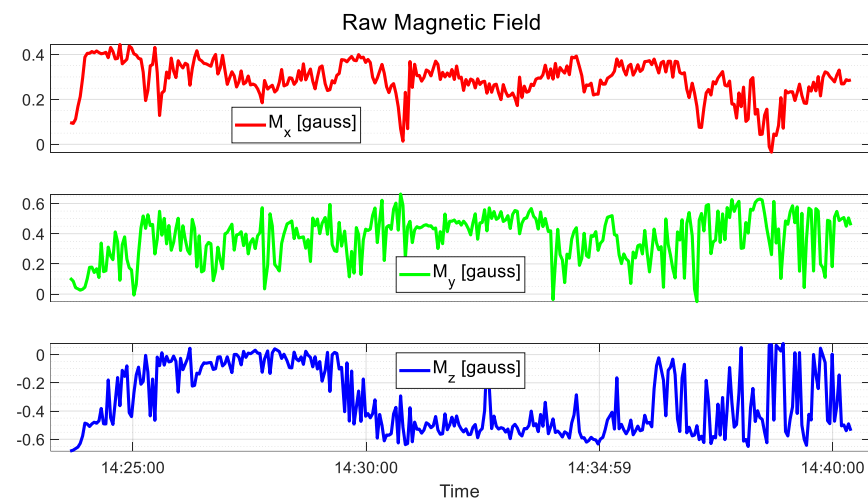


Figure 4.60 Raw magnetic field measured by the radioprobe sensors during the flight.

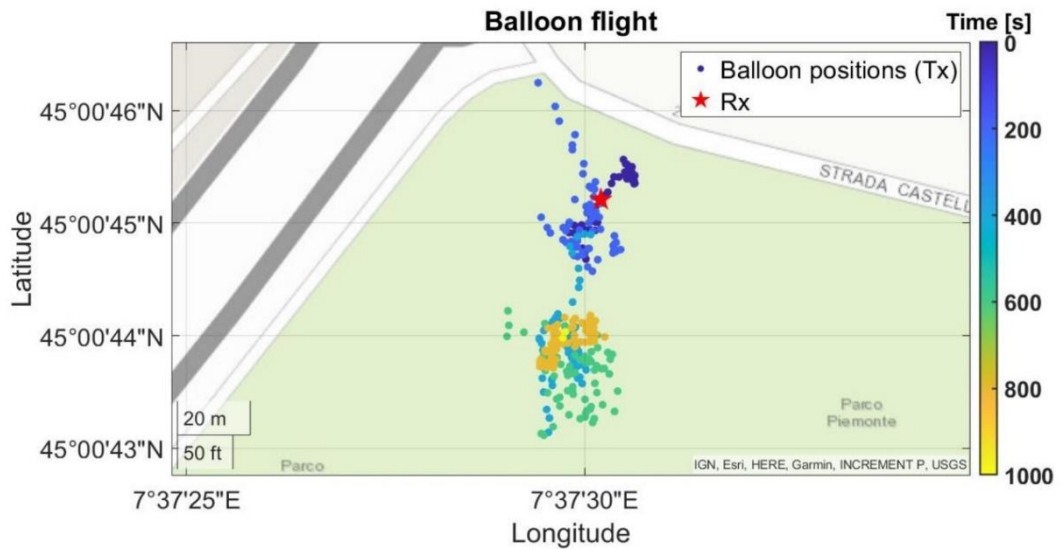


Figure 4.61 Trajectory followed by the radioprobe system (radioprobe board and biodegradable balloon) during the low-atmosphere flight, displayed on a map. The color bar displays the time elapsed.

In addition, although the temperature, pressure and relative humidity measurements were not the scope of this test, Figure 4.62 displays these data to show the radioprobe's ability to also detect these fluctuations.

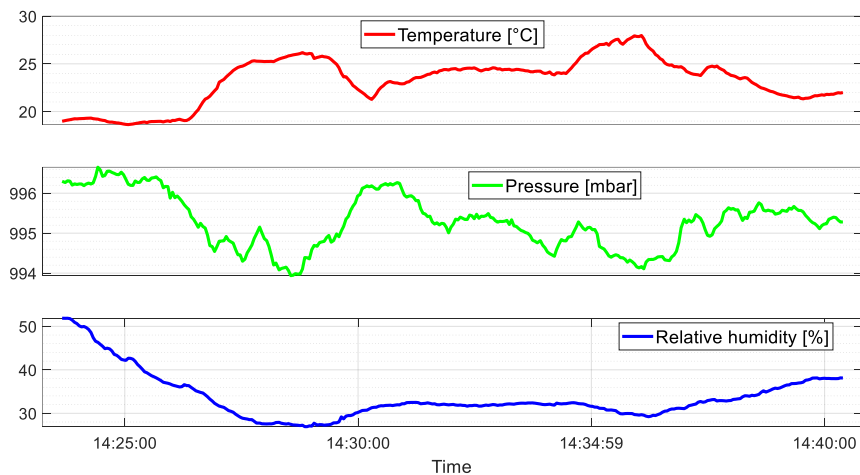


Figure 4.62 Temperature, atmospheric pressure and relative humidity fluctuations measured by the radioprobe sensors during the flight

As result of this test, the operation not only of the tracking and position unit, but also the temperature, pressure, and humidity sensor stage, were evaluated in a low-laying atmospheric environment. The obtained outputs reveal the capability of the radioprobe to sense acceleration, angular rate, and magnetic field fluctuations when being transported inside a real atmosphere. Also, the temperature, pressure, and relative humidity variations along the air travel were successfully detected by the instrument. Regarding the communication link in a dynamic environment, it worked adequately during the completion of the experiment. In total 331 data packets were sent by the radioprobe. The entire set of packets transmitted by the moving system were correctly received by the ground station. The SNR values observed ranged from +9 dB to -12 dB. The RSSI values ranged from -65 dBm to -109 dBm.

Part of this work has been published in the *Journal MDPI Sensors* (Paredes Quintanilla et al., 2021).

4.4 Power Consumption Analysis

As previously mentioned, power consumption is one of the most critical constraints that determines the radioprobe's life span. The energy provided to every single radioprobe operational stage is supplied by the power supply unit, where the power source is given by a primary electrical battery. Various actions were taken to reduce the energy usage of the radioprobe's electronic circuit thus extending the battery lifetime. The main strategies to save power, not only at the architectural level but also at the algorithm level, are explained in the next subsection 4.4.1. The quantification of the system energy consumption is described in subsection 4.4.2.

4.4.1 Power saving strategies

4.4.1.1 Low power design

This strategy was applied at the architectural level as previously mentioned in subsection 3.3.1.5- Power Supply Unit. During the whole design of the radioprobe system, each single component was carefully analyzed and selected to provide an adequate operation according to the project specifications while keeping low power consumption. The selection process considered different options for electronic components and, based on their characteristics and power requirements, the most power-saving ones were selected.

In addition, multiple low voltages were considered for the operation of the different sections of the circuit. This technique allows to save power by providing less energy to certain areas and also to reduce leakage of power. For instance, part of the positioning and tracking measurement unit (GNSS receiver and LNA circuitries) works at 1.8 V, while the rest of the units work at 3.3 V. Instead of incorporating two voltage regulators in the design, the dual LP3996SD voltage regulator was selected to provide both voltage levels to the circuit as can be seen in Figure 4.63.

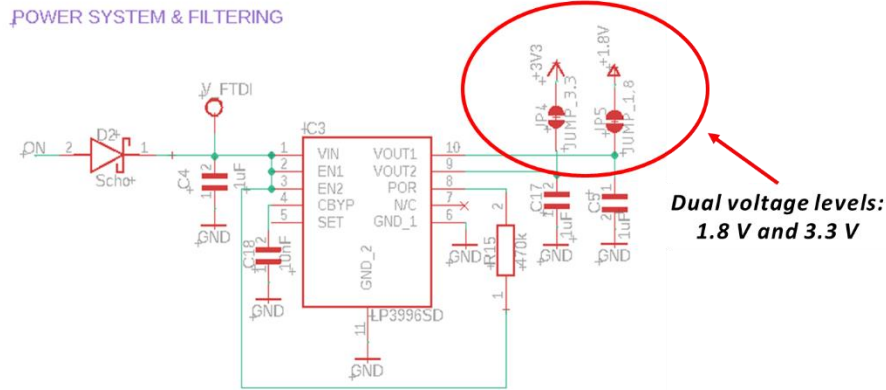


Figure 4.63 Power system and filtering schematic diagram. Different voltage levels of the circuit.

Furthermore, the design includes various isolation points where the different radioprobe blocks can be isolated or disabled according to the user needs. For instance, JP3, JP4 and JP5 (see subsection 3.5.1: Schematic Diagram Design) can be used to connect/disconnect the units working at 1.8 V, the units working at 3.3 V, and the transmission unit. Also, the radioprobe circuit include a low-power LED, which is useful as visual feedback during the execution of a program. It is routed in a way that is normally off and can be enabled/disabled by software.

Another strategy to reduce power consumption was the adoption of electronic components that feature options either to enable/disable their operation or activating low power modes like stand-by and sleep modes. In this way, if certain components or blocks are not required to function, they can be disabled or sent to a power-saving mode thus conserving power.

4.4.1.2 Software control

Another type of strategy to save the radioprobe's power budget was the use of software control techniques. One of them was the usage reduction, to the minimum possible, of the different sensors embedded in the circuit. Their sampling rates were set to the lowest values while allowing the retrieve of adequate amounts of information.

Additionally, since the radio transmission use is one of the main cause of power consumption in battery-powered devices and not only, the LoRa transmission data rates were limited as much as possible. For that, the measurements acquired by the temperature, pressure, humidity and IMU sensors were partially processed at the radioprobe side to downsize the total amount of data to be sent to the ground stations. Also, the data packet numbers were reduced by aggregating two or more messages into a unique data packet. In this manner, a single packet containing more information could be transmitted thus saving power from transmission processes.

Another action taken to improve the power consumption of the system was the software control of the GNSS receiver, which can be considered as the most power-consuming sensor embedded in the radioprobe system. The duty cycle of the GNSS was carefully managed to provide only the essential information required to update the Kalman's filter reference position during the postprocessing stage. It was

controlled to switch on and off over a regular interval of time to get geolocation and time information.

Moreover, the GNSS receiver was programmed to operate only in the super E-mode. This mode allows to have a good performance of the device while decreasing its energy consumption. In fact, when comparing it with previous u-blox versions, this mode provides triple saving of power whilst keeping high degrees of accuracy in speed and positioning (*ZOE-M8B / U-Blox*, 2020). Furthermore, if the GNSS is periodically enabled and disabled, the external LNA can be automatically duty-cycled to extra reduce energy utilization.

4.4.2 Current Consumption Measurement

After applying the different techniques mentioned before to save the available power budget of the radioprobe system, the total current consumption of the tiny radioprobe was properly quantified (Figure 4.64). The measurements were made to a fully operating radioprobe, that is, a microcontroller executing all the tasks and instructions to control the different units, the TPH and IMU sensors continuously acquiring the data of interest, the GNSS receiver working in acquisition and tracking modes, and the transmission system sending the data packets. As a result, the measured average current consumption of the device was approximately 90 mA, with periodic short peaks of 123 mA.

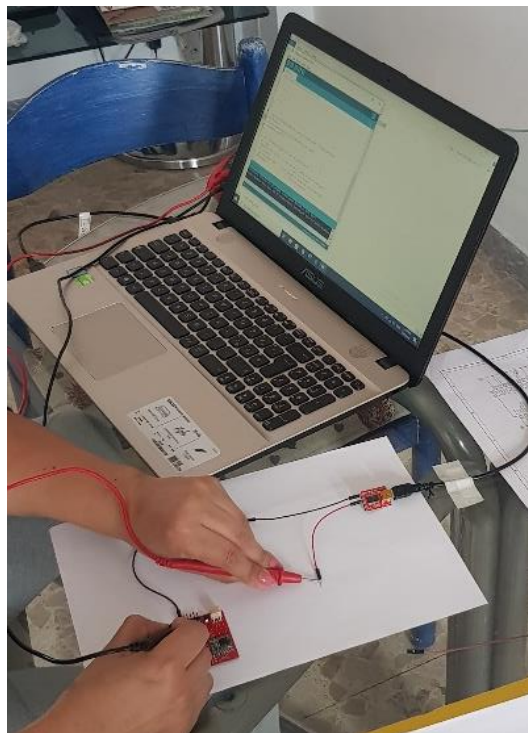


Figure 4.64 Current consumption measurement of a fully operating radioprobe

As a result, when assessing the service life of the selected battery in external conditions, various experimental tests resulted in an alive radioprobe measuring, processing, and sending data for a time span of approximately 60 minutes.

According to this, it is possible to say that the adopted strategies to reduce energy consumption, applied at architectural and software level of the radioprobe design, provided optimal results. The newly developed devices can successfully measure small-scale fluctuations in warm clouds from the inner turbulence time scale, which develops in a time scale of few minutes.

Chapter 5

Conclusions and future work

This PhD. thesis presents the electronic design of a novel in-situ experimental method for the study of small-scale turbulence effects in cloud formation by means of the development of an innovative radioprobe system. This system is based on a WSN and consists of miniaturized radioprobes conceived to passively track small-scale turbulence fluctuations in the Lagrangian description, which gives the uniqueness to this work. Moreover, it includes ground stations able to receive and process the data collected by the tiny radioprobes during their in-cloud travel.

Different areas of research were integrated to implement this work, among them, low power wireless sensor networks communication links, antenna embedding and impedance matching, electronic board design and assembly, wireless sensor nodes, sensors and instrumentation for meteorological measurements, and sensors and instrumentation for device tracing. This knowledge integration allowed the creation of an entire and reliable radioprobe system capable of measuring and conveying meteorological and motion data via a long-range power-saving radio link to the ground stations.

Outcomes from various laboratory and field measurements proved that the newly designed radioprobe board performs satisfactorily and offers accurate data while providing unique attributes for an instrumented weather balloon development. For instance, its compact size (5 cm x 5 cm) and ultra-light weight (7 g without considering the battery) are essential characteristics to ensure a minimal inertia and a minimum volume (compared to the followed trajectory) of the measuring instrument. Also, this allows the easy embedding of the electronics into the balloon and the achievement of the buoyancy required by the system to explore turbulence from the Lagrangian point of view.

In addition, the radioprobe's power autonomy for a time span of approximately 60 minutes, ensures the measurement of small-scale cloud fluctuations from the inner turbulence time scale, which is enough for the scope of this research project.

Furthermore, the radioprobe has been designed to be expendable since its retrieval after the in-cloud measurement is not envisaged. To this end, the instrument includes a communication system that enables it to send wirelessly the collected data to ground.

Moreover, each mini radioprobe embeds different sensors to measure temperature, pressure, and humidity of local inner warm clouds and ambient air. Also, it includes sensors to measure velocity and acceleration fluctuations of the balloon motion along its path, which subsequently (through temporal and spatial–

spectral analysis) will provide wavelength, frequency, and kinetic energy information to describe the properties of shallow warm cloud systems.

In accordance with the atmospheric spectra derived from in-field observations of the atmosphere portion of interest, each radioprobe is able to provide accurate information for the ranges required by the system. For instance, temperature from 0 °C to +30 °C, external pressure from 400 mbar to 1100 mbar, and relative humidity from 0 % RH to 100 % RH. Although these are the expected values inside the cloud observing target, the radioprobe's sensors can accurately measure values beyond the ranges, making the instrument suitable for other applications.

According to the features provided by the low-cost instrumentation embedded in the devices and considering that the physical size of the instrumented balloon (balloon + electronics) will provide an implicit inertia to the system, it can be said that a radioprobe could be able to measure wavelengths in the order of 1 m up to a few km, velocities from 30 cm/s up to 5 m/s, and accelerations up to ± 4 g, which is something that has not been reached before with instrumented balloons working as passive drifters. In fact, these features suggest that the electronics embedded in a 30-centimeters diameter balloon can behave as a quasi Lagrangian marker at the small-scale turbulence domain when released into shallow warm clouds.

The radioprobes can communicate correctly with the ground stations up to 5 km of separation using a low power technology. Considering that the foreseen observational domain in which these devices will work ranges from a few meters in the vertical axis extent and a few kilometers in the horizontal axis extent, this transmission range is enough for the study of a warm cloud (or a part of it) and a section of adjacent air.

Since power consumption is one of the most critical constraints that determines the radioprobe's life span, different strategies were implemented to reduce the energy usage of the radioprobe's electronic circuit. For instance, at the architectural level, every single electronic component was carefully selected based not only on their features but also power requirements. In addition, the PCB was designed to provide different low voltages thus delivering less energy to certain areas and reducing leakage of power. Also, the design offers the possibility of isolating distinct electronic blocks according to the user needs and, electronic components featuring low power operation such as stand-by and sleep modes. In the same way, at the algorithm level, various software control techniques were applied to improve the radioprobe's power budget. Among them are the sensor's usage reduction to the minimum possible while allowing the retrieve of adequate amounts of information, the partial processing of the information at the radioprobe side to downsize the total amount of data to be sent to the ground stations, the merging of different data messages into a unique data packet to reduce the transmission data rates, and the GNSS software control to provide only the essential information required at the lowest power mode. These adopted strategies ensure the radioprobe's power autonomy for a time span sufficient to measure small-scale cloud fluctuations from the inner turbulence time scale.

Referring to the ground stations, they are able to capture the data coming from the radioprobes during the in-cloud flight; to provide signal quality information

(SNR and RSSI); to parse, organize, store, and process the time-based information; and to provide a preliminary graphical output of the information collected.

Given that the final goal of this research project is the generation of an in-field cloud Lagrangian dataset, future work includes the embodiment of the newly designed radioprobe boards into the final bio balloons, and the testing of the complete system in real warm cloud environments over land and alpine environments. To this end, several instrumented balloons working as a single system and transmitting simultaneously the collected cloud data to the ground stations is envisaged. This joint operation will make possible the accurate study of small-scale turbulence effects on warm clouds thus, providing unique information essential to contribute to the current understanding of cloud formation. The cloud-based Lagrangian datasets will be shared with the scientific community through the open access database of the Project COMPLETE.

Some field experiments are planned in the upcoming months to collect in-cloud data with the radioprobe system here presented. A first Lagrangian-based experiment will be conducted at the Environmental Research Station Schneefernerhaus UFS in the German Alps, which is the highest European research station located approximately at 2650 m a.s.l. A second field experiment will be carried out at the Osservatorio astronomico della Valle d'Aosta, which is an astronomical observatory located in the proximity of the Italian Alps.

Since the radioprobe system presented in this PhD thesis is a novel in-situ experimental method for measuring the influence of small-scale turbulence in cloud formation, the patenting process of the complete instrument design (electronics + bio balloon) has started in collaboration with the Technology Transfer and Industrial Liaison Department of the Politecnico di Torino. The areas for the patent application could include:

- Science: microphysics of Earth atmospheric warm clouds
- Meteorology at the meso-scale level, for aviation and surface weather.
- Urban and sub-urban micro-clima

Moreover, a new Proof of Concept Project aimed at the optimization of the current radioprobe version will start next December. This project will be funded by the LINKS Foundation, which is an institution that operates in applied research, innovation, and technology transfer. The optimization process will include weight and size shrinkage of the electronic board, improvement of the microcontroller capabilities, and software optimization.

References

- Adafruit Feather 32u4 RFM95* / *Adafruit*. (n.d.). Adafruit Feather 32u4 RFM95 LoRa Radio- 868 or 915 MHz. Retrieved March 4, 2021, from <https://www.adafruit.com/product/3078>
- Adafruit Ultimate GPS Breakout* / *Adafruit*. (2015). Adafruit Ultimate GPS Breakout - 66 Channel w/10 Hz Updates - Version 3.
- Adelantado, F., Vilajosana, X., Tuset-Peiro, P., Martinez, B., Melia-Segui, J., & Watteyne, T. (2017). Understanding the Limits of LoRaWAN. *IEEE Communications Magazine*, 55(9), 34–40. <https://doi.org/10.1109/MCOM.2017.1600613>
- Agilent Technologies, Inc. (2006). *Advanced Calibration Techniques for Vector Network Analyzers*. 86.
- Akyildiz, I. F., & Vuran, M. C. (2010). *Wireless Sensor Networks*. John Wiley & Sons, Incorporated. <http://ebookcentral.proquest.com/lib/polito-ebooks/detail.action?docID=547208>
- Altium Designer 20.2 User Manual* / *Altium*. (n.d.). Adding Via Stitching & Via Shielding to a PCB in Altium Designer. Retrieved November 24, 2020, from <https://www.altium.com/documentation/altium-designer/via-stitching-and-via-shielding-ad>
- AN3192 *Application note* / *STMicroelectronics*. (2010). <https://www.pololu.com/file/0J434/LSM303DLH-compass-app-note.pdf>
- ANT-868-CW-RCS-xxx / *Linx*. (n.d.). Retrieved March 4, 2021, from <https://www.mouser.cn/datasheet/2/238/ant-868-cw-rcs-1659515.pdf>

Antenna Selection Guide For ISM Bands / Radiocrafts. (2017). WP008: Antenna Selection Guide For ISM Bands.

Application Note AN-00501 / Linx. (n.d.). Retrieved November 4, 2021, from <https://linxtechnologies.com/wp/wp-content/uploads/an-00501.pdf>

Arduino / Arduino. (n.d.). Retrieved March 4, 2021, from <https://www.arduino.cc/>

Arduino Nano / Arduino Official Store. (n.d.). Retrieved December 21, 2020, from <https://store.arduino.cc/arduino-nano>

Arduino—Program Structure / Tutorialspoint. (n.d.). Retrieved March 4, 2021, from https://www.tutorialspoint.com/arduino/arduino_program_structure.htm

AT16802: Antenna Tune Up. (2016). 24.

ATmega32U4 / Microchip. (n.d.). ATmega32U4. Retrieved March 4, 2021, from <https://www.microchip.com/wwwproducts/en/ATmega32u4>

ATmega328P / Microchip. (n.d.). Retrieved November 24, 2020, from <https://www.microchip.com/wwwproducts/en/ATmega328p>

Augustin, A., Yi, J., Clausen, T., & Townsley, W. (2016). A Study of LoRa: Long Range & Low Power Networks for the Internet of Things. *Sensors*, 16(9), 1466. <https://doi.org/10.3390/s16091466>

Automatic sounding station. (n.d.). Retrieved January 26, 2021, from <https://www.vaisala.com/sites/default/files/documents/AS15-Datasheet-B210402EN-G.pdf>

Ayyalasomayajula, S., Gylfason, A., Collins, L. R., Bodenschatz, E., & Warhaft, Z. (2006). Lagrangian Measurements of Inertial Particle Accelerations in Grid Generated Wind Tunnel Turbulence. *Physical Review Letters*, 97(14), 144507. <https://doi.org/10.1103/PhysRevLett.97.144507>

Balanis, C. A. (2005). *Antenna theory: Analysis and design* (3rd ed). John Wiley.

- Basso, T. C., Perotto, G., Musacchio, C., Merlone, A., Athanassiou, A., & Tordella, D. (2020). Evaluation of Mater Bi and Polylactic Acid as materials for biodegradable innovative mini-radiosondes to track small scale fluctuations within clouds. *Materials Chemistry and Physics*, 253, 123411. <https://doi.org/10.1016/j.matchemphys.2020.123411>
- Beals, M. J., Fugal, J. P., Shaw, R. A., Lu, J., Spuler, S. M., & Stith, J. L. (2015). Holographic measurements of inhomogeneous cloud mixing at the centimeter scale. *Science*, 350(6256), 87–90. <https://doi.org/10.1126/science.aab0751>
- Bertoldo, S., Paredes, M., Allegretti, M., Carosso, L., & Lucianaz, C. (2018). *Progress on the realization of a LoRa® based communication system for atmospheric monitoring probes.*
- Bertoldo, S., Paredes, M., Carosso, L., Allegretti, M., & Savi, P. (2019). *Empirical indoor propagation models for LoRa radio link in an office environment.* 5.
- BME280 / BOSCH. (n.d.). BME280 Humidity Sensor Measuring Relative Humidity, Barometric Pressure and Ambient Temperature. Retrieved November 24, 2020, from <https://www.bosch-sensortec.com/products/environmental-sensors/humidity-sensors-bme280/>
- Bodenschatz, E. (2015). Clouds resolved. *Science*, 350(6256), 40–41. <https://doi.org/10.1126/science.aad1386>
- Bodenschatz, E., Malinowski, S. P., Shaw, R. A., & Stratmann, F. (2010). Can We Understand Clouds Without Turbulence? *Science*, 327(5968), 970–971. <https://doi.org/10.1126/science.1185138>
- Bony, S., Stevens, B., Frierson, D. M. W., Jakob, C., Kageyama, M., Pincus, R., Shepherd, T. G., Sherwood, S. C., Siebesma, A. P., Sobel, A. H., Watanabe,

- M., & Webb, M. J. (2015). Clouds, circulation and climate sensitivity. *Nature Geoscience*, 8(4), 261–268. <https://doi.org/10.1038/NGEO2398>
- Brenguier, J.-L., & Bourrianne, T. (1998). Improvements of Droplet Size Distribution Measurements with the Fast-FSSP (Forward Scattering Spectrometer Probe). *JOURNAL OF ATMOSPHERIC AND OCEANIC TECHNOLOGY*, 15, 14.
- Bruyn-Cotton, V. (2012). *Cloud classification*. Own work. (https://commons.wikimedia.org/wiki/File:Cloud_types_en.svg), „Cloud types en“, <https://creativecommons.org/licenses/by-sa/3.0/legalcode>
- Businger, S., Chiswell, S. R., Ulmer, W. C., & Johnson, R. (1996). Balloons as a Lagrangian measurement platform for atmospheric research. *Journal of Geophysical Research: Atmospheres*, 101(D2), 4363–4376. <https://doi.org/10.1029/95JD00559>
- Businger, S., Johnson, R., & Talbot, R. (2006). Scientific Insights from Four Generations of Lagrangian Smart Balloons in Atmospheric Research. *Bulletin of the American Meteorological Society*, 87(11), 1539–1554. <https://doi.org/10.1175/BAMS-87-11-1539>
- C0G (NP0) Dielectric / AVX. (n.d.). Retrieved March 3, 2021, from <https://www.avx.com/products/ceramic-capacitors/surface-mount/c0g-np0-dielectric/>
- Ceramic Resonators. Application Notes. (n.d.). Retrieved March 3, 2021, from https://www.digikey.it/Web%20Export/Supplier%20Content/Abracon_535/PDF/Abracon_AN_CeramicResonator.pdf
- Chang, K., Bench, J., Brege, M., Cantrell, W., Chandrakar, K., Ciochetto, D., Mazzoleni, C., Mazzoleni, L. R., Niedermeier, D., & Shaw, R. A. (2016). A Laboratory Facility to Study Gas–Aerosol–Cloud Interactions in a

- Turbulent Environment: The Π Chamber. *Bulletin of the American Meteorological Society*, 97(12), 2343–2358.
<https://doi.org/10.1175/BAMS-D-15-00203.1>
- Chen, R., Li, Z., Kuligowski, R. J., Ferraro, R., & Weng, F. (2011). A study of warm rain detection using A-Train satellite data. *Geophysical Research Letters*, 38(4). <https://doi.org/10.1029/2010GL046217>
- Chen, S., Yau, M. K., & Bartello, P. (2018). Turbulence Effects of Collision Efficiency and Broadening of Droplet Size Distribution in Cumulus Clouds. *Journal of the Atmospheric Sciences*, 75(1), 203–217.
<https://doi.org/10.1175/JAS-D-17-0123.1>
- Chronograf: Complete Dashboarding Solution for InfluxDB. (n.d.). *InfluxData*. Retrieved March 4, 2021, from <https://www.influxdata.com/time-series-platform/chronograf/>
- Climate system. (2021). In *Wikipedia*.
https://en.wikipedia.org/w/index.php?title=Climate_system&oldid=1008921862
- Climate system / Glossary of Meteorology*. (n.d.). Retrieved March 5, 2021, from https://glossary.ametsoc.org/wiki/Climate_system
- Cloud / Glossary of Meteorology*. (n.d.). Retrieved March 5, 2021, from <https://glossary.ametsoc.org/wiki/Cloud>
- Cloud classification / Glossary of Meteorology*. (n.d.). Retrieved March 11, 2021, from https://glossary.ametsoc.org/wiki/Cloud_classification
- Cloud Classification / NOAA*. (n.d.). Cloud Classification and Characteristics; NOAA's National Weather Service. Retrieved March 11, 2021, from https://www.weather.gov/lmk/cloud_classification

- Cloud classification summary* / WMO. (n.d.). International Cloud Atlas. Retrieved March 24, 2021, from <https://cloudatlas.wmo.int/cloud-classification-summary.html>
- Cloud development* / Oklahoma Climatological Survey. (n.d.). Retrieved March 5, 2021, from <https://okfirst.mesonet.org/train/meteorology/Clouds.html>
- Cloud names and classifications* / Met Office. (n.d.). Met Office. Retrieved March 11, 2021, from <https://www.metoffice.gov.uk/weather/learn-about/weather/types-of-weather/clouds/cloud-names-classifications>
- Cloudwatcher, T. G. (2011). *Altostratus cloud*. Own work. (https://commons.wikimedia.org/wiki/File:Altostratus_undulatus.jpg), „Altostratus undulatus“, <https://creativecommons.org/licenses/by-sa/3.0/legalcode>
- Cloudy Earth* / NASA. (2015, May 8). [Text.Article]. NASA Earth Observatory. <https://earthobservatory.nasa.gov/images/85843/cloudy-earth>
- Cooper, K. B., & Chattopadhyay, G. (2014). Submillimeter-Wave Radar: Solid-State System Design and Applications. *IEEE Microwave Magazine*, 15(7), 51–67. <https://doi.org/10.1109/MMM.2014.2356092>
- Cooper, W. A., Lasher-Trapp, S. G., & Blyth, A. M. (2013). The Influence of Entrainment and Mixing on the Initial Formation of Rain in a Warm Cumulus Cloud. *Journal of the Atmospheric Sciences*, 70(6), 1727–1743. <https://doi.org/10.1175/JAS-D-12-0128.1>
- Cloud-MicroPhysics-Turbulence-Telemetry: An inter-multidisciplinary training network for enhancing the understanding and modeling of atmospheric clouds* / COMPLETE Project / H2020 / CORDIS / European Commission. (2015). Retrieved November 23, 2020, from <https://cordis.europa.eu/project/id/675675>

- Couch-scratching-cats. (2021). *Stratocumulus cloud*. Own work.
https://commons.wikimedia.org/wiki/File:Flat_Stratocumulus_Cloud.jpg
- Croce, D., Gucciardo, M., Mangione, S., Santaromita, G., & Tinnirello, I. (2018). Impact of LoRa Imperfect Orthogonality: Analysis of Link-Level Performance. *IEEE Communications Letters*, 22(4), 796–799.
<https://doi.org/10.1109/LCOMM.2018.2797057>
- CSTNE8M00GH5L000R0 / Murata. (n.d.). Retrieved March 3, 2021, from
<https://www.murata.com/en-eu/products/productdetail?partno=CSTNE8M00GH5L000R0>
- Dabberdt, W. F., Shellhorn, R., Cole, H., Paukkunen, A., Hörhammer, J., & Antikainen, V. (2003). RADIOSONDES. In J. R. Holton (Ed.), *Encyclopedia of Atmospheric Sciences* (pp. 1900–1913). Academic Press.
<https://doi.org/10.1016/B0-12-227090-8/00344-4>
- Descriptions of Fluid Flows* / The Pennsylvania State University. (2020).
https://www.me.psu.edu/cimbala/Learning/Fluid/Introductory/descriptions_of_fluid_flows.htm
- Devenish, B. J., Bartello, P., Malinowski, S. P., Reeks, M. W., & Vassilicos, J. C. (2012). *Droplet growth in warm turbulent clouds*. 29.
- Doerenbecher, A., Basdevant, C., Drobinski, P., Durand, P., Fesquet, C., Bernard, F., Cocquerez, P., Verdier, N., & Vargas, A. (2016). Low-Atmosphere Drifting Balloons: Platforms for Environment Monitoring and Forecast Improvement. *Bulletin of the American Meteorological Society*, 97(9), 1583–1599. <https://doi.org/10.1175/BAMS-D-14-00182.1>
- Dubovik, O., Schuster, G. L., Xu, F., Hu, Y., Bösch, H., Landgraf, J., & Li, Z. (2021). Grand Challenges in Satellite Remote Sensing. *Frontiers in Remote Sensing*, 2, 1. <https://doi.org/10.3389/frsen.2021.619818>

- EAGLE* / Autodesk. (n.d.). *EAGLE | PCB Design And Electrical Schematic Software* | Autodesk. Retrieved March 4, 2021, from <https://www.autodesk.com/products/eagle/overview>
- EAGLE* (program). (2021). In *Wikipedia*. [https://en.wikipedia.org/w/index.php?title=EAGLE_\(program\)&oldid=1009578641](https://en.wikipedia.org/w/index.php?title=EAGLE_(program)&oldid=1009578641)
- Elert, G. (n.d.). *Buoyancy*. The Physics Hypertextbook. Retrieved March 19, 2021, from <https://physics.info/buoyancy/>
- Ernst, O. (2017). *Cumulus cloud, Swabian Alps.jpg*—*Wikipedia*. (https://commons.wikimedia.org/wiki/File:Cumulus_cloud,_Swabian_Alps.jpg), <https://creativecommons.org/licenses/by-sa/4.0/legalcode>
- ETSI EN 300 220-2*. (n.d.). Retrieved November 24, 2020, from https://www.etsi.org/deliver/etsi_en/300200_300299/30022002/03.02.01_60/en_30022002v030201p.pdf
- Eugster, S. A. (2011). *Cirrus clouds*. Own work. Simon A. Eugster (https://commons.wikimedia.org/wiki/File:Cirrus_clouds_with_3D_look.jpg), „Cirrus clouds with 3D look“, <https://creativecommons.org/licenses/by-sa/3.0/legalcode>
- Fletcher, S. J. (2017). Observations. In *Data Assimilation for the Geosciences* (pp. 599–626). Elsevier. <https://doi.org/10.1016/B978-0-12-804444-5.00014-3>
- Geerts, B., Raymond, D. J., Grubišić, V., Davis, C. A., Barth, M. C., Detwiler, A., Klein, P. M., Lee, W.-C., Markowski, P. M., Mullendore, G. L., & Moore, J. A. (2018). Recommendations for In Situ and Remote Sensing Capabilities in Atmospheric Convection and Turbulence. *Bulletin of the American Meteorological Society*, 99(12), 2463–2470. <https://doi.org/10.1175/BAMS-D-17-0310.1>

- Gerashchenko, S., Sharp, N. S., Neuscamman, S., & Warhaft, Z. (2008). Lagrangian measurements of inertial particle accelerations in a turbulent boundary layer. *Journal of Fluid Mechanics*, 617, 255–281. <https://doi.org/10.1017/S0022112008004187>
- Gifford, F. (1955). A SIMULTANEOUS LAGRANGIAN-EULERIAN TURBULENCE EXPERIMENT. *Monthly Weather Review*, 83(12), 293–301. [https://doi.org/10.1175/1520-0493\(1955\)083<0293:ASLTE>2.0.CO;2](https://doi.org/10.1175/1520-0493(1955)083<0293:ASLTE>2.0.CO;2)
- Global Energy Budget / NASA GPM*. (n.d.). Precipitation Education. Global Energy Budget. Retrieved August 24, 2021, from <https://gpm.nasa.gov/education/lesson-plans/global-energy-budget>
- GNSS applications. (2021). In *Wikipedia*. https://en.wikipedia.org/w/index.php?title=GNSS_applications&oldid=999491319
- GNSS-Ceramic-Chip-Antenna_AA088.pdf* (2020). Retrieved 4 January 2021, from https://www.unictron.com/antenna-embedded/wp-content/uploads/sites/6/2020/11/GNSS_Chip_Antenna321605-AA088_spec-IH2U14W1H2A0100.pdf. *GNSS_Chip_Antenna321605-AA088_spec-IH2U14W1H2A0100.pdf*. (n.d.). Retrieved January 4, 2021, from https://www.unictron.com/antenna-embedded/wp-content/uploads/sites/6/2020/11/GNSS_Chip_Antenna321605-AA088_spec-IH2U14W1H2A0100.pdf
- Golshan, M., Abdunabiev, S., Tomatis, M., Fraternali, F., Vanni, M., & Tordella, D. (2021). Intermittency acceleration of water droplet population dynamics inside the interfacial layer between cloudy and clear air environments. *International Journal of Multiphase Flow*, 140, 103669. <https://doi.org/10.1016/j.ijmultiphaseflow.2021.103669>

- GPS coordinates, latitude and longitude with interactive Maps.* (2021).
<https://www.gps-coordinates.net/>
- Grabowski, W. W., & Wang, L.-P. (2012). *Growth of Cloud Droplets in a Turbulent Environment*. 34.
- Hartmann, D. L. (2016). *Global Physical Climatology*. Elsevier.
- Hearts, K. of. (2010). *Cirrocumulus clouds*. Own work.
 (https://commons.wikimedia.org/wiki/File:Cirrocumulus_clouds_Thousand_Oaks_July_2010.jpg), „Cirrocumulus clouds Thousand Oaks July 2010“,
<https://creativecommons.org/licenses/by-sa/3.0/legalcode>
- Heintzenberg, J., & Charlson, R. J. (Eds.). (2009). *Clouds in the perturbed climate system: Their relationship to energy balance, atmospheric dynamics, and precipitation*. MIT Press.
- Hoffmann, F., Yamaguchi, T., & Feingold, G. (2019). Inhomogeneous Mixing in Lagrangian Cloud Models: Effects on the Production of Precipitation Embryos. *Journal of the Atmospheric Sciences*, 76(1), 113–133.
<https://doi.org/10.1175/JAS-D-18-0087.1>
- Hoppel, W. A., Frick, G. M., Fitzgerald, J. W., & Wattle, B. J. (1994). A Cloud Chamber Study of the Effect That Nonprecipitating Water Clouds Have on the Aerosol Size Distribution. *Aerosol Science and Technology*, 20(1), 1–30. <https://doi.org/10.1080/02786829408959660>
- How Do Clouds Form? | NASA.* (n.d.). NASA Climate Kids. Retrieved March 5, 2021, from <https://climatekids.nasa.gov/cloud-formation/>
- How to Properly Implement Chip Antennas | Laird Connectivity.* (n.d.). Retrieved March 3, 2021, from <https://www.lairdconnect.com/resources/white-papers/how-to-implement-chip-antennas>

Hubbert, J. C., Wilson, J. W., Weckwerth, T. M., Ellis, S. M., Dixon, M., & Loew, E. (2018). S-Pol's Polarimetric Data Reveal Detailed Storm Features (and Insect Behavior). *Bulletin of the American Meteorological Society*, 99(10), 2045–2060. <https://doi.org/10.1175/BAMS-D-17-0317.1>

Hygroscopic Nucleus / *Encyclopedia.com*. (n.d.). Retrieved March 5, 2021, from <https://www.encyclopedia.com/earth-and-environment/ecology-and-environmentalism/environmental-studies/hygroscopic-nucleus>

Inertial measurement unit. (2021). In *Wikipedia*. https://en.wikipedia.org/w/index.php?title=Inertial_measurement_unit&oldid=1007636024

InfluxDB. (2021). In *Wikipedia*. <https://en.wikipedia.org/w/index.php?title=InfluxDB&oldid=1002006739>

InfluxDB Open Source Time Series Database | InfluxDB. (n.d.). *InfluxData*. Retrieved March 4, 2021, from <https://www.influxdata.com/products/influxdb-overview/>

Intergovernmental Panel on Climate Change. (2014). Clouds and Aerosols. In *Climate Change 2013 – The Physical Science Basis: Working Group I Contribution to the Fifth Assessment Report of the Intergovernmental Panel on Climate Change* (pp. 571–658). Cambridge University Press. <https://doi.org/10.1017/CBO9781107415324.016>

Interp1 / *MathWorks*. (n.d.). 1-D Data Interpolation (Table Lookup) - MATLAB Interp1. Retrieved January 28, 2021, from <https://it.mathworks.com/help/matlab/ref/interp1.html>

Iribarne, J. V., & Cho, H.-R. (1980). Atmospheric Dynamics. In J. V. Iribarne & H.-R. Cho (Eds.), *Atmospheric Physics* (pp. 149–197). Springer Netherlands. https://doi.org/10.1007/978-94-009-8952-8_7

- Unictron-ISM-868MHz-Ceramic-Chip-Antenna_AA071.pdf*. (2020). Retrieved January 4, 2021, from http://unictron.com/antenna-embedded/wp-content/uploads/sites/6/2020/11/Unictron-ISM-868MHz-Ceramic-Chip-Antenna-503005-AA701-H2U64U1H2B0200_spec-%EF%BC%AD.pdf
- Isopycnic surface* / *Glossary of Meteorology*. (n.d.). American Meteorology Society. Retrieved March 1, 2021, from https://glossary.ametsoc.org/wiki/Isopycnic_surface
- Jekeli, C. (2000). *Inertial Navigation Systems with Geodetic Applications*. De Gruyter, Inc, De Gruyter.
- Kalman filter. (2021). In *Wikipedia*. https://en.wikipedia.org/w/index.php?title=Kalman_filter&oldid=1008080480
- Katul, G. G., Geron, C. D., Hsieh, C.-I., Vidakovic, B., & Guenther, A. B. (1998). Active Turbulence and Scalar Transport near the Forest–Atmosphere Interface. *Journal of Applied Meteorology and Climatology*, 37(12), 1533–1546. [https://doi.org/10.1175/1520-0450\(1998\)037<1533:ATASTN>2.0.CO;2](https://doi.org/10.1175/1520-0450(1998)037<1533:ATASTN>2.0.CO;2)
- Keysight Technologies. (n.d.). *1-Port Calibration (reflection test)*. Retrieved January 4, 2021, from http://ena.support.keysight.com/e5071c/manuals/webhelp/eng/measurement/calibration/basic_calibrations/1_port_calibration_reflection_test.htm
- Kim, Y., & Bang, H. (2019). Introduction to Kalman Filter and Its Applications. In F. Govaers (Ed.), *Introduction and Implementations of the Kalman Filter*. IntechOpen. <https://doi.org/10.5772/intechopen.80600>

- Kok, M., & Schon, T. B. (2016). Magnetometer Calibration Using Inertial Sensors. *IEEE Sensors Journal*, 16(14), 5679–5689. <https://doi.org/10.1109/JSEN.2016.2569160>
- Kräuchi, A., Philipona, R., Romanens, G., Hurst, D. F., Hall, E. G., & Jordan, A. F. (2016). Controlled weather balloon ascents and descents for atmospheric research and climate monitoring. *Atmospheric Measurement Techniques*, 9(3), 929–938. <https://doi.org/10.5194/amt-9-929-2016>
- Kumar, B., Götzfried, P., Suresh, N., Schumacher, J., & Shaw, R. A. (2018). Scale Dependence of Cloud Microphysical Response to Turbulent Entrainment and Mixing. *Journal of Advances in Modeling Earth Systems*, 9.
- Kumar, B., Schumacher, J., & Shaw, R. A. (2014). Lagrangian Mixing Dynamics at the Cloudy–Clear Air Interface. *Journal of the Atmospheric Sciences*, 71(7), 2564–2580. <https://doi.org/10.1175/JAS-D-13-0294.1>
- Lagrangian and Eulerian specification of the flow field. (2021). In *Wikipedia*. https://en.wikipedia.org/w/index.php?title=Lagrangian_and_Eulerian_specification_of_the_flow_field&oldid=1010012021
- Lamb, D., & Verlinde, J. (2011). *Physics and Chemistry of Clouds*. Cambridge University Press. <http://ebookcentral.proquest.com/lib/polito-ebooks/detail.action?docID=807307>
- Lau, K. M., & Wu, H. T. (2003). Warm rain processes over tropical oceans and climate implications: WARM RAIN PROCESSES OVER TROPICAL OCEANS. *Geophysical Research Letters*, 30(24). <https://doi.org/10.1029/2003GL018567>
- Lavric, A., & Popa, V. (2017). Internet of Things and LoRaTM Low-Power Wide-Area Networks: A survey. *2017 International Symposium on Signals*,

<https://doi.org/10.1109/ISSCS.2017.8034915>

Le Nguyen Binh. (2017). *Wireless and Guided Wave Electromagnetics* (1st ed.). CRC Press.

Le Treut, H., Somerville, R., Cubasch, U., Ding, Y., Mauritzen, C., Mokssit, A., Peterson, T., & Prather, M. (2007). *Historical Overview of Climate Change Science. Chapter 1*. <https://www.osti.gov/etdeweb/biblio/20962163>

Lehmann, K., Siebert, H., & Shaw, R. A. (2009). Homogeneous and Inhomogeneous Mixing in Cumulus Clouds: Dependence on Local Turbulence Structure. *Journal of the Atmospheric Sciences*, 66(12), 3641–3659. <https://doi.org/10.1175/2009JAS3012.1>

Lehmann, K., Siebert, H., Wendisch, M., & Shaw, R. A. (2007). Evidence for inertial droplet clustering in weakly turbulent clouds. *Tellus B: Chemical and Physical Meteorology*, 59(1), 57–65. <https://doi.org/10.1111/j.1600-0889.2006.00229.x>

Lévêque, E. (2006). An introduction to turbulence in fluids, and modelling aspects. *EAS Publications Series*, 21, 7–42. <https://doi.org/10.1051/eas:2006105>

Li, X.-Y., Brandenburg, A., Svensson, G., Haugen, N. E. L., Mehlig, B., & Rogachevskii, I. (2018). Effect of Turbulence on Collisional Growth of Cloud Droplets. *Journal of the Atmospheric Sciences*, 75(10), 3469–3487. <https://doi.org/10.1175/JAS-D-18-0081.1>

Liu, C., & Zipser, E. J. (2009). “Warm Rain” in the Tropics: Seasonal and Regional Distributions Based on 9 yr of TRMM Data. *Journal of Climate*, 22(3), 767–779. <https://doi.org/10.1175/2008JCLI2641.1>

Lopez, J. (2008). *Wireless Sensor Network Security*.

- LoRa Applications* / Semtech. (n.d.). Retrieved March 3, 2021, from <https://www.semtech.com/loralora-applications>
- LoRaWAN Modulation settings (EU band)* / IoTNET. (n.d.). Retrieved March 3, 2021, from <https://www.iotnet.eu/wp/characteristics-and-advantages/>
- Low Altitude Balloon Measurement Platforms*. (n.d.). Retrieved January 20, 2021, from https://www.arl.noaa.gov/wp_arl/wp-content/uploads/Review/Posters/Balloon.pdf
- LP3996* / Texas Instruments. (n.d.). Retrieved February 10, 2021, from https://www.ti.com/lit/ds/snvs360d/snvs360d.pdf?ts=1612959466078&ref_url=https%253A%252F%252Fwww.google.com%252F
- LSM9DS1* / STMicroelectronics. (n.d.). LSM9DS1 - 9-Axis INEMO Inertial Module (IMU): 3D Magnetometer, 3D Accelerometer, 3D Gyroscope with I2C and SPI - STMicroelectronics. Retrieved March 3, 2021, from <https://www.st.com/en/mems-and-sensors/lsm9ds1.html>
- Lu, J., Fugal, J. P., Nordsiek, H., Saw, E. W., A Shaw, R., & Yang, W. (2008). Lagrangian particle tracking in three dimensions via single-camera in-line digital holography. *New Journal of Physics*, 10(12), 125013. <https://doi.org/10.1088/1367-2630/10/12/125013>
- Ludwig, S. A., Burnham, K. D., Jiménez, A. R., & Touma, P. A. (2018). *Comparison of attitude and heading reference systems using foot mounted MIMU sensor data: Basic, Madgwick, and Mahony*. 10598, 105982L-105982L – 7. <https://doi.org/10.1117/12.2296568>
- Madgwick, S. O. H. (2010). *An efficient orientation filter for inertial and inertial / magnetic sensor arrays*. /paper/An-efficient-orientation-filter-for-inertial-and-%2F-Madgwick/bfb456caf5e71d426bd3e2fd529ee833a6c3b7e7

- Madgwick, S. O. H., Harrison, A. J. L., & Vaidyanathan, R. (2011). Estimation of IMU and MARG orientation using a gradient descent algorithm. *2011 IEEE International Conference on Rehabilitation Robotics*, 1–7.
<https://doi.org/10.1109/ICORR.2011.5975346>
- Malik, N. A. (2018). Turbulent particle pair diffusion: A theory based on local and non-local diffusional processes. *PLOS ONE*, 13(10), e0202940.
<https://doi.org/10.1371/journal.pone.0202940>
- Malinowski, S. P., Gerber, H., Jen-La Plante, I., Kopec, M. K., Kumala, W., Nurowska, K., Chuang, P. Y., Khelif, D., & Haman, K. E. (2013). Physics of Stratocumulus Top (POST): Turbulent mixing across capping inversion. *Atmospheric Chemistry and Physics*, 13(24), 12171–12186.
<https://doi.org/10.5194/acp-13-12171-2013>
- Markowski, P. M., Richardson, Y. P., Richardson, S. J., & Petersson, A. (2018). Aboveground Thermodynamic Observations in Convective Storms from Balloonborne Probes Acting as Pseudo-Lagrangian Drifters. *Bulletin of the American Meteorological Society*, 99(4), 711–724.
<https://doi.org/10.1175/BAMS-D-17-0204.1>
- Merlone, A., Lopardo, G., Sanna, F., Bell, S., Benyon, R., Bergerud, R. A., Bertiglia, F., Bojkovski, J., Böse, N., Brunet, M., Cappella, A., Coppa, G., del Campo, D., Dobre, M., Drnovsek, J., Ebert, V., Emardson, R., Fernicola, V., Flakiewicz, K., ... Underwood, R. (2015). The MeteoMet project - metrology for meteorology: Challenges and results: The MeteoMet project - metrology for meteorology. *Meteorological Applications*, 22, 820–829.
<https://doi.org/10.1002/met.1528>
- Mitzner, K. (2007). *Complete PCB design using OrCad capture and layout*. Elsevier/Newnes.

National Research Council. (2007). *Earth Science and Applications from Space: National Imperatives for the Next Decade and Beyond*.

Niedermeier, D., Voigtländer, J., Schmalfuß, S., Busch, D., Schumacher, J., Shaw, R. A., & Stratmann, F. (2020). Characterization and first results from LACIS-T: A moist-air wind tunnel to study aerosol–cloud–turbulence interactions. *Atmospheric Measurement Techniques*, 13(4), 2015–2033. <https://doi.org/10.5194/amt-13-2015-2020>

Nimbostratus cloud. (2021). In *Wikipedia*. https://en.wikipedia.org/w/index.php?title=Nimbostratus_cloud&oldid=1001360174

NJG1143UA2. (n.d.). Products. Retrieved March 3, 2021, from [/electronic_device/products/NJG1143UA2.html](https://www.nj.gov/electronic_device/products/NJG1143UA2.html)

Node-RED. (n.d.). Retrieved March 4, 2021, from <https://nodered.org/>

Noureldin, A., Karamat, T. B., & Georgy, J. (2012). *Fundamentals of Inertial Navigation, Satellite-based Positioning and their Integration*. Springer Science & Business Media.

Nowacki, K. (2020). *Cumulonimbus incus nad Warszawq, Polska*. Own work. (https://commons.wikimedia.org/wiki/File:Cumulonimbus_incus_over_Warsaw,_Poland.jpg), <https://creativecommons.org/licenses/by-sa/4.0/legalcode>

Nuijens, L., Emanuel, K., Masunaga, H., & L’Ecuyer, T. (2017). Implications of Warm Rain in Shallow Cumulus and Congestus Clouds for Large-Scale Circulations. *Surveys in Geophysics*, 38(6), 1257–1282. <https://doi.org/10.1007/s10712-017-9429-z>

P9371A VNA / Keysight. (n.d.). P9371A Keysight Streamline USB Vector Network Analyzer, 6.5 GHz. Retrieved January 4, 2021, from

<https://www.keysight.com/en/pdx-2916408-pn-P9371A/keysight-streamline-series-usb-vector-network-analyzer?cc=IT&lc=ita>

Panahandeh, G., Skog, I., & Jansson, M. (2010). Calibration of the accelerometer triad of an inertial measurement unit, maximum likelihood estimation and Cramér-Rao bound. *2010 International Conference on Indoor Positioning and Indoor Navigation*, 1–6. <https://doi.org/10.1109/IPIN.2010.5646832>

Parametri ambientali | INRiM. (n.d.). Misure Riferibili Di Parametri Climatici Locali. Retrieved January 28, 2021, from <http://in.inrim.it/luc/meteo/index.php>

Paredes, M., Bertoldo, S., Carosso, L., Lucianaz, C., Marchetta, E., Allegretti, M., & Savi, P. (2019). Propagation measurements for a LoRa network in an urban environment. *Journal of Electromagnetic Waves and Applications*, 33(15), 2022–2036. <https://doi.org/10.1080/09205071.2019.1661287>

Paredes Quintanilla, M. E., Abdunabiev, S., Allegretti, M., Merlone, A., Musacchio, C., Pasero, E. G. A., Tordella, D., & Canavero, F. (2021). Innovative Mini Ultralight Radioprobes to Track Lagrangian Turbulence Fluctuations within Warm Clouds: Electronic Design. *Sensors*, 21(4), 1351. <https://doi.org/10.3390/s21041351>

PiccoloNamek. (2005). *Stratus nebulosus opacus cloud*. Own work. (<https://commons.wikimedia.org/wiki/File:Stratus-Opacus-Uniformis.jpg>), „Stratus-Opacus-Uniformis“, <https://creativecommons.org/licenses/by-sa/3.0/legalcode>

Picture Climate: Balloons Aren't Just for Birthdays | NOAA. (n.d.). Retrieved November 24, 2020, from <https://www.ncdc.noaa.gov/news/picture-climate-balloons-aren%E2%80%99t-just-birthdays>

- Pinsky, M. B., Khain, A. P., Grits, B., & Shapiro, M. (2006). Collisions of Small Drops in a Turbulent Flow. Part III: Relative Droplet Fluxes and Swept Volumes. *Journal of the Atmospheric Sciences*, 63(8), 2123–2139. <https://doi.org/10.1175/JAS3730.1>
- Pöllö. (2010). *English: Smoke plumes from the chimneys of a power plant in Helsinki, Finland.* Own work. (https://commons.wikimedia.org/wiki/File:Smoke_plume_from_power_plant_chimney.jpg), „Smoke plume from power plant chimney“, Excerpt and additional information by Miryam Paredes, <https://creativecommons.org/licenses/by/3.0/legalcode>
- Pommereau, J.-P. (2003). OBSERVATION PLATFORMS | Balloons. In *Encyclopedia of Atmospheric Sciences* (pp. 1429–1438). Elsevier. <https://doi.org/10.1016/B0-12-227090-8/00254-2>
- Pozar, D. M. (2012). *Microwave engineering / David M. Pozar* (4th ed). Wiley.
- Pumir, A., & Wilkinson, M. (2016). Collisional Aggregation Due to Turbulence. *Annual Review of Condensed Matter Physics*, 7(1), 141–170. <https://doi.org/10.1146/annurev-conmatphys-031115-011538>
- Radiosonde. (2020). In *Wikipedia*. <https://en.wikipedia.org/w/index.php?title=Radiosonde&oldid=996615579>
- Radiosondes / NOAA*. (n.d.). Radiosondes; NOAA’s National Weather Service. Retrieved August 24, 2021, from <https://www.weather.gov/jetstream/radiosondes>
- Radkevich, A., Lovejoy, S., Strawbridge, K. B., Schertzer, D., & Lilley, M. (2008). Scaling turbulent atmospheric stratification. III: Space–time stratification of passive scalars from lidar data. *Quarterly Journal of the Royal Meteorological Society*, 134(631), 317–335. <https://doi.org/10.1002/qj.203>

- Raza, U., Kulkarni, P., & Sooriyabandara, M. (2017). Low Power Wide Area Networks: An Overview. *IEEE Communications Surveys & Tutorials*, 19(2), 855–873. <https://doi.org/10.1109/COMST.2017.2652320>
- Reduced instruction set computer. (2021). In *Wikipedia*. https://en.wikipedia.org/w/index.php?title=Reduced_instruction_set_compiler&oldid=1007274003
- RFM95W / HOPERF. (n.d.). RFM95W LoRa Module. Retrieved November 24, 2020, from <https://www.hoperf.com/modules/lora/RFM95.html>
- Richardson, L. F., & Walker, G. T. (1926). Atmospheric diffusion shown on a distance-neighbour graph. *Proceedings of the Royal Society of London. Series A, Containing Papers of a Mathematical and Physical Character*, 110(756), 709–737. <https://doi.org/10.1098/rspa.1926.0043>
- Rizzi, M., Ferrari, P., Flammini, A., & Sisinni, E. (2017). Evaluation of the IoT LoRaWAN Solution for Distributed Measurement Applications. *IEEE TRANSACTIONS ON INSTRUMENTATION AND MEASUREMENT*, 66(12), 10.
- Rubinstein, F. (2007). *Altocumulus cloud*. Own work. (https://commons.wikimedia.org/wiki/File:Altocumulus_cloud.jpg), „Altocumulus cloud“, <https://creativecommons.org/licenses/by-sa/3.0/legalcode>
- Salazar, J. P. L. C., Jong, J. D., Cao, L., Woodward, S. H., Meng, H., & Collins, L. R. (2008). Experimental and numerical investigation of inertial particle clustering in isotropic turbulence. *Journal of Fluid Mechanics*, 600, 245–256. <https://doi.org/10.1017/S0022112008000372>
- Schematic design* / Autodesk. (n.d.). Fusion 360 Help | Schematic Design. Retrieved March 4, 2021, from

<https://help.autodesk.com/view/fusion360/ENU/?guid=ECD->

SCHEMATIC

- Schmidt, J. M., Flatau, P. J., Harasti, P. R., Yates, Robert. D., Delene, D. J., Gapp, N. J., Kohri, W. J., Vetter, J. R., Nachamkin, J. E., Parent, M. G., Hoover, J. D., Anderson, M. J., Green, S., & Bennett, J. E. (2019). Radar Detection of Individual Raindrops. *Bulletin of the American Meteorological Society*, 100(12), 2433–2450. <https://doi.org/10.1175/BAMS-D-18-0130.1>
- Shaw, R. A. (2003). Particle-turbulence interactions in atmospheric clouds. *Annual Review of Fluid Mechanics*, 35(1), 183–227. <https://doi.org/10.1146/annurev.fluid.35.101101.161125>
- Shaw, R. A., Cantrell, W., Chen, S., Chuang, P., Donahue, N., Feingold, G., Kollias, P., Korolev, A., Kreidenweis, S., Krueger, S., Mellado, J. P., Niedermeier, D., & Xue, L. (2020). Cloud–Aerosol–Turbulence Interactions: Science Priorities and Concepts for a Large-Scale Laboratory Facility. *Bulletin of the American Meteorological Society*, 101(7), E1026–E1035. <https://doi.org/10.1175/BAMS-D-20-0009.1>
- Shew, W. L., Gasteuil, Y., Gibert, M., Metz, P., & Pinton, J.-F. (2007). Instrumented tracer for Lagrangian measurements in Rayleigh–Bénard convection. *Review of Scientific Instruments*, 78(6), 065105. <https://doi.org/10.1063/1.2745717>
- Siebert, H., Franke, H., Lehmann, K., Maser, R., Saw, E. W., Schell, D., Shaw, R. A., & Wendisch, M. (2006). Probing Finescale Dynamics and Microphysics of Clouds with Helicopter-Borne Measurements. *Bulletin of the American Meteorological Society*, 87(12), 1727–1738. <https://doi.org/10.1175/BAMS-87-12-1727>

- Siebert, H., Gerashchenko, S., Gylfason, A., Lehmann, K., Collins, L. R., Shaw, R. A., & Warhaft, Z. (2010). Towards understanding the role of turbulence on droplets in clouds: In situ and laboratory measurements. *Atmospheric Research*, 97(4), 426–437. <https://doi.org/10.1016/j.atmosres.2010.05.007>
- Siebert, H., Lehmann, K., & Shaw, R. A. (2007). On the Use of Hot-Wire Anemometers for Turbulence Measurements in Clouds. *Journal of Atmospheric and Oceanic Technology*, 24(6), 980–993. <https://doi.org/10.1175/JTECH2018.1>
- Siebert, H., Lehmann, K., & Wendisch, M. (2006). Observations of Small-Scale Turbulence and Energy Dissipation Rates in the Cloudy Boundary Layer. *JOURNAL OF THE ATMOSPHERIC SCIENCES*, 63, 16.
- Siebert, H., Shaw, R. A., Ditas, J., Schmeissner, T., Malinowski, S. P., Bodenschatz, E., & Xu, H. (2015). High-resolution measurement of cloud microphysics and turbulence at a mountaintop station. *Atmos. Meas. Tech.*, 10.
- Siebert, H., Shaw, R. A., & Warhaft, Z. (2010). Statistics of Small-Scale Velocity Fluctuations and Internal Intermittency in Marine Stratocumulus Clouds. *Journal of the Atmospheric Sciences*, 67(1), 262–273. <https://doi.org/10.1175/2009JAS3200.1>
- Sistema automatico di radiosondaggio dell'atmosfera | Arpa Piemonte.* (n.d.). [Pagina]. Sistema automatico di radiosondaggio dell'atmosfera. Retrieved January 26, 2021, from <http://www.arpa.piemonte.it/approfondimenti/temi-ambientali/meteorologia-e-clima/meteo/sistema-automatico-di-radiosondaggio-dell2019atmosfera>
- Sitnikov, N. M., Borisov, Yu. A., Chekulaev, I. I., Efremov, D. I., Akmulin, D. V., Sitnikova, V. I., & Ulanovskii, A. E. (2014). Returnable upper-air sonde

- based on unmanned or remotely-piloted aerial vehicles for atmospheric balloon sounding. *Russian Meteorology and Hydrology*, 39(9), 634–638.
<https://doi.org/10.3103/S106837391409009X>
- Smith chart. (2021). In *Wikipedia*.
https://en.wikipedia.org/w/index.php?title=Smith_chart&oldid=10079622
 15
- Sonde. (2021). In *Wikipedia*.
<https://en.wikipedia.org/w/index.php?title=Sonde&oldid=1001302741>
- Stechmann, S. N., & Stevens, B. (2010). Multiscale Models for Cumulus Cloud Dynamics. *JOURNAL OF THE ATMOSPHERIC SCIENCES*, 67, 17.
- Sukkarieh, S., Nebot, E. M., & Durrant-Whyte, H. F. (1999). A high integrity IMU/GPS navigation loop for autonomous land vehicle applications. *IEEE Transactions on Robotics and Automation*, 15(3), 572–578.
<https://doi.org/10.1109/70.768189>
- Sun, B., Reale, A., Seidel, D. J., & Hunt, D. C. (2010). Comparing radiosonde and COSMIC atmospheric profile data to quantify differences among radiosonde types and the effects of imperfect collocation on comparison statistics. *Journal of Geophysical Research*, 115(D23), D23104.
<https://doi.org/10.1029/2010JD014457>
- Swenson, S., Argrow, B., Frew, E., Borenstein, S., & Keeler, J. (2019). Development and Deployment of Air-Launched Drifters from Small UAS. *Sensors*, 19(9), 2149. <https://doi.org/10.3390/s19092149>
- SX1272/3/6/7/8: LoRa Modem / SEMTECH. (n.d.). Retrieved November 24, 2020, from <https://www.rs-online.com/designspark/rel-assets/ds-assets/uploads/knowledge-items/application-notes-for-the-internet-of-things/LoRa%20Design%20Guide.pdf>

SX1276 / Semtech. (n.d.). SX1276 | 137MHz to 1020MHz Long Range Low Power Transceiver | Semtech. Retrieved March 3, 2021, from <https://www.semtech.com/products/wireless-rf/lora-transceivers/sx1276>

Taylor, F. W. (2005). *Elementary climate physics / F.W. Taylor*. Oxford University Press.

TELA chip antenna / Unictron. (n.d.). TELA Chip Antenna Technology. Retrieved March 3, 2021, from <https://www.unictron.com/antenna-embedded/technology/tela-chip-antenna/>

The Earth's Radiation Budget | NASA. (n.d.). Retrieved March 8, 2021, from https://science.nasa.gov/ems/13_radiationbudget

The Importance of Understanding Clouds | NASA EOS. (2005). <https://eospsa.nasa.gov/publications/importance-understanding-cloud>

TLM SERIES / TADIRAN. (n.d.). TLM SERIES Lithium Metal Oxide Batteries. Retrieved March 3, 2021, from <http://www.tadiranbat.com/high-power-tlm.html>

TLM-1520HPM / TADIRAN. (n.d.). Retrieved March 3, 2021, from <https://tadiranbatteries.de/pdf/tadiran-lithium-metal-oxide-batteries/TLM-1520HPM.pdf>

Toschi, F., & Bodenschatz, E. (2009). Lagrangian Properties of Particles in Turbulence. *Annual Review of Fluid Mechanics*, 41(1), 375–404. <https://doi.org/10.1146/annurev.fluid.010908.165210>

Turbulence. (2021). In *Wikipedia*. <https://en.wikipedia.org/w/index.php?title=Turbulence&oldid=100034334>

2

Turbulence | Glossary of Meteorology. (n.d.). Retrieved March 12, 2021, from <https://glossary.ametsoc.org/wiki/Turbulence>

- TXS0108E* / *Texas Instruments*. (n.d.). Retrieved March 3, 2021, from https://www.ti.com/lit/ds/symlink/txs0108e.pdf?ts=1614719163351&ref_url=https%253A%252F%252Fwww.google.com%252F
- Uhlig, E.-M., Borrmann, S., & Jaenicke, R. (1998). Holographic in-situ measurements of the spatial droplet distribution in stratiform clouds. *Tellus B: Chemical and Physical Meteorology*, 50(4), 377–387. <https://doi.org/10.3402/tellusb.v50i4.16210>
- Vector Network Analyzer VNA Calibration* / *Electronics Notes*. (n.d.). How to Calibrate a Vector Network Analyzer, VNA. Retrieved January 4, 2021, from <https://www.electronics-notes.com/articles/test-methods/rf-vector-network-analyzer-vna/how-to-calibrate-vna.php>
- Wallace, J. M., & Hobbs, P. V. (2006). *Atmospheric science: An introductory survey* (2nd ed). Elsevier Academic Press.
- Ward, A. (2005). *The Importance of Understanding Clouds*. 6.
- Warhaft, Z. (2008). Laboratory studies of droplets in turbulence: Towards understanding the formation of clouds. *Fluid Dynamics Research*, 41(1), 011201. <https://doi.org/10.1088/0169-5983/41/1/011201>
- Waspnote lora* / *Libelium*. (n.d.). Retrieved March 3, 2021, from https://www.libelium.com/downloads/documentation/waspnote_lora_868mhz_915mhz_sx1272_networking_guide.pdf
- Weather balloon. (2021). In *Wikipedia*. https://en.wikipedia.org/w/index.php?title=Weather_balloon&oldid=1009945170
- Whale, T. H. F. S. (2009). *Thick cirrostratus clouds forming a halo around the sun. Photo taken in Langley, BC*. Self-photographed. (<https://commons.wikimedia.org/wiki/File:Cirrostratus-Langley.jpg>),

„Cirrostratus-Langley“, <https://creativecommons.org/licenses/by-sa/3.0/legalcode>

What is a Dropsonde? | Earth Observing Laboratory. (n.d.). Retrieved March 16, 2021, from <https://www.eol.ucar.edu/content/what-dropsonde>

What is a Radiosonde? - Radiosonde Museum of North America. (n.d.). Retrieved March 17, 2021, from <https://radiosondemuseum.org/what-is-a-radiosonde/>

What is GNSS? | EGNOS User Support. (n.d.). Retrieved March 3, 2021, from https://egnos-user-support.essp-sas.eu/new_egnos_ops/european-gnss/what-gnss

What is IMU? | Arrow. (n.d.). What Is IMU? Inertial Measurement Unit Working & Applications. Retrieved March 3, 2021, from <https://www.arrow.com/en/research-and-events/articles/imu-principles-and-applications>

What is LoRa? | Semtech LoRa Technology | Semtech. (n.d.). Retrieved March 3, 2021, from <https://www.semtech.com/lora/what-is-lora>

What is LoRaWAN® | LoRa Alliance®. (n.d.). *LoRa Alliance®.* Retrieved March 3, 2021, from https://loro-alliance.org/resource_hub/what-is-lorawan/

What is the Difference Between GNSS and GPS? | Symmetry Electronics. (n.d.). Retrieved March 3, 2021, from <https://www.semiconductorstore.com/blog/2015/What-is-the-Difference-Between-GNSS-and-GPS/1550/>

White, J. F. (2004). *High Frequency Techniques.*

Wick, G. A., Hock, T. F., Neiman, P. J., Vömel, H., Black, M. L., & Spackman, J. R. (2018). The NCAR–NOAA Global Hawk Dropsonde System. *Journal of Atmospheric and Oceanic Technology*, 35(8), 1585–1604. <https://doi.org/10.1175/JTECH-D-17-0225.1>

- Wireless Sensor Networks: Types & Their Applications* / *ELPROCUS*. (2014, March 15). ElProCus - Electronic Projects for Engineering Students. <https://www.elprocus.com/introduction-to-wireless-sensor-networks-types-and-applications/>
- Wiring* / *WIRING*. (n.d.). Retrieved March 4, 2021, from <http://wiring.org.co/>
- Young, D. F., Munson, B. R., Okiishi, T. H., & Huebsch, W. W. (2010). *A Brief Introduction to Fluid Mechanics*. John Wiley & Sons.
- Zarchan, P., & Musoff, H. (2015). *Fundamentals of Kalman filtering: A practical approach* (Fourth edition., Vols. 246, 246.). American Institute of Aeronautics and Astronautics, Inc.
- Zhou, Q., Yu, G., Li, H., & Zhang, N. (2020). A Novel MEMS Gyroscope In-Self Calibration Approach. *Sensors*, 20(18), 5430. <https://doi.org/10.3390/s20185430>
- ZOE-M8B* / *U-Blox*. (2020). Retrieved January 20, 2021, from https://www.u-blox.com/sites/default/files/ZOE-M8B_DataSheet_%28UBX-17035164%29.pdf

Appendix A: Initial tests

Before the integration of the radioprobe systems, different initial tests were carried out to test almost every single operational unit in a separate way. They are explained in detail in the following subsections.

I. Software environment and microcontroller

The very first step consisted in testing the core of the data processing and control unit, that is the microcontroller. As mentioned in subsection 3.3.1.1, the ATmega328P-AU device from Microchip was selected for the radioprobe design. To this end, the development board Arduino Nano (Figure A.1), which embeds the ATmega328P, was used to test the microcontroller's capabilities and communication interfaces.

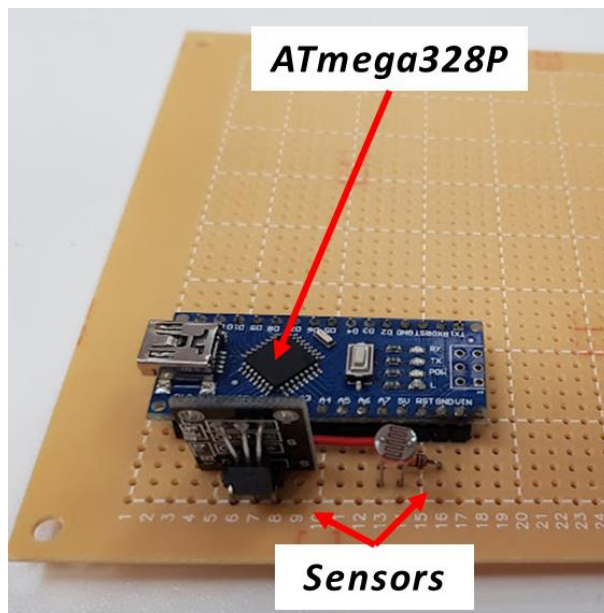


Figure A.1 Development board Arduino Nano embedding the microcontroller ATmega328P

The source code was written using Arduino platform, which is an open-source platform used for designing, developing, and building electronic projects (*Arduino / Arduino*, n.d.). This platform includes the hardware consisting of a physical programmable circuit board (microcontroller and other electronic components) and the software (Integrated Development Environment IDE), which is used for writing and uploading the programming code to the board. The programming language framework used to program Arduino is based on Wiring, which is a C++ based open-source programming framework for microcontrollers (*Wiring / WIRING*, n.d.). The Arduino program structure is formed by three main parts (*Arduino - Program Structure / Tutorialspoint*, n.d.):

1. **Structure:** contains a Setup section and a Loop Section. The former is the preparation part that allows setting modes, communications, etc., while the latter is the execution part that holds the code to be run consecutively, allowing the program to change and respond.
2. **Values:** contain the variables (expressions used to store values) and the constants (labels for certain values). Variables can be declared in three regions of the program: inside a function or a block (local variables), in the definition of function parameters (formal parameters), and outside of all functions (global variables).
3. **Functions:** allow segmenting codes that perform a defined task.

II. Communication technology

To test LoRa as communication technology, the first step consisted in the development of the programming code to control and enable the transceivers, both in the transmitter and receiver devices. For this purpose, two modules Adafruit Feather 32u4 LoRa Radio already described in subsection 3.2.2.1 were used in a point-to-point configuration. They include an embedded microcontroller and a LoRa-based transceiver working in the ISM license-free frequency band of interest. The control code was developed using Arduino programming language and uploaded to the main microcontroller through the IDE software.

a. Test 1

In order to determine the proper operation of the written programming code set in the transceivers, different performance tests were performed. The first test included a short-range communication link (approximated distance of 2 m) between the transmitter or end-node and the receiver. A single message including a counter was sent periodically to verify possible losses of data. As result, the data packets were successfully transmitted and received without any corruption. The transmitter node and the messages transmitted and received are shown in Figure A.2 and Figure A.3.

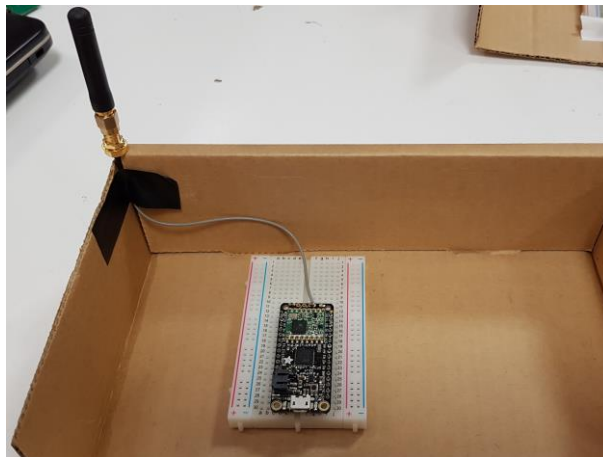


Figure A.2 LoRa-based transmitter node to initially test communication technology

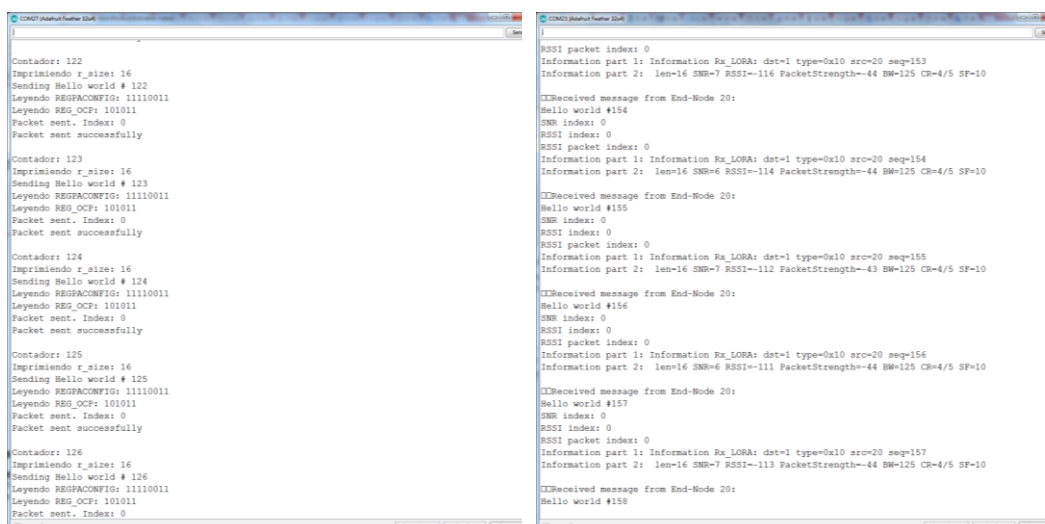


Figure A.3 Short-range transmission test to initially test communication technology. Left side transmitter serial port output. Right side receiver serial port output

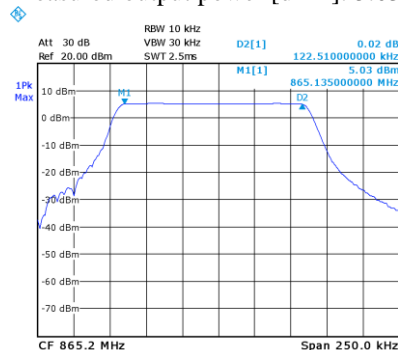
Since the output power is configured through the set of different registers in the transceiver, the next test consisted of measuring the real output power provided by the device. To this end, the transceiver's output power was tested directly using a Spectrum Analyzer (SA) to corroborate that the module is effectively sending the signal with the power specified in the programming code. The measurements were made using the SA model R&S ZVL connected to the transmitter. Various configuration modes were set to the registers to achieve either 5, 10 and 14 dBm as output power at a frequency band of 865.2 MHz, spreading factor of 10 and coding rate of 4. These results can be seen in Table A.1, Table A.2, and Table A.3.

Table A.1 Output power tests using a set output power of 5 dBm at different bandwidth

Set output power [dBm]: 5

Bandwidth [KHz]: 125

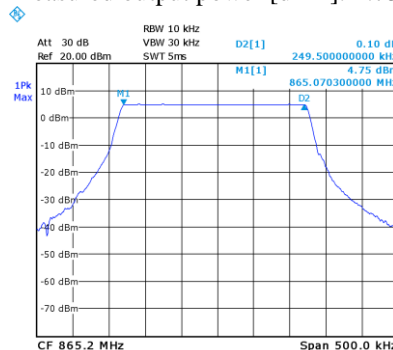
Measured output power [dBm]: 5.03



Date: 25.JAN.2018 11:08:34

Bandwidth [KHz]: 250

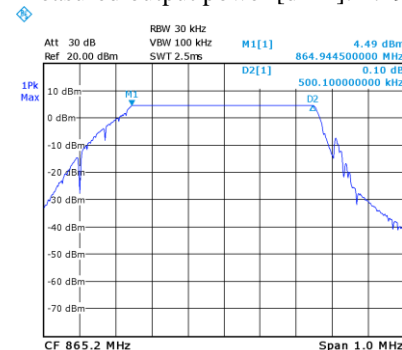
Measured output power [dBm]: 4.75



Date: 25.JAN.2018 11:39:34

Bandwidth [KHz]: 500

Measured output power [dBm]: 4.49



Date: 25.JAN.2018 11:48:46

Table A.2 Output power tests using a set output power of 10 dBm at different bandwidth

Set output power [dBm]: 10

Bandwidth [KHz]: 125

Measured output power [dBm]: 9.71

Bandwidth [KHz]: 250

Measured output power [dBm]: 9.86

Bandwidth [KHz]: 500

Measured output power [dBm]: 9.76

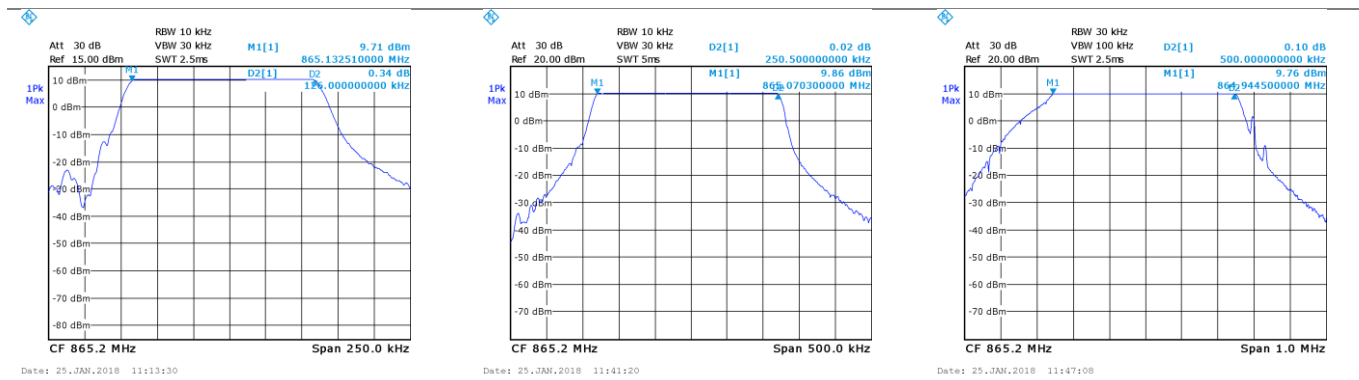
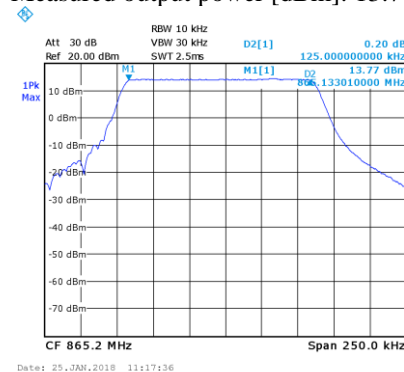


Table A.3 Output power tests using a set output power of 14 dBm at different bandwidth

Set output power [dBm]: 14

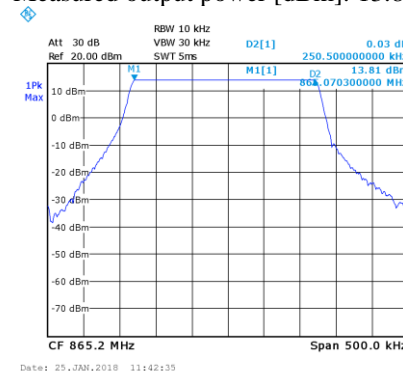
Bandwidth [KHz]: 125

Measured output power [dBm]: 13.77



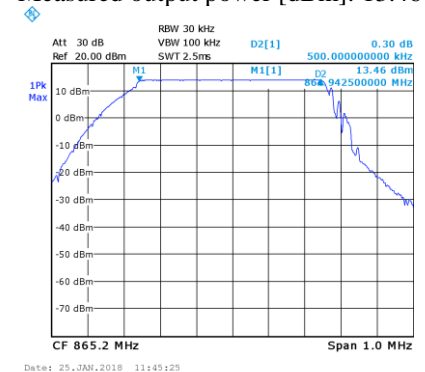
Bandwidth [KHz]: 250

Measured output power [dBm]: 13.81



Bandwidth [KHz]: 500

Measured output power [dBm]: 13.46



The results indicate that the real output power provided by the transmitter using different bandwidths is in agreement with the programmed output power in the transceiver registers. The values show that no significant losses are introduced to the system due to cables and connectors.

b. Test 2

An additional test was performed inside the Department of Electronics and Telecommunications (DET) of the Politecnico di Torino (POLITO) in order to determine the transmission ranges and signal quality of a packet sent using LoRa technology at longer distances in an indoor environment. The topology used was a single point-to-point network, formed by an end-node transmitting the messages and a receiver gathering them. The antennas used for both, transmitter and receiver were quarter-wave antennas with omnidirectional pattern already described in subsection 3.2.4.2, working in the range from 850 to 880 MHz, central frequency at 868 MHz and peak gain of 3.16 dBi. The test consisted in sending various LoRa packets including a counter from the end-node. The aim of the counter was to identify the losses of packets having a known progressive number in the data frame. The packets were received with both, the receiver connected to a PC serial port and a spectrum analyzer placed closely. Although the noise floor of the instrument is

significantly higher with respect to the sensitivity of the LoRa receiver, it was also used as equipment setup to measure the receiver power values of the incoming packets whenever possible.

The receiver module was programmed in order to provide information about the signal quality, that is SNR and RSSI of the packets. The parameters used for this configuration were 5 dBm of programmed output power, central frequency at 865.2 MHz, spreading factor of 10, and a bandwidth of 125 kHz. The fixed location of the receiver and the different positions of the transmitter are shown in Figure A.4. Some pictures of the experiment are shown in Figure A.5. The results of the measurements are reported in Table A.4. (Bertoldo et al., 2018).

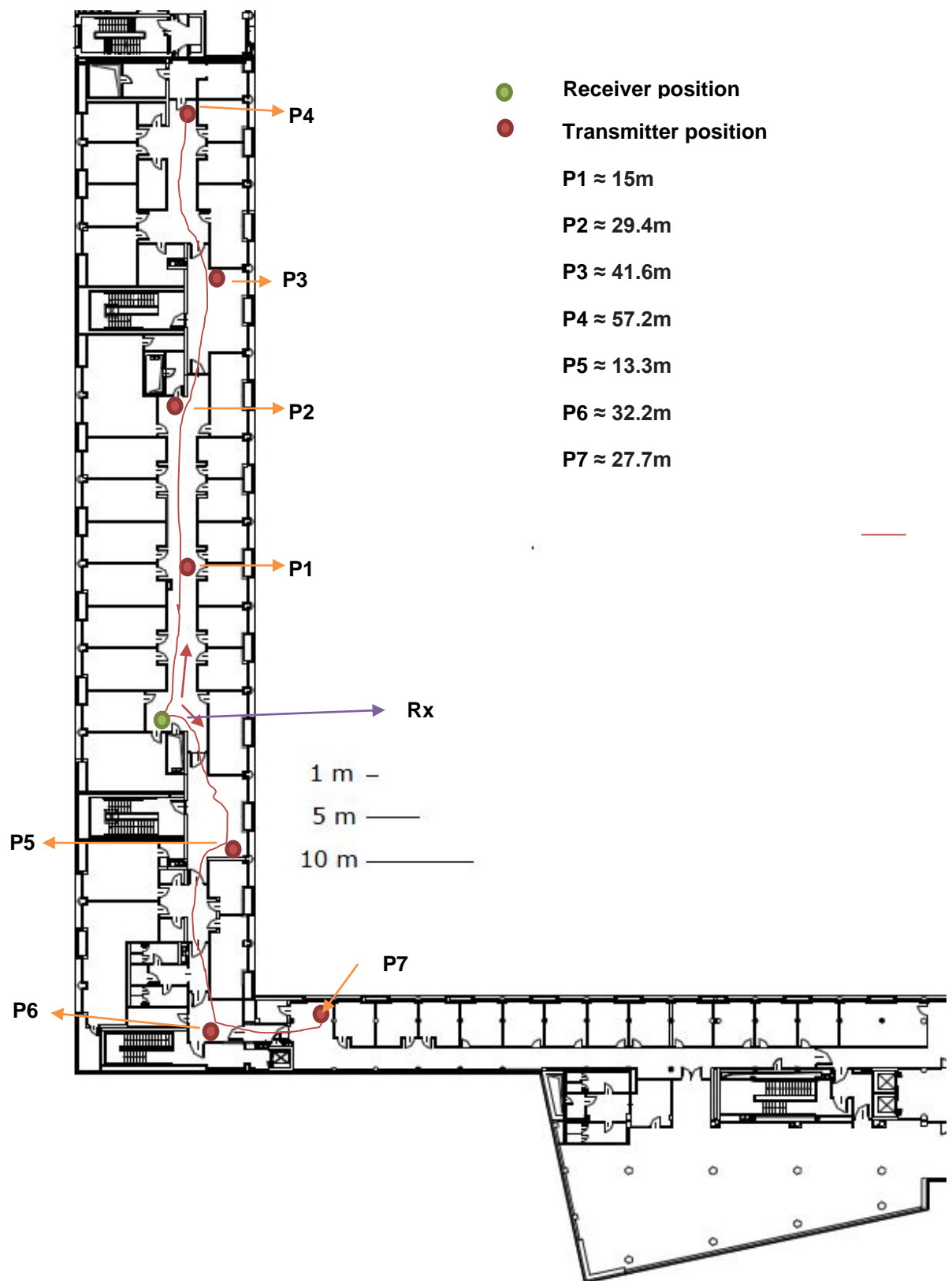


Figure A.4 System setup test 2. Point-to-point configuration used to determine the transmission ranges reached by the communication system in an indoor environment, displayed on a map. Transmitter (P1 to P7) and receiver (Rx) positions, with relative distance indications.



Figure A.5 Some pictures of the indoor communication test. Left: Location of receiving station. Right: Location of the transmitter position at P7. DET POLITO. Floor 4th

Table A.4 Results of indoor measurements. DET POLITO. Floor 4th

Position	Distance [m]	SNR mean [dB]	RSSI mean [dBm]	Received power (Spectrum Analyzer) [dBm]	Received packets [%]
P1	15.0	8	-55	-35.0	99
P2	29.4	8	-71	-54.7	100
P3	41.6	8	-75	-54.4	100
P4	57.2	7	-93	-75.4	100
P5	13.3	8	-69	-52.6	100
P6	32.2	8	-85	-69.0	100
P7	27.7	7	-93	-77.8	100

As result of these propagation measurements in an indoor environment, different communication links were tested to understand the transmission ranges and signal quality when using LoRa technology with a low output power. The maximum propagation distance tested between the receiver and the transmitter was 57.2 m. The SNR mean varied between 7 and 8 dB and the RSSI mean of the packets from -55 to -93 dBm. Most of the packets were successfully received at all positions from P1 to P7.

c. Test 3

A third test using a single point-to-point network configuration, comprising an end-node transmitting the messages and a receiver gathering them, was performed but this time in an outdoor environment. This was the first outdoor experiment performed on the rooftop of the DET of POLITO in order to determine the transmission ranges and signal quality of the sent packets using LoRa technology in open-air urban environment. The receivers (Ground station and Spectrum Analyzer) were placed close to the fixed position 1, and the transmitter was located

at positions from 1 to 4. Same as the indoor measurements, the receiver module was programmed to provide information about the signal quality. Also, the transmitter was configured to provide 5 dBm of output power at 865.2 MHz, spreading factor of 10 and bandwidth of 125 kHz. The transmitted signal consisted of blocks of 200 LoRa packets for each location. The fixed location of the receiver and the different positions of the transmitter are shown in Figure A.6. Some pictures of the experiment are shown in Figure A.7. The results of the measurements are reported in Table A.5.

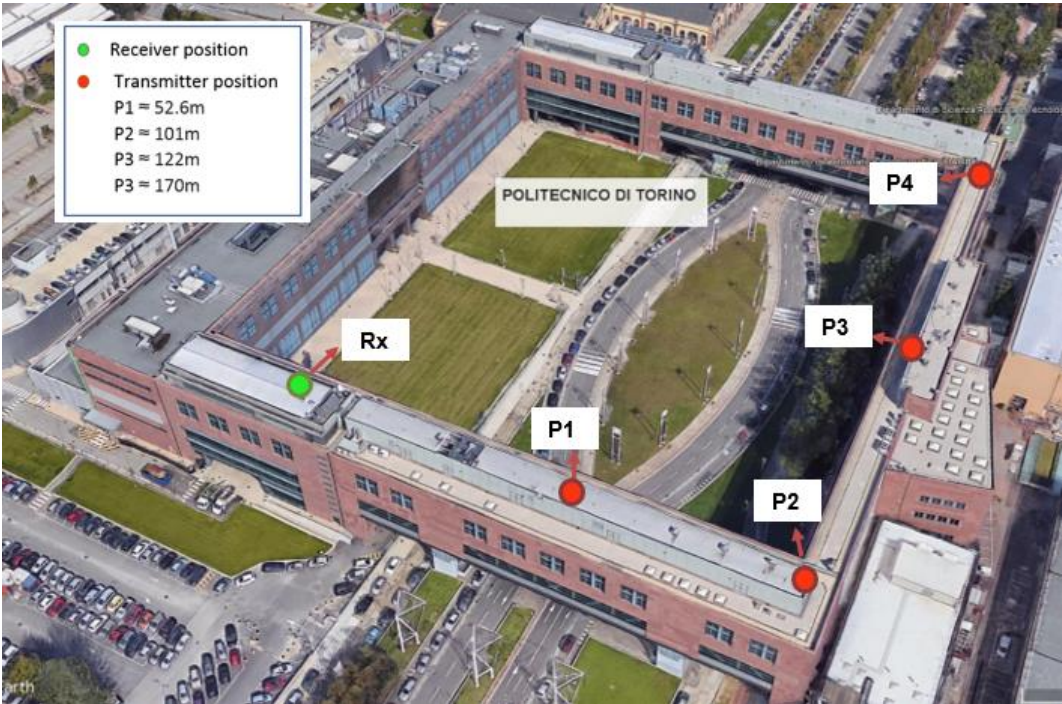


Figure A.6 System setup test 3. Point-to-point configuration used to determine the transmission ranges reached by the communication system in an open urban environment, displayed on a map. Transmitter (P1 to P4) and receiver (Rx) positions, with relative distance indications. Google earth view.



Figure A.7 Some pictures of the outdoor communication test. Left: Location of the transmitter position at P4. Right: Location of receiving station. DET POLITO. Rooftop

Table A.5 Results of outdoor measurements. DET POLITO. Rooftop

Position	Distance [m]	SNR mean [dB]	RSSI mean [dBm]	Received power (Spectrum Analyzer) [dBm]	Received packets [%]
P1	52.6	7	-80	-68.2	100
P2	101.0	8	-92	-74.7	100
P3	122.0	8	-82	-69.3	100
P4	170.0	7	-87	-71.1	100

This experiment provided the first propagation results in an urban open environment using LoRa technology at low power. The transmitted packets at different distances were correctly received at the receiver side, both using the ground station and the SA. The transmitter was in Line-of-sight (LOS) with the receivers at all positions. The maximum propagation distance reached with this experiment was 170 m and the SNR mean ranged from 7 and 8 dB.

d. Test 4

The fourth test run was performed in an outdoor environment similarly to the previous one but this time having larger separation distances between the transmitter and the receiver positions. The network setup used was a single point-to-point configuration with an end-node transmitting data packets and a receiver collecting them. The transmitter was placed at different positions on the rooftop of the DET at POLITO, and the receiver instrumentation (ground station and SA) was placed in a building of the surroundings. In a similar way, the receiver module was programmed to provide signal quality information of the received packets. The transmitter was set to supply an output power of 5 dBm at a central frequency of 865.2 MHz, spreading factor of 10 and bandwidth of 125 kHz. The location of the receiver instruments (Rx) and the transmitter positions (P1 to P3) are shown in Figure A.8. Some pictures of the experiment are shown in Figure A.9. The results of the measurements are reported in Table A.6.



Figure A.8 System setup test 4. Point-to-point configuration used to determine the transmission ranges reached by the communication system in an open urban environment, displayed on a map. Transmitter (P1 to P3) and receiver (Rx) positions, with relative distance indications. Google earth view.

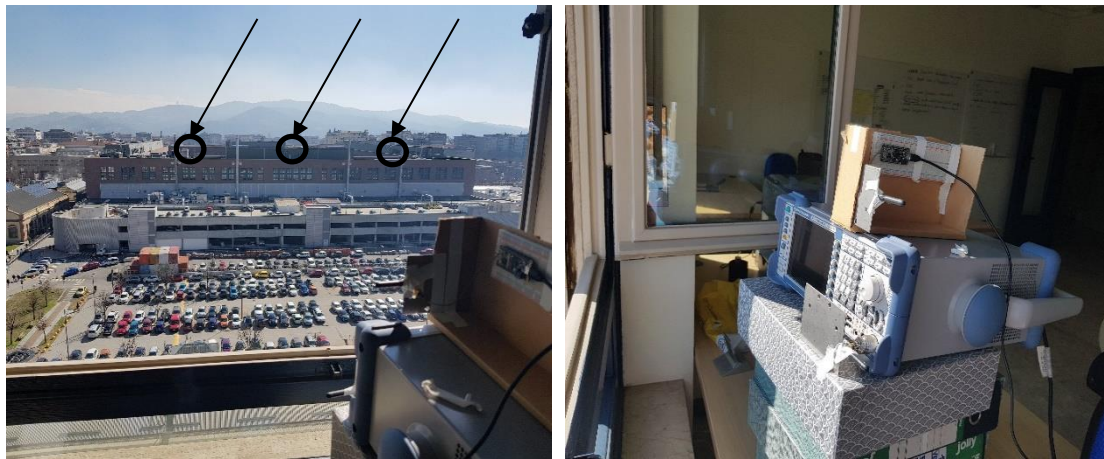


Figure A.9 Some pictures of the outdoor communication test. Left: Receiver view of the location of the transmitter placed at different positions. Rooftop of DET POLITO. Right: Receiving station. Building in the surroundings.

Table A.6 Results of outdoor measurements. DET POLITO. Rooftop

Position	Distance [m]	SNR mean [dB]	RSSI mean [dBm]	Received power (Spectrum Analyzer) [dBm]	Received packets [%]
P1	341.0	6	-94	-83.4	100
P2	274.0	1	-95	-86.8	100
P3	350.0	0	-95	-86.8	100

From the obtained results, it is possible to verify again the correct operation of the communication link in an open environment at longer ranges. The maximum reached transmission distance of this test was 350 m. Although the link between the receiver and the transmitter located on P2 was obstructed by a metallic structure, which is a common situation for an urban environment, the totality of packets were correctly received during the completion of the experiment.

e. Test 5

Similarly, this test was performed in an outdoor urban environment using a point-to-point setup with the aim of testing longer communication links between the receiver and transmitter. The receiver system (ground station and SA) was placed in an office of POLITO on the 4th floor, and the transmitters at different positions along an adjacent avenue. The transmitter module was programmed to provide a power output of 14 dBm, working in the frequency of 865.2 MHz, with a spreading factor of 10 and bandwidth of 125 kHz. The receiver was set to receive the packets and add signal quality information to the message. In total, 200 packets were sent during the experiment. There was line-of-sight between the receiver and transmitter during the measurements. The location of the transmitter at different positions (from P1 to P3) and the receiver location (Rx) are displayed in Figure A.10. Some pictures of the experiment are shown in Figure A.11. The results of the measurements are reported in Table A.7.

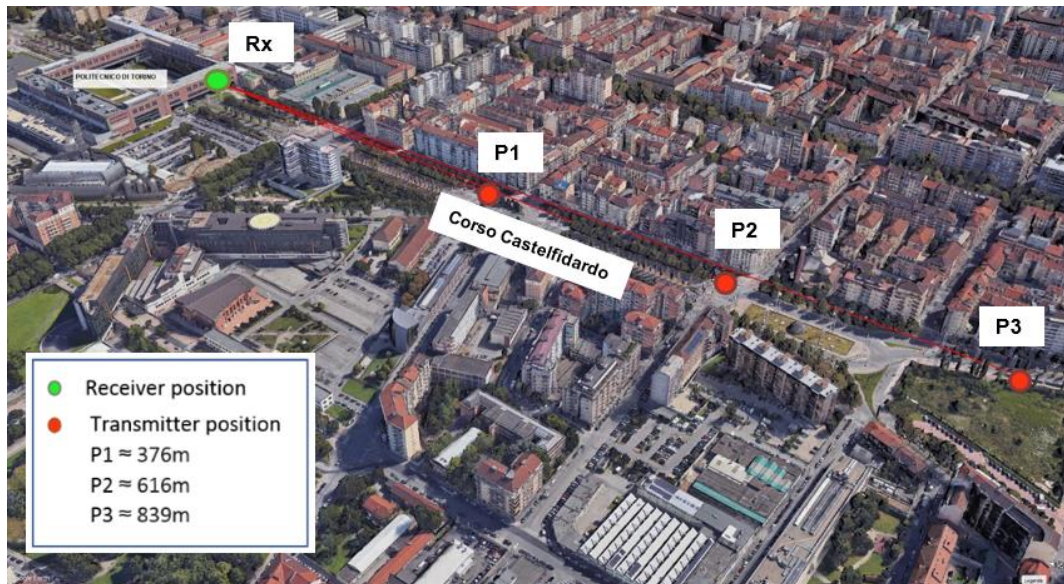


Figure A.10 System setup test 5. Point-to-point configuration used to determine the transmission ranges reached by the communication system in an open urban environment, displayed on a map. Transmitter (P1 to P3) and receiver (Rx) positions, with relative distance indications. Google earth view.

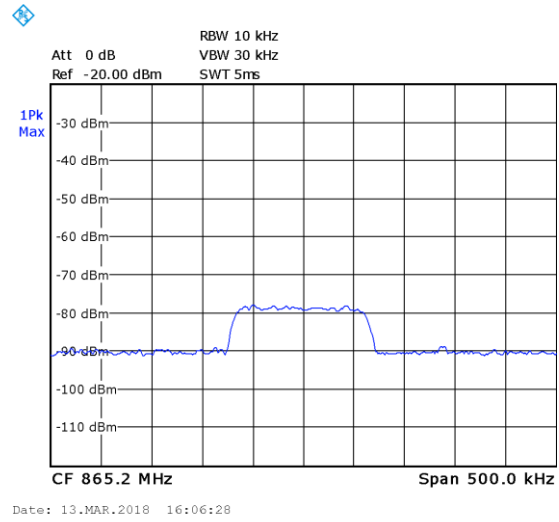


Figure A.11 Some pictures of the outdoor communication test. Left: Receiver view of the location of the receiver placed at POLITO. Right: Power spectrum signal received by the SA when the transmitter was placed at P1

Table A.7 Results of outdoor measurements. DET POLITO. Rooftop

Position	Distance [m]	SNR mean [dB]	RSSI mean [dBm]	Received power (Spectrum Analyzer) [dBm]	Received packets [%]
P1	376.0	1	-99	-78	> 99
P2	616.0	-2	-97	-85	> 99
P3	839.0	-7	-98	Not detected	96

As result of these propagation measurements, three transmission links were tested to understand the transmission ranges that can be reached by the system in an open urban condition. The maximum propagation distance tested was 839 m between the transmitter and the receiver. As expected, the SNR value decreased as the communication link distance increased; however, most of the packets were received. From Table A.7, it is possible to see negative SNR values for P2 and P3, which is an implicit LoRa characteristic showing its capacity to detect low power signals. In fact, for the longest distance, the LoRa receiver was able to detect the signal whereas the SA was not.

f. Test 6

This test was made to test the performance of the communication link in an open area using a star topology setup. It consisted of five end nodes transmitting simultaneously messages and, a receiver in the middle. The measurements were performed in the campus of POLITO, with the receiver placed at the ground level (Rx) and surrounded by the transmitters (T1 to T5) placed at a height of approximately 20 m above the floor level. Each transmitter was programmed to send the packets embedding a counter in the data frame for the identification of packet losses. Moreover, the end nodes T1, T2 and T3 incorporated additional

information in the packets, the two firsts acceleration data and the last one resistance data, this with the aim of testing the communication system channel under busy conditions. The receiver was configured to receive the packets sent by the end nodes and supply signal quality information. The transmitters were configured to provide 5 dBm of output power at 865.2MHz, spreading factor of 10 and bandwidth of 125 kHz. The fixed locations of both, the receiver and the transmitters are shown in Figure A.12. Some pictures of the experiment are shown in Figure A.13.

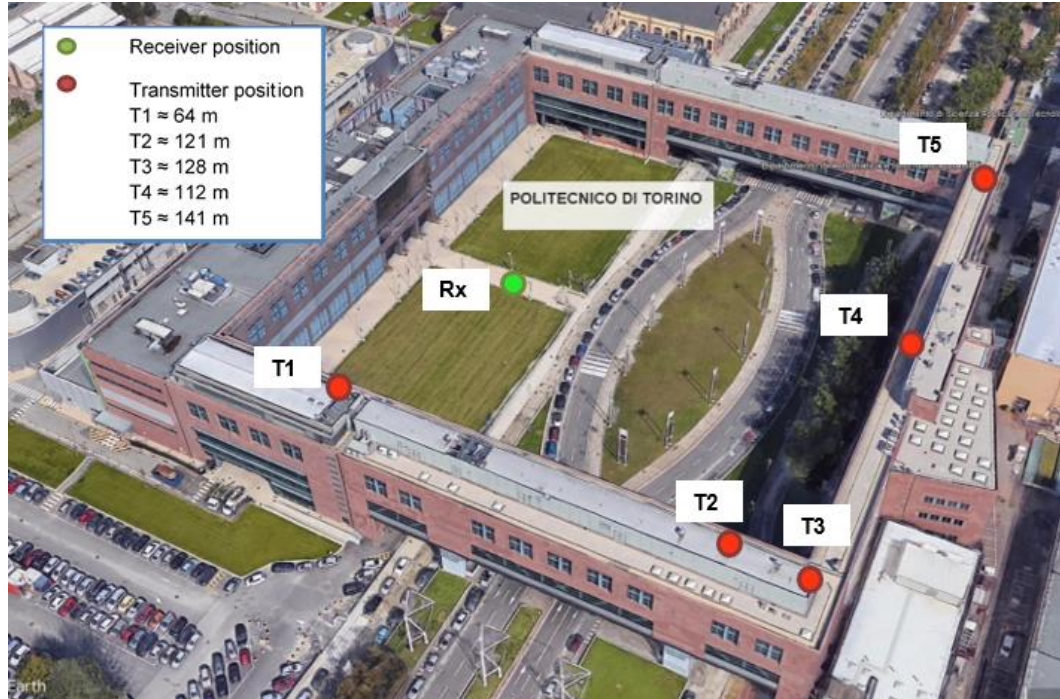


Figure A.12 System setup test 6. Star topology configuration used to determine the transmission ranges reached by the communication system in an open urban environment, displayed on a map. Transmitter (T1 to T5) and receiver (Rx) positions, with relative distance indications. Google earth view.



Figure A.13 Some pictures of the star topology communication test. Left: Receiving station placed at ground level and position of three transmitter on rooftop. Right: Location of the transmitter T4.

The results of the measurements are reported in Table A.8. Figure A.14 shows the SNR values obtained for the three most significant configurations: T1 smallest distance between the transmitter and receiver, T2 intermediate distance between the

transmitter and receiver and, T5 furthest distance between the transmitter and receiver.

Table A.8 Results of star topology setup in an outdoor environment.

Position	Distance [m]	SNR mean [dB]	RSSI mean [dBm]	Received packets [%]
T1	64	6	-88	94
T2	121	6	-99	83
T3	128	6	-95	88
T4	112	6	-98	84
T5	141	6	-92	64

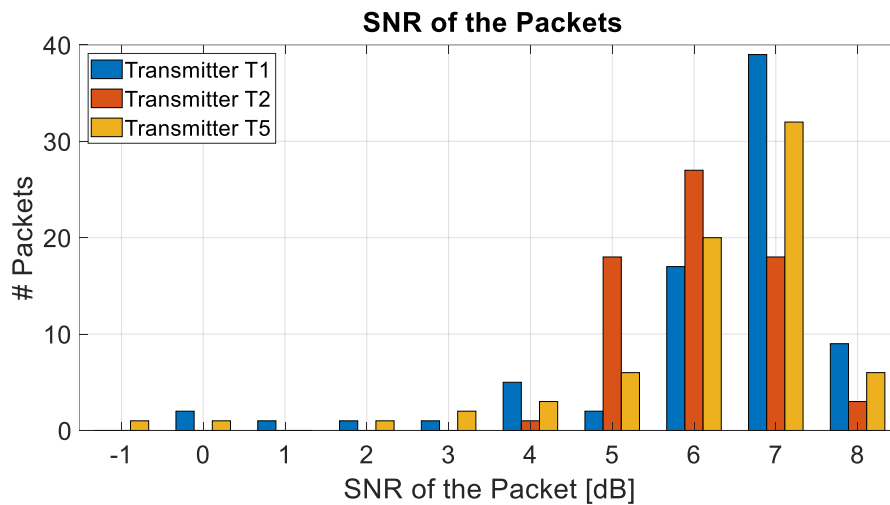


Figure A.14 SNR of the received signals from transmitters T1, T2 and T5 for the star topology setup measurements.

As a result of this test using a star topology network configuration, it was possible to see the behavior of the system under busy conditions where all the transmitters were sending moderate data frames simultaneously. Because the distance between the transmitters and the receiver varied from 64 m to 141 m, the SNR mean was 6 dB for all the cases. The main key fact obtained from this test was the number of correctly received packets from each transmitter at the receiver side. From the results, it is possible to notice that there were some collisions on the communication channel and some packets were lost. For instance, the percentage of acquired packets from the closest end node was higher than from the others end nodes placed at longer distances. On average, 17 % of the packets were dropped, going from a minimum of 6 % to a maximum of 36 % for the five positions. Based on the results and, given that the final network design includes multiple radioprobes sending information simultaneously to ground, a mechanism to overcome possible collision problems must be implemented.

The results obtained from the last three field tests (test 4, test 5 and, test 6) have been published in the *Journal of Electromagnetic Waves and Applications* (Paredes et al., 2019).

g. Test 7

This test field experiment was aimed at testing the radiocommunication link in a cloud environment using a point-to-point dynamic configuration. It was performed at the Umweltforschungsstation Schneefernerhaus (UFS), which is the highest German's Environmental Research Station. The UFS is located near to the top of the Mt. Zugspitze at 2652 m and is prevalently immersed in clouds. This time, the end node embedded not only the transmitter but also an accelerometer to get a first idea of possible accelerations found in real clouds. The end node was attached to some Helium-filled latex balloons through a nylon thread. The transmitter was configured to send LoRa packets including acceleration data measurements taken during the flight. It was set to supply 5 dBm of output power at 865.2MHz, spreading factor of 10 and bandwidth of 125 kHz. The receiver was placed on a fixed position on ground. It was previously programmed to gather the transmitted data and provide signal quality information. The maximum separation distance between the end node and the receiver was about 150 m. Figure A.15 shows some pictures of the experiment. The obtained results are displayed in Figure A.16, Figure A.17, and Figure A.18.

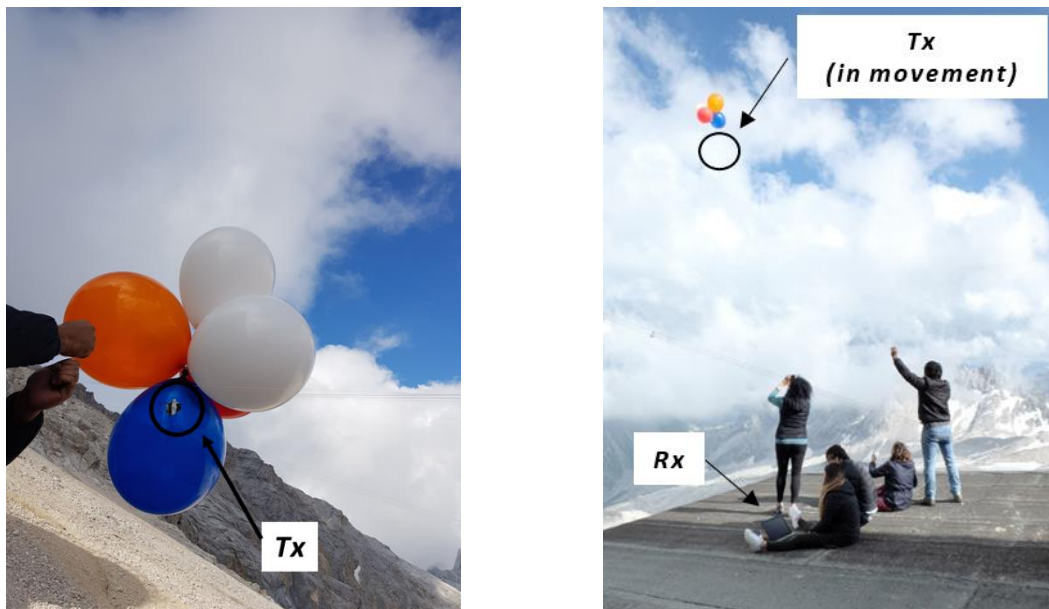


Figure A.15 Some pictures of the dynamic point-to-point communication test. Left: Release of the end node held by some latex balloons. Right: Transmitter in movement and receiving station placed at ground level.

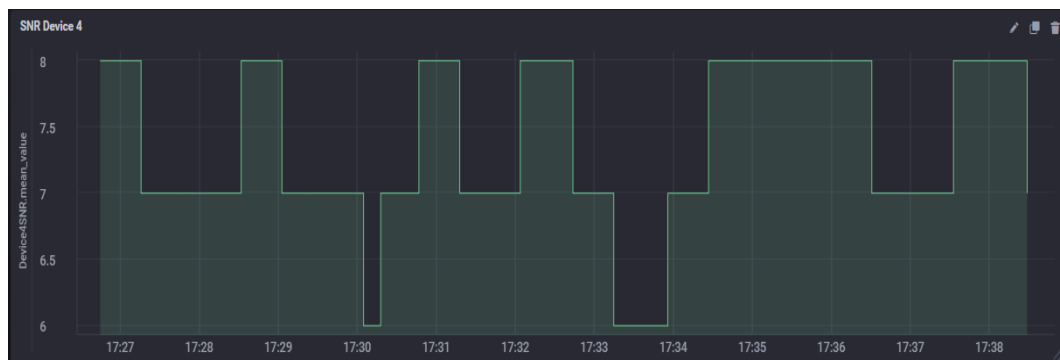


Figure A.16 SNR of the received packets during the field test 7.

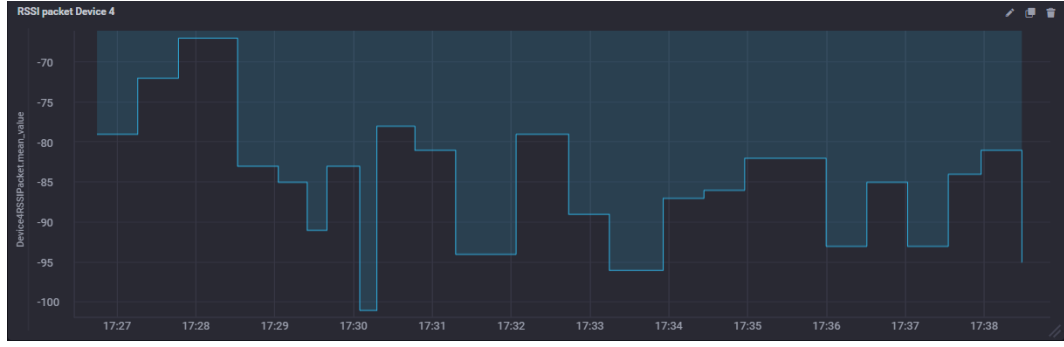


Figure A.17 RSSI of the received packets during the field test 7.

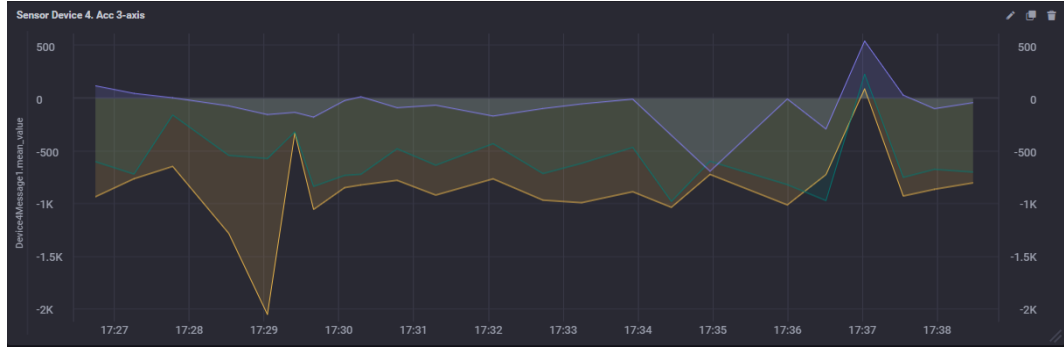


Figure A.18 Acceleration measured during the field test 7. X-axis displayed in orange, y-axis displayed in green, z-axis displayed in purple.

Although the distances adopted for the test were much smaller than the expected range (1 – 2 km), this field experiment provided an idea of the communication technology performance in a dynamic cloud environment. As expected, during the measurements, the SNR values did not change much, having a mean value of 6 dB, with minimum and maximum values of 6 and 8 dB respectively. The RSSI mean value obtained was -84 dBm, with minimum and maximum values of -102 and -66 dBm respectively. The totality of packets were correctly received during the completion of the experiment, which lasted for approximately 12 minutes.

h. Characterization of the balloon material

The communication technology was also used to test a set of different materials suitable for the development of the radioprobe enclosure. It consisted in studying the signal attenuation effect introduced by the balloon in the path between the transmitter and the receiver antennas. This test was performed inside the DET of POLITO.

The system setup is displayed in Figure A.19. At the transmitter side, a signal generator model R&S SMB100A was used to create various electronic signals at three different central frequencies: 370 MHz, 868 MHz, and 2.49 GHz. Its output was connected to the antennas working at the mentioned frequencies via a SMA cable. During the measurements, for each frequency, the antennas were covered by

the different potential materials for the envelop construction: Mylar or biaxially-oriented polyethylene terephthalate (BoPet), Polycaprolactone (PCL), Polyethylene terephthalate (Pet) with Aluminum (Al), thin Pet with stainless steel, and thick Pet with stainless steel. At the receiver side, a spectrum analyzer model R&S ZVL was connected to the corresponding antenna pair to measure the power spectrum received. Figure A.20 shows some pictures of the experiment. The attenuation introduced by each material at the different tested frequencies is summarized in Table A.9.

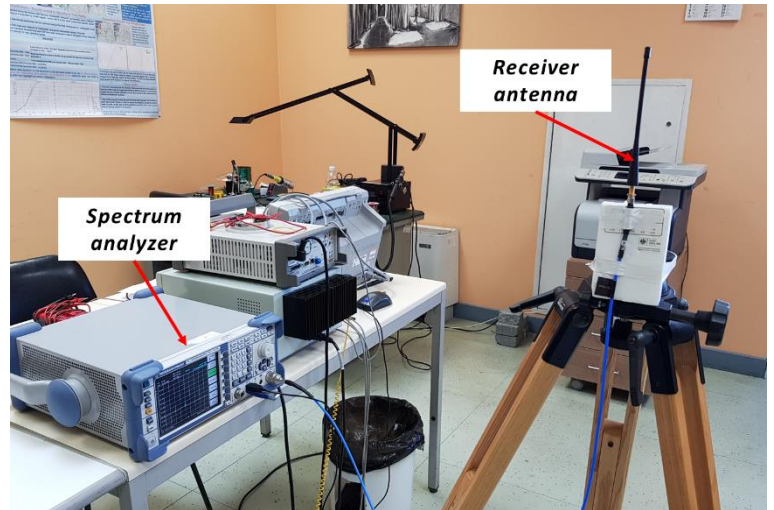
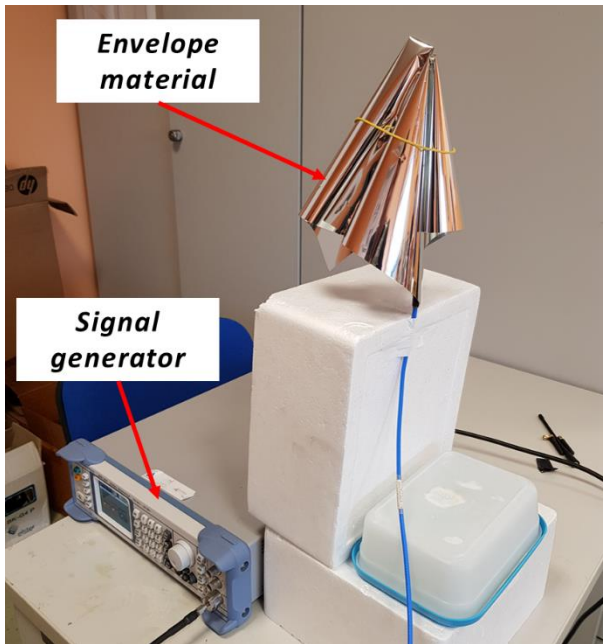


Figure A.19 System setup used to determine the signal attenuation effect introduced by the envelope materials. Left: Transmitter side. Right: Receiver side.

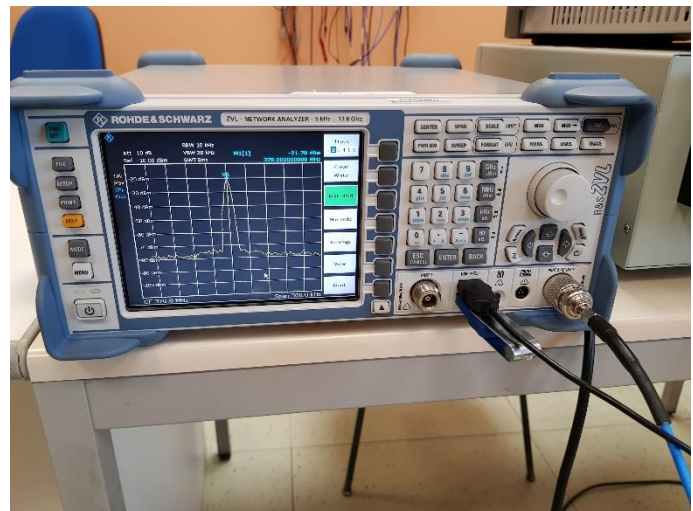


Figure A.20 Some pictures of the experiment. Left: Test using a Mylar balloon envelope. Right: Power spectrum measured at the receiver side.

Table A.9 Signal attenuation introduced by some envelope materials

Material	Attenuation introduced [dB]		
	370 MHz	868 MHz	2.49 GHz
Mylar (BoPet)	6	6	12
PCL	1	1	7
Pet with Al	9	10	19
Pet with stainless steel (thick)	2	7	15
Pet with stainless steel (thin)	1	1	13

As a result of these measurements, some materials owning good features for the realization of the radioprobes' envelop were tested in terms of signal attenuation introduced to the system. This test was very useful to identify the materials that hamper the most the electromagnetic transmission at the frequency of interest (868 MHz). The PCL material, which is a biodegradable polyester, provided the best results.

III. Temperature, Pressure and Relative Humidity sensor

As mentioned previously in subsection 3.3.1.3 - Temperature, Barometric Pressure and Relative Humidity Measurement, the BME280 device has been selected to be embedded in the radioprobes and measure temperature, pressure, and relative humidity in the atmosphere. In order to test the performance of this electronic device, a commercially available development board from Adafruit including the BME280 unit was acquired. The programming code for controlling the temperature, humidity, and pressure sensors of the BME280 was tested and modified according to the project requirements. It was written using the Arduino platform. The mother board used to control and read the measurements was the Arduino Nano (*Arduino Nano / Arduino Official Store*, n.d.). It is a small board based on the ATmega328 microcontroller, which has been selected as the main radioprobe's microcontroller also. Figure A.21 shows the main board and the BME280 development board used.

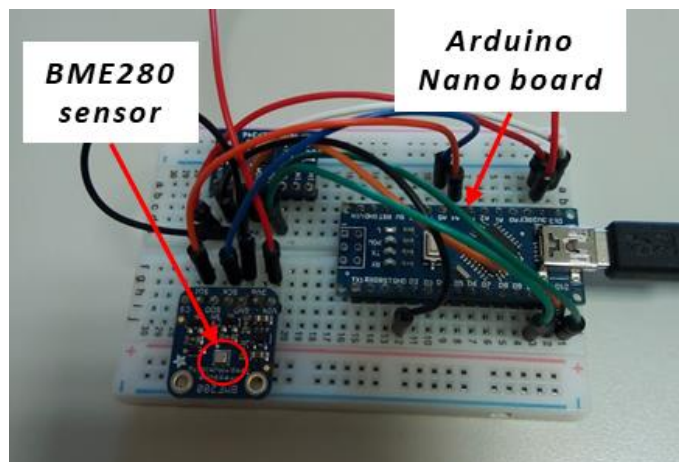


Figure A.21 Controlling board Arduino Nano and development board BME280

a. Calibration

To determine the proper operation of the programming code and the sensors' operability, the initial calibration tests were performed in laboratory. They consisted of measuring the temperature, pressure and relative humidity of the environment and contrast those data with the available ones in a rough way. Although the bias in the measurements were removed as much as possible, a precise reference inside a controlled environment was required to fully adjust the sensor readings.

To do so, and, for the purpose of properly calibrating the sensors, a set of calibration experiments were carried out in the Applied Thermodynamics Laboratory of the Italian National Metrology Institute (INRiM). Together with the programming code for controlling the sensors, the database and visualization tools were properly programmed and tested beforehand. The mentioned tools allowed acquiring, storing, manipulating, and visualizing in real time the information coming from the sensors, thus, making easier their calibration. The electronic board containing the humidity, temperature and pressure sensors was placed inside a climatic chamber model Kambic KK190 CHLT explicitly built for meteorology and climate metrology (Merlone et al., 2015). Here, the temperature and humidity parameters could be precisely modified according to the user settings. Since the BME280 unit was surrounded by other electronic components, high values of humidity were not envisaged to protect them from possible damages. The rest of the system was placed outside: control board (Arduino Nano) and acquisition system PC. The output pins of the development BME280 board were connected to the control board through a long 8 Pair Unshielded Twisted Pair (UTP) cable. The PC included the software tools for updating the programming code to the microcontroller, storing the data, and visualizing it. The equipment setup is shown in Figure A.22.

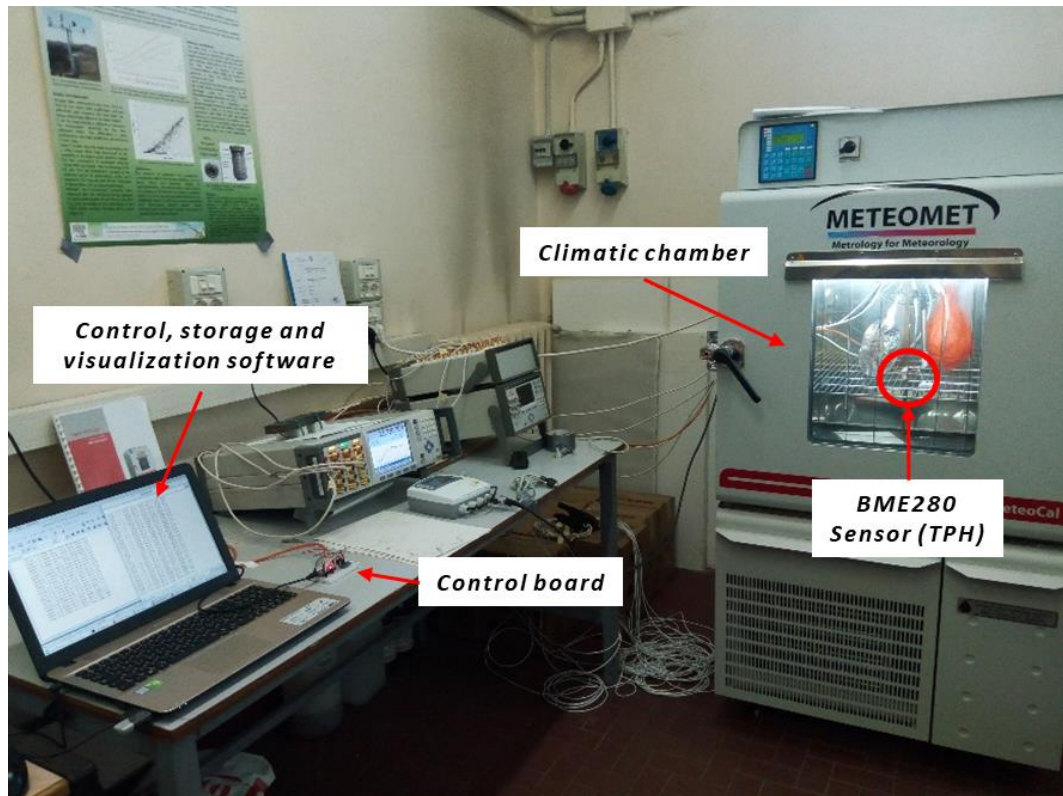


Figure A.22 Experiment setup for calibration and testing. Applied Thermodynamics Laboratory INRiM

Inside the climatic chamber, two additional temperature probes and one humidity sensor were placed as reference instruments for comparison purposes. The reference temperature probes were resistance thermometers model Pt100 connected externally to a high-precision Super-Thermometer FLUKE 1594a. The reference humidity probe used was a Delta Ohm model connected externally to a datalogger model HD27.17TS. These instruments are shown in Figure A.23, Figure A.24, and Figure A.25. At the same time, two extra reference temperature probes were added to test two different materials for the radioprobe enclosure. However, the results of the enclosure experiment are not presented here since it is not the scope of this work.

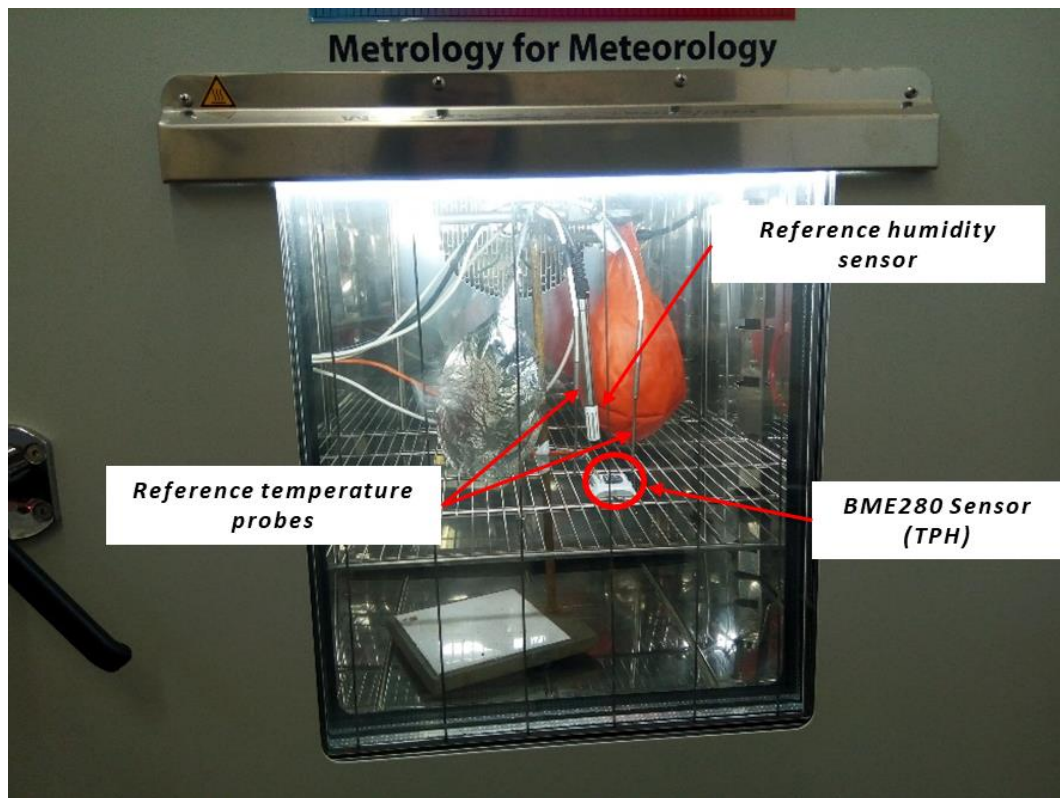




Figure A.25 Front panel of the humidity datalogger HD27.17TS Delta OHM used as reference

The climate chamber was set to provide a temperature of +20 °C and a relative humidity of 30 RH % as initial configuration. Based on the values provided by the INRiM temperature probes and the radioprobe temperature sensor, the controlling algorithm of the microcontroller was improved to match as much as possible the temperature reference readings. Similarly, the relative humidity values of the radiosonde sensor were modified to coincide with the readings of the INRiM humidity sensor. It is important to mention that the climatic chamber needed some time before achieving the set values. This can be seen from Figure A.26, which shows the radioprobe sensor measurements during the process of reaching the system stability and the initial sensor calibration.

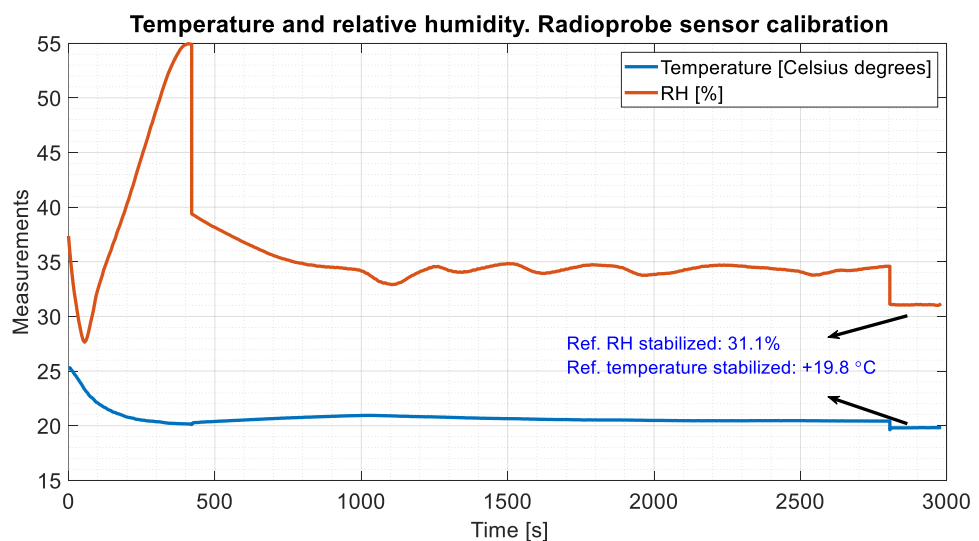


Figure A.26 Initial setting process measured by the radioprobe sensors until reaching the system stability. Temperature and humidity measurements. Calibration process.

The radioprobe sensor module was also programmed to measure pressure and to provide an estimated altitude according to the readings. Although no reference sensors for these parameters were used during this experiment, the pressure and altitude values were stored and plotted as can be seen in Figure A.27.

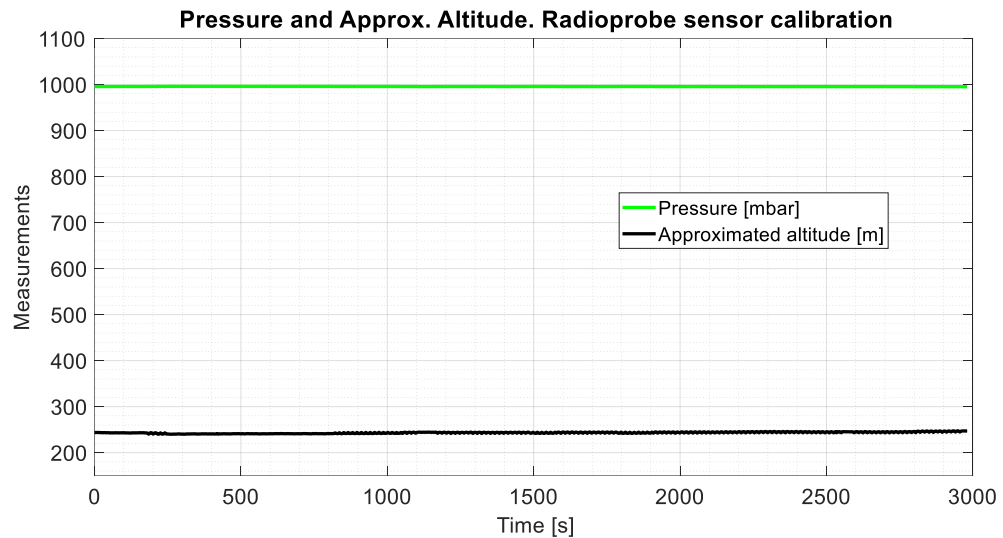


Figure A.27 Initial setting process measured by the radioprobe sensors until reaching the system stability. Temperature and humidity measurements. Pressure and approximated altitude measurements. Calibration process.

Once the radioprobe sensor readings matched those from the reference sensors, another additional test was done to fully verify the calibration process. Keeping the same equipment configuration, the climate chamber was programmed to provide a set of controlled variations, for both temperature and humidity to verify the sensors' response. From the initial configuration (temperature = +20° C, relative humidity = 30 %), small incremental steps in temperature (until +30° C) were applied to the climate chamber. For this experiment, the relative humidity was set to a fixed value of 30 %. Figure A.28 and Figure A.29 show the response of the radioprobe sensors vs. the reference sensor readings during the thermal increase steps from +24°C to +30°C, both in temperature and relative humidity.

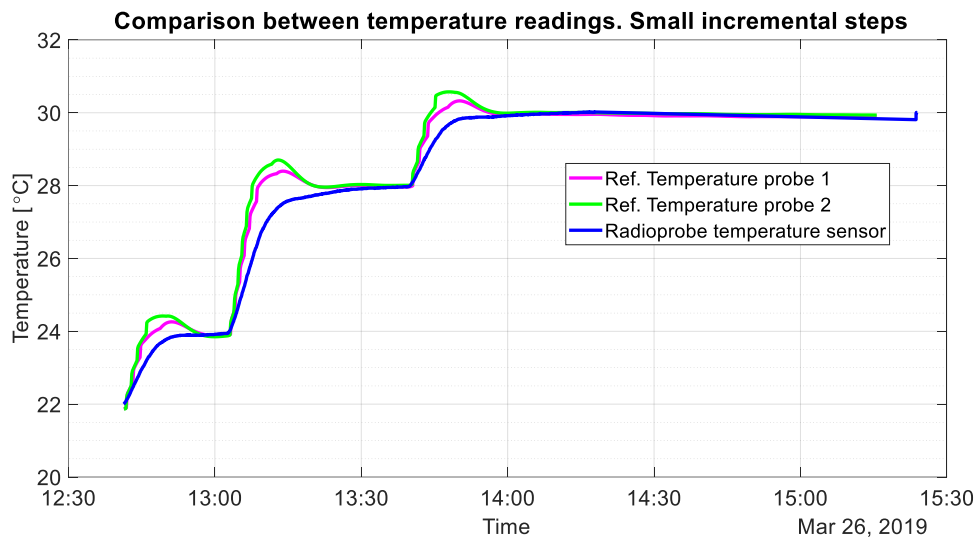


Figure A.28 Comparison between temperature measurements during the thermal increase steps from +24°C to +30°C. Temperature calibration process.

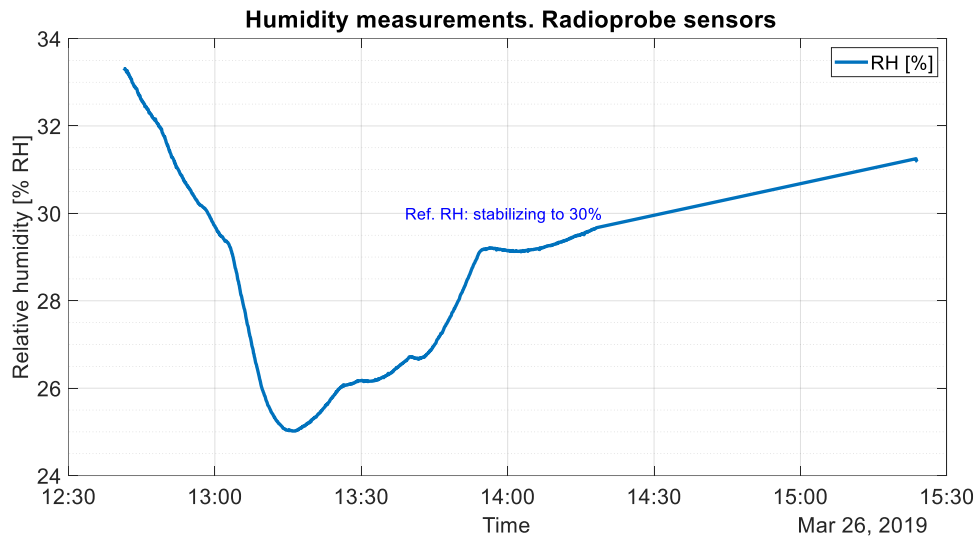


Figure A.29 Relative humidity measurements during the thermal increase steps from +24°C to +30°C. Relative humidity constant. Temperature calibration process.

In a similar way, the radioprobe humidity sensor was calibrated and tested. Once the temperature inside the climate chamber was stabilized to +30 °C, the relative humidity was decreased in steps, from 30 % to 20 % and then to 15 %. Since the information generated by the reference humidity sensor could not be extracted from the datalogger, the comparison and calibration were done based on the time at which the values were set at the climate chamber. Figure A.30 shows the radioprobe sensor measurements during these humidity decremental steps, both in RH and temperature.

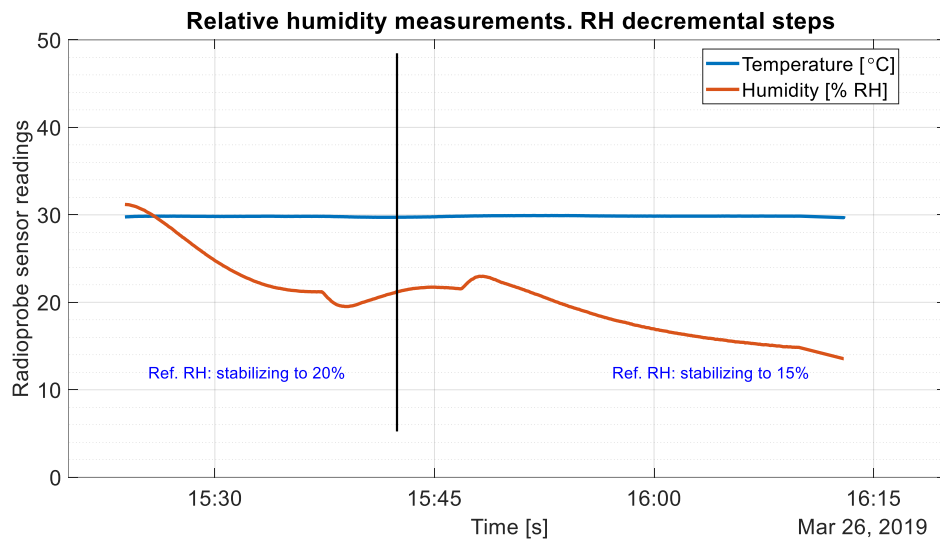


Figure A.30 Relative humidity measurements during the humidity decrease steps from 30 % RH to 15 % RH. Humidity calibration process.

From the obtained results, using high-precision sensors as reference and when applying thermal incremental steps and humidity decremental steps in time, the performance of the radioprobe sensors was evaluated. The radioprobe sensor measurements followed the same trend as the reference ones, specially at the periods where the system was stable. It can be said that the radioprobe sensors provided good accuracy as stated in the datasheet of the sensor device, making them suitable for the purpose of the final mini radioprobe design.

b. Test 1

To fully verify the performance of the proposed radioprobe sensors, an additional experiment, with larger ranges and variations, was performed. The aim of this test was to simulate the real environment in which the final radiosondes will be released. The system configuration was identical to that one from the calibration setup (see previous subsection “Calibration”); however, here just one temperature probe was used as reference. The other three temperature probes were used to evaluate the properties of some radioprobe balloons. These results are not presented here since it is not the scope of this thesis.

The climatic chamber was set initially to a temperature equal to +30 °C. Once the system was stable, the chamber was set to 0 °C and then to -10 °C. These temperature cycles were done simulating very extreme environments for the purpose of the radioprobes. This is because warm clouds are composed of liquid water and the temperatures found there will be always above 0 °C. The results of this experiment are shown in Figure A.31 and Figure A.32.

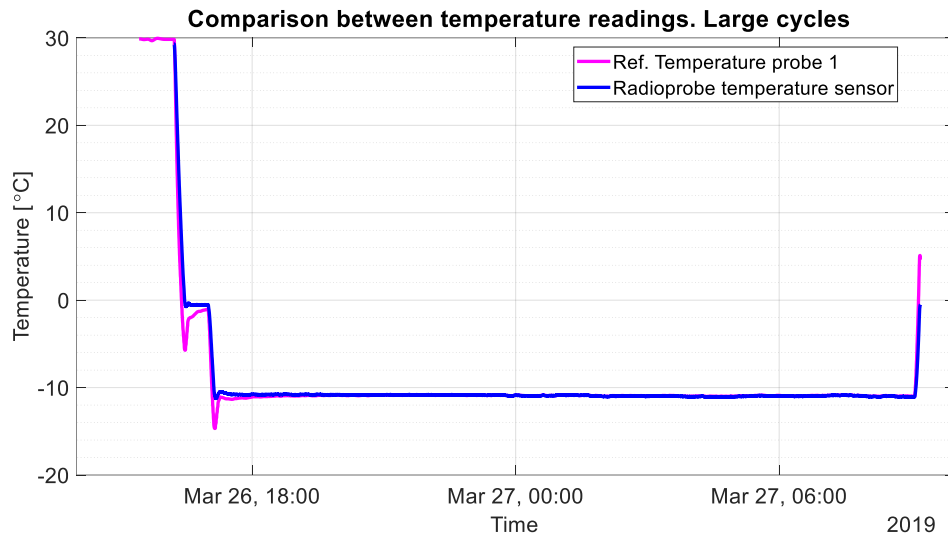


Figure A.31 Comparison between temperature measurements during large cycles. Thermal variations steps: +30 °C, 0 °C and -10 °C.

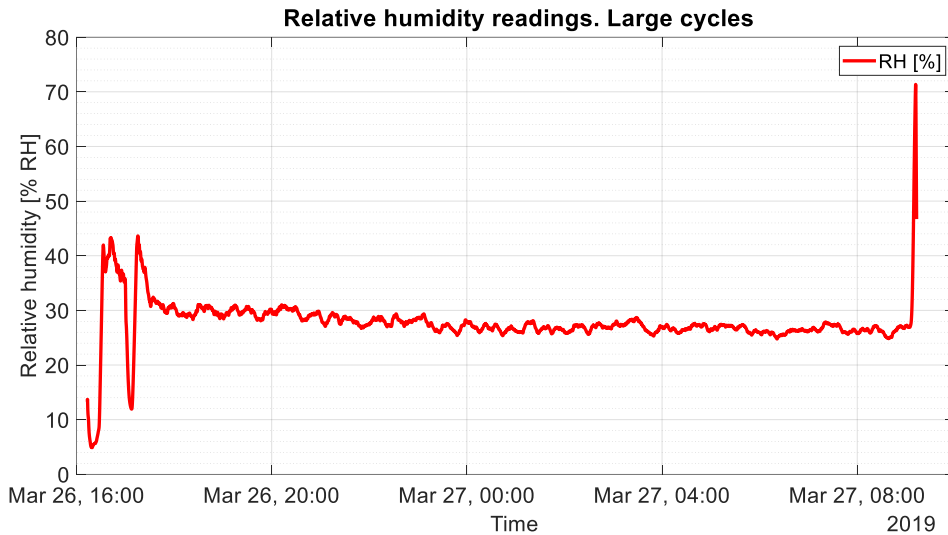


Figure A.32 Relative humidity measurements during large cycles. Thermal variations steps: +30 °C, 0 °C and -10 °C. Relative humidity constant.

As seen during the calibration measurements also, the temperature and humidity sensors proposed for the radioprobes responded positively according to their technical specifications. The differences in the readings were within acceptable ranges as displayed on the above plots. Once the final radioprobe boards are built, similar experiments must be done to find the fitting curves to fully match the proposed sensor readings to the reference values, hence reducing or eliminating in this way possible measurement inaccuracies.

IV. Positioning and tracking sensors

As mentioned previously in subsection 3.3.1.4 – Positioning and tracking Measurement, the IMU LSM9DS1 and the ZOE-M8B GNSS receiver have been selected to be embedded in the radioprobes. The main function of the IMU unit is to provide force, angular rate, and orientation information of the radiosonde flight.

The main function of the GNSS unit is to provide periodic reference position information during the flight, which is used for removing drifts in the IMU output as a post-processing step.

a. IMU Calibration

In order to test the IMU, the development board Adafruit LSM9DS1 embedding the inertial module was used. It was connected to the mother board Adafruit Feather 32u4 already described in subsection 3.3.2.1. The source code provided by the manufacturer was modified according to the needs and uploaded to the board using Arduino platform. The sensor measurements were extracted by the microcontroller using reading commands through the I²C interface.

Inertial sensors are subject to low frequency faults caused by systematic errors (bias) on the sensor readings and unit's misalignment (Sukkarieh et al., 1999). Sensor bias accumulates with time and leads to drifts in the velocity, position and attitude data provided by the inertial device. To avoid these problems, calibration processes of the IMU sensor are strongly required. In this way, the sensor bias can be determined and removed.

Calibration consists in comparing well-known reference information with the output delivered by the instrument (Zhou et al., 2020). This makes possible the identification of coefficients that allow to match the sensor readings with those coming from the reference information. For the radiosondes, these calibration steps are needed before the flight starts and while the IMU sensor is at rest. To this end, a piece of calibration code was developed and added to the main source code to control the IMU. It consisted in measuring acceleration, angular rotation, and attitude when the sensor was not experiencing any rotation. Then, the bias coefficients were computed and removed.

Accelerometer calibration

In order to calibrate the accelerometer embedded in the IMU, a reference force vector applied simultaneously to the three components is necessary (Panahandeh et al., 2010). For this purpose, gravity acceleration is the reference force commonly used (Noureldin et al., 2012). When the IMU is kept static and the only force to the device is gravity, the accelerometer output will be the reaction to the gravity vector.

Based on this, the IMU containing the accelerometer was placed onto a nearly horizontal plane with its sensitivity axis facing up. In total, 10000 samples were taken at a sampling rate of 100 Hz. Subsequently, the accelerometer was placed onto the same plane with its sensitivity axis facing downwards. Similarly, 10000 samples were taken at a sampling rate of 100 Hz. This procedure was applied to each axis of the accelerometer. With the obtained measurements, the mean acceleration for each accelerometer component was found, then the bias computed according to the next formula:

$$b_a = \frac{f_{up} + f_{down}}{2} \text{ (Noureldin et al., 2012)}$$

Where,

b_a is the accelerometer bias

f_{up} is the acceleration mean with the sensitive axis facing up

f_{down} is the acceleration mean with the sensitive axis facing down

The systematic errors or bias values of the accelerometer under test are shown in Table A.10. The accelerometer measurements during a stationary state after the bias removal are shown in Figure A.33.

Table A.10 Accelerometer's systematic error (n = 10000 samples, sampling frequency = 100Hz)

Component	f_{up} mean [m/s ²]	f_{down} mean [m/s ²]	Bias value [m/s ²]
x	9.48	-10.18	-0.35
y	9.67	-9.86	-0.09
z	9.72	-9.97	-0.13

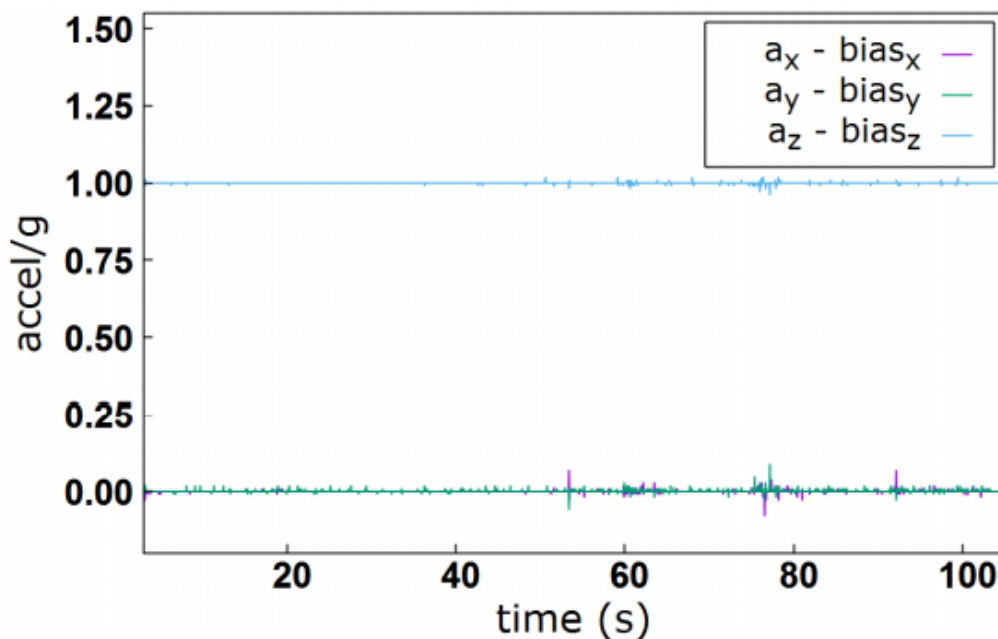


Figure A.33 Accelerometer measurements after bias removal

Gyroscope calibration

When the IMU is kept static, the true angular rate velocity is equal to zero, then what the gyroscope is measuring is the bias error (Zhou et al., 2020). The bias error can be computed as the average of various gyroscope measurements during a stationary period.

In order to get these bias values, the IMU containing the gyroscope was kept stationary and 10000 samples for each frame were taken at a sampling rate of 100 Hz. The systematic errors or bias values of the gyroscope under test are shown in Table A.11. The gyroscope measurements during a stationary state after the bias removal are shown in Figure A.34.

Table A.11 Gyroscope's systematic error (n = 10000 samples, sampling frequency = 100Hz)

Component	Bias value [degrees / s]
x	0.16
y	1.13
z	-1.86

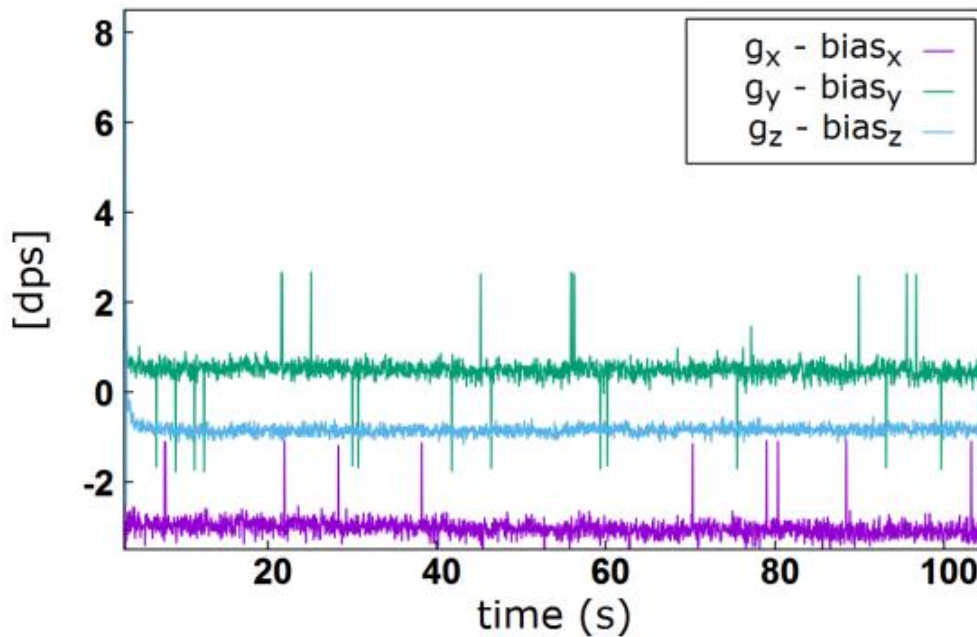


Figure A.34 Gyroscope measurements after bias removal

Magnetometer calibration

Magnetometers measure the local magnetic field, which can be then used to determine the heading of a system with respect to the Earth's magnetic North (*AN3192 Application Note* / *STMicroelectronics*, 2010). When no magnetic disturbances are present, the device's output provides a constant magnetic field vector pointing the local magnetic north (Kok & Schon, 2016). However, magnetometer's measurements are affected and distorted by the presence of magnetic fields created by nearby objects. To minimize the difference between the magnitude of the magnetic field measured by the sensor and the magnitude of the local magnetic field, the magnetometer calibration is required.

To do so, the 8-shaped pattern approach was used. It consisted in placing the magnetometer parallel to ground and move it in a figure 8 pattern while accumulating the magnetic field measurements along the three axes. Ideally, the magnitude of the magnetic field vector would be relatively constant thus the magnetometer's measurements should also be constant regardless the sensor

orientation. However, in real scenarios, magnetic field distortions lead to sensor magnetic field measurements varying with orientation. With the 8-shaped pattern, 10000 samples for each axis were taken at a sampling rate of 100 Hz. Then the average offset in the measurements was found as shown in Table A.12. The magnetometer measurements during a stationary state after the bias removal are shown in Figure A.35.

Table A.12 Magnetometer systematic error (n = 10000 samples, sampling frequency = 100Hz)

Component	Mean max value [Gauss]	Mean min value [Gauss]	Bias value [Gauss]
x	10.12	-3.92	3.10
y	8.66	-3.08	2.79
z	13.16	-2.21	5.47

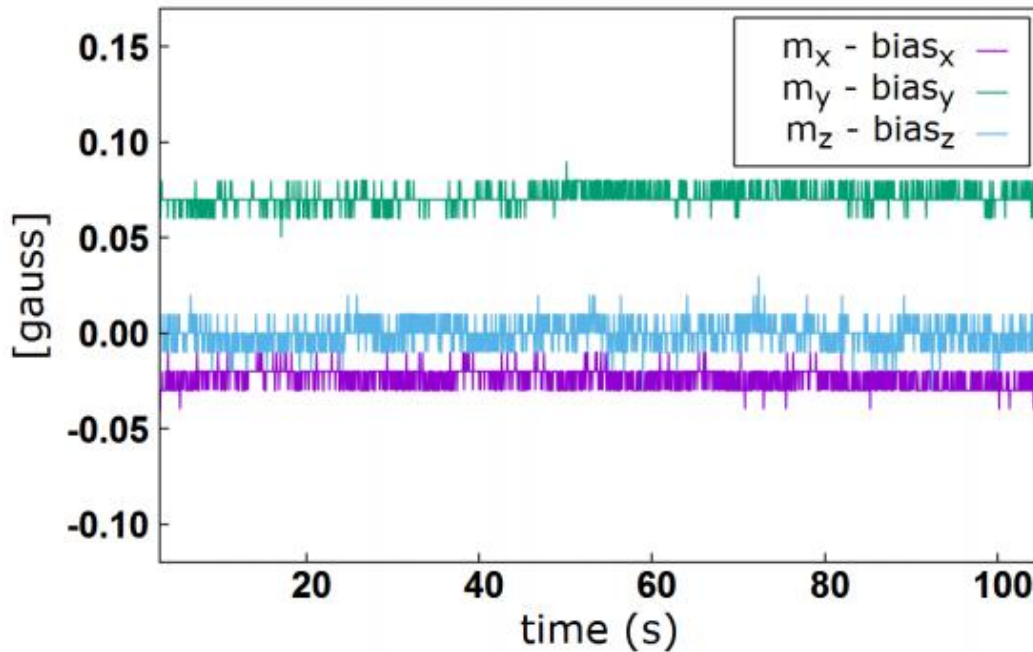


Figure A.35 Magnetometer measurements after bias removal

It should be noticed that even if the bias is removed, white noise introduced by the IMU sensors will result in drifts in the measurements (Sukkarieh et al., 1999). In order to tackle this problem, the use of GNSS observations together with the implementation of post-processing filters, will allow the correction of the IMU measurements thus a better estimation of the radioprobe motion.

b. GNSS test

In order to test the GPS module data, the development board Adafruit Ultimate GPS Breakout (*Adafruit Ultimate GPS Breakout* / *Adafruit*, 2015, p. 3) embedding the MTK3339 GPS module was used. Although this module does not include the ZOE-M8B module selected for the final design, it was used considering the fact that the GPS receiver is an external sensor where the obtained data is bounded (Sukkarieh et al., 1999). Moreover, this GPS breakout board provided the easy of

making the physical connections with the main board that the ZOE-M8B did not offered due to its extremely reduced size. The GPS module was connected to the mother board Adafruit Feather 32u4 already described in subsection 3.3.2.1. The source code provided by the manufacturer was modified according to the needs and uploaded to the board using Arduino platform. The sensor measurements were extracted by the microcontroller using reading commands through the UART interface. The system setup is shown in Figure A.36. The received messages from the GPS receiver and the translation of the GPS sentences on a map are shown in Figure A.37.

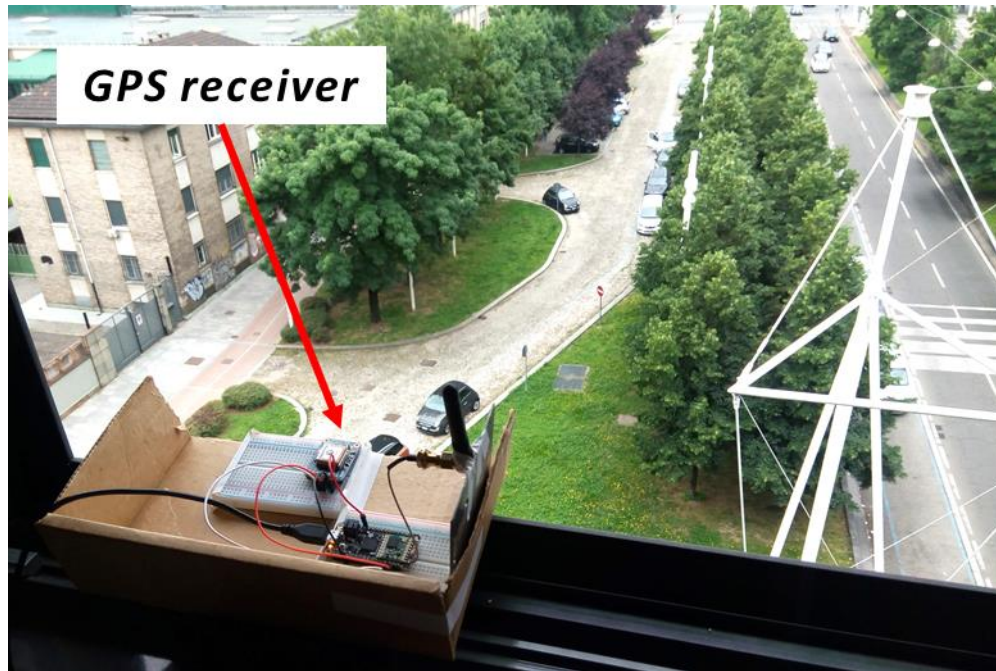


Figure A.36 System setup to test the GPS signals.

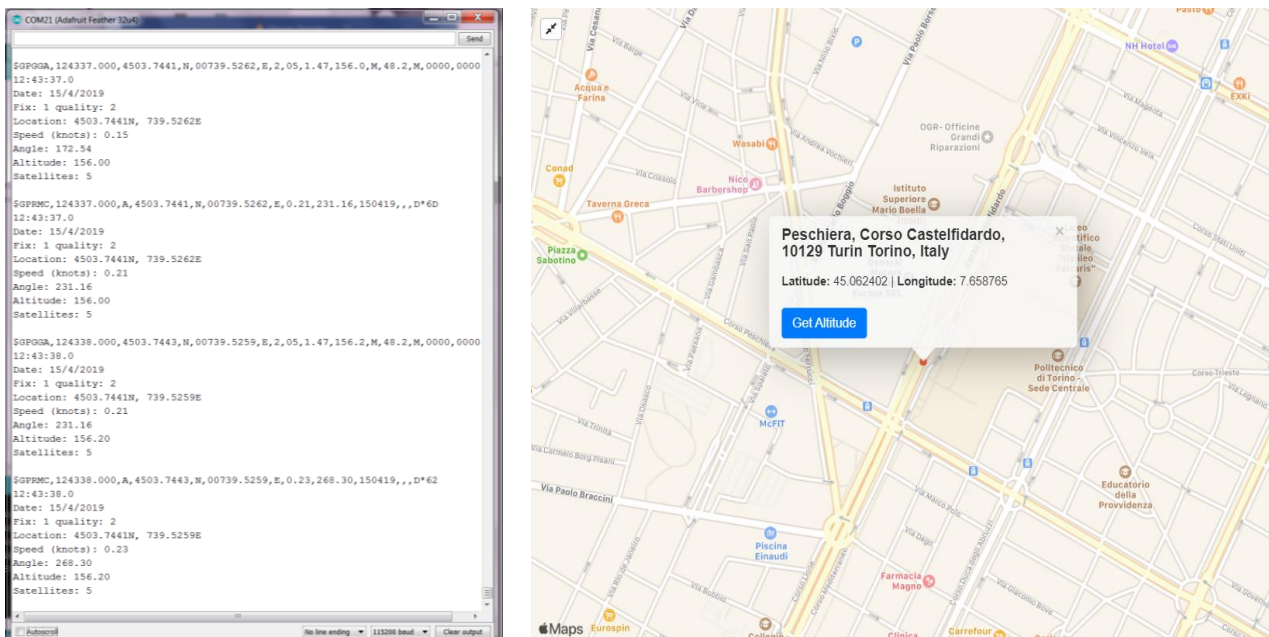


Figure A.37 Left: Received GPS sentences. Right side: Translation of the GPS sentences on a map (GPS Coordinates, Latitude and Longitude with Interactive Maps, 2021)

From , it is possible to see that the NMEA messages received from the GPS, both GPRMC and GPGLA sentences, are correct after their translation on the map. During this test, 5 satellites were available at the moment of the data collection. This was due to the location of the instruments close to the window, though the location data was reasonably accurate.

As mentioned previously, being the GPS an absolute sensor, its errors in the data are bounded. However, since faults can come up when the GPS signals are reflected off surfaces, obstructions in the signal path must be avoided. Since the final scope of the radioprobes is their release in open area environments, environmental obstructions (i.e., trees, buildings, tunnels, etc.) are not envisaged.